ABSTRACT

Title of Document: DEVELOPMENT OF THERMOELASTIC
                             COOLING SYSTEMS

                             Suxin Qian, Doctor of Philosophy, 2015

Directed By: Minta Martin Professor Reinhard Radermacher,
                             Department of Mechanical Engineering

Thermoelastic cooling, or elastocaloric cooling, is a cutting-edge solid-state based

alternative cooling technology to the state-of-the-art vapor compression cooling

systems that dominate the world today. Being environment friendly without any

global warming potential, these thermoelastic cooling systems could reduce energy

expenses and carbon emission since they are potentially more efficient than the vapor

compression cycle (VCC). Nevertheless, as a result of its immature nature, its

realistic application potential requires comprehensive research in material

fundamentals, cycle design, system simulation, the proof-of-concept prototype

development and testing. Therefore, understanding the performance potential and

limitations of this emerging new cooling technology, building the theoretical

framework and guiding future research are the objectives of this dissertation.

Thermodynamic fundamentals of elastocaloric materials are introduced first. Cycle

designs and theoretical performance evaluation are presented together with a detailed

physics-based dynamic model for a water-chiller application. The baseline system

coefficient of performance (COP) is 1.7 under 10 K system temperature lift. To

enhance the system performance, a novel thermo-wave heat recovery process is

proposed based on the analogy from the highly efficient "counter-flow" heat exchanger. Both the theoretical limit of the "counter-flow" thermo-wave heat recovery and the practical limitations by experimentation have been investigated. The results indicated that 100% efficiency is possible in theory, 60% ~ 80% heat recovery efficiency can be achieved in practice. The world first of-its-kind proof-of-concept prototype was designed based on the dynamic model, fabricated and tested using the proposed heat recovery method. Maximum cooling capacity of 65 W and maximum water-water temperature lift of 4.2 K were measured separately from the prototype. Using the validated model, performance improvement potentials without manufacturing constraints in the prototype are investigated and discussed. The COP is 3.4 with the plastic insulation tube and tube-in-tube design, which can be further improved to 4.1 by optimizing the system operating parameters. A quantitative comparison is made for thermoelastic cooling and other not-in-kind cooling technologies in order to provide insights on its limitations, potential applications, and directions for future research. Though under current research status, the system efficiency is only 0.14 of Carnot efficiency, which is less than 0.21 for conventional VCC systems, the framework carried out in this dissertation shows a technically viable alternative cooling technology that may change the future of our lives.

DEVELOPMENT OF THERMOELASTIC COOLING SYSTEMS

By

Suxin Qian

Dissertation submitted to the Faculty of the Graduate School of the
University of Maryland, College Park, in partial fulfillment
of the requirements for the degree of
Doctor of Philosophy
2015

Advisory Committee:
Professor Reinhard Radermacher, Chair
Professor Ichiro Takeuchi
Professor Marino diMarzo
Professor Jungho Kim
Professor Bao Yang
Professor Yunho Hwang

Acknowledgements

I would like to thank my advisor Prof. Reinhard Radermacher for providing me the chance to conduct my research in CEEE and an opportunity to work on this challenging project. His deep insights, continuous guidance, visions and passions in this field always inspired me. I would also thank Dr. Ichiro Takeuchi for his critics to polish my dissertation from a material scientist's perspective. Thanks to Dr. Yunho Hwang as my research advisor for his ideas, expertise and support to this project. Thanks to Dr. Jungho Kim, Dr. Marino diMarzo and Dr. Bao Yang for serving on my committee.

My deep thanks to my wife, Jingjing, who supported me and encouraged during the most difficult time of my Ph.D. study. Thanks to my parents and grandparents for their love, kind support and understanding. I would have not been able to finish this dissertation without my families' support.

Ideas and discussions with my colleagues in CEEE are always helpful, especially Dr. Jiazhen Ling and Jan Muehlbauer. My deep thanks to Dr. Yiming Wu, Dr. Yi Wang and Dr. Yunlong Geng, for their expertise to help me develop the prototype in this dissertation. I'd also like to express my gratitude to the technical help and professional assistants from my colleagues on this project in UTRC and PNNL. Finally, I would like to thank CEEE, Department of Energy, GDF-Suez, and University of Maryland Graduate School for their financial support.

Table of Contents

List of Tables

List of Figures

Nomenclature

$A*$	material constant related to hysteresis energy [J·g^{-1}]
A	area [m^2]
A$_f$	austenite finish temperature [K]
A$_s$	austenite start temperature [K]
AECR	active elastocaloric regenerator
AMR	active magnetic regenerator
Bi	Biot number
COP	coefficient of performance
c_p	specific heat [J·g^{-1}·K^{-1}]
D	mechanical efficiency loss factor
DSC	differential scanning calorimetry
DTM	dead thermal mass
ESD	energy storage density
E	Young's modulus [MPa]
E_e	electric field intensity [N·C^{-1}]
F	cyclic loss factor
Fo	Fourier number
GWP	global warming potential
g'''	generation term in energy equation [W·m^{-3}]
HCFCs	Hydrochloroflurocarbons
HFCs	Hydrofluorocarbons

HR	heat recovery
HTF	heat transfer fluid
H	magnetic field [A·m^{-1}]
Δh	latent heat [J·g^{-1}]
h	heat transfer coefficient [W·m^{-2}·K^{-1}]
$h*$	specific enthalpy [J·g^{-1}]
I	current [A]
ID	internal diameter [m]
K	material constant related to elasticity [MPa]
k	thermal conductivity [W·m^{-1}·K^{-1}]
$LMTD$	log-mean temperature difference [K]
L	length [m]
$l*$	Non-dimensional length [-]
M_f	martensite finish temperature [K]
M_s	martensite start temperature [K]
MOGA	multi-objective genetic algorithm
m	mass [kg]
$\dot{m}$	mass flow rate [kg·s^{-1}]
Δm	magnetic moment change [A·m^2·kg^{-1}]
N	tube number [-]
NIK	not-in-kind
OD	outside diameter [m]
ODE	ordinary differential equations

PEEK	polyether-ether-ketone
p	pressure [kPa]
P	polarization [$C \cdot m^{-2}$]
Q	amount of heat transferred [J]
$\dot{Q}$	capacity [W]
q	capacity per unit mass [$J \cdot g^{-1}$]
RHS	right hand side
RHX	recuperative heat exchanger
$\bar{r}$	non-dimensional ratios
ra	nitinol heat transfer area to volume ratio [m^{-1}]
s	specific entropy [$J \cdot g^{-1} \cdot K^{-1}$]
Δs	specific entropy change of martensitic phase change [$J \cdot g^{-1} \cdot K^{-1}$]
SCP	specific cooling power [$W \cdot g^{-1}$]
SMA	shape memory alloy
SMP	shape memory polymer
sec	second
T	temperature [°C]
$\dot{T}$	temperature change rate [$K \cdot s^{-1}$]
ΔT_{ad}	material adiabatic temperature span [K]
ΔT_{lift}	system temperature lift [K]
$\Delta T_{approach}$	heat exchanger approach temperature [K]
T_c	heat pump heat source/cold side temperature [K]
T_h	heat pump heat sink/hot side temperature [K]

TMR	thermal mass ratio between SMA and HTF inside SMA bed [-]
TMR_{HR}	thermal mass ratio between SMA and regenerator [-]
t	time, or duration [sec]
t*	heat recovery coefficient
u	fluid mean velocity [m·s^{-1}]
u*	specific internal energy [J·g^{-1}]
$\dot{V}$	volumetric flow rate [m^3·s^{-1}]
V	volume [m^3]
v	specific volume [m^3·kg^{-1}]
VCC	vapor compression cycle
W	work [J]
$\dot{W}$	power [W]
w	specific work [J·g^{-1}]
x	characteristic length [m]
Z	thermoelectric materials figure-of-merit [K^{-1}]
α	thermal diffusivity [m^2·s^{-1}]
α_L	thermal expansion coefficient [K^{-1}]
α_S	Seebeck coefficient [V·K^{-1}]
β	contact area ratio [-]
δ	equivalent thickness [m]
ε*	effectiveness
ε	strain [-]
σ	stress [MPa]

γ	non-dimensional latent heat [-]
η	efficiency [-]
κ	thermal mass factor [-]
ρ	density [kg·m^{-3}]
ρ_e	electric resistivity [Ω·m]
τ	time constant [sec]
ξ	martensite phase fraction
$\dot{\xi}$	martensite phase fraction change rate [s^{-1}]
$\mu_0 H$	magnetic field [Tesla, or T]
Φ_{mat}	normalized materials level *COP*, or materials exergetic efficiency [-]
Φ_{sys}	system exergetic efficiency (normalized to materials *COP*) [-]
Ψ	uniformity index
Δ	material constant related to strain [-]

Subscripts

ad	adiabatic
AM	austenite to martensite
bs	baseline
cond	conduction
cyc	cycle
f	fluid
HT	heat transfer
hp	heat pump

init	initial
mat	material
mot	motor
LH	loading head
MA	martensite to austenite
M	martensite
m	intermediate
opt	optimum
pc	phase change
rec	recovery
s	solid, solid heat exchanger or bed
sat	saturation
tot	total
trsm	transmission
+ or ld	loading
- or uld	unloading

Chapter 1:   Introduction

1.1   *Background and Motivation*

Recently, traditional refrigerants in a vapor compression system, such as hydrochloroflurocarbons (HCFCs) and hydrofluorocarbons (HFCs), have been considered as greenhouse gases exaggerating the global warming crisis. After the Montreal Protocol, HCFCs have been banned to save the ozone layer and HFCs became of the most widely used family of refrigerants today as substitutes. However, most of the HFCs have high global warming potential (GWP), each of which molecule is equivalent to more than 1,000 CO_2 molecules (EPA database, 2014). Moreover, the atmospheric lifetime of these HFCs are also quite long, varying from 2.4 years to 270 years. Therefore, when the HTFs are released to atmosphere through leaks, servicing, and equipment disposal, it would continuously contribute to global warming, unless we can find a way to reduce the HFCs emission by replacing either HFCs refrigerant family, or the entire vapor compression cooling systems.

The most widely used and straightforward approach was to find a substitute refrigerant. According to Calm's classification (2008), we are now looking for the 4th generation refrigerant, which ideally should have zero/low ozone depletion potential, low GWP, and better thermal performance and transient response. Nevertheless, it was also pointed out that achieving these goals might need some compromise. R123 has very low GWP, good flame suppression, good thermal performance, short atmospheric lifetime but non-zero ODP (0.011). This is a good example to show

tradeoffs between ozone depletion and climate change. Toxicity and flammability were additional resistance to screen out more potential candidates, especially for automotive uses, such as DP-1 as an alternative to R134a. Hydrocarbons, such as R290 and its mixture with other HFCs were recommended as alternatives for R12 and R22 since these alternatives demonstrated slightly higher thermal performance (Mohanraj et al., 2009). Other natural refrigerants were more often used for their specific applications and required special designs, such as vacuum operation for water, trans-critical cycle for carbon-dioxide and toxicity countermeasures for ammonia.

Alternatively, there is another challenging and ambitious approach. That is, to find a not-in-kind (NIK) cooling technology without using any climate endangering fluid. Although it sounds to be attractive, developing a new cooling technology from scratch to commercial level is risky and challenging. Figure 1-1 provides a classification of the closed loop NIK cooling technologies. It should be noted that open loop technologies, such as evaporative cooling, are not included. The first category, solid-state, is totally free from using GWG and does not pollute ozone layer as well, therefore, is the most promising candidate from climate impact perspective disregarding other aspects. Whereas, other NIK technologies are still depending on a liquid or gaseous working fluid, and might be involved with the same climate concern as the vapor compression systems.
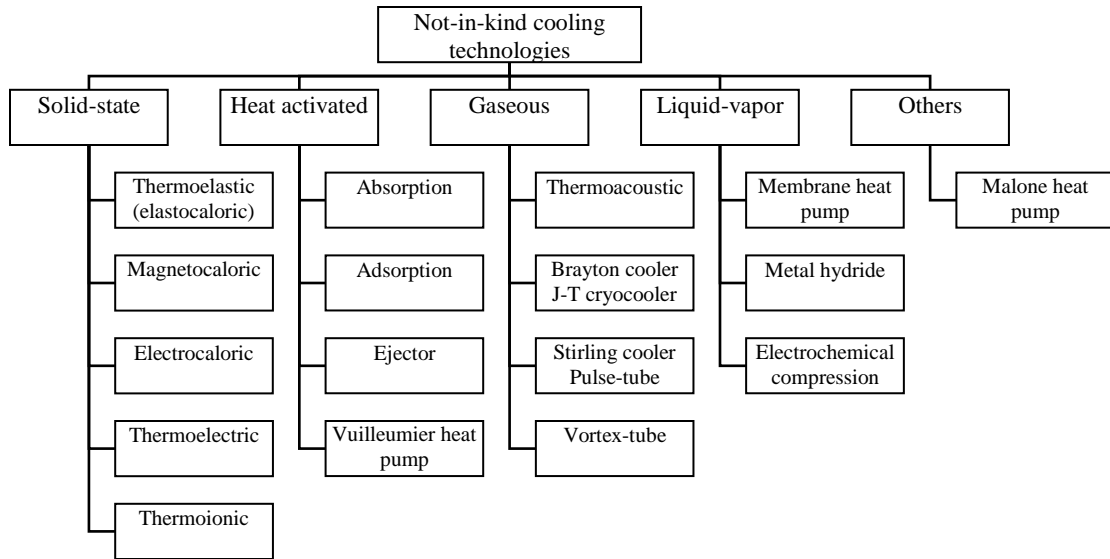
Figure 1-1: Classification of some closed loop NIK cooling technologies as an overview of thermoelastic cooling. (J-T: Joule-Thompson)

As indicated by Figure 1-1, thermoelastic cooling, also known as elastocaloric cooling, belongs to the solid-state category. The main motivation of this study, is to explore the applicability of this new cooling technology. In fact, in a few recent review papers discussing those alternative technologies or NIK technologies, thermoelastic cooling was too new to be listed (Bansal et al., 2011, Bansal et al., 2012, Goetzler et al., 2012, Brown and Domanski, 2014). It should be noted that in the study by Brown and Domanski (2014) and their early reference (Fischer et al., 1994), the "thermoelastic heat pump" in fact referred to the elastomer or shape memory polymer (SMP) heat pump, not the thermoelastic heat pump based on shape memory alloy (SMA). The only mentioned literature had a sophisticated NIK technologies quantitative ranking, but unfortunately, was based on very rough performance estimation for thermoelastic cooling since very little knowledge was available at that time (Goetzler et al., 2014).

3

The terminology "thermoelasticity" has long been used in solid mechanics textbooks (Fung, 1965, Swalin, 1962). Thermoelastic, literally means "relating to elasticity in connection with heat" from Oxford dictionary, generally referring to the change in size or shape and corresponding stress of a solid object to temperature change (heating/cooling), or the reverse temperature change due to solid deformation. In fact, the change of size according to temperature change was well known, that in most cases a solid material expands while heated and contracted while being cooled down. Its reverse process, however, was often neglected, since the temperature change of common materials is usually negligible during an adiabatic compression or a tension process. Quantitatively speaking, the temperature increases by 0.2 K under 50 MPa uniaxial compression principal stress for cement (Beghi et al., 1986). Taking the value of 1.5 $J \cdot g^{-1} \cdot K^{-1}$ as the specific heat for cement, the corresponding energy density per unit mass is 0.3 $J \cdot g^{-1}$. This effect is much more significant for elastomers, such as rubber and some other polymers, due to their micro scale nature that the carbon molecules in the chain can spin when stretched and correspondingly change entropy significantly in the macro scale. The reported adiabatic temperature change for polymethylmethacrylate (PMMA) was as high as 5 K under 190 MPa stress at 25°C room temperature, which is corresponding to 7.5 $J \cdot g^{-1}$ energy density per mass if specific heat of 1.5 $J \cdot g^{-1} \cdot K^{-1}$ was used (Rodriquez and Filisko, 1982). With adiabatic temperature change of up to 9.1 K, natural rubber has the highest energy density of 17 $J \cdot g^{-1}$ (Mitchell and Meier, 1968).

In this study, the meaning of "thermoelastic", however, refers only to the caloric effect associated with uniaxial stress/strain change in SMAs, unless otherwise

mentioned. The thermoelastic or elastocaloric effect in a SMA is different from that in those aforementioned materials, since it involves a solid-solid phase change process and the latent heat associated with it. Figure 1-2 is a comparison between the stress induced phase change for SMA, and the pressure induced phase change for a vapor-liquid system.

(a) Stress induced phase change releasing latent heat ($\sigma_{sat} < \sigma_{sys}$)

(b) Releasing stress leads to reversed phase change and absorbing latent heat ($\sigma_{sat} > \sigma_{sys}$)

(c) Pressure induced condensation releasing latent heat ($P_{sat} < P_{sys}$)

(d) Pressure induced boiling absorbing latent heat ($P_{sat} > P_{sys}$)
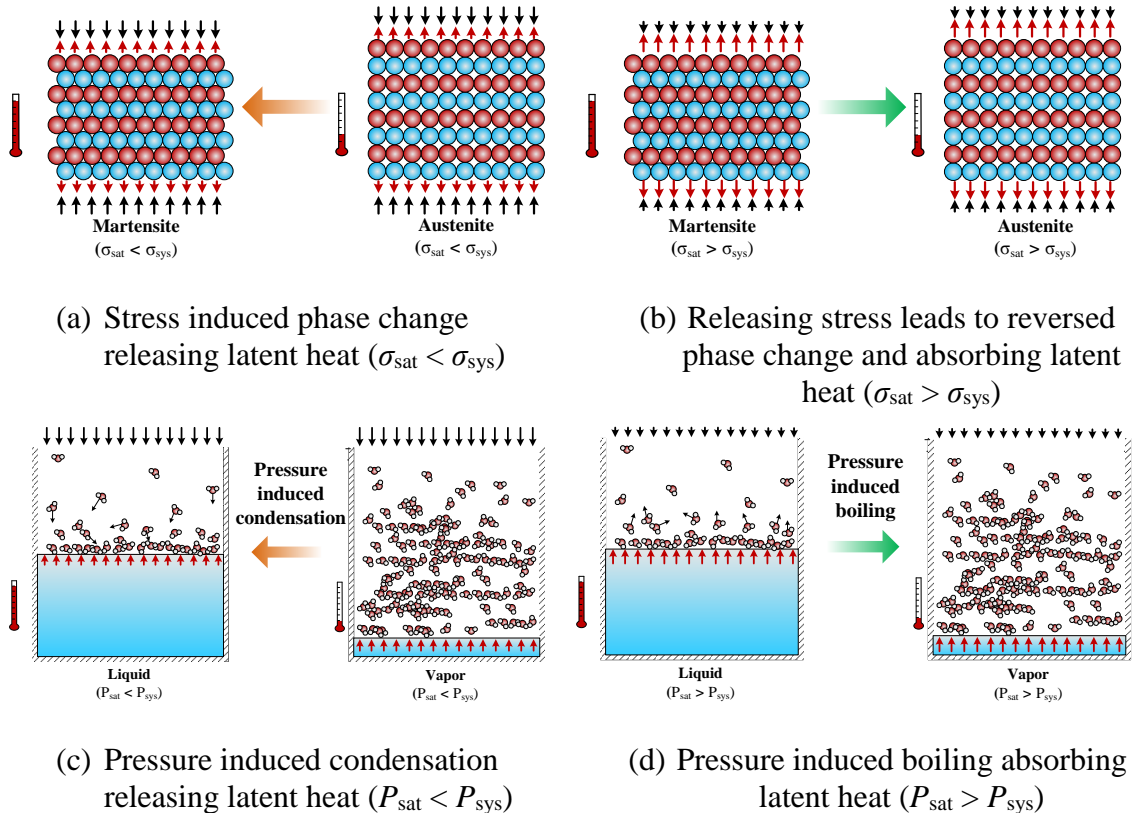
Figure 1-2: Illustration of stress induced martensitic phase transformation process, a.k.a. elastocaloric or thermoelastic effect in a SMA material and comparison to adiabatic vapor-liquid phase change.

As shown in Figure 1-2 (a), when the SMA is subject to an external stress greater than the phase change stress (or "saturation stress") under current temperature, the SMA undergoes phase transformation from austenite to martensite (AM), and

releases latent heat. In contrast to the vapor-liquid system, the vapor condenses and releases latent heat when the vapor pressure is higher than the saturation pressure under the system's current temperature, which is the case in the condenser coils for a vapor compression heat pump. The reverse process creates cooling. Figure 1-2 (b) shows the opposite martensite to austenite (MA) process, when the applied stress is removed and is less than the phase change stress at given temperature, when it absorbs heat to generate the cooling effect. The corresponding process in the vapor-liquid system is the flashing evaporation cooling process when the vapor pressure is lower than the saturation pressure, where the low pressure is created by a compressor suction port or a vacuum pump.

Sophisticated system and several key components are necessary, in order to turn the elastocaloric effect into a continuously operating thermoelastic cooling system, as illustrated in Figure 1-3. The core of the system is the SMA material, which could be made in various shapes under different driving mechanisms. A superior SMA material with high thermal performance, long fatigue life, and low cost is the key to a successful development of thermoelastic cooling system. Therefore, the SMAs with large elastocaloric effect are reviewed and summarized in this study. The second most important part is the mechanical driving system (work input interface). It is always preferred to have a robust design with low friction, large power density and easy implementation. The opportunities are utilizing design of driving mechanism from both SMA heat engine and SMA (or elastomer) heat pump as the basis to design the future thermoelastic cooling system. The development status, especially the driving mechanism of SMA heat engine, SMA cooling/heat pump system, and elastomer heat

pumps, are also summarized in this study. The third feature is heat transfer, which is extensively discussed throughout different chapters in this thesis, including the cycle design, novel designs and optimization. The next, but of equally essential part, is the regenerator/heat recovery (HR) design. The heat recovery/regenerator is used to increase the overall system temperature lift, and improve the system performance via an additional heat exchanger or heat transfer process. Since heat recovery/regeneration helps to improve more, it is much more important for thermoelastic cooling and other NIK technologies than vapor compression cooling. The terminology "regenerator" originally refers to a high volumetric density storage type heat exchanger used in gaseous cooling systems. Here, heat recovery is a more appropriate terminology since solid-state material is used. Nevertheless, the heat recovery/regenerator designs used in various cooling technologies are summarized and compared, to provide a basis and guide future thermoelastic cooling system design and development. It should be noted that the review of heat recovery/regenerator design could also be informative and helpful to all those related NIK cooling technologies, since most of the researchers only focused on their own field, and there has not been any review and comparison among different technologies for the heat recovery/regenerator designs yet. Work recovery by a conjugated SMA design is an important feature to improve the efficiency of the driving system. More details regarding this design is covered in Chapter 5.
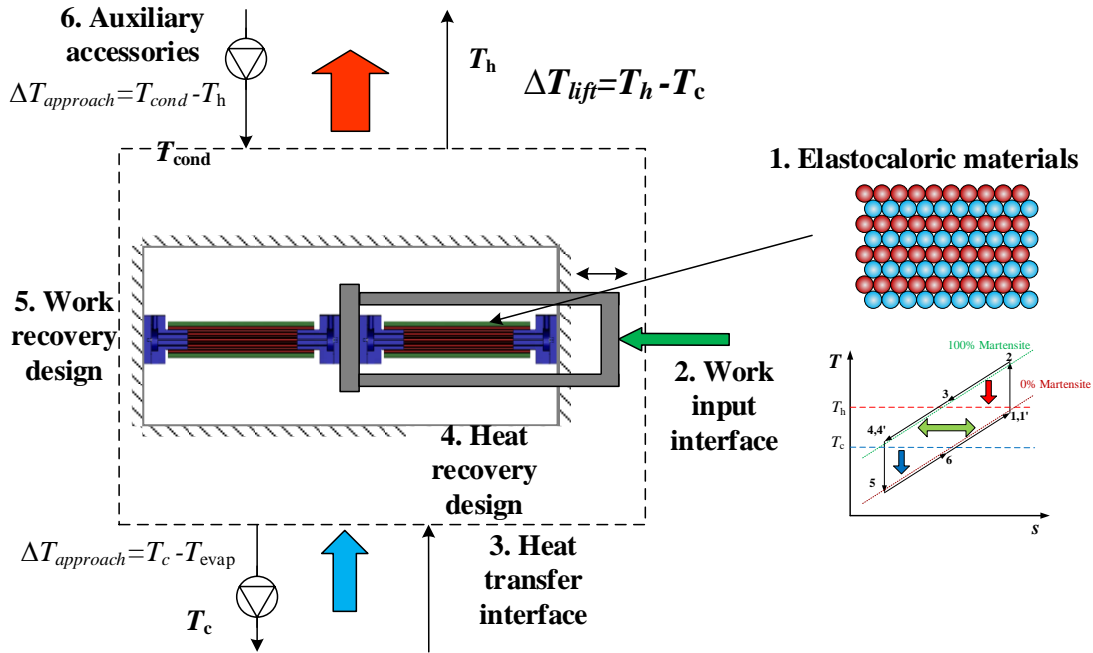
Figure 1-3: Illustration of key components in a thermoelastic cooling system.

1.2   *Literature Review on Thermoelastic Cooling*

To be able to build a successful thermoelastic cooling system, essential knowledge from the material with elastocaloric effect, to the system layout, and corresponding thermodynamic cycles is necessary, where both heat engine cycle for power and heat pump cycle for cooling are needed. This section reviews the most important SMA materials with large elastocaloric effect. The thermoelastic heat engines using SMA are summarized, focusing on the system layout, driving mechanism design and potential challenges. Unfortunately, there were only a few literature available for SMA heat pump. On the other hand, elastomer or SMP heat pump made some endeavors during the past few decades but, has been proved to be limited by the materials' poor fatigue life. Nevertheless, the various driving mechanism designs that have been utilized previously could be taken as lessons learned for thermoelastic

8

cooling applications.

1.2.1 Materials with Large Elastocaloric Effect

The materials used for thermoelastic cooling is associated with the elastocaloric effect. It refers to the latent heat released/absorbed during the solid-solid phase change process, induced by the uniaxial loading, i.e. tensile or compressive force. This solid-solid phase change is between martensite and austenite (or parent phase) in SMAs. Unlike typical crystals, the unique recoverable large strain during the solid-solid phase change in SMAs is also referred to the superelasticity (SE).

SMAs have been applied as actuators, couplings, smart materials and biomedical structures during the last few decades. However, we are more interested in investigating the thermal performance or energy conversion capabilities as a byproduct of those SMAs. This session mainly focuses on the thermal aspects of potential SMAs. A comprehensive review of shape memory materials, including SMAs, shape memory ceramics and SMPs, was carried out by Otsuka and Wayman (1998).

The first SMA was reported by Chang and Read (1951) in an Au-47.5 at % Cd alloy. Other early following studies were focusing on using either solid-state mechanics or use electron-microscope to understand the physics behind the phase change phenomena. However, thermal performance was not as important and barely reported in those early SMAs, including Ag-Cd (Krishnan and Brown, 1973), Au-Cd (Lieberman et al., 1955), Ag-Zn (Cornelis and Wayman, 1974) and In-Tl (Basinski and Christian, 1954).

After those early successes in finding binary alloys, people later discovered more and more complicated ternary alloys, and alloys even with four or five elements. The Ni-base alloys, especially Ni-Ti alloy, had become the most popular SMA and dominated the market after its discovery in 1959 (Buehler et al., 1963) from Naval Ordnance Laboratory, where the Ni-Ti was named for "nitinol" since then. Ni-Ti alloy and copper based alloys are most widely used as engineering functional materials for a variety of applications, including automotive, aerospace, mini actuators and sensors, biomedical, and orthopedic surgery (Jani et al., 2014). Ternary Ni-based alloys were aimed to improve its performance for different applications. Saburi (1998) suggested that Cu addition could be used to reduce the stress-hysteresis in the stress-strain curve for pure Ni-Ti alloy, when the Cu percentage was less than 10%. Copper could also avoid aging effect, but its latent heat is reduced (Bechtold et al., 2012). Extensive studies have been conducted in University of Tsukuba, Japan for Ni-based alloys using other substitutive elements. Adding Nb (niobium) increased the hysteresis, which was not favorable for energy conversion application, but was convenient for coupling devices (Saburi, 1998, Piao et al., 1992). Ti-Ni-Pd alloy was also studied (Golberg et al., 1995, Shimizu et al., 1998), but only performed partial shape memory alloy, i.e. low strain recovery ratio.

Cu-based family of SMAs were also popular, since Cu is much cheaper than Ti. Binary alloy, including Cu-Zn (Romero and Pelegrina, 2003) and Cu-Sn (Miura et al., 1975) were investigated in literature. Most literature were focused on ternary alloys, which improved both the mechanical and thermal performance of the SMAs. Cu-Au-Zn alloy was one of the early study (Miura et al., 1974), unfortunately with small

adiabatic temperature span. University de Barcelona, Spain, was the pioneer and dominant the research in studying the thermal performance of other Cu-based SMAs alternatives, including Cu-Zn-Al (Bonnot et al., 2008), Cu-Al-Ni (Picornell et al., 2004), and Cu-Al-Be (Manosa et al., 1993). Among them, Cu-Al-Ni and Cu-Zn-Al were regarded as most promising materials, since they have demonstrated higher latent heat than other options. However, all Cu-based SMAs were facing the same fatal concern of poor fatigue due to their brittle nature, which limits their real life applications.

Ferrous alloys were not as popular as Ni-based and Cu-based SMAs. Most literature were focusing on the shape recovery degree for a new composition, or studying phase change physics via the microscope photos. Only a few studies addressed the latent heat of ferrous alloys, which was much smaller when compared with that of Ni-based and Cu-based alloys. The phase transformation temperature range was also narrower. Nevertheless, ferrous alloys do not have fatal issues such as brittleness shown in Cu-based SMAs, and still have potential for improvements, by adding other elements like Si, Co, and even C (Maki, 1998).

A detailed comparison was listed in Table 1-1. Standardized testing for more elastocaloric materials is urgently needed since thermal performance measurements were conducted mainly during the past two decades, and current data were only available for a few candidates.

Table 1-1: List of elastocaloric effect shape memory alloys.

Materials Composition	Category	ΔT_{ad} [°C]	Density [kg·m^{-3}]	ESD* [MJ·m^{-3}]	Cons	References
Ag-Cd	phased out SMAs	/	/	/	little knowledge on thermal performance	Krishnan and Brown, 1973
Ag-Zn		/	/	/		Cornelis and Wayman, 1974
Au-Cd		/	/	/		Lieberman et al., 1955
In-Tl		/	/	/		Basinski and Christian, 1954
Cu-Zn	Cu-based SMAs	11.3 – 14	8500 – 8550	39 – 49	brittle aging poor fatigue	Romero and Pelegrina, 2003
Cu-Zn-Al		11.7-19.0	7800 – 8000	37 – 64		Bonnot, et al., 2008
Cu-Al-Ni		13.6	7100 – 7200	34 – 44		Picornell et al., 2004
Cu-Al-Mn		9 - 15	7100 - 7500	28 - 37		Sutou et al., 2004
Cu-Al-Be		9.4 – 16	7000 – 7300 ***	26 – 47		Manosa et al., 1993, Planes et al., 1992
Cu-Sn		/	/	/		Miura et al., 1975
Cu-Au-Zn		3.9 -- 4.9	10812 ***	14 – 18		Miura et al., 1974
Fe-Ni-Co-Ti	ferrous SMAs	/	/	/	small latent heat	Maki et al., 1984
Fe-Pd		2.3	10729 ***	5.9		Xiao et al., 2013
Fe-Pt		/	/	/		Foos et al., 1975
Fe-Rh		5.2	10111	24.7		Nikitin et al., 1992
Ni-Ti	Ni-based SMAs	17 – 23	6400 – 6500	60 – 82	high cost	Cui et al., 2012a
Ti-Ni-Cu		6.1 – 15.5	6500	33 – 82		Nam et al., 1990, Bechtold et al., 2012
Ti-Ni-Nb		/	/	/		Piao et al., 1992
Ti-Pd-Ni		/	/	/		Shimizu et al., 1998
Ni-Fe-Ga		10.7 – 11.7	8600	42 – 46		Pataky et al., 2015
Ni-Fe-Ga-Co		9 – 10	8600	35 – 40		Xiao et al., 2015

*: here T_{pc} means the phase change temperature range, ESD means energy storage density
**: estimated based on other Cu-based alloys
***: density estimated based on the alloy composition averaged pure substances density

1.2.2 Thermoelastic Heat Engines

Using SMAs as low temperature heat source driven heat engines attracted a few generations of engineers' interest, since it could be compact and capable to operate under small temperature difference. Banks (1975) invented the first continuously operating SMA heat engine. It was a flywheel (drum) connected with 20 Ni-Ti wires. The eccentric position of the wheel hub caused the Ni-Ti wire to be contracted to the original length when heated and stretched when cooled down, which eventually drove the wheel continuously spinning. Johnson (1977) improved Banks design by adding the regeneration process and changed the layout accordingly. In his design, two pulleys with slight different diameters were used. Since one pulley at the heat source was smaller than the other, the Ni-Ti wire was stretched when leaving the heat source and contracted back to its original shape on the other way back. As shown in Figure 1-4 (b), the counter-flow regenerator located in the middle was designed to exchange sensible heat between two Ni-Ti wires or sheets. Johnson (1985) further applied two-way SMA effect to enhance the energy conversion efficiency. Pachter (1979) invented an updated two pulleys engine by synchronizing the pulleys together using an additional chain. Recent thermoelastic heat engine patents focused on either much larger scale or much smaller scale. Kirkpatirck et al. (2008) disclosed a microelectromechanical system (MEMS) based heat engine, which took advantage of the thin film made of SMA oscillation when exposed to temperature gradient. They claimed that the micro scale surface area to volume ratio significantly increased and contributed to performance improvement. On the other hand, GM patented several

inventions for power plant scale energy harvesting and conversion (Wittorf et al., 2012).
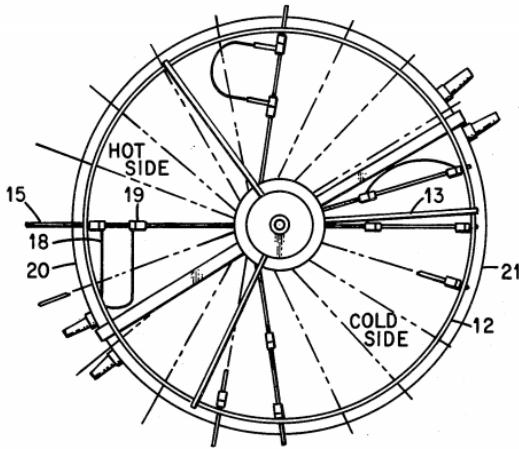
(a) Rotating flywheel (drum) design with NiTi wires (Banks, 1975)
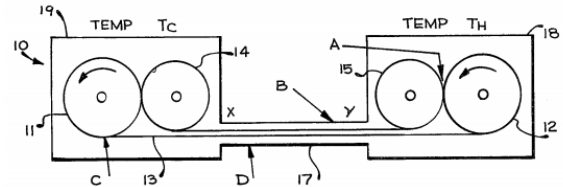
(b) Two pulleys design with regenerator in the middle (Johnson, 1977)
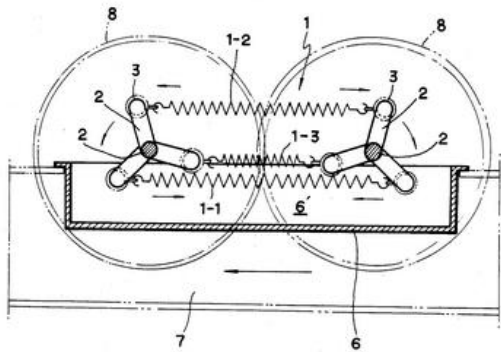
(c) Twin-crank type design (Shin et al., 1987)
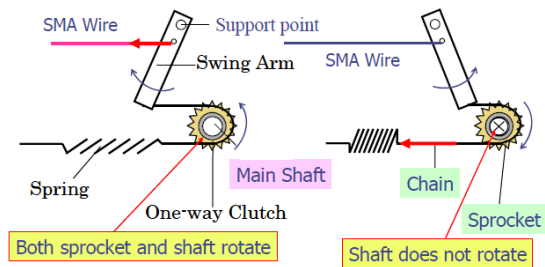
(d) Single swing arm type design (Kaneko, 2011)
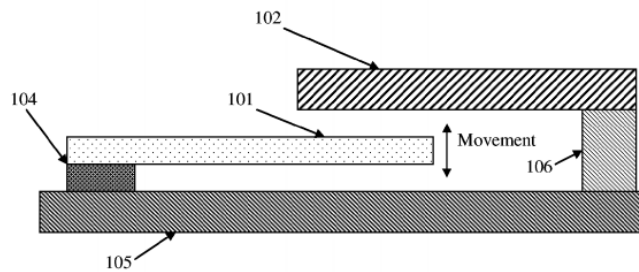
(e) Oscillation beam type MEMS heat engine design (Kirkpatrick et al., 2008)

Figure 1-4: Demonstration of various thermoelastic heat engines designs.

Wakjira (2001) designed and developed a SMA heat engine by modifying the two

pulleys design. The improvement was the pitch sprockets, which engaged the SMA chain to avoid any slip between pulleys and SMA chain and therefore reduce the potential friction. However, no experimental or simulation results were reported for the prototype heat engine. Schiller (2002) designed, simulated and tested a twin-crank engine. Multiple wires were used between two cranks and the prototype was proved to be functioning well. The efficiency of the heat engine, however, was still not answered. Details of more than twenty inventions were summarized in his study also. Using mechanics and dynamics details, Sato et al. (2008) established the power generation characteristics equation to measure the engine's power output in a lab scale prototype connected to the generator. The maximum measured power was 1.16 W. Later, Sato et al. (2011) built a larger scale prototype with the same layout and achieved 3.74 W power on the load side. They also reported the optimum rotation speed and explained the physics of the optimum rotation speed via analytical approach. Kanada (2008) demonstrated another small scale prototype with two pulleys design using Ni-Ti wires. The measured torque was proportional to the Ni-Ti winding number over the small pulley, and 6 N·m torque was measured. They even applied the engine on a tricycle with 44 wires looped between the pulleys. Kaneko and Enomoto (2011) demonstrated a reciprocating heat engine, which used one swing arm with a spring to transform the linear reciprocating motion of SMA wire to the shaft rotation. However, the operation requires a clutch and therefore the prototype was not operating continuously. The maximum report power for this prototype was around 90 mW. Zhu et al. (2001a, 2001b) developed a sophisticated system model to evaluate the performance of a twin-crank heat engine and then compared the model

15

prediction with previous experimental data.

There were also some theoretical analysis studies. Gil and Planell (1999) used previously defined ideal thermoelastic heat engine efficiency equation for several SMAs with different compositions including Ti-Ni-Cu, Ni-Ti, Cu-Al-Ni, Cu-Zn-Al, Au-Cu-Zn, Au-Ag-Cd, Au-Cd, Ag-Cd, and In-Tl, and concluded that Ti-Ni-Cu had the highest efficiency among them. Early works on deriving the analytical efficiency relies on simple equilibrium stress-strain model (Tong and Wayman, 1974, Ahler, 1975, Wayman and Tong, 1975, Delaey and Lepeleire, 1976, Cunningham and Ashbee, 1977), where only a single stress-saturation temperature is needed and computation is simple. Ziolkowski (1993) used three different one dimensional constitutive models to evaluate the heat engine cycle performance for the Ni-Ti and Cu-Zn-Al alloys, considering cycles with and without regenerative heat exchanger. Liu (2004) introduced a systematic way to analyze the work production from an idealized SMA wire working under the thermoelastic heat engine cycle. There are two concerns for the current literatures of SMA heat engines. First, most of the simple equilibrium analysis and the sophisticated dynamic model used the homogeneity assumption, as a common ground in continuum mechanics and thermodynamics, but could deviate from reality to a significant amount under some circumstances (Furst et al., 2012). To avoid complexity in calculation of the work needed to drive the cooling/heat pump cycle, experimental tested data were used to fit in a simple one-dimensional constitutive model, in order to evaluate the loading/unloading energy related to the coefficient of performance (COP) for this study. Such decoupling of stress-strain relation from temperature allows us to understand more physics on the

system level performance, rather than focusing on all the details of the material level performance, without losing much accuracy as long as real experimental loading/unloading data are applied. Second, for simplicity consideration, neither the previous analytical approach nor the simulation considers heat recovery/regeneration process to improve the efficiency in the past. Besides, the control volume of the system they considered is only the SMA itself, excluding any heat transfer fluid loops and associated losses. It should be noted that the consideration of fluid lines is much more important for cooling/heat pump system than power cycle, because of the more complicated fluid loops, especially when heat recovery loop is applied.

1.2.3 Thermoelastic Heat Pumps

In the past, elastomer refrigerators were called "thermoelastic refrigerators" as well, since the well-known thermoelastic heating/cooling effect from the rubber band (a.k.a. SMPs). The operating principle was quite simple. Heat was rejected when rubber was stretched and produced the cooling effect when released. They are different from the SMA based thermoelastic cooling, since there is no latent heat or phase transformation in elastomers. The driving mechanism, however, could be similar, since the heating/cooling of elastomers also come from force loading and unloading.

There were quite a few patents for elastomer heat pump/refrigerator. Cochran (1962) was among one of the earliest inventors, who used rotation to drive elastomer blades on an "impeller" to cool and heat two streams of air. Later, a manually actuated elastomer was patented by NASA (Hutchinson, 1971). After 1980s, Elastek Inc.

patented series of inventions, mainly focused on elastomer bed consisted of several layer of elastomers (DeGregoria, 1994, DeGregoria, 1995). The state of elastomer cooling was summarized in Oak Ridge National Laboratoray's (ORNL) report (Fischer et al., 1994). Brayton cycle, with COP of 6 operated under 17 K temperature lift was mentioned in the report, believed to be simulated by Elastek's model. Lyon et al. (1984) demonstrated a polyurethane-urea heat pump with a similar design to Banks (1975). They claimed the material had long-term stability when operating under small stain mode without crystallizing inside rubber, and reported up to 28 W power output at optimum speed 75 Hz at 77 K temperature difference conditions.
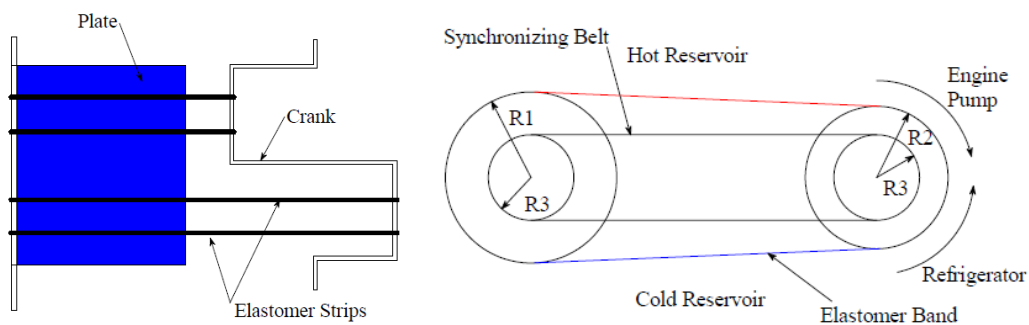
Left: single-crank driven elastomer heat pump with two elastomer beds

Right: two pulleys driven elastomer heat pump

Figure 1-5: Two driving system design of elastomer heat pumps (Gerlach, 2009).

Gerlach et al. (2002) introduced some more details on elastomer heat pump cycle and measurement of the rubber's specific heat. A proof-of-concept single-crank driven prototype was built and the temperature lift was measured to be around 1 K. However, heat recovery/regeneration was not considered in their work. They also reported that the friction between the rubber and aluminum plate heat source/sink was

large enough to cause continuous temperature increase. A two pulleys design was proposed by Gerlach (2009) but no test result was provided.
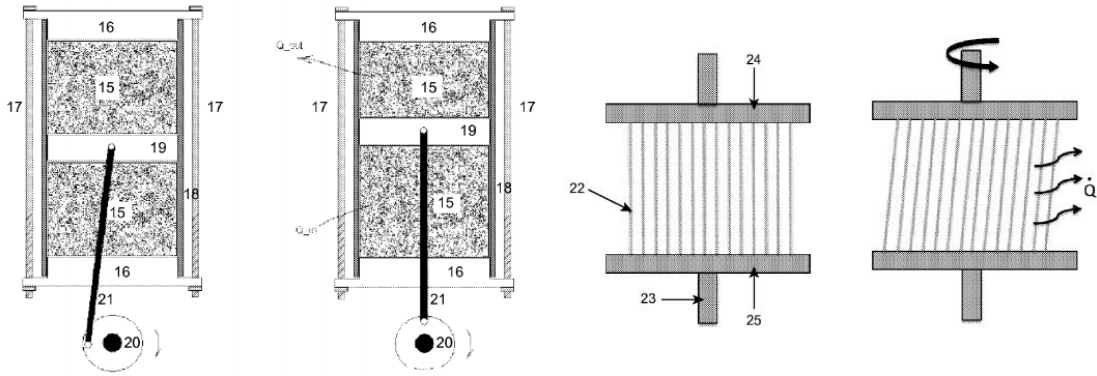
(a) Piston compressive driven design

(b) Rotating bird cage tensile driven design
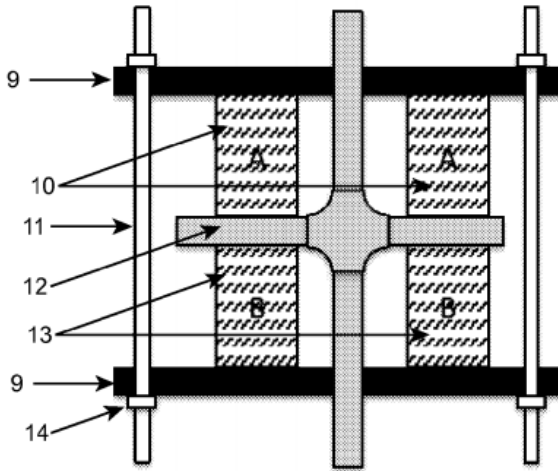
(c) Dual compressive driven design
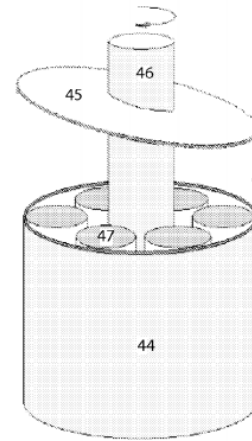
(d) Rotation compression design

Figure 1-6: Some SMA heat pump driving system design. (Cui et al., 2012b)

So far, there was no more recent updates on the state of the elastomer heat pumps, which could be a result of the following two reasons. The first and most critical limitation for elastomer materials is the poor fatigue. The technology will not be able to survive unless proven to be able to last for at least 100,000 cycles (Fischer et al., 1994). Secondly, it was pointed out that the low thermal conductivity of rubber could

be another limiting factor to efficiently transferring heat when compared with metallic SMAs (Hugenroth, 2002).

Another major difference between SMAs and elastomers is that SMAs can be driven by both tension and compression, while elastomers cannot be compressed. This results in variety of new designs options in thermoelastic cooling/heat pump driving system. Hugenroth (2002) patented the two pulleys design for SMAs operated under Brayton cycle, but unfortunately no heat recovery/regeneration was implemented. Cui et al. (2012) patented various driving mechanism with heat recovery/regeneration, for both compression and tension options. Recently, Schmidt et al. (2015) developed a demonstrator using Ni-Ti plate. By applying tensile force, the SMA plate cyclically rejects heat to a solid-state heat sink driven by a secondary motor, and absorbs heat from a solid-state heat source. Another demonstrator developed by Ossmer et al. (2015) also utilized Ni-Ti plate. The indirect tension driving mechanism saved the secondary driving motor for the heat sink and heat source, when compared with the design by Schmidt et al. (2015).

1.2.4   Summary

So far, various SMAs with large elastocaloric effect has been discussed in literature. Based on several metrics, Ni-Ti and Ti-Ni-Cu were the best, and several Cu-based SMAs also demonstrated their potentials.

SMAs and SMPs have been used in heat engines to produce power, as well as heat pumps to provide heating/cooling. One most important lesson to learn is the design of mechanical energy conversion layout, so that a more compact, more efficient and

simpler driving mechanism can be applied to the thermoelastic cooling/heat pump application. Table 1-2 summarizes the mechanical system designs for the above mentioned systems. There were mainly three common designs: twin-crank with SMA wires, two pulleys with SMA wire, and piston/plate tension or compression for bulk or other shape SMAs.

Table 1-2: Summary of driving system design for thermoelastic heat engine, elastomer heat pump and thermoelastic heat pumps.

System	Material	Mechanism	References
Thermoelastic heat engines	SMAs wire	Rotating flywheel	Banks, 1975
	SMAs wire/sheet/belt	Two pulleys tensile with/without synchronizing belt	Johnson, 1977, Johnson, 1985 Pachter, 1979
	SMAs wire	Twin-crank design	Shin et al., 1987
	SMAs wire	Single swing arm design	Kanedo, 2011
	SMAs beam	Single beam oscillation	Kirkpatirck et al., 2008
Elastomer heat pumps	Rubber	Single-crank driven Too much friction	Gerlach, 2009
	Rubber sheet/belt	Two pulleys driven	Gerlach, 2009
Thermoelastic heat pumps	SMAs wire/sheet	Two pulleys tensile driven	Hugenroth, 2002
	SMAs	Dual compressive driven	Cui et al., 2012b
	SMAs	Piston compressive driven	Cui et al., 2012b
	SMAs wire	Rotation bird cage double-ring tensile driven	Cui et al., 2012b
	SMAs wire	Drum/crankshaft driven	Cui et al., 2012b
	SMAs	Rotation compression driven	Cui et al., 2012b
	SMA plate	Tensile driven	Schmidt et al., 2015
	SMA plate	Single or double bridges Indirect tensile driven	Ossmer et al., 2015

1.3   *Literature Review on Heat Recovery/Regeneration Designs*

The term heat recovery and regeneration means to take advantage of the available heating/cooling internally from a cooling cycle/apparatus. It can be achieved by a component, usually a regenerator or a heat exchanger, or a fluid heat transfer process, also known as heat recovery. This terminology does not refer to waste heat or renewable energy utilization in this study.

Different cooling technologies have different need for heat recovery and regeneration. The review in this study covers cooling technologies used for typical air-conditioning, refrigeration, and cryogenics. Some technologies are not able to provide any useful cooling without regeneration, such as magnetocaloric, electrocaloric and thermoacoustic cooling. Some others have only a slight performance improvement by using heat recovery/regeneration, such as vapor compression cooling and absorption cooling. Here, the heat recovery/regeneration designs were divided into two parts, based on their own operating conditions, which could be either cyclic or steady state.

1.3.1   Heat Recovery/Regeneration Design for Cyclically Operated Systems

Cooling and heat pump systems under cyclically operated conditions include adsorption cooling, magnetocaloric cooling, Stirling cycle cooling, thermoacoustic cooling, thermoelastic cooling and electrocaloric cooling. The heat recovery/regeneration process is much more crucial for cyclically operated systems, since at least a significantly amount of the system, usually including the refrigerant, main heat exchangers, and some heat transfer fluid, are undergoing a huge temperature variation within each cycle. The parasitic sensible heating/cooling due to

the above mentioned "dead thermal mass" neutralizes part of the useful heating/cooling power generated from the refrigerant, and therefore should be minimized. It should be noted that only the parasitic sensible heating/cooling of the refrigerant itself is unavoidable, and the rest dead thermal masses are to be minimized. Heat recovery/regeneration is such a process, to reduce the impact of these parasitic heating/cooling by using the regenerator to take advantage of cycling the energy inside a cycle more wisely.

This terminology also varies between different cooling technologies. For adsorption cooling, heat recovery and regeneration were both used in literature. On the contrary, regeneration/regenerator was dominantly used in terms of magnetocaloric cooling, and Stirling cycle as well.

1.3.1.1 Heat Recovery for Adsorption Systems

Adsorption cooling/heat pumping systems are thermally driven cooling systems, and have their advantage when waste heat or low grade thermal energy are available. Early adsorption systems were solar powered ice makers operated with the cycle time of a day, where only one adsorbent bed was usually used to store the solar energy during the daytime (Pons and Guilleminot, 1986). The need to provide continuous cooling led to multiple adsorbent beds design operated under much faster frequency, i.e. minute rather than a day, where at least one bed could provide cooling while others being regenerated. At a much faster frequency, it became significantly necessary to apply heat recovery/regeneration between multiple beds to reduce the total thermal energy consumption.

The concept of thermal-wave heat recovery/regeneration in an adsorption heat pump

was introduced by Shelton et al. (1989, 1990). The idea of utilizing rejected heat from one adsorption bed to preheat the other led to the novel design of thermal-wave adsorption cycle, where a single loop fluid rejects heat to heat sink, heats the bed and performs heat recovery/regeneration at the same time. In the proposed system, the bed heat exchangers were designed in a way that a steep temperature gradient profile was required. The temperature profile was perpendicular to the heat transfer fluid flow direction, and the gradient was parallel to and flowing with the flow. The idea was partially validated in a lab scale adsorption system (Miles, 1996), and some simulation studies (Amar et al., 1996, Sun et al., 1997). Pons and Feng (1996), Pons et al. (1996) extended the original "steep" thermal-wave idea to triangle wave. The measured data (Pons et al., 1996) indicated that the temperature profile would evolve over time. The steep wave at the beginning of a cycle eventually became almost a triangle wave. The triangle wave, however, was not preferred for refrigerant mass transfer, since it caused a lower average bed temperature during the desorption process when compared with steep square wave case, and therefore led to a lower overall driving pressure at the adsorbent surface.

Another way to achieve thermal-wave heat recovery was proposed by Critoph (1994, 1998). Different from the thermal-wave heat recovery proposed by Shelton et al. (1989), gaseous refrigerant vapor was used to achieve all the heat transfer and heat recovery, without using any liquid phase heat transfer fluid inside the adsorbent beds. The thermal-wave referred to the similar steep temperature gradient inside the bed, which was perpendicular to the refrigerant vapor flow direction. There were two major improvements when compared with Shelton's (1989) thermal-wave: forced

convection of refrigerant vapor enhanced not only the heat transfer to the adsorbent bed, but also the critical mass transfer process. Secondly, saving the liquid external heat transfer fluid reduced a significant amount of unnecessary thermal mass contributing to the cycling loss. The disadvantage was poor heat transfer from vapor phase refrigerant when compared with liquid phase heat transfer fluid.

The third approach, or a more intuitive method for two beds adsorption system, was applied by Douss et al. (1988), Harkonen and Aittomaki (1991), Qiu et al. (2001), Liu et al. (2005), Chen et al. (2010), and Qian et al. (2013). Unlike previous two approaches, in this design, the adsorption/desorption processes were separated from heat recovery/regeneration processes. The two adsorbent beds were heated/cooled during the adsorption/desorption process first, followed by an internal heat recovery between the two beds. The advantage of this design is the possibility of applying mass recovery as well, which could not be achieved by the two thermal-wave heat recovery designs without any modifications.

1.3.1.2 Regenerator for Magnetocaloric Cooling

Magnetocaloric effect has long been used in cryogenics, especially been used to approach the 0 K limit. High Curie temperature alloys, high efficiency, and cycles capable to provide continuous cooling are requried to bring the demagnetization cooling principle to refrigeration and air-conditioning applications near room temperature.

One of the earliest endeavor (Brown, 1976) studied several cycle options, especially Stirling cycle analogous to a gaseous Stirling cycle. Liquid fluid was chosen to be the regenerator working substance surrounded by a vertical cylinder, wherein the

magnetic material bed (or solid-state refrigerant) consisted of granules moves up and down between heat sink and heat source. Eventually, a temperature gradient would be established between top and bottom throughout the entire fluid bsaed regenerator. This study also pointed out that water could circulate between top and bottom instead of moving the magnetic material beds up and down. They also pointed out that the magnetic material's physical properties, i.e. specific heat and thermal conductivity, would vary at different stages of the cycle, and could possibly lead to parasitic regeneration loss.

Following this idea, Barclay et al. (1979) demonstrated a reciprocating prototype pumping heat from 2K to 4K without measurable cooling capacity. Magnetic material $Gd_2(SO_4)_3$ salt was used to maximize the forced convection heat transfer with help of mini channels inside it. Helium was filled inside the cylinder as regenerator. The measured data confirmed that a temperature gradient was established inside the helium regenerator, however, did not follow an ideal profile due to the mixing of helium at different temperatures caused by the moving salt pill filled with magnetic material.

The phrase "active magnetic regeneration/regenerator" (AMR) was proposed by (Barclay and Steyert, 1982), referring to movable regenerator such as fluid or moving magnetic material beds, in contrast to those static passive regenerators made of lead or stainless steel in most other cryogenic cooling applications. Several options listed in this patent laid as the early foundation and development of AMR concept. Later, AMR concept was extended to using magnetic material beds themselves as regenerator (Barclay, 1983). The later work also introduced a specific way to achieve

the proposed AMR design, by using a rotary wheel with multi-layer magnetic materials with different Curie temperatures as a cascaded system to maximize the overall system temperature lift. Compared with previous studies, in the rotary wheel design, the superconducting magnet was fixed, yet the magnetic material was rotating between strong field region and weak field region instead. Also, the multi-layer design was a cascaded system aiming to increase the system temperature lift, and the same method was applied in most of the recent studies and prototypes. The cycle was also proposed to be similar to a gaseous Brayton cycle, instead of previous Stirling-like cycle design.

More studies suggested that the fluid heat capacity, or thermal mass, played an important role in the AMR's performance. The ratio between the heat capacity of the fluid and that of the magnetic material beds was suggested to be the key parameter (DeGregoria, et al., 1991). Those early AMR designs were categorized into the first limit group, in which the heat capacity of fluid, i.e. liquid helium in most cases, is much larger than the magnetic materials. The proposed new AMR is belong to the second limit, in which the fluid thermal mass is negligible when compared with the magnetic materials.

DeGregoria et al. (1993) proposed more possibilities to apply the AMR's design by using different magnetic material beds layout and system driving mechanisms.

Hu and Xiao (1995) introduced a new mathematical method to analyze the AMR's time averaged heat fluxes and temperature profiles based on the energy-temperature equations.

Later, more studies have been focused on determining the "ideal" adiabatic

temperature span – local temperature profile, i.e. $\Delta T_{ad}(T)$ where the adiabatic temperature span referes to the temerpature drop during the adiabatic demagnetization process. By using the analytical approach for both Ericsson cycle and Brayton cycle, Cross et al. (1988) came to the conclusion that linear profile was preferred. Smaili and Chahine (1998) studied the polynomial $\Delta T_{ad}(T)$ relation. By varying the order of the polynomial correlation, they concluded that there was no universal preferred polynomial relation. A more recent study by Zhang et al. (2000) suggested a more complicated polynomical correlation. From a different approach, Rowe and Barclay (2003) revisited this problem by choosing entropy change $\Delta S - T$ rather than sticking with the $\Delta T_{ad}(T)$ relation. They used the minimum entropy generation method to conclude the required $\Delta S - T$ relation for an ideal magnetic material.

Since the methodology and practices of AMR had been successful for more than twenty years, more recent studies on AMR were more focused on system level performance and optimization. Gao et al. (2006) demonstrated a lab scale reciprocating AMR prototype under 4 K temperature lift, providing maximum 25 W cooling capacity. On the other hand, Zimm et al. (2006) designed and constructed a rotary AMR achieving maximum temperature lift of 25 K. Vasile and Muller (2006) steped one more step towards complexity. By adding more magnetic beds, changing the HTF circuits and adding more magnets, the cascaded cycle was designed to achieve higher temperatuer lift. In their novel design, the magnets were moving rather than the magnetic material beds. Engelbrecht et al. (2011) tested a stacked plate regenerator, in constrast to the dominant packed bed regenerator studied in most of the literature, aiming to improve the heat transfer performance, i.e. NTU.

Unfortunately, the tested results did not enhance the system performance. Aprea et al. (2011) developed a multi-layer regenerator model to consider the detailed behavior of each layer magnetic material performance. Tusek et al. (2011) conducted a parametric study for the geometries and operating paraemters, i.e. flow rates and cycling frequencies, of the packed bed AMR, in addition to an earlier work (Nielsen et al., 2010).

Recently, more large scale AMR prototypes have been built and tested, with higher system temperature lift by cascading more magnetic bed layers as well. Bahl et al. (2014) summarized the measured data from their rotary AMR using Gd packed beds as regenerators. 1 kW cooling capacity and 25K maximum temperature lift were achieved. Jacobs et al. (2014) used six layers $La(FeSi)_{13}H$ packed beds as regenerators for the rotary AMR, and measured 3042 W cooling capacity under zero temperature lift condition. On the other hand, more layers were added to maximize the overall system temperature lift. Tusek et al. (2014) compared the temperature lift of a linear reciprocating AMR consisted of stacked plate regenerators by using different layers of La-Fe-Co-Si alloy with Gd packed bed. A similar study was done by Legait et al. (2014).

1.3.1.3 Regenerator for Stirling Refrigerator

Stirling cooling cycle has been mainly used for cryocoolers and refrigerators. The concept of Stirling cycle was quite old, but practically there has been variants cycles and prototypes built similar to the original Stirling refrigerator design. Therefore, the Gifford-McMahon (GM) cryocooler was discussed here as well.

The working fluid is in gaseous phase in most cases, which undergoes large

29

temperature variations during the compression and expansion processes. Yet the gaseous fluids have small specific heat, regenerator is still necessary, due to the above mentioned large temperature variations.

The most widely used regenerator was based on a metal porous structure, or simply a mesh. A stainless steel screen was applied by Walker and Vasishta (1971), de Monte (1997), Veprik et al. (2005), and Guo et al. (2013). Organ (1999) used a metal wire matrix as the regenerator for a miniature Stirling cycle cryocooler. The regenerator, either mesh or wire matrix, is used to restore the heat rejected by gas before the gaseous working fluid flows to the expansion chamber, which is used to preheat the gas once they finished refrigeration during the reversed flowing process. In most cases, the temperature of the regenerator is not uniform, and the thermal conduction caused by the temperature gradient inside the regenerator along the gas flow direction contributes to loss.

Another approach was proposed by Watanabe et al. (1996), that a counter-flow regenerator or recuperator consisted of CuNi tubes could be used directly. In their design, however, steady state flow was used rather than oscillating gaseous flow back and forth.

McMahon and Gifford (1960) first developed the so-called GM cryocooler, which has been widely used in cryogenics area since 1980s. By allowing the compressor to operate at different frequency from the displacer, the GM cryocooler reduced the compressor size significantly (de Waele, 2011) compared with the prior-art Stirling cryocoolers. The machine valve switching was designed to be operated around 1 Hz. Traditional metal mesh was used as the regenerator. An improved design of

regenerator for a GM cryocooler was conducted by Kuriyama, et al. (1996). To increase the regenerator specific heat at low temperature range, regenerator composed of magnetic material Er_3Ni granules was used.

Stirling cycle and its variants were mostly used for cryogenic applications, which were also summarized by the following two review studies (de Waele, 2011, Radebaugh, 2009). According to them, an ideal regenerator working under high frequency regeneration, i.e. 1-100 Hz, should have the following properties: high heat capacity per volume; high specific area to enhance heat transfer from gas; and zero flow resistance to minimize pressure drop.

1.3.1.4 Regenerator for Thermoacoustic Refrigerators

Thermoacoustic refrigerators refer to generating cooling from an amplified sound wave, or converting cooling from acoustic energy. The idea was originally from modifying a piston-based Stirling engine (refrigerator) operated under high frequency to a pistonless Stirling engine taking advantage of acoustic energy proposed by Ceperley (1979). This modification was followed by the fast development in 1980s, later known as the pulse-tube refrigerators (PTR), or traveling-wave thermoacoustic refrigerators (Mikulink et al., 1984, Radebaugh et al., 1986), since the enhanced PTR took advantage of the resonator. The PTRs were usually more compact than the Stirling refrigerators, operated under 1-100 Hz depending on the device. Stainless steel tubes filled with mesh phosphor-bronze screen was used as regenerator in their device. Later improvement studies on PTR (Gardner and Swift, 1997, Zhu et al., 1997, Tward et al., 2002) mainly sticked with the traditional metal mesh regenerator design. Recently, in a design to achieve 6K cryocooler, Nast et al. (2007) used the

four stages cascaded constant flow PTR to get higher system's temperature lift. Since it was a constant flow system, three counter-flow recuperators were used as the regenerator.

The second type thermoacoustic refrigerator was the standing-wave refrigerator. Different from the traveling-wave refrigerator, in a standing-wave refrigerator, a stack rather than a porous and high heat capacity regenerator was used. From an engine point of view, the standing-wave design was simpler than the traveling-wave, since the gas parcel within the stack was primarily in phase (Garrett, 2004). Unfortunately, all the stacks used in the standing-wave thermoacoustic refrigerators were not the same as a regenerator, since there was no heat transfer between the stack and gaseous working fluid, and the gaseous working fluid was undergoing an adiabatic pressure variation process inside the stacks (Bosel and Trepp, 1999, Garrett et al., 1993, Nsofor and Ali, 2009, Paek et al, 2007, Reid and Swift, 2000, Sakamoto and Watanabe, 2004, Tijani et al., 2002). Miya et al. (2008) proposed to add copper mesh on each side of the honeycomb ceramic stack to enhance heat transfer to gas, but it was still an enhancement to the stack, not the regenerator.

Garrett (2004) summarized the difference between the stack for standing-wave refrigerator and the regenerator used for the traveling-wave refrigerator. The Lautrec number, defined as the ratio between the hydraulic radius and the thermal penetration depth, was used as a criterion to differentiate a stack and a regenerator. When the thermal penetration depth is larger than the hydraulic radius of the porous bed, it is a regenerator, since gaseous working fluid has a meaningful heat transfer interaction with the porous bed. Otherwise, the heat transfer is blocked within the thermal

penetration depth domain, and therefore, the stacks are considered to be the adiabatic boundary to the gaseous working fluid.

1.3.1.5 Others

Thermoelastic cooling (a.k.a. elastocaloric cooling), and electrocaloric cooling are two recently developed alternative cooling technologies. Therefore, not much studies have been carried out to study the regenerator and heat recovery process design in these two cooling technologies.

Gu et al. (2013) was the first one who demonstrated an elastocarloric cooling prototype with a regenerator design. An external stainless steel plate was used as the regenerator tos transfer the sensible energy from/to the electrocaloric material bed. Several layers of regenerator were stacked between the electrocaloric material layers. No fluid was used to keep the prototype as compact as possible. Guo et al. (2014) developed a fluid based electrocaloric cooling prototype, in which a HTF was used as an internal regenerator by flowing them through the electrocaloric material bed back and forth. It is similar to the magnetocaloric material design (Brown, 1976). A more detailed summary was conducted by a review study (Ozbolt et al., 2014). The term active electrocaloric regenerator (AER) was defined and refered to using electrocaloric material beds as regenerator itself, similar to the AMR's design. The major challenge for electrocaloric material bed flowing fluid internally was the the arrangment of electrodes. Ozbolt et al. (2014) provided several optional AERs design, including regular parallel plate design and honeycomb shape design.

1.3.2 Recuperator/Heat Recovery Design for Systems Operated Under Steady

State Condition

Different from the systems that are cyclically operated, those under steady state operating conditions do not need to compensate for the parasitic sensible heating/cooling of the supporting materials, i.e. heat exchangers, pipe walls and heat transfer fluids. Instead, the only term left needs to deal with is the refrigerant itself, which again is unavoidable as clearly demonstrated on a *T-s* diagram. As a result, it is not as necessary as those aforementioned cyclically operated systems to apply the heat recovery/regeneration, since only the parasitic sensible heating/cooling of the refrigerant itself needs to be recovered/regenerated.

Another major difference is the configuration of the heat recovery/regenerator devices. Under steady state, no fluid is required to travel back and forth. As a result, a simple counter-flow heat exchanger is capable to handle this feature. This is also the reason leading to the slight terminology difference, especially for cryogenics. "Recuperator" or "recuperative heat exchanger (RHX)" were more commonly used for systems operated under steady state condition, rather than the "regenerator" for cyclically operated systems. The place to implement the counter-flow heat exchanger varies from different cooling technologies. For example, the suction-line heat exchanger for vapor compression cooling is located between the vapor in suction line and the liquid from exit of condenser. The solution heat exchanger for absorption cooling, however, is located inside the solution circuit. Depending on the detailed location, the terminology for heat recovery/recuperation varies. Yet, the overall goal is always the same, to minimize the parasitic sensible heating/cooling of the

refrigerant.

1.3.2.1 Suction-line Heat Exchanger for Vapor Compression Cooling

Suction-line heat exchanger (SLHX), also known as liquid-suction heat exchanger, are common accessories installed in a vapor compression refrigeration system to improve the system performance. More subcooling is provided to the liquid refrigerant exiting the condenser by using vapor with lower temperature at suction-line, which increases the cooling capacity and sometimes the compressor work (Klein et al., 2000). The compressor power is determined based on a reduced refrigerant mass flow rate and compressor efficiency associated with an increased refrigerant temperature. Consequently, the performance improvement benefit of applying SLHX depends on the competition between the increase of cooling capacity and compressor work, and varies with working fluid (Domanski and Didion, 1994) and even operating conditions such as evaporating pressure (Hermes, 2013) or temperatures (Mastrullo et al., 2007).

ASHRAE (2010a) listed several available options for the counter-flow SLHXs:

- Liquid and suction line soldered together

- Shell-and-coil or shell-and-tube heat exchangers

- Tube-in-tube (or concentric tube) heat exchangers

- Plate heat exchangers

In the literature, the first type of SLHX was the most popular one due to its simplicity. Especially in refrigerators where capillary tube is commonly used instead of expansion valves, where the capillary tube is usually soldered to the outer surface

of the vapor suction-line as the non-adiabatic capillary tube SLHX. Yang and Bansal (2005) developed a one-dimensional model to investigate the performance enhancement potentials for a R22 refrigerator. Bansal and Yang (2005) applied a modified model to study some more complicated process inside the non-adiabatic capillary tube called re-condensation. Agrawal and Bhattacharyya (2008) developed a similar one-dimensional model for a transcritical CO_2 heat pump cycle and conducted parametric studies for a variety of geometric parameters. Herms et al. (2008) developed an improved one-dimensional model with less computational time and validated the model for six refrigerants. Silva et al. (2011) constructed a transcritical CO_2 test facility for the non-adiabatic capillary tube SLHX to validate their model. They also concluded that the SLHX's length was the key parameter contributing to the performance improvement.

The second type of SLHX, shell-and-coil heat exchanger, was also studied by Kang et al. (2006) for a R22 water chiller. They measured 7.5% higher cooling capacity and 3.2% higher COP, when compared with a baseline system without SLHX. Navarro-Esbri et al. (2005) developed a test facility for a water chiller using three different refrigerants and a tube-in-tube (concentric) SLHX. After comparing their model with the available models, they claimed that the neglecting pressure drop led to the major deviation between the model predicted results and the measured data.

System level researches were aiming to study the system COP improvement for specific applications. Ge and Tassou (2011) used the sensitivity analysis for a CO_2 refrigeration system in a supermarket. Fernandez et al. (2010) constructed a CO_2 heat pump water heater, and concluded that the system COP improved by 7.9% when a

SLHX was implemented.

1.3.2.2 Solution Heat Exchanger for Absorption cooling

Different from solid adsorption cooling using solid-state adsorbent, absorption cooling/heat pump operates under steady state flow conditions, where liquid solution composed of absorbent and refrigerant is used. Similar to the vapor compression systems, the absorption cooling system also has a condenser to reject heat, an evaporator to generate cooling and an expansion valve to maintain the pressure difference. In addition, a solution circuit replaces the mechanical compressor to pump vapor refrigerant from low pressure to high pressure. The solution heat exchanger/economizer (SHX) is to recover the available sensible heat from the strong solution exiting from the desorber (generator) to the incoming weak solution stream from absorber as much as possible.

It has been a long tradition in the industry to implement solution heat exchangers. In the systematic analysis by Herold et al. (1996), SHX was already a standard component for all the variations of single effect absorption cooling system. ASHRAE (2010b) summarized the types of heat exchangers used as the solution heat exchanger for absorption cooling systems. The plate heat exchangers and shell-and-tube heat exchangers are the most widely used ones. The most common material used is mild steel or stainless steel. In literature, the plate heat exchanger was most widely used, due to its high heat transfer coefficient, low pressure drop and compactness. Flamensbeck et al. (1998) designed and constructed a 45 kW double effect absorption heat pump, using stainless steel plate heat exchanger as the two SHXs. Ventas et al. (2011) developed a single effect absorption heat pump using NH_3-$LiNO_3$ working

pair, where the SHX was a stainless steel fusion type plate heat exchanger. Gutierrez-Urueta et al. (2012) developed a LiBr-H_2O absorption test facility to investigate the performance of the absorption chiller with adiabatic absorber configuration. Again, stainless steel plate heat exchanger was used as SHX.

1.3.2.3 Recuperative Heat exchanger for Joule-Thomson and Brayton Cooler

Both Joule-Thomson (J-T) cryocooler and Brayton cryocooler are based on the gaseous Joule-Thomson cooling effect, in which the gas temperature drops during the expansion process. The only difference between them is whether or not a moving part, i.e. an expander substitutes the throttle valve. In a J-T cooler, the gaseous fluid undergoes the isenthalpic expansion process via the throttle valve. In a Brayton cooler, since the expander generates work from the fluid, the isentropic expansion process is able to produce more cooling than the pure J-T cooler.

The key component for both systems is the RHX. ASHRAE (2010c) summarized the design of RHXs, and found that the coiled-tube (coiled tube-in-shell) heat exchangers and the plate-fin heat exchangers are most commonly used in industry. It was also pointed out that one of the major challenges for these heat exchangers was the significant heat conduction via the metal heat exchanger from the cold end to the warm end, due to large temperature lift throughout the system. Choosing a proper material needs a tradeoff between maximizing the heat transfer rate between two streams of fluids, and minimizing the above mentioned conduction loss.

Most miniature J-T cryocoolers in literature followed the Hampson type RHX design, where the evaporator, expansion device and counter-flow RHX are in the single assembly. Coiled tube-in-shell heat exchanger, with enhanced helical fins for gaseous

heat transfer on the external surface of coil was extensively proposed, simulated and tested in National University of Singapore (Xue et al., 2001, Ng et al. 2002, Chua et al., 2006). Not only was the heat conduction along tube wall a significant loss, but the huge pressure drop along the capillary tube also contributed to significant fluid property variations as well. Another tube-in-tube RHX design was optimized by Lerou et al. (2005). Other system level studies in terms of RHX effectiveness were also carried out (Maytal et al., 2006, Derking et al., 2012).

Brayton coolers are usually in much larger size, especially when turbines are applied as the expansion device. Foster et al. (2011) reported a 10 kW high temperature lift air-cycle Brayton heat pump for food industry, operating between -50°C and 100°C. The recuperator used in their system was a four series connected plate-fin heat exchanger. Another miniature Brayton cryocooler was developed by Zagarola and McCormick (2006), using tube-in-shell heat exchanger as the recuperator.

1.3.3   Comparisons and Summary

Heat recovery/regeneration design improves system performance significantly, and is necessary in most NIK cooling technologies. The larger the temperature lift/temperature variation the system undergoes, the more significant saving heat recovery/regeneration can provide. As to cyclically operated systems, the heat recovery/regenerator reduces the parasitic sensible heating/cooling required for both refrigerant and dead thermal masses from involved supporting structures, heat exchangers, heat transfer fluid, and pipes. On the contrary, the counter-flow heat exchanger/recuperative heat exchanger in those systems operated under steady state

condition only recover the parasitic sensible heating/cooling for refrigerant itself.

One common challenge existing in all heat recovery/regeneration design is the heat conduction in the regenerator, or thermal energy dissipation by heat conduction. This issue becomes worse for cryogenic applications since the temperature span across the regenerator/recuperative heat exchanger is much larger than those of air-conditioning and refrigeration applications. In literature, reducing the heat conduction along flow direction of regenerator for Stirling cooler and thermoacoustic cooler was the key point in designing the system. Similarly, reducing the heat conduction loss from high temperature side to low temperature side was mentioned in almost all literature for J-T and Brayton cryocoolers. In solid-state cooling field, the intrinsic heat conduction loss in an AMR for magnetocaloric cooling and AER for electrocaloric cooling also deteriorates their system performance, especially when the thermal conductivity of the metal alloy is high. Fortunately, adsorption cooling does not have this concern, since the thermal conductivity of the common adsorbent is significantly lower than metals.

Table 1-3 is a summary of heat recovery/regeneration methods for cyclically operated systems. The design of heat recovery/regeneration is also closely related to their system configurations. In an adsorption cooling system, the traditional thermal-wave (Shelton et al., 1989, Pons et al., 1996) combined heat recovery and adsorption/desorption processes together, while the two-bed heat recovery (Douss et al., 1988) was capable of adding an extra mass recovery phase, with the tradeoff by adding more system complexity. In an electrocaloric cooling machine, one can use solid-state refrigerant directly as heat sink/source (Gu et al., 2013), or choose heat

transfer fluid to deliver heating/cooling (Ozbolt et al., 2014). Magnetocaloric systems were also evolved from using static fluid columns as regenerator to flowing small amount of heat transfer fluid through the AMR magnetic material beds.

(i) Beginning of simultaneous heating, cooling and heat recovery

(i) After demagnetization of bed A and magnetization of bed B, beginning of simultaneous heat transfer and regeneration

(ii) End of simultaneous heating, cooling and heat recovery

(ii) After demagnetization of bed A and magnetization of bed B, end of simultaneous heat transfer and regeneration, bed A delivers cooling and absorbs heat, bed B delivers heating and rejects heat

(iii) System schematic
(a) Low conductivity solid thermal-wave for adsorption cycles (Shelton et al., 1990)

(iii) System schematic
(b) The combined cascaded cycle with simultaneous cooling, heating and regeneration (Jacobs et al., 2014)

Figure 1-7: Illustration of adsorption thermal-wave heat recovery and magnetocaloric AMR regenerator designs.

Since this study focuses on thermoelastic cooling, the two most closely related solid-

state cooling technologies under cyclically operated conditions were compared here in Figure 1-7. Note that both pumps in that figure are two-way pumps, which is used to switch flow direction every half cycles. The adsorption thermal-wave heat recovery process is plotted on the left side, where the temperatures at different locations in the two adsorbent beds are indicated by the color. The goal of the heat recovery process is to heat desorber bed A and cool down adsorber bed B, by using a steep thermal-wave propagating from left to right for both solid beds. The low thermal conductivity nature of solid desiccant materials in those two adsorbent beds allows the formation of such steep thermal-wave. The two spheres are used as trackers to understand the flow conditions. In the adsorption heat recovery process, graphically the thermal-wave front in both beds propagates the entire bed length, so is indicated by the flow trackers. On the right side, the AMR regeneration process is also plotted. The temperature within the magnetic bed A drops adiabatically as soon as it is demagnetized, and regeneration process allows the fluid close to the exit (right side) of bed A to deliver the useful cooling from bed to the load, vice versa for the exit side of bed B. Meanwhile, the temperature at the inlet of bed A comes from the heat sink directly, which is used to pre-heat the left side before next half cycle. It is an intrinsic cascade design, since each local region inside the bed only pumps heat between its neighbors. For example, the exit of magnetic bed A only absorbs heat from the cooling load (lowest temperature) to a slightly higher temperature region at its neighboring left. One can also tell this by looking at the flow tracer. The fluid only moves a little bit and pumps heat locally during the simultaneous heating/cooling and regeneration process locally.

42

Table 1-3: Summary of heat recovery/regeneration methods for cyclically operated systems.

Technology	Regenerator material	Regenerator type	Highlight	Reference
Adsorption (>50°C)	HTF	Thermal-wave	Steep square wave	Shelton et al., 1989, 1990
	HTF	Thermal-wave	Smooth triangle wave	Pons and Feng, 1996 Pons et al., 1996
	Refrigerant	Convective thermal-wave	Steep square wave	Critoph, 1994, 1997
	HTF	Two-bed	Capable to add mass recovery	Douss et al., 1988
Magnetocaloric (0-20°C)	Helium	Reciprocating external regenerator	Designed for Stirling cycle	Brown, 1976 Barclay, 1979
	Helium	Rotating external regenerator	Defined "AMR"	Barclay and Steyert, 1982
	Three layer Gd bed	Rotating internal regenerator	Cascade cycle + regeneration	Barclay, 1983
	Packed bed of $Er_xGd_{(1-x)}Al_2$	Reciprocating AMR	Cascade cycle + regeneration	DeGregoria et al., 1991
	Three layer packed bed GdEr	Rotating AMR	Achieved 25K ΔT_{lift}	Zimm et al., 2006
	Stacked plates	Reciprocating AMR	Plate not superior to packed bed	Engelbrecht et al., 2011
	Six layer packed bed	Rotating AMR	Achieved 3 kW cooling	Jacobs et al., 2014
Stirling (>100°C)	Stainless steel mesh	Passive	Most widely used method	de Monte, 1997
	CuNi tubes	Counter-flow heat exchanger	/	Watanabe et al., 1996
	Er_3Ni granules bed	Passive	GM Stirling machine, high frequency	Kuriyama, et al., 1996
Thermoacoustic (0-20°C)	Phosphor-bronze screen	Passive	PTR, high frequency	Radebaugh et al., 1986
	No	Stack	No regenerator	Garrett et al., 1993
Electrocaloric (<5°C)	Stainless steel plate	Passive external regenerator	Achieved 2.5K temperature lift	Gu et al., 2013
	HTF	Internal regenerator	/	Guo et al., 2014
	Electrocaloric material bed	Reciprocating AER	Proposed various regenerator layouts	Ozbolt et al., 2014

Figure 1-8 is a demonstration of various AER's designs for electrocaloric cooling. A good regenerator should have high heat transfer coefficient, low pressure drop and low electric resistance to reduce parasitic Joule heating.
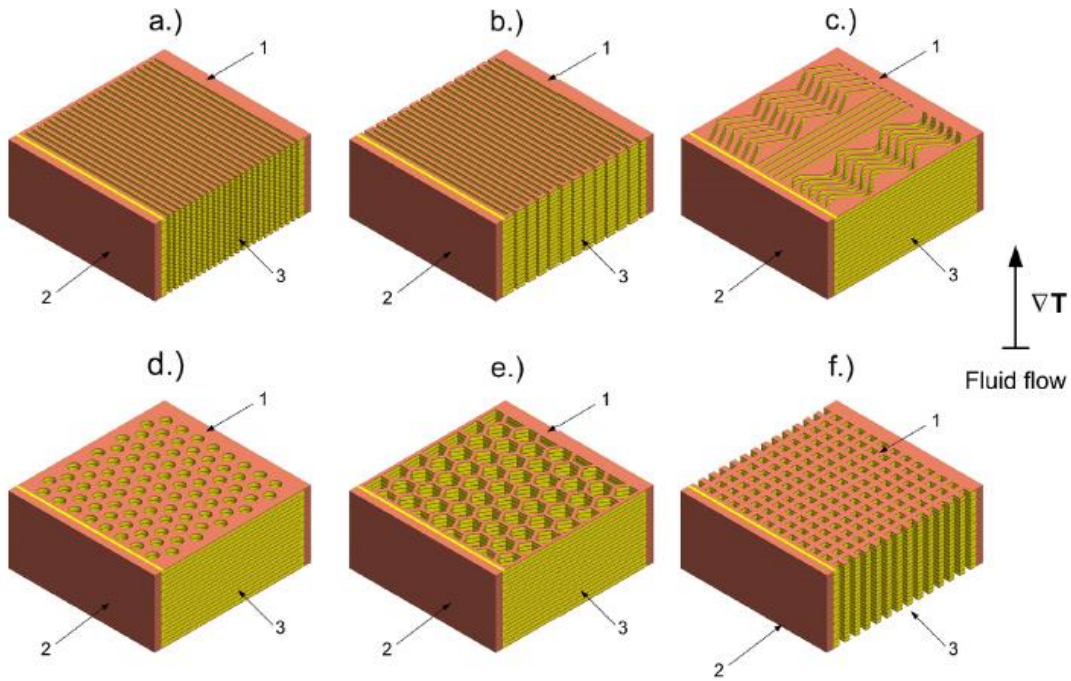
Figure 1-8: Electrocaloric cooling: various AER designs (Ozbolt et al., 2014).

Table 1-4 is a summary of recuperator/heat recovery methods for systems operated under steady state condition. Unlike the various heat recovery/regeneration design in cyclically operated systems, the heat recovery techniques here are almost the same, by using a counter-flow heat exchanger. The detailed heat exchanger difference mainly depends on the phase of the working fluid in the systems. For example, plate heat exchangers are mainly used for absorption systems, since both streams are in liquid phase. When a gas phase is involved, shell-and-coil and plate-fin heat exchangers are applied for vapor compression SLHX and Brayton coolers, respectively.

Table 1-4: Summary of recuperator/heat recovery methods for systems operated under steady state condition.

Technology	Regenerator material	Regenerator type	Highlight	Reference
Vapor Compression (20-50°C)	Copper	Soldered non-adiabatic capillary tube	Most widely used	Silva et al., 2011
	Copper	Shell-and-coil	Accumulator built in SLHX	Kang et al., 2006
	Copper	Tube-in-tube	Turbulence enhancement inner tubes	Navarro-Esbri et al., 2005
Absorption (>100°C)	Stainless steel	Plate type	Most widely used	Flamensbeck et al., 1998
Joule-Thomson (>100°C)	Copper and Stainless steel	Coiled tube-in-shell	Miniature design	Ng et al., 2001
	Glass wafer	Tube-in-tube	/	Lerou et al., 2005
Brayton (>100°C)	Stainless steel	Plate-fin	Four series counter-flow HXs	Foster et al., 2011
	/	Coiled tube-in-shell	Miniature cryocooler	Zagarola and McCormick, 2006

Figure 1-9 shows different implementations of SLHXs for vapor compression systems. As mentioned earlier, the soldered non-adiabatic capillary tube was most popular due to its simplicity. The coiled shell-and-tube heat exchangers were also widely used for cryogenic applications, including J-T and Brayton cryocoolers in Figure 1-10.
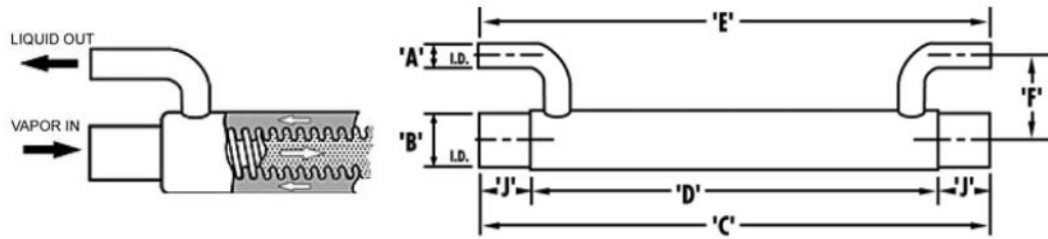
(a) Tube-in-tube SLHX (Navarro-Esbri et al., 2005)

① Accumulator inlet

② Accumulator outlet

③ IHX inlet

④ IHX outlet
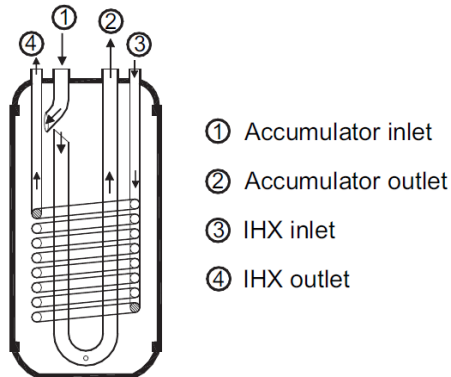
(b) Accumulator built-in shell-and-tube SLHX (Kang et al., 2006)
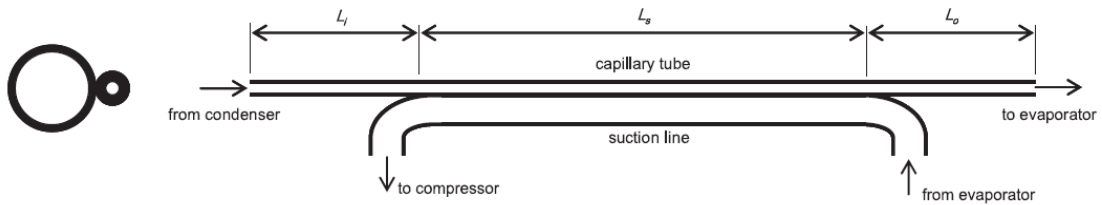
(c) Soldered non-adiabatic capillary tube (Silva et al., 2011)

Figure 1-9: Recuperator/heat recovery for vapor compression cooling: SLHXs.
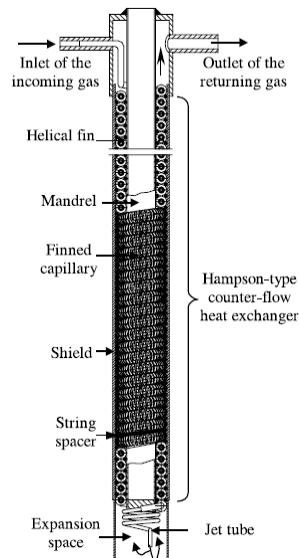
(a) J-T cryocooler with coiled tube-in-shell counter-flow recuperator (Ng et al., 2002)

46

(b) Coiled tube-in-shell counter-flow recuperator in a miniature Brayton cryocooler
(Zagarola and McCornick, 2006)

Figure 1-10: Coiled tube-in-shell counter-flow recuperators used in cryogenic

applications.

1.4   *Literature Review Summary and Research Gaps*

The area of using SMA for thermoelastic cooling and heat pump is indeed an unexplored field with variety of opportunities and challenges. The knowledge obtained so far includes some but limited data of the SMA elastocaloric performance including the entropy change and stress-strain characteristics, some mechanics design lessons from a few thermoelastic heat engines and elastomer heat pumps, as well as how to design a heat recovery/regeneration process. These are the bases to develop our own thermoelastic cooling theories and prototypes. Here is a summary of literature review for research gaps.

First, studies in terms of measuring comprehensive elastocaloric effect have been carried out only in the past few years. Most of the materials studies were still addressing their mechanical superelasticity behaviors rather than the elastocaloric effect. To be more specific, so far only a few materials with enough data can be compared, i.e. Ni-Ti, Ti-Ni-Cu and some Cu-based SMAs. Materials investigations are still needed. Comprehensive physical properties for each SMA with large

elastocaloric effect are preferred in a single study rather than from multiple literature, since different groups might use different composition specimen and have different impurities, including bulk density, specific heat, thermal conductivity and others to enable system level simulations. In addition, the stress-strain relations for both tensile and compression are also requested to predict how much work is needed in a cooling system. If possible, materials scientists should fit their measured stress-strain curves into known constitutive models so that their results could be implemented much easier. For example, such model parameters fitting has been done extensively in adsorption isotherms (Nietsch, 1996, Chua et al., 2002). Besides, the caloric effect measurement should be continued to find more potential candidate SMAs.

Second, there is no published SMA based thermoelastic cooling system prototype before 2015. Recently, the two reported demonstrators by Schmidt et al. (2015) and Ossmer et al. (2015) are still far away from a functioning scalable prototype. In addition, with the several proposed driving mechanisms for thermoelastic cooling as listed in Table 1-2, none of the ideas have been built and tested. Also, no friction countermeasures were deployed for any of the driving mechanism, which was one of the major challenges in these systems. Additionally, most of the driving mechanism designs have a tradeoff between heat transfer enhancement and system simplicity.

To develop a thermoelastic cooling system, not only the driving mechanism is important, but the heat transfer and heat recovery/regeneration is also equivalently crucial. Unfortunately, the only related literature in terms of thermoelastic cooling were all in material level. The heat transfer and heat recovery/regeneration are based on the cooling cycle first, and therefore, the thermodynamic cycle analysis is needed.

System level dynamic simulations based on the cycle analysis are needed to predict the performance including cooling capacity and COP. Heat transfer enhancement measures can be investigated based on the model since then.

To be more specific for heat recovery/regeneration, current solid-state cooling systems under cyclic mode are either with very low thermal conductivity (i.e. adsorption) to enable the large temperature gradient, or working under cascade cycle to maximize the overall temperature lift (i.e. magnetocaloric and electrocaloric cooling). In a thermoelastic cooling system, however, the SMAs usually have high thermal conductivity, which leads to almost uniform temperature within the solid-state SMA bed, contradicting the large temperature gradient requirement for a thermal-wave heat recovery as in an adsorbent bed. In addition, elastocaloric effect is usually much higher than the magnetocaloric and electrocaloric effect, and therefore a single-stage heat pump is enough. Nevertheless, the available heat recovery/regeneration methods found in literature could be a basis for current study to develop the most suitable heat recovery/regeneration method for thermoelastic cooling application.

1.5   *Research Objectives*

To fill the research gap in this area, the proposed study aims developing the research framework including both the fundamental and prototype development including its experimental evaluation. This thesis intends to explore the following aspects.

(1) Thermodynamic fundamental of elastocaloric materials

(2) Cycle design and theoretical system performance prediction

(3) Novel heat recovery process method

(4) Developing a proof-of-concept prototype

(5) Enhancing the system performance based on a validated model

(6) Comparing the performance of thermoelastic cooling with other technologies

The fundamental part of this thesis focuses on the thermodynamic cycle analysis of the thermoelastic cooling systems, analytical COP and cooling capacity derivation, transient system model development and performance predictions. In addition to that, an important feature of this thesis is to propose a novel heat recovery process designed especially for thermoelastic cooling. The second application part focuses mainly on prototypes development and testing. Besides, with prototype testing experiences, ideas to further enhance the system performance are discussed together with multi-objective optimization study using genetic algorithm. Lastly, the not-in-kind cooling technologies ranking is quantitatively identified.

Chapter 2:   Thermodynamic   Fundamental   of

Elastocaloric Materials

This chapter introduces the basic thermodynamic knowledge of the martensitic phase change in SMAs, including the Maxwell equations and the phase diagram. A quantitative comparison of various SMAs based on data from literature is summarized.

2.1   Thermodynamics of Elastocaloric Materials

SMAs have been used mainly for biomedical applications in the past due to its superior superelastic mechanical performance.

Following the convention of the classic thermodynamics, and by analogy to the magnetocaloric effect (Tishin and Spichkin, 2003) and electrocaloric effect (Ozbolt et al., 2014), the internal energy, enthalpy and entropy of the elastocaloric materials can be defined as following. Note that the sign in Eq. (2-1) for elastocaloric materials is opposite to that in the classic solid-state thermodynamics, since increase in strain represents work transfer into the system.

$$du^* \equiv Tds + \frac{\sigma}{\rho}d\varepsilon \qquad\qquad (2\text{-}1)$$

$$dh^* \equiv Tds - \varepsilon d\sigma / \rho \qquad\qquad (2\text{-}2)$$

$$ds = \left(\frac{\partial s}{\partial T}\right)_{\sigma} dT + \left(\frac{\partial s}{\partial \sigma}\right)_{T} d\sigma \qquad\qquad (2\text{-}3)$$

The Maxwell relations can be derived using the above definitions, and are shown in

Eq. (2-4).

$$\left(\frac{\partial T}{\partial \varepsilon}\right)_s = \frac{1}{\rho}\left(\frac{\partial \sigma}{\partial s}\right)_\varepsilon, \quad \left(\frac{\partial T}{\partial \sigma}\right)_s = -\frac{1}{\rho}\left(\frac{\partial \varepsilon}{\partial s}\right)_\sigma \qquad (2\text{-}4)$$

$$\left(\frac{\partial s}{\partial \sigma}\right)_T = \frac{1}{\rho}\left(\frac{\partial \varepsilon}{\partial T}\right)_\sigma, \quad \left(\frac{\partial s}{\partial \varepsilon}\right)_T = -\frac{1}{\rho}\left(\frac{\partial \sigma}{\partial T}\right)_\varepsilon$$

Assuming a reversible heating and cooling process, based on the definition of specific heat under constant stress process and the first law of thermodynamics, the following equation can be derived.

$$c_\sigma = \left(\frac{\partial h*}{\partial T}\right)_\sigma = T\left(\frac{\partial s}{\partial T}\right)_\sigma = c_p \qquad (2\text{-}5)$$

Eq. (2-6) is set to be zero to describe the isentropic adiabatic phase change process upon loading. The Maxwell relation in Eq. (2-4) is used to substitute one of the partial derivative coefficient in Eq. (2-3). By integrating the loading process from zero to maximum stress, it yields the value of theoretical adiabatic temperature span in Eq. (2-7). This equation is not applicable to use, however, due to the complicated terms and comprehensive measures required. Instead, direct measurements are more straightforward, including measurement of temperature change during the loading and unloading process, or using the latent heat from DSC with the specific heat c_p, as is discussed in more details in session 2.2.

$$ds = \frac{c_\sigma}{T}dT + \left(\frac{\partial \varepsilon}{\partial T}\right)_\sigma d\sigma = 0 \qquad (2\text{-}6)$$

$$\Delta T_{ad} = -\int_0^\sigma \frac{T}{c_\sigma}\left(\frac{\partial \varepsilon}{\partial T}\right)_\sigma d\sigma \qquad (2\text{-}7)$$

The most important relation for elastocaloric materials from elastocaloric effect

52

perspective is the Clausius-Clapeyron equation (Otsuka and Wayman, 1998), which correlates the constitutive relation of elastocaloric material with the latent heat of the phase transformation, as shown in Eq. (2-8).

$$\left(\frac{d\sigma}{dT}\right)_{sat} = -\frac{\rho\Delta s}{\varepsilon_M} \tag{2-8}$$

where the left hand side stands for the transformation stress and temperature ratio under equilibrium conditions, and right hand side is the ratio between the volumetric entropy change and the phase transformation strain.

However, caution is needed when using Eq. (2-8), due to the non-trivial hysteresis related with elastocaloric materials and deviation from equilibrium phase change. If the hysteresis is not negligible, specifications on which saturation temperature/stress is needed for Eq. (2-8). The hysteresis is a complicated result of many factors, to name but a few, including alloying, composition, thermal treatment, cycling (operation) and aging (Ortin and Delaey, 2002). Despite the various causes of the hysteresis, it measures the amount of energy dissipated during a cycle. In other words, minimum hysteresis is preferred from a thermal efficiency perspective. Figure 2-1 visualizes the hysteresis under two different driving modes and on the phase diagram as well. Figure 2-1 (a) shows the thermally driven hysteresis under the constant zero stress condition. The thermally driven cycle represents a heat engine cycle, which converts heat into strain variation (linear motion or vibration) and dissipates heat to a low temperature heat sink. The elastocaloric material starts below the martensitic finish temperature (M_f) and is heated. It remains in a single phase martensite until reaching the austenite start temperature (A_s). Phase transformation from martensite to

austenite takes place upon further heating until it reaches the austenite finish temperature (A_f). The austenite phase remains during the reverse cooling process before it becomes the martensite start temperature (M_s). Further cooling transforms austenite back to martensite until it reaches M_f. In a thermally driven cycle, heat from an excessive temperature level is required to induce the martensite to transform into austenite. During the reverse phase change process, a lower temperature heat sink is needed. Ideally, all four temperatures should be equal if there is no hysteresis, such as the boiling temperature and condensation temperature under the constant pressure are identical in a vapor-liquid system.

Figure 2-1 (b) represents the hysteresis associated with a stress-driven cycle under the constant temperature condition, which is used for a cooling or heat pump system. The stress keeps increasing to the saturation stress σ_{AM} corresponding to M_s, when the austenite starts its phase transformation into martensite. Since A_s is higher than M_s, the reverse phase change saturation stress σ_{MA} is lower than σ_{AM} under the same temperature.

Figure 2-1 (c) shows the well-known linear relation between the phase transformation saturation stress and the temperature reported for various elastocaloric materials in the past (Bekker and Brinson, 1997, 1998, Liang and Rogers, 1990, Lu and Weng, 1997). The real shape of the saturation stress-temperature curve may not be strictly linear due to many other factors. The four intersection states on the temperature scale represents the four temperatures under the stress-free condition in Figure 3(a). The four curves divide the entire domain into five sub-areas, and therefore can be used as a phase diagram. The term phase diagram here follows the traditional

thermodynamics convention for a single specie's gas-liquid-solid system (Moran et al., 2011), which is different from the alloys community, where phase diagram for elastocaloric materials mainly refers to the phase distribution when the alloy composition varies (Otsuka and Wayman, 1998, Otsuka and Ren, 2005, Recarte et al., 1999). Above the M_f curve is the single phase martensite, and austenite single phase is located below the A_f curve. Due to hysteresis, there are two regions where both phases exist in equilibrium, which are the area between the M_s and M_f and the area between A_s and A_f, respectively. The region between the two start curves represents the metastable states.

Following the gas-liquid-solid convention, a stress-strain-temperature surface visualizes the combined relation of Figure 2-1 (a), (b) and (c), as demonstrated in Figure 2-1 (d). This approach has been demonstrated for a Ni-Ti binary alloy in literature (McNichols and Cory, 1987, Peyroux et al., 1998, Schiller, 2002). In Figure 2-1 (d), martensite single phase surface is bounded by red lines, which is adjacent to the A-M two-phase surface. The M-A two-phase surface deviates from the A-M surface due to the hysteresis. Given context of a vapor-liquid system, there is only a single two-phase surface since there is no hysteresis between boiling and condensation. The states in between the M-A and A-M two-phase surfaces are metastable. Austenite is conjugated to the M-A two-phase surface, which is bounded by the green lines. The four stress-temperature curves in Figure 2-1 (c) are in fact the projections of the boundaries of the aforementioned A-M and M-A two-phase surfaces in the stress-temperature plane. The constant stress hysteresis loop in Figure 2-1 (a) is the intersection curves of the phase diagram in Figure 2-1 (d) with the zero-

stress plane. The constant stress hysteresis loop slope also represents the thermal expansion coefficient for single-phase austenite and single-phase martensite, as illustrated in Figure 2-1 (d). The slope of the single-phase surfaces measure the Young's modulus under the uniaxial loading condition.
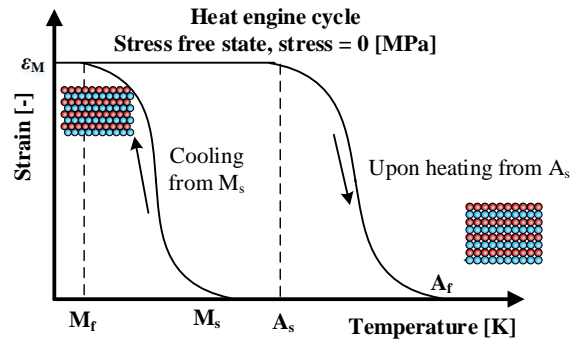
(a) Temperature hysteresis for a heat engine cycle under the stress-free state
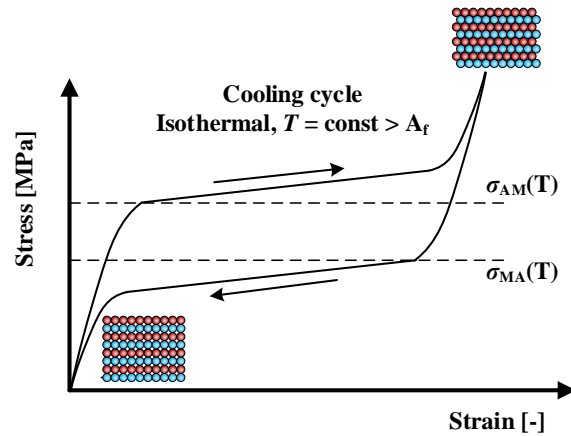
(b) Stress and temperature hysteresis for a cooling cycle under the isothermal

condition
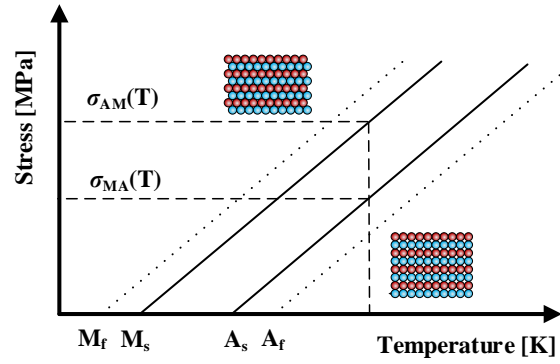
(c) Graphical interpolation of the constitutive relation for elastocaloric materials
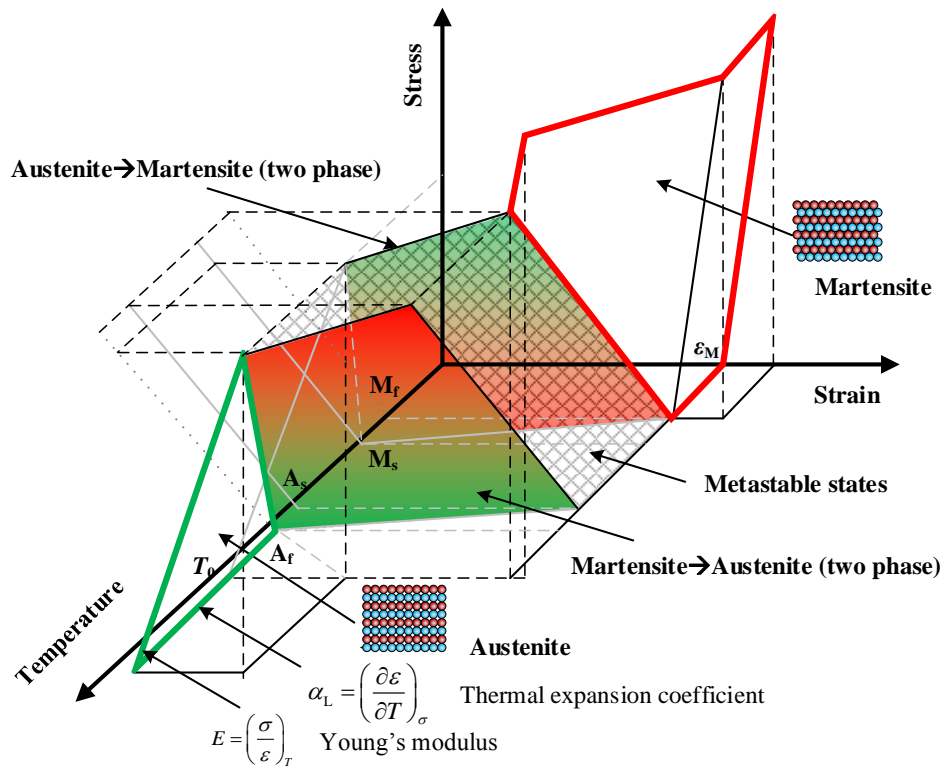
(d) A three dimensional phase diagram

Figure 2-1: Graphical representation of hysteresis curves, constitutive relation and a three-dimensional figure of the phase diagram of elastocaloric materials.

2.2   *Thermodynamic Performance of Elastocaloric Materials*

Criterions to rank elastocaloric SMAs are as follows:

- Adiabatic temperature span (ΔT_{ad}) and non-dimensional latent heat (γ)

The adiabatic temperature span is a direct measurement of the material's cooling capacity. It is defined in Eq. (2-9). It favors materials with larger latent heat and smaller specific heat. The latent heat can be measured by DSC following a thermally driven phase change process, or by direct measure of the adiabatic temperature span, i.e. ΔT_{ad}, when assuming the entire latent heat is absorbed by the elastocaloric material itself during the stress induced phase change process

Non-dimensional latent heat is a normalized adiabatic temperature span, defined as the ratio between the adiabatic temperature span and the systems' temperature lift, as shown in Eq. (2-10). When the ratio is above 1, it means that the material is able to run in a system while providing the required temperature lift in the denominator of Eq. (2-10). Otherwise, the cycle will not function unless heat recovery/regeneration is added.

$$\Delta T_{ad} = \frac{\Delta h}{c_p}\Big|_S \qquad\qquad (2\text{-}9)$$

$$\gamma = \frac{\Delta T_{ad}}{\Delta T_{lift}} \qquad\qquad (2\text{-}10)$$

- Phase change temperature range (T_{pc})

If the SMAs phase change temperature range is out of the air-conditioner and refrigerators requirement, no matter how large the performance metrics are, the material is still not useful. This range offers an intuitive way to see if a cooling application is capable of using a specific SMA as the solid-state refrigerant.

- Energy storage density (ESD)

ESD is another expression of the latent heat. It represents the volumetric latent heat, therefore a denser SMA is more favorable. The definition is in Eq. (2-11).

$$ESD = \rho \Delta h \tag{2-11}$$

- Relative cooling power (RCP)

This metric was commonly used in literature in terms of magnetocaloric effect and elastocaloric effect, since it could be computed directly out of the differential scanning calorimetry (DSC) results (Gschneidner and Pecharsky, 2000, Gschneidner et al., 2005, Casillo-Villa et al., 2011). It represents the accumulated latent heat over a temperature span, including both sensible and latent. This concept is important, since the real case entropy-temperature curve usually does not follow the ideal spike shape. Instead, the latent heat, or the entropy change spikes span over a temperature range, and therefore the accumulated power over such temperature range (usually less than 5K) represents the useful cooling/heating power. The definition is in Eq. (2-12). It can be regarded as another way to measure the latent heat other than the straightforward 1st metric.

$$RCP = \int_{\Delta T} \Delta s \left(\sigma, h^*, T \right) dT \tag{2-12}$$

- Material coefficient of performance (COP_{mat})

The material coefficient of performance (COP_{mat}) measures the energy conversion efficiency, from only the material property perspective without considering the system details. Nevertheless, there is no path independent cycle, so does thermoelastic cooling. Therefore, the COP_{mat} is path dependent, or in other words, may vary with different cycles.

When considering the material level COP, several idealizations to the cycle are necessary, including assumption that 100% unloading energy is recoverable and 100% heat recovery/regeneration efficiency.

Here, the stress-strain relations of different SMAs were predicted by a simple physics based one-dimensional constitutive model proposed by Muller and Xu (1991) and applied by Fedelich and Zanzotto (1991). It was simple since only the loading direction deformation geometry was used in addition to the homogeneous phase change assumption. Most importantly, the hysteresis physics was included. Muller and Xu (1991) assumed a symmetric quadratic free energy formulation to consider the hysteresis caused by domain elastic interactions (micro-scale friction). Fedelich and Zanzotto (1991) then applied the model to plot loading-unloading curves and described their graphical interpretations. The experimental data for different alloys, including Ni-Ti (Cui et al., 2012), Cu-Zn-Al tensile (Bonnot et al., 2008, Sato et al., 1984), Cu-Zn-Al compressive (Sittner and Novak, 2000, Gall et al., 1998), Cu-Al-Ni tensile (Chen et al., 2009, Yin et al., 2013), Cu-Al-Ni compressive (Picornell et al., 2004), Fe-Pd compressive (Xiao et al., 2013), and Ti-Ni-Cu (Bechtold et al., 2012), were used to fit in the Fedelich-Zanzotto-Muller-Xu (1991) model for three parameters: A, K and Δ (following Fedelich and Zanzotto's nomenclature).

Following the method proposed by Ziolkowski (1993) for a thermoelastic heat engine, the COP_{mat} for two different cycles can be derived: Brayton and Stirling. The difference between them is whether the loading/unloading processes are isothermal or isentropic.

First, the phase change stress (or "saturation stress") at given temperature is given by

Eq. (2-13). Note that the subscript "AM" refers to austenite to martensite, vice versa. The difference between loading/unloading stresses at the same temperature is a direct measure of the hysteresis.

$$\sigma_{AM}(T) = \frac{\rho}{\Delta}(T\Delta s - \Delta u^* + A^*)$$

$$\sigma_{MA}(T) = \frac{\rho}{\Delta}(T\Delta s - \Delta u^* - A^*)$$

(2-13)

For Stirling cycle, the amount of cooling per unit mass per cycle is in Eq. (2-14):

$$q_c = \sigma_{MA}(T_c) \cdot \frac{\Delta}{\rho} + \Delta u^* = T_c\Delta s - A^*$$

(2-14)

The amount of loading energy per unit mass per cycle w_+ is in Eq. (2-15):

$$w_+(T_h) = \left[\sigma_{AM}(T_h) \cdot \Delta + \frac{\sigma_{AM}^2(T_h)}{2K}\right] / \rho$$

(2-15)

The amount of unloading energy per unit mass per cycle w_- is in Eq. (2-16):

$$w_-(T_c, T_h) = \left[\sigma_{MA}(T_c) \cdot \Delta + \frac{\sigma_{AM}^2(T_h)}{2K}\right] / \rho$$

(2-16)

Therefore, the COP$_{mat}$ for Stirling cycle is equal to Eq. (2-17):

$$COP_{mat} = \frac{q_c(T_c)}{w_+(T_h) - w_-(T_c)} = \frac{T_c\Delta s - A^*}{(T_h - T_c)\Delta s + 2A^*}$$

(2-17)

Similarly, the COP$_{mat}$ for Brayton cycle is equal to Eq. (2-18):

$$COP_{mat} = \frac{q_c\left(T_c - \frac{\Delta T_{ad}}{2}\right)}{w_+\left(T_h + \frac{\Delta T_{ad}}{2}\right) - w_-\left(T_c - \frac{\Delta T_{ad}}{2}\right)} = \frac{\left(T_c - \frac{\Delta T_{ad}}{2}\right)\Delta s - A^*}{(T_h - T_c + \Delta T_{ad})\Delta s + 2A^*}$$

(2-18)

Note here the difference between loading/unloading adiabatic temperature spans is

ignored.

Also, COP_{mat} in Eq. (2-17) becomes Carnot COP under the same temperature conditions when the hysteresis constant $A*$ becomes zero. In other words, hysteresis is the material level irreversibility. Details on how to extract $A*$ from measured stress-strain curves from literature can be found in Appendix A.

COP_{mat} in Eq. (2-18) is less than that of Stirling cycle, since the constant temperature heat source/sink do not match with the variable temperature heat transfer process. The Brayton cycle has intrinsic irreversibility other than the contribution from hysteresis constant $A*$.
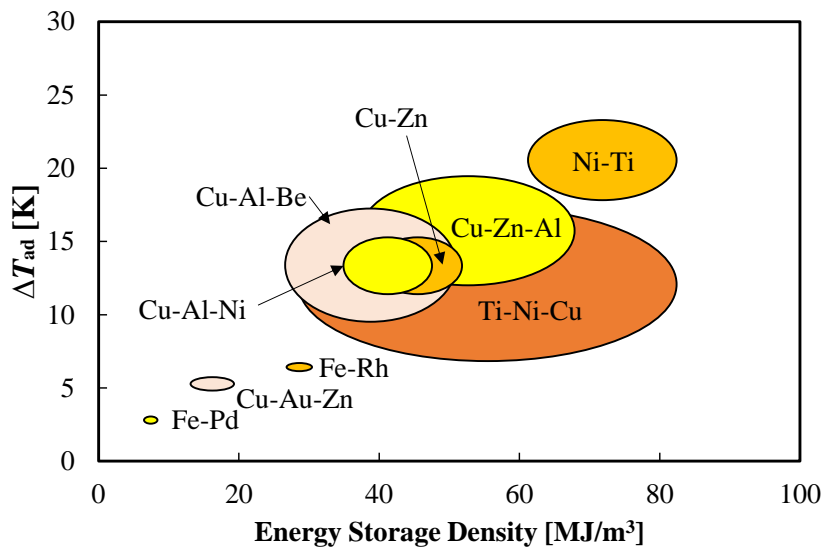
Figure 2-2: SMAs comparison based on adiabatic temperature span and energy storage density.

Figure 2-2 projects those materials on a $\Delta T_{ad} - ESD$ diagram. Since Cu-based alloys have higher density than Ni-Ti, they are closer to Ni-Ti from the 3rd metric ESD. Ferrous SMAs are also denser, but their latent heat are too small to catch up with

other SMAs. Also, Ni-Ti is the only material on the "Pareto front" and could be regarded as the best material from both the 1st and 3rd criterions.

Figure 2-3 shows the materials on the $\Delta T_{ad} - \text{COP}_{mat}$ diagram. Ni-Ti is no longer the only dominant choice from the 1st and 5th metrics. Ti-Ni-Cu has smaller ΔT_{ad}, but higher COP_{mat} due to small hysteresis. Also, the difference between tensile and compressive driving mechanism is more significant. For Ni-Ti, it results in more than four times higher COP when switching to compression. For Cu-based SMAs, tensile is usually a better choice.
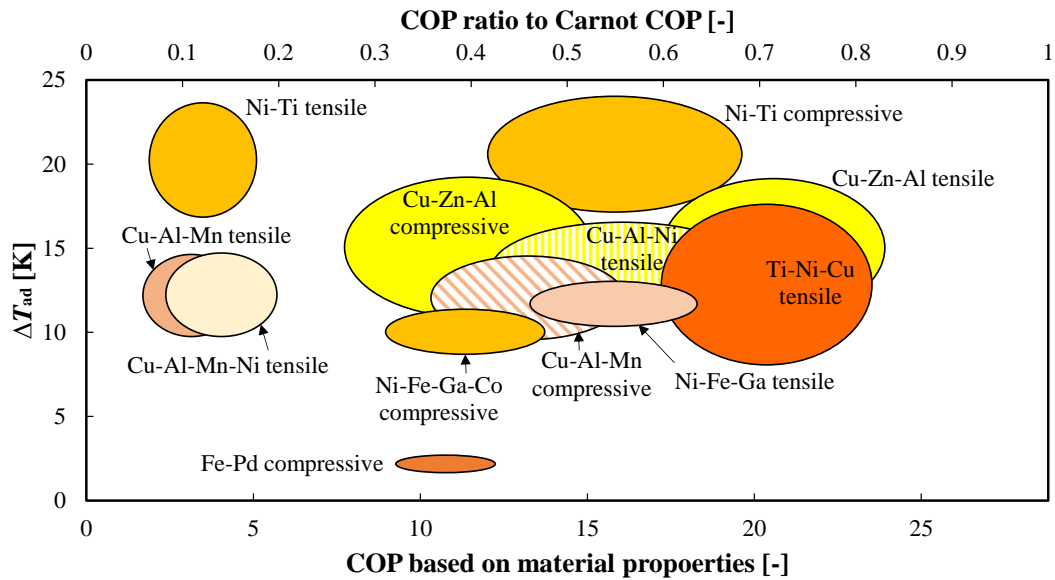
Figure 2-3: SMAs comparison based on adiabatic temperature span and material COPs under 10K temperature lift.

From the above analysis, the small latent heat is a limiting factor for ferrous SMAs. Ni-Ti, Ti-Ni-Cu, Cu-Zn-Al and Cu-Al-Ni are some promising SMAs for the thermoelastic cooling application.

Chapter 3: Cycle Analysis and Dynamic Modeling

Given the thermodynamic essentials, viable cycles for thermoelastic cooling system are proposed in this chapter. An easy-to-use analytical equation to predict the COP of a thermoelastic cooling system is presented. Based on the heat transfer energy equation and martensitic phase transformation dynamics, a transient model is developed in Simulink to conduct a few parametric studies. In the end of this chapter, a breakdown COP chart is presented to guide the performance improvement potentials.

3.1 *Thermodynamic Cycles Analysis*

The cooling/heat pump cycle is a reversed power cycle. Within each cycle, heat is pumped from a low temperature heat source (conditioned space, denoted by T_c) to a high temperature heat sink (ambient, denoted by T_h), with the expense of consuming power. For ideal thermoelastic material operated under Carnot cycle, the cooling, heating and power input within one cycle are represented from Eq. (3-1) to Eq. (3-3):

$$q_c = T_c \Delta s \tag{3-1}$$

$$q_h = T_h \Delta s \tag{3-2}$$

$$w = q_c - q_h = -(T_h - T_c)\Delta s \tag{3-3}$$

Here the entropy change associated with the martensitic phase change is a material parameter, which is determined based on the material composition and operating temperature. Practically, the power consumption within one cycle is no less than the reversible case, caused by the hysteresis loss of the irreversibility during the crystal

64

structure transformation from martensite to austenite and any friction in the transmission system and driving system.

Generally speaking, a thermoelastic cooling/heat pump cycle can be achieved via two basic thermodynamic cycles: reversed Brayton cycle in Figure 3-1 and reversed Stirling cycle in Figure 3-2. The reversed Brayton cycle consists of two isentropic processes and two iso-stress processes. It starts from state 1 at unstressed austenite, then is loaded to state 1' and its martensitic phase change starts. The associated latent heat is released from state 1' to state 2 adiabatically, causing the temperature to rise on the T-s diagram. Afterwards, the SMA is cooled down approaching the heat sink's temperature at T_h, while still being fully stressed at martensite. Before fully unloaded, the SMA can be further cooled down to state 4 when heat recovery is applied by exchanging the sensible heat between one set of SMA material starting at state 3, and another set of SMA material just finished cooling the conditioned space at state 6. A 100% heat recovery efficiency does not violate any laws of thermodynamics, which means temperature of state 4 could be identical to temperature of state 6. A detailed study on how to achieve high efficient heat recovery is introduced in Chapter 4. A reversed adiabatic phase change back to austenite takes place from state 4' to state 5 during the unloading process. The rest of the cycle remains unstressed, during the cooling process to the conditioned space from 5 to 6, and reversed heat recovery process from 6 back to 1 with the other set of SMA materials coming from 3 to 4. The heat recovery process conserves energy internally, and the heat rejected to sink should be equal to the heat absorbed from the conditioned space added by the work needed to drive one cycle. It should be noted that the area underneath 1-1'-2 in the σ-ε

(stress-strain) diagram is the loading work, and area underneath 4-4'-1 is the unloading work, which could be fully recovered if designed properly. Therefore, the area surrounded by the cycle on σ-ε diagram is the net power input with 100% work recovery design.
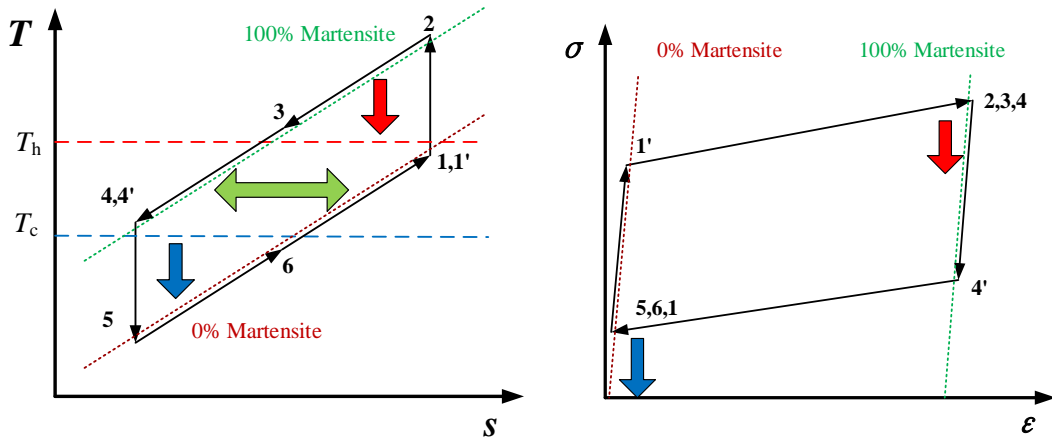
Figure 3-1: Illustration of reversed Brayton cycle and its variation as a thermoelastic cooling cycle.

The reversed Stirling cycle in Figure 3-2 contains two iso-stress heat transfer processes, and two isothermal phase change processes. The cycle begins at unstressed state 1, and is stressed to state 1' before the phase change. Different from reversed Brayton cycle, the SMA material is cooled during the martensitic phase transformation process from state 1' to state 2, therefore keeps a constant temperature while releasing the latent heat. The iso-stress heat recovery process from state 2 to state 3 is essentially the same as previously introduced. Afterwards, the unloading process from state 3 to state 4 via state 3' takes place with the isothermal heating process, where the conditioned room air is cooled down by the system. Another iso-stress heat recovery process (4→1) completes the cycle.

For Stirling cycle in Figure 3-2, one necessary condition is that the heat recovery efficiency is 100%. If the heat recovery efficiency is less than 100%, Figure 3-3 presents an alternative option by combining reversed Brayton cycle and reversed Stirling cycle together as a hybrid cycle. Processes 1→2 and 4→5 are isentropic loading and unloading, respectively, which compensate for the deviation of heat recovery efficiency from 100%. The rest are similar to the Stirling cycle.
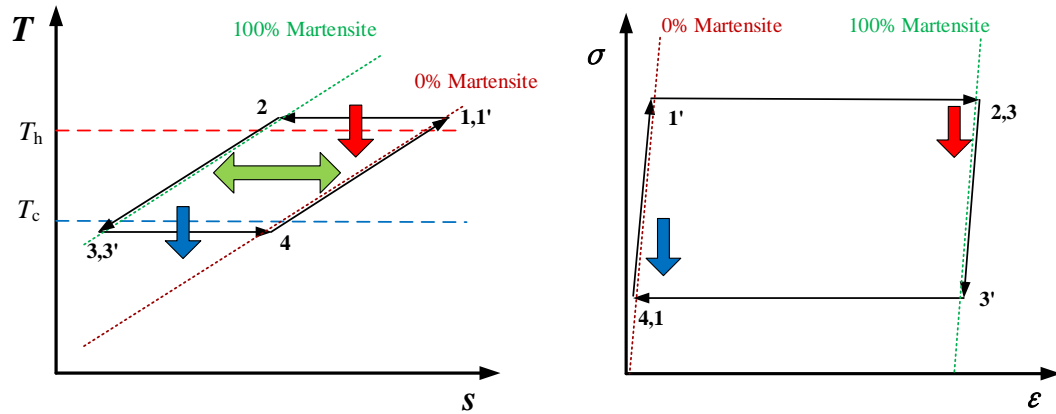
Figure 3-2: Illustration of reversed Stirling cycle and its variation as a thermoelastic cooling cycle.
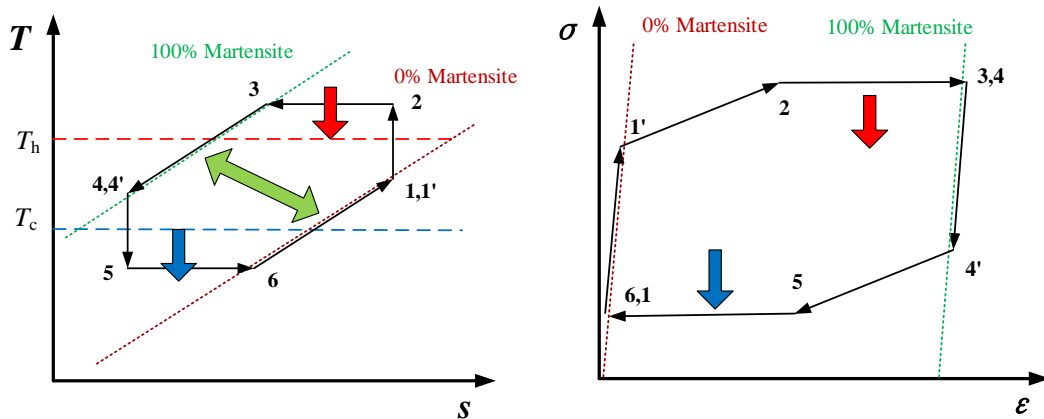
Figure 3-3: A hybrid cycle design as a combination of reversed Brayton cycle and reversed Stirling cycle.

67

The previous three cycles plotted in Figure 3-1 through Figure 3-3 are all ideal cycles, since loading and unloading processes are assumed to be reversible. However, two reasons contribute to irreversibility of the martensitic phase change. First, similar to an irreversible pool boiling process for a liquid that requires superheat, excess driving potential (excess stress) is needed to initiate the martensitic phase change. Secondly, there is irreversibility (friction) associated with the propagation of crystal molecular structure change during the martensitic phase change process. Both of them generate entropy during the loading (1→2) and unloading (4→5) process, as shown in Figure 3-4 for a realistic thermoelastic cooling cycle on a *T-s* diagram.
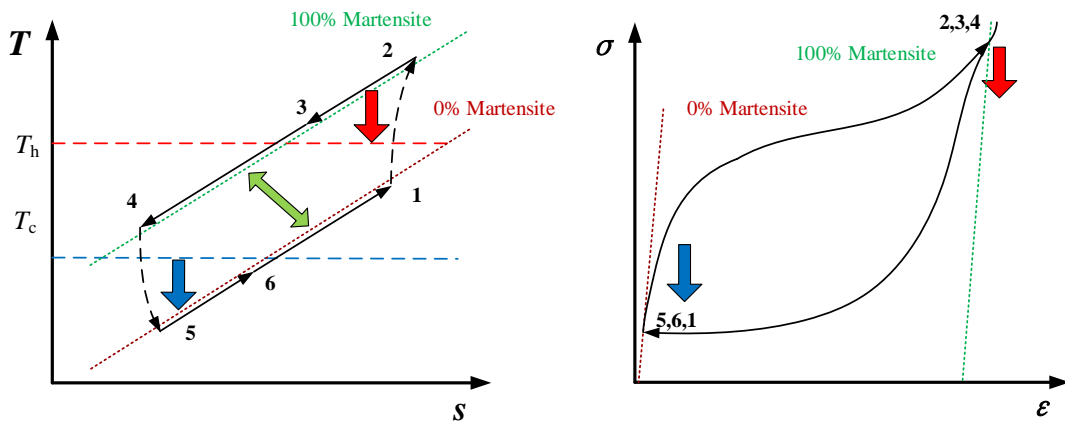
Figure 3-4: Illustration of a "real" thermoelastic cooling cycle similar to reversed Brayton cycle.

The COP_{mat} for Stirling cycle and Brayton cycle can be found in Eq. (2-17) and Eq. (2-18), respectively.

Note here the difference between loading/unloading adiabatic temperature spans is ignored. By comparing Eq. (2-17) with Eq. (2-18), one can clearly conclude that the Brayton cycle is less efficient than Stirling cycle, as quantitatively indicated by Table

3-1 as well. Instead of using two constant temperature heat source/sink as discussed above, the Brayton cycle is more efficient if two variable temperature heat source/sink are used.

Table 3-1: Physical properties and phase change parameters of some common SMA with giant elastocaloric effect. (*)

Materials	NiTi	CuZnAl	CuAlNi
ρ [kg/m^3]	6400-6500 (6500)	7500-8000 (7900)	7100-7200 (7150)
c_p [J/kg·K]	470-620 (550)	390-400 (400)	373-480 (440)
k [W/m·K]	8.6-18 (18)	84-120 (120)	30-75 (75)
Δs [J/kg·K]	42	19-26 (20)	20-30 (20)
ΔT_{ad} [K]	22.9 (300 K)	15.0 (300 K)	13.6 (300 K)
T_{pc} [°C]	-200 – 200	-200 – 150	- 200 – 200
A [J/kg]	150	155	280
K [MPa]	1.72×10^4	3.10×10^4	4.90×10^3
Δ	0.02	0.025	0.029
$w+$ (Brayton) [J/g]	5.64	1.58	3.02
$w-$ (Brayton) [J/g]	4.14	0.78	1.99
w_{net} (Brayton) [J/g]	1.50	0.80	1.03
γ	2.29	1.50	1.36
COP_{mat} (Brayton)	2.5 (Tensile)	6.9 (Tensile)	7.6 (Tensile)
	8.0 (Compressive)	6.8 (Compressive)	5.2 (Compressive)
COP_{mat}	3.4 (Tensile)	11.9 (Tensile)	11.9 (Tensile)
(Stirling)	15.5 (Compressive)	11.4 (Compressive)	7.2 (Compressive)
Data reference	**	***	****

* The numbers in bracket are specific numbers used for all calculation in this study.
NiTi: Ni 55 wt%; CuZnAl: Cu 65 wt% - 70 wt%, Al 13 wt% - 23 wt%; CuAlNi: Al 12-15 wt%, Cu 80 wt% - 85 wt%.
Also, 288 K to 298 K heat pump with 10 K temperature lift is used to evaluate the non-dimensional latent heat γ and other temperature dependent parameters here in this table.
**: Cui et al., 2012, Smith et al., 1993, Otsuka and Wayman, 1998
***: Ziokolwski, 1993, Otsuka and Wayman, 1998, Bonnot et al., 2008, Manosa et al., 1993, Manosa et al., 2009, Sittner and Novak, 2000, Manosa et al., 2013, Gall et al., 1998, Lashley et al., 2007
****: Friend and Hamilton, 1995, Rodriguez and Brown, 1980, Huang, 2002, Chen et al., 2009, Picornell et al., 2001, Picornell et al., 2004

The important criterion derived in Chapter 2, γ, known as the so-called "non-dimensional latent heat", can be found in Eq. (2-10) and is used in Table 3-1 and from Eq. (3-13) to Eq. (3-15).

For a Brayton cycle design, the time scale of phase change is much smaller than the

heat transfer time scale.

The derivation of the analytical COP and cooling capacity requires physical understanding of the solid-state material temperature change during a single cooling cycle.

Assuming:

- Lump temperature for solid-state materials

- Same heat transfer effectiveness for both solid-state materials during both cooling and heating process

- Same cooling and heating heat recovery efficiency

- Same adiabatic temperature span for stress induced phase change

For adiabatic phase change process:

$$T_2 - T_1 = T_4 - T_5 = \Delta T_{ad} \tag{3-4}$$

For solid-state material, heat transfer processes (2→3 and 5→6):

$$\frac{T_2 - T_3}{T_2 - T_h} = \frac{T_6 - T_5}{T_c - T_5} = \varepsilon^* \tag{3-5}$$

For heat recovery process (3→4 and 6→1'):

$$\frac{T_3 - T_4}{T_3 - T_6} = \frac{T_{1'} - T_6}{T_3 - T_6} = \eta_{HR} = \eta \tag{3-6}$$

The material cooling capacity could be evaluated by

$$\dot{Q}_{material} = \frac{mc_p}{t_{cyc}} (T_6 - T_5) \tag{3-7}$$

where m is the total mass of solid-state material in the system, and t_{cyc} is the cycle duration, as shown in Figure 3-5.

70
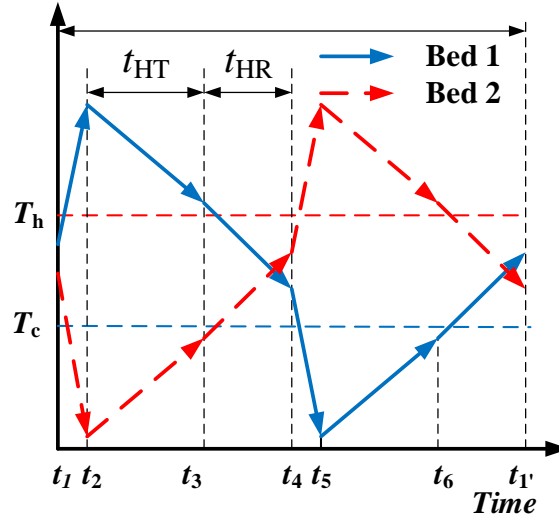
Figure 3-5: Illustration of the temperature profiles of solid-state thermoelastic SMA beds during one cooling cycle.

The fluid cooling capacity deviates from the material cooling capacity, since part of the cooling power released from the solid-state material is lost along the pipeline to the heat exchanger due to fluid mixing, heat loss to ambient, and most importantly, the cyclic loss as a result of cyclical variation of temperature from the dead thermal mass in the system. More details in terms of the cyclic loss are discussed in 3.3.4 and Chapter 6. Such difference caused by irreversibility could be measured by a factor less than 1, defined in Eq. (3-8). It should be noted that this factor F is not a constant, instead, it is determined based on the system configuration, ratio between the thermal mass of SMA and dead thermal mass, and cycling frequency.

$$F \equiv \frac{\dot{Q}_{fluid}}{\dot{Q}_{material}} \tag{3-8}$$

On the other hand, the real power consumption to drive the solid-state material loading-unloading process also deviates from the theoretical value. This difference is

71

due to motor efficiency η_{mot}, transmission efficiency η_{trsm}, and work-recovery efficiency η_{rec}. A similar factor could be applied to evaluate this deviation, defined in the following manner:

$$D \equiv \frac{\dot{W}_{ideal}}{\dot{W}_{real}} = \eta_{mot}\eta_{trsm}\frac{w_+ - w_-}{w_+ - \eta_{rec}w_-} \tag{3-9}$$

In the context of vapor compression heat pump, this factor D is similar to the compressor efficiency. Work recovery is similar to an expansion device, where part of the available energy from the high pressure refrigerant is re-used to reduce compressor work. Taken materials' hysteresis into account, the specific loading energy w_+ and unloading energy w_- in Eq. (3-9) are derived in Eq. (2-15) and Eq. (2-16), respectively.

Based on the graphical interpretation in Figure 3-5, two more equations are given:

$$\frac{\dot{Q}_{material}}{\dot{Q}_{latent}} = \frac{T_6 - T_5}{T_2 - T_1} \tag{3-10}$$

$$\Delta T_{lift} \equiv T_h - T_c \tag{3-11}$$

The system COP is defined as the ratio between gain and cost:

$$COP = \frac{\dot{Q}_{fluid}}{\dot{W}_{real}} = \frac{\dot{Q}_{fluid}}{\dot{Q}_{latent}} \cdot \frac{\dot{Q}_{material}}{\dot{Q}_{latent}} \cdot \frac{\dot{Q}_{latent}}{\dot{W}_{ideal}} \cdot \frac{\dot{W}_{ideal}}{\dot{W}_{real}}$$

$$= F \cdot \frac{\dot{Q}_{material}}{\dot{Q}_{latent}} \cdot COP_{mat} \cdot D \tag{3-12}$$

The second term could be evaluated from Eq. (3-4) to Eq. (3-7):

$$\frac{\dot{Q}_{material}}{\dot{Q}_{latent}} = \frac{\varepsilon*\left(\Delta T_{ad} - \Delta T_{lift}\left(1-\eta\right)\right)}{\Delta T_{ad}\left[1+\left(1-\varepsilon*\right)\left(1-2\eta\right)\right]}$$
$$= \frac{\varepsilon*\left(\gamma+\eta-1\right)}{\gamma\left[1+\left(1-\varepsilon*\right)\left(1-2\eta\right)\right]}$$

(3-13)

Based on the above discussions and the use of COP$_{mat}$ for Brayton cycle in Eq. (2-18), the system COP and cooling capacity are:

$$COP = F \cdot \frac{\varepsilon*\left(\gamma+\eta-1\right)}{\gamma\left[1+\left(1-\varepsilon*\right)\left(1-2\eta\right)\right]} \cdot D \cdot COP_{mat}$$

(3-14)

$$\dot{Q}_{fluid} = F \cdot \frac{mc_p \Delta T_{lift}}{t_{cyc}} \cdot \frac{\varepsilon*\left(\gamma+\eta-1\right)}{\left[1+\left(1-\varepsilon*\right)\left(1-2\eta\right)\right]}$$

(3-15)

It should be noted that factor F is not self-contained within the above equations set. It can be evaluated externally by dynamic modeling or experiment.

3.2 *Dynamic Model Development*

Assumptions used in the dynamic model are as follows:

- Martensitic phase transformation time scale and loading time scale are negligible compared with the heat transfer time scale.

- Radial heat transfer time scale is negligible compared with axial direction, Bi$_\delta$ = 0.01.

- Uniaxial loading and uniform phase transformation

- Constant thermophysical properties within the small temperature range of interest

- Incompressible flow and uniform velocity profile at any cross section inside the nitinol tube

- Uniform fluid temperature profile at any cross section inside the nitinol tube

73

- No heat transfer from nitinol tubes to surrounding

- No radiation heat transfer

It should be noted that the first assumption is crucial to the dynamic model numeric simulation, not only because of the decoupling of the problem, but also transforms a stiff problem to a normal problem and therefore stabilize the computation.
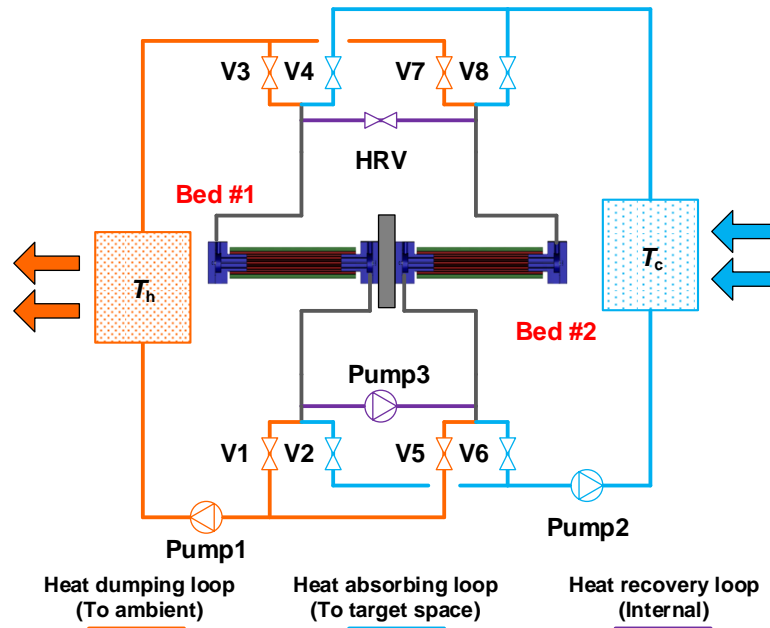
Figure 3-6: Schematic of the heat transfer fluid loop used for the numerical model.

Figure 3-6 shows the schematic of the thermoelastic cooling system modeled. There are four basic components in the model: thermoelastic material beds, heat source/sink, mechanical power computation, and connecting pipes (three colors representing different loops). The governing equation of thermoelastic material beds are the energy equations for solid tube and fluid inside, as shown in Eq. (3-16) and Eq. (3-17). For solid energy equation Eq. (3-16), the first term identifies the conduction along axial direction (flow direction), and the second term measures the

74

convective heat transfer between solid and fluid contact with solid. Most importantly, the last term is determined by the thermoelastic effect, which is positive during the austenite to martensite transformation process, negative during the opposite process, and remains zero when there is no phase transformation. This simplification of the martensitic phase change latent heat assuming that the loading/unloading processes are independent on temperatures of solid makes sense, since the time scale for phase change (~0.1 sec) is much smaller than the time scale for heat transfer (~ sec). It is an ideal scenario that the stress-strain relation could be decoupled from temperature, and is accurate enough for a cooling system level dynamic simulation. Such decoupling leads to the calculation of generation term much easier, as indicated in Eq. (3-18). In Eq. (3-18), the loading process releases heat, therefore generation term is greater than zero when the deformation strain rate is greater than zero. Both latent heat released from the phase change process Δh and mechanical stress induced deformation energy $w+$ are accounted, vice versa. It also holds for single phase heat transfer and heat recovery process, since the time derivative of normalized strain is zero when no phase change occurs. Here since a uniform phase change is assumed, the martensite phase fraction rate is the same as deformation strain rate. The strain profile is determined in Table 3-2.

$$\frac{\partial T_s}{\partial t} = \alpha_s \frac{\partial^2 T_s}{\partial x^2} - \frac{h}{\delta \cdot (\rho c_p)_s} (T_s - T_f) + \frac{g'''}{(\rho c_p)_s}$$

(3-16)

$$\frac{\partial T_f}{\partial t} = \alpha_f \frac{\partial^2 T_f}{\partial x^2} - \frac{4h}{ID \cdot (\rho c_p)_f} (T_f - T_s) - u_f \frac{\partial T_f}{\partial x}$$

(3-17)

$$g''' = \begin{cases} \rho(\Delta h + w_+) \cdot \dfrac{d\varepsilon}{\varepsilon_{max} dt} = \rho(T_s \Delta s + A)\dot{\bar{\varepsilon}} & \dot{\bar{\varepsilon}} = \dot{\xi} \geq 0 \\[4mm] \rho(\Delta h + w_-) \cdot \dfrac{d\varepsilon}{\varepsilon_{max} dt} = \rho(T_s \Delta s - A)\dot{\bar{\varepsilon}} & \dot{\bar{\varepsilon}} = \dot{\xi} < 0 \end{cases} \tag{3-18}$$

Table 3-2: Valves and pumps sequence of the thermoelastic cooling system

model.

Process	1→1'→2	2→3	3→4	4→4'→5	5→6	6→1'
Description	Adiabatic phase change	Heat transfer	Heat recovery	Adiabatic phase change	Heat transfer	Heat recovery
V1	X	O	X	X	X	X
V2	X	X	X	X	O	X
V3	X	O	X	X	X	X
V4	X	X	X	X	O	X
V5	X	X	X	X	O	X
V6	X	O	X	X	X	X
V7	X	X	X	X	O	X
V8	X	O	X	X	X	X
HRV	X	X	O	X	X	O
Pump1	X	O	X	X	O	X
Pump2	X	O	X	X	O	X
Pump3	X	X	O	X	X	O
$\dot{\bar{\varepsilon}}$	$1/t_+$	0	0	$1/t_+$	0	0

Note: "X" is close/off, "O" is open/on.

Adiabatic boundary conditions are applied for solid in Eq. (3-19) and commonly used boundary conditions for fluid are set in Eq. (3-20).

$$\frac{\partial T_s}{\partial x}\bigg|_{x=0, x=L} = 0 \tag{3-19}$$

$$T_f\big|_{x=0} = T_{f,in} \tag{3-20}$$

A uniform temperature water tank model is applied for both the heat source/sink, as

shown in Eq. (3-21). The heat source is assumed to have an instantaneous capacity $\dot{Q}_c$, which is determined by a PID controller using T_c and $T_{c,\text{set}}$ as control signals. The set points for heat source T_c and heat sink T_h are determined based on the temperature lift.

$$m_c c_{p,f} \frac{dT_c}{dt} = \dot{m}_c c_{p,f} \left(T_{in} - T_c \right) + \dot{Q}_c \tag{3-21}$$

For the connecting pipes, only fluid energy equation is used, with a correcting factor κ to account for the thermal mass contribution from solid pipe wall, as shown in Eq. (3-22) and Eq. (3-23).

$$\frac{\partial T_f}{\partial t} = \frac{k_f}{\kappa \left(\rho c_p \right)_f} \frac{\partial^2 T_f}{\partial x^2} - \frac{4h_{air}}{\kappa \left(\rho c_p \right)_f OD} \left(T_f - T_{amb} \right) - \frac{u_f}{\kappa} \frac{\partial T_f}{\partial x} \tag{3-22}$$

$$\kappa = \frac{\left(mc_p \right)_f + \left(mc_p \right)_s}{\left(mc_p \right)_f} = \frac{\left(\rho c_p \right)_f ID^2 + \left(\rho c_p \right)_s \left(OD^2 - ID^2 \right)}{\left(\rho c_p \right)_f ID^2} \tag{3-23}$$

The valve/pump sequences specified in

Table 3-2 are used to determine the flow rate and corresponding velocity for each pipe in Figure 3-6. When the valves are closed, it is assumed that the flow stops instantaneously without any delay, vice versa. Water is used as the heat transfer fluid for all fluid loops. The following correlation are currently used to predict the pipe flow heat transfer coefficient h, for both regular pipes and thermoelastic material tubes:

- Laminar flow: $Nu_D = 3.66$ (fully developed constant wall temperature)

- Turbulent flow: $Nu_D = 0.023 \mathrm{Re}_D^{4/5} \mathrm{Pr}^n$ (Dittus-Boelter equation)

Similar to other cyclically operated cooling systems such as adsorption chiller, the

thermoelastic cooling system's instantaneous cooling capacity, or the second term in Eq. (3-21), is also varying all the time. Instead, the time average cooling capacity during the cyclic steady state condition is used, and COP is also evaluated based on the time average capacity, as shown in Eq. (3-24) and Eq. (3-25):

$$\bar{\dot{Q}}_c = \frac{\int_0^{t_{cyc}} \dot{Q}_c \mathrm{d}t}{t_{cyc}} \tag{3-24}$$

$$COP = \frac{\bar{\dot{Q}}_c t_{cyc}}{m_s \left(w_+ - \eta_{rec} w_- \right)} \eta_{mot} \eta_{trms} \tag{3-25}$$

In this study, it is assumed that $\eta_{mot} \eta_{trms} = 0.9$, and work recovery efficiency $\eta_{rec} = 0.9$. m_s in Eq. (3-25) is the total mass of SMA in each bed.

To quantitatively study the thermoelastic cooling system performance, and investigate the most favorable material from a thermodynamic system perspective, various physical properties and loading test data are summarized in Table 3-1 for analytical and numerical modeling use in later part of this study.

3.3   *Results and Discussions*

3.3.1   Analytical COP

Figure 3-7 through Figure 3-9 show the COP and cooling capacity curves predicted by Eq. (3-14) and Eq. (3-15). The non-dimensional latent heat γ evaluated at 10 K lift is available in Table 3-1. Figure 3-7 shows how sensitive the performance is depending on heat recovery performance, if the cycle duration remains constant. The maximum COP improvements for all three alloys are all beyond 100% from worst

case scenario to ideal case. The improvement is even more than 50% when the heat recovery efficiency increases from 30% to 70%. It should be noted that it favors the higher specific heat materials by means of improving the heat recovery efficiency, since heat recovery reduces more internal parasitic sensible heat for higher specific heat materials.
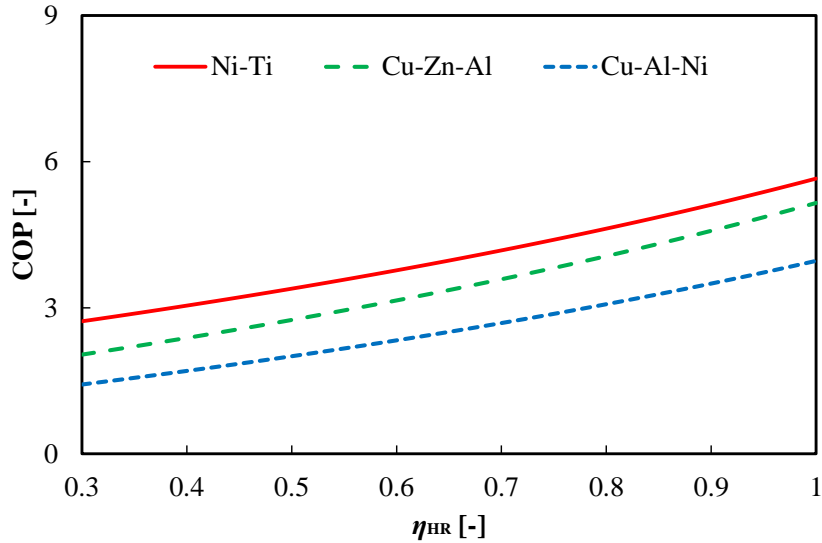
Figure 3-7: Analytical COP as a function of heat recovery efficiency (Three SMAs compressive loading mode, F = 0.9, ΔT_{lift} = 10 K, ε^* = 0.8, D = 0.85).

Figure 3-8 indicates that any insufficient heat transfer (process 2→3, 5→6 in Figure 3-5) will lead to significant performance deterioration. For normal operation conditions, the effectiveness is usually greater than 0.8. The COP improvement from 0.8 to 1 is 19%, which is not as significant as heat recovery efficiency. It should be noted that unlike heat recovery efficiency, the COP improvement by means of effectiveness is only a system perfectiveness and is independent of SMA properties.
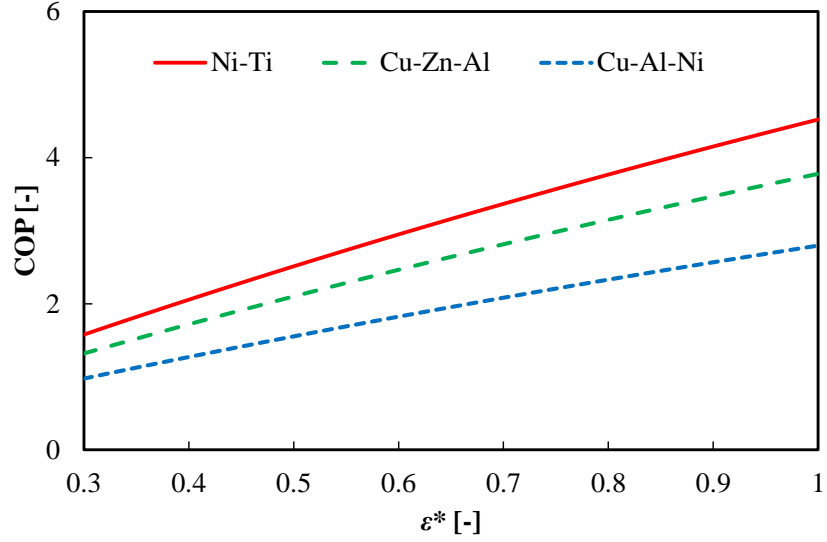
Figure 3-8: Analytical COP as a function of heat transfer effectiveness (Three SMAs compressive loading mode, $F = 0.9$, $\Delta T_{lift} = 10$ K, $\eta = 0.6$, $D = 0.85$).

Figure 3-9 plots how fast the performance decreases when the system temperature lift increases. The VCC system COP is plotted as a baseline. Figure 3-9 indicates a concave decreasing trend, which could be depicted by the derivative of COP curves, interception of COP at 0 K temperature lift, and interception of maximum temperature lift when COP drops to zero, in Eq. (3-26) through Eq. (3-28):

$$\frac{\partial COP}{\partial \Delta T_{lift}} = -F \cdot D \cdot \frac{\varepsilon^* \left[(2-\eta)\Delta s + 2A \cdot (1-\eta) / \Delta T_{ad} \right]}{1 + (1-\varepsilon^*)(1-2\eta)} \cdot \frac{COP_{mat}}{\left(\Delta T_{lift} + \Delta T_{ad} \right)\Delta s + 2A} \tag{3-26}$$

$$COP(\Delta T_{lift} = 0\,\text{K}) = F \cdot D \cdot \frac{T_c \Delta s - A}{2A} \cdot \frac{\varepsilon^*}{1 + (1-\varepsilon^*)(1-2\eta)} \tag{3-27}$$

$$\Delta T_{lift,\max} = \frac{\Delta T_{ad}}{1-\eta} \tag{3-28}$$

The Eq. (3-28) shows that the maximum temperature lift is not dependent on any material properties, and thus is a system performance index. Under the extreme case

when the heat recovery efficiency becomes 100%, there is no limit on the maximum system temperature lift anymore, and COP becomes independent on temperature lift as well, as indicated by Eq. (3-14).
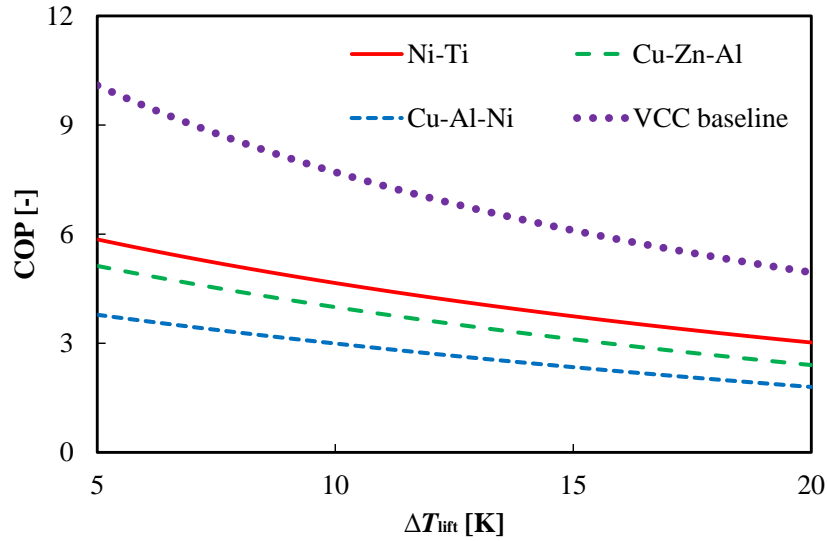
Figure 3-9: Analytical COP as a function of temperature lift (Three SMAs under compressive loading mode, $F = 0.9$, $\varepsilon^* = 0.95$, $\eta = 0.7$, $D = 0.85$).

3.3.2 Effect of Operating Parameters

Before discussing the effect of operating parameters, including flow rates and cycle duration, let's take a look at the model predicted temperature profiles in Figure 3-10. Figure 3-10 (a) plots the temperature profile of two Ni-Ti beds for four complete cooling cycles under the "cyclic steady state" condition. All the simulation results used for discussion in this thesis is sampled under such "cyclic steady state" condition. Figure 3-10 (a) is also comparable to the concept schematic in Figure 3-5. Figure 3-10 (b) plots the model predicted temperature profile of heat source and sink. The temperature lift determines the set points for heat sink and source, and the

temperature curves are approaching their set points controlled by two PID controllers.
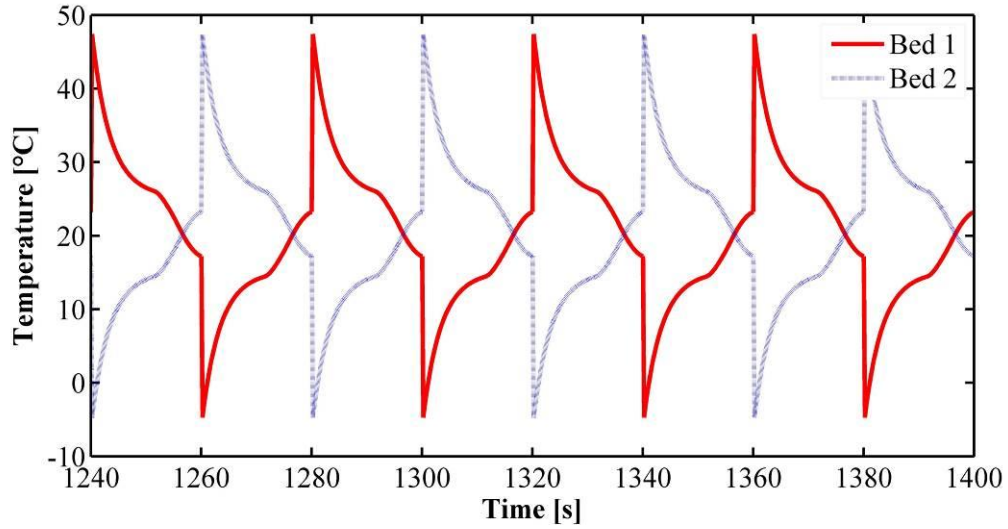
(a) Temperature profiles of two Ni-Ti beds during cyclic steady state
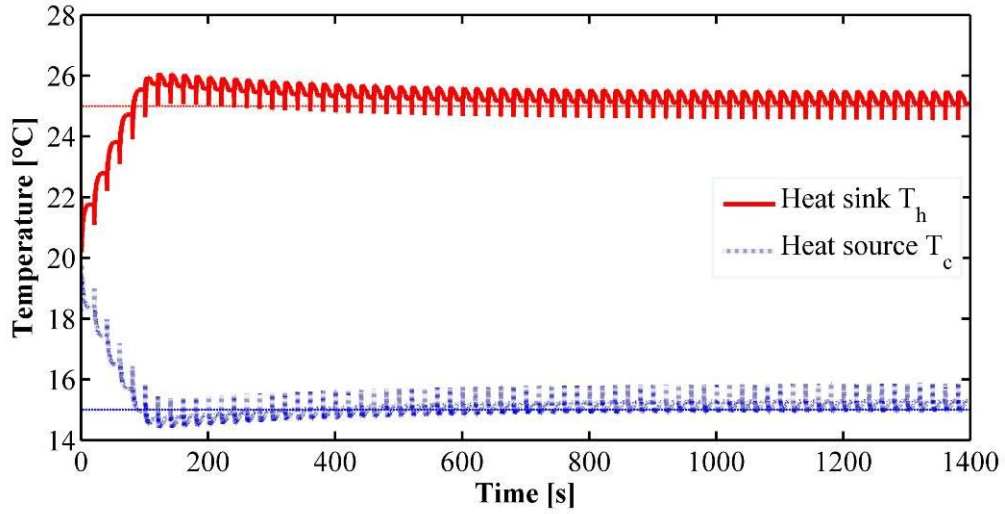
(b) Temperature profiles of heat source and heat sink. (Two dashed lines are set points for heat sink and heat source, $T_{c,set} = 15°C$, $T_{h,set} = 25°C$)

Figure 3-10: Temperature profiles predicted by the numerical model (Ni-Ti alloy, $u_{HT} = 1.2$ m/s, $u_{HR} = 0.1$ m/s, L = 0.254 m, OD = 0.005 m, ID = 0.004 m, N = 19, $\Delta T_{lift} = 10$ K, half cycle duration $t_{cyc} = 20$ s).

It should be noted that the heat recovery duration in this study is determined based on the following equation according to Chapter 4, unless otherwise noted.

$$t_{HR} = t^* \times \left(\frac{L}{u_{HR}} + \frac{L_{HR,pipe}}{u_{HR,pipe}} \right) \tag{3-29}$$
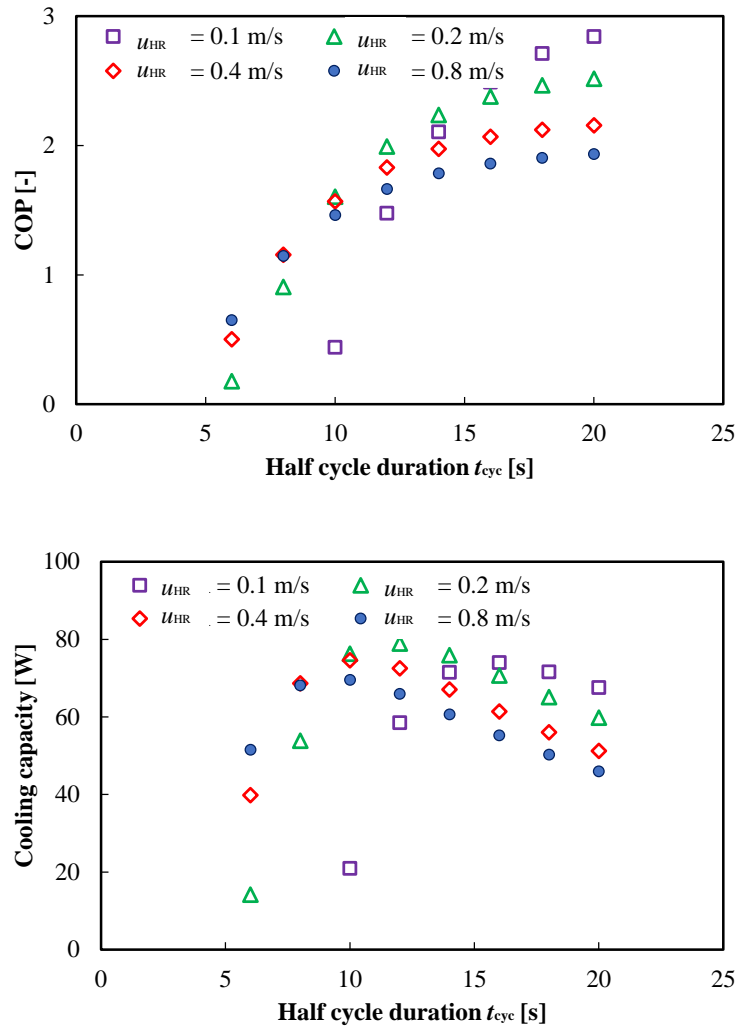
Figure 3-11: Model predicted COP and cooling capacity as a function of cycle duration (Ni-Ti alloy, u_{HT} = 1.2 m/s, L = 0.254 m, OD = 0.005 m, ID = 0.004 m, N = 19, ΔT_{lift} = 10 K).

The first term t^* in Eq. (3-29) is the heat recovery coefficient, or a non-dimensional

heat recovery time, and is found to be 1.2 in order to result in the optimum heat recovery efficiency, as is discussed in Chapter 4. The two terms inside bracket measure the total time duration for the fluid to travel half of the heat recovery loop, which is equal to the time required to flow through one Ni-Ti bed, in addition to the time required to flow through the connecting heat recovery pipes between two Ni-Ti tubes beds.

Figure 3-11 shows that the cycle duration is the most significant contributing factor to the system performance. A longer cycle has higher a more "complete" heat transfer and a more reversible heat recovery, therefore both heat transfer effectiveness ε^* and heat recovery efficiency η increase. As indicated by Eq. (3-14), the COP increase with a higher ε and η. This indicate that within a longer cycle duration, the total cooling generated per cycle increases with a constant work input per cycle. However, the time averaged generated cooling per cycle is not necessarily increasing as well. As indicated by Eq. (3-15), a longer cycle result in a higher numerator and denominator at the same time, and an optimum duration could be found in Figure 3-11 cooling capacity plot.

Similarly, Figure 3-12 plots the contribution of another important parameter to the performance, the flow rate (or corresponding velocity over the Ni-Ti tube) during the heat transfer process u_{HT}. A higher flow rate increases convective heat transfer coefficient, and therefore the heat transfer effectiveness increases as well. Since the cycle duration remains constant, both COP and cooling capacity increases until a plateau is reached when $u_{HT} = 0.4$ m/s. This is because the majority bottleneck to limit a higher effectiveness is the heat transfer duration rather than heat transfer flow

rate at that point. The second observation is that the COP and capacity curves have tiny oscillation at different flow rate rather than increasing monotonically to a saturation values. This is due to the temperature oscillation transient effect during the heat transfer process when the thermal mass of fluid inside the heat source/sink is in the same magnitude as the Ni-Ti bed fluid.
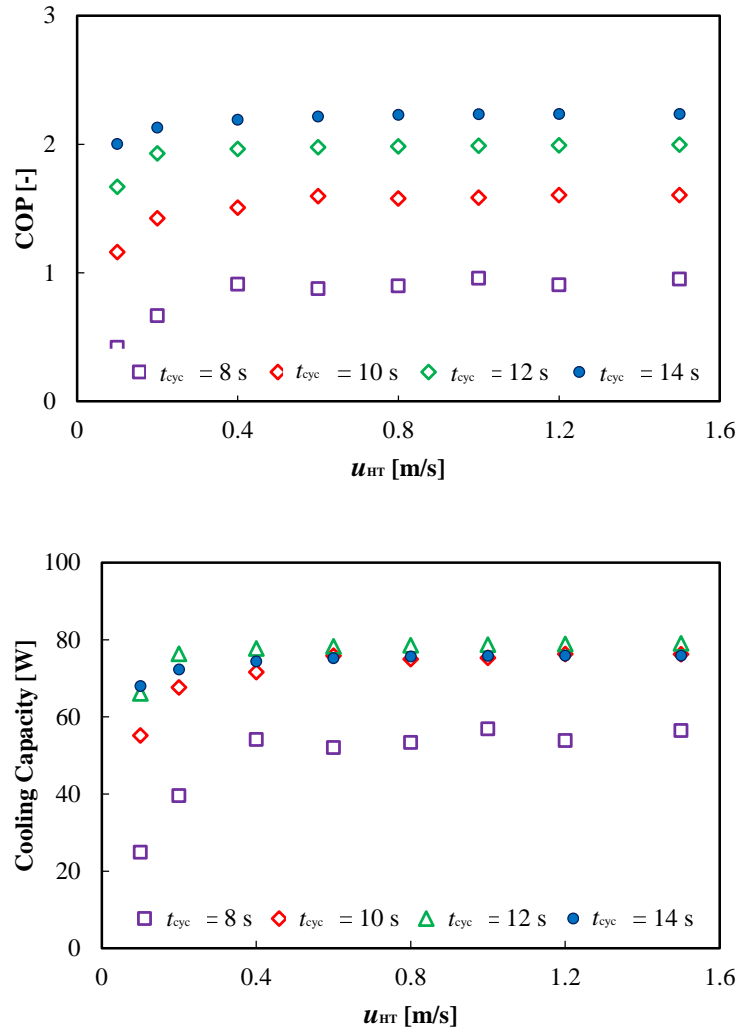
Figure 3-12: Model predicted COP and cooling capacity as a function of heat transfer flow rate (Ni-Ti alloy, u_{HR} = 0.2 m/s, L = 0.254 m, OD = 0.005 m, ID = 0.004 m, N = 19, ΔT_{lift} = 10 K).
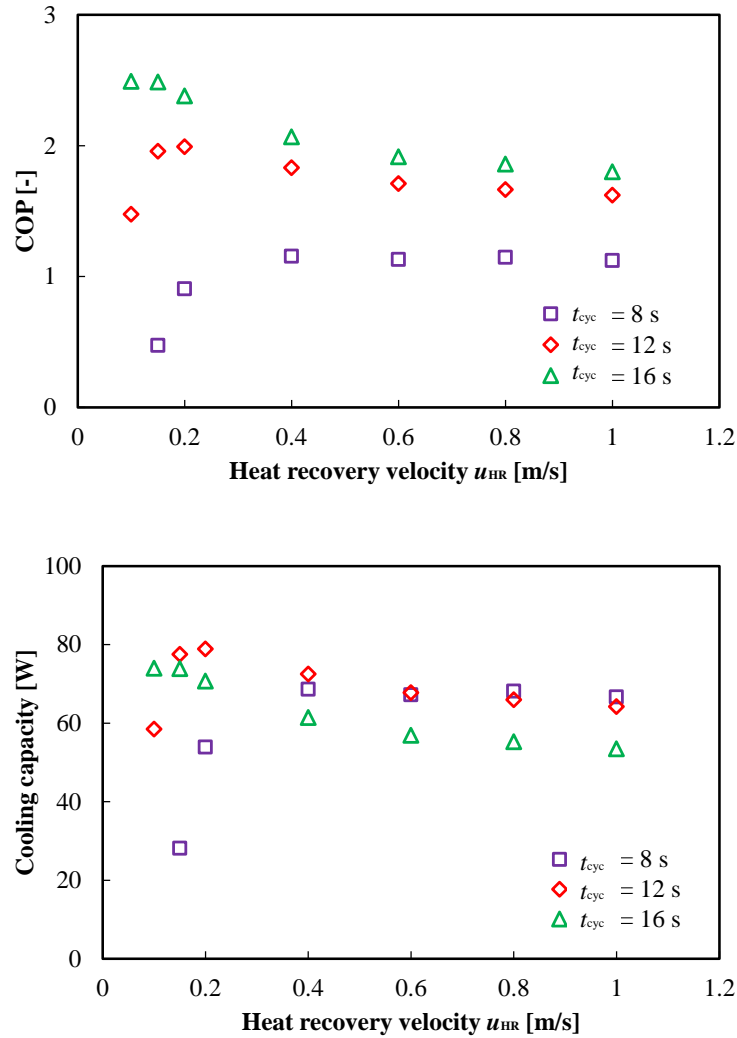
Figure 3-13: Model predicted COP and cooling capacity as a function of heat recovery flow rate (Ni-Ti alloy, u_{HT} = 1.2 m/s, L = 0.254 m, OD = 0.005 m, ID = 0.004 m, N = 19, ΔT_{lift} = 10 K).

Regarding the heat recovery flow velocity u_{HR}, Figure 3-13 shows that an optimum u_{HR} exists but differs under different cycle duration. A slower heat recovery process is considered to be a more reversible design, but requires a longer heat recovery duration according to Eq. (3-29), and therefore leaves less time for heat transfer. By using the analytical COP in Eq. (3-14) again, the first effect is that a smaller u_{HR}

returns a higher heat recovery efficiency η, with a side effect of smaller heat transfer effectiveness ε^*. These two major contradictory effect result in the existence of the optimum u_{HR}.

3.3.3   Effect of Geometry Parameters

Unlike fluid refrigerants used in vapor compression system, solid-state materials used in thermoelastic cooling have unique shapes and geometries. The geometries could significantly contribute to the transient behavior during the heat transfer and heat recovery process. For the following session's parametric study, the overall Ni-Ti volume is maintained constant to guarantee the same amount of material latent heat.
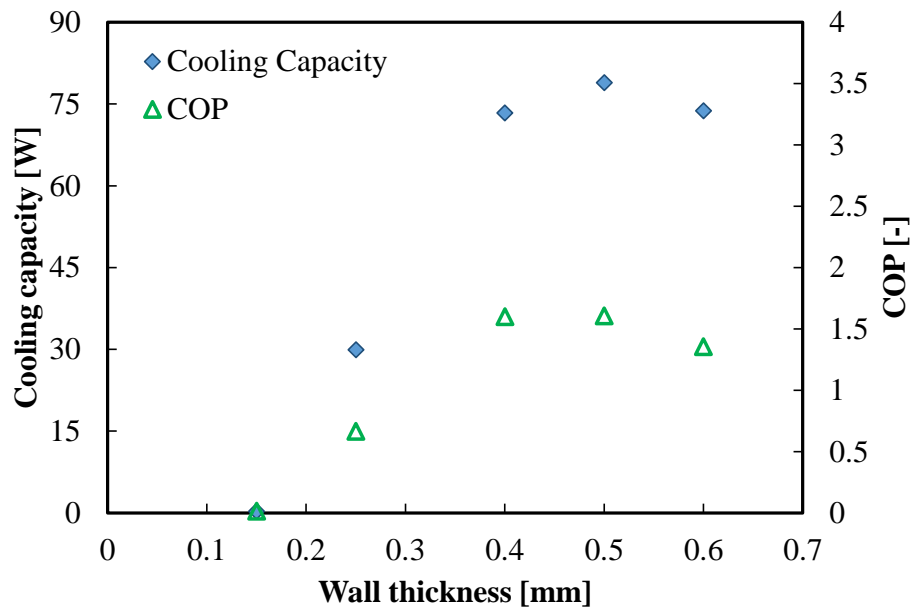
Figure 3-14: Effect of Ni-Ti tube wall thickness on COP and system cooling capacity (Ni-Ti alloy, u_{HT} = 1.2 m/s, u_{HT} = 0.2 m/s, L = 0.254 m, OD = 0.005 m, ΔT_{lift} = 10 K, N = 13 – 59).

As shown in Figure 3-11, the system cooling capacity does not increase linearly when

the cycle frequency increases, which is due to low heat transfer effectiveness and heat recovery efficiency. In other words, the Ni-Ti tube's thermal mass does not allow heat transfer with high frequency, and thus might be a limitation to increase the cycle frequency. One way to resolve this issue is to use thinner wall with smaller thermal mass per Ni-Ti tube. Figure 3-14 shows the effect of Ni-Ti tube wall thickness on both COP and cooling capacity. The Ni-Ti OD remains constant while varying different wall thicknesses. However, the cooling capacity and COP trend are not as expected to increase as wall thickness decreases.

To better understand the physics, Figure 3-15 plots the bed cooling capacity curves. The significant difference between Figure 3-14 and Figure 3-15 indicate that the amount of cooling extracted from Ni-Ti tubes do increase when reducing the wall thickness, but the cooling power could not be delivered to the heat source T_c. As the tube wall becomes thinner, the ratio of the dead thermal mass of HTF to the useful thermal mass of the Ni-Ti tubes increases significantly. As a result, the dominant dead thermal mass of HTF inside those Ni-Ti tubes neutralizes most of the useful cooling generated from the Ni-Ti tubes, especially under high frequency (short cycle duration) cases, contributing to the cyclic loss, as discussed in Figure 3-17 and later chapters. A few possible improvement designs to reduce the dead thermal mass of HTF and increasing the cycling frequency are to be discussed in Chapter 6 and Chapter 8.
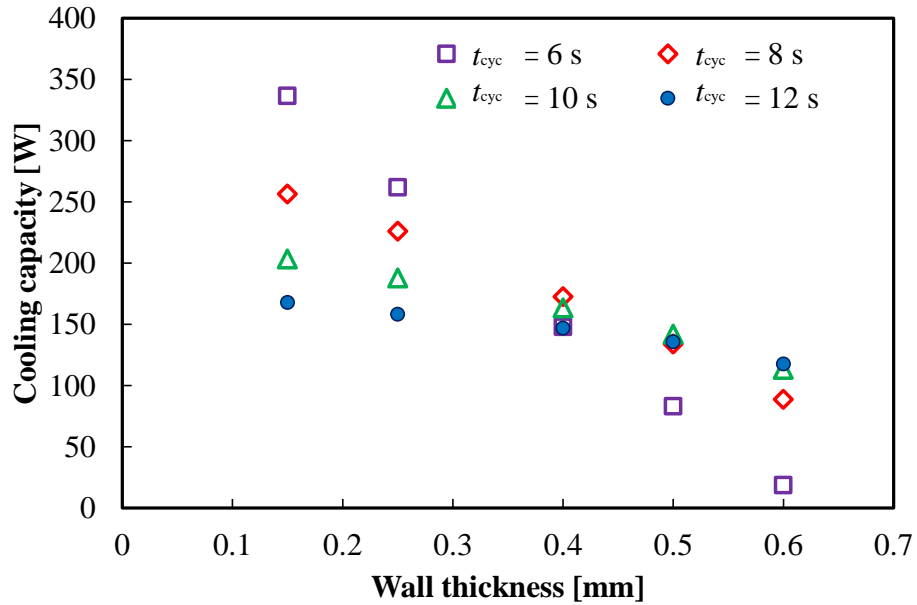
Figure 3-15: Illustration of Ni-Ti bed's cooling capacity when varying Ni-Ti tube wall thickness. (Note that the bed's cooling capacity is different from system cooling capacity due to the cyclic loss)

Figure 3-16 shows the impact of Ni-Ti tube length on the system COP and cooling capacity. The influence of tube length is not as significant as other parameters shown before. Longer tube slightly reduces the fluid heat transfer driven potential since the fluid temperature changes more along the Ni-Ti tubes, and therefore has a slightly negative impact on the heat transfer effectiveness ε^*. The heat recovery is considered to be more reversible with a longer tube length, and therefore Ni-Ti tube length has a slightly positive impact on the heat recovery efficiency η. The combination of these two effects contributes to the curves shown in Figure 3-16.
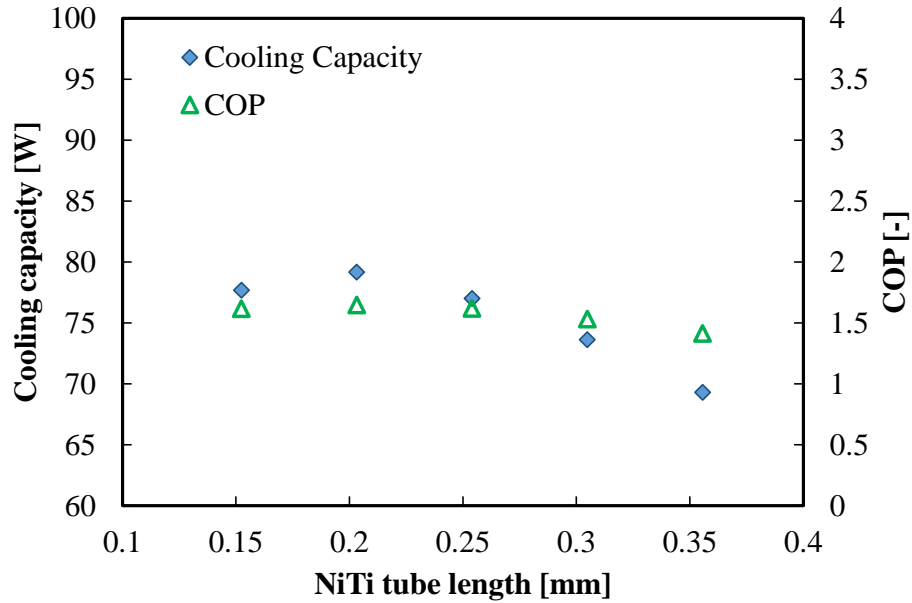
Figure 3-16: Effect of Ni-Ti tube length on COP and cooling capacity (Ni-Ti alloy, u_{HT} = 1.2 m/s, u_{HT} = 0.2 m/s, ID = 0.004 m, OD = 0.005 m, ΔT_{lift} = 10 K, N = 14 – 32).

3.3.4 Loss Contributions

Previous sessions focus how the system COP is determined by the operating and geometric parameters. This session focuses on an overview of loss contributions. Figure 3-17 left plot is a breakdown chart showing how the COP is degrading from Carnot COP and COP_{mat} to the system COP including the parasitic pump loss. The two COP_{mat} are evaluated using Eq. (2-17) and Eq. (2-18) under isothermal and adiabatic compression, respectively. These two numbers could be boosted if other alloys are applicable for a system, when their mechanical properties and fatigue life are within tolerance. The first stage loss is due to irreversible phase change, which is also measured by the material constant A^* in Eq. (2-17) and Eq. (2-18). Unlike liquid-

90

vapor phase change, solid-state phase change is highly irreversible contributed by "friction" interaction between different domains. The second stage loss is due to inefficiency of adiabatic compression, since the constant temperature heat source/sink do not match with the variable temperature heat transfer process in a Brayton cycle. The next stage loss is due to mechanical driving system inefficiency, which is also measured by the factor D defined in Eq. (3-9). When assuming a 90% motor efficiency, and 90% work recovery efficiency, it yields the D to be 0.70. The fourth stage loss is due to heat transfer effectiveness and heat recovery efficiency less than 100%, which is shown in Eq. (3-13). The COP_{bed} equals to 3.7 for a typical case simulation. The last stage loss is due to cyclic loss together with pumps parasitic power consumption. Factor F in Eq. (3-8) measures the cyclic loss, which is due to cyclic heating/cooling of fluid and corresponding pipe walls. If the HTF pumps power consumption is considered, assuming it to be equal to 20% of motor work, a system COP of 1.7 is achieved.

Losses contributions

1. Irreversible Martensitic phase change losses (hysteresis)

2. Adiabatic compression loss

5. Cyclic losses and pump work

3. Mechanical losses due to motor efficiency η_{mot} and work recovery efficiency η_{rec}

4. Heat transfer losses for solid-state refrigerant only, due to effectiveness ε and heat recovery efficiency η_{HR}

(a) COP = 1.7 for a typical cycle studied and corresponding losses

(b) COP = 7.7 for a cycle with 50% reduced losses expect pump work and cyclic loss

Figure 3-17: Illustration of breakdown COP chart of the studied compressive thermoelastic cooling system (Ni-Ti alloy, operating on 10 K temperature lift from 15°C to 25°C, with a set of typical operating parameters).

This typical case evaluation is a starting point, since it's a random design with no optimization. The previous parametric studies indicate that a lot of design and operating parameters do have optimum solution. Therefore, it is possible to reduce the third and fourth stages losses through optimizing the operating parameters and geometric parameters. It is also possible to use the hybrid cycle instead of the Brayton

cycle to improve the COP_{mat}. With a conservative estimation with no improvement on cyclic loss and pump work consumption, a COP improvement estimation is then plotted on the right side of Figure 3-17, assuming first to fourth stages losses could be reduced to half compared to the left side baseline scenario. The system COP is estimated to be 7.7 at 10K lift under this estimation. A more conservative estimation could also be made, assuming the first stage loss remains the same since motor efficiency could not be improved significantly, with a system COP of 5.2. A few improvement methods and their impact to the system performance is quantitatively discussed in Chapter 6.

3.4   *Chapter Summary and Conclusions*

This study discusses the thermodynamic fundamentals of thermoelastic cooling from the following aspects:

- Three ways of cycle design on *T-s* and stress-strain diagrams, applicable for both tensile driving mode and compressive driving mode.

- Analytical COP derivation and physical interpretation, applicable for both tensile and compressive driving modes using Brayton cycle design with heat recovery (regeneration).

- Development of a dynamic model for a compressive thermoelastic cooling system under Brayton cycle.

- Parametric study on important operating parameters and design geometric parameters using the dynamic model. Optimum solutions exist for the following parameters: cycle duration, heat recovery flow rate, SMA tube

wall thickness and length.

- Discussion on the breakdown COPs of the Brayton design compressive thermoelastic cooling system, analyzing the loss contributions. A typical case system COP considering driving motor efficiency and necessary parasitic pump power consumption is 1.7, and an estimated system COP with improvement ranges from 5.2 to 7.7, all evaluated under 10K lift. Possible performance improvement methods are: looking for more efficient SMA material, optimizing operating and geometric parameters, better design heat transfer loops or use high efficient pumps, and more efficient design of mechanical driving system.

Chapter 4:   Novel Thermo-wave Heat Recovery

The Brayton cycle introduced in Chapter 3 requires a high efficient heat recovery process. In this chapter, a specific design of the high efficient heat recovery process is introduced, which is also known as the "time scale counter-flow heat recovery", based on a natural analogy to the well-known counter-flow heat exchangers. Intrinsically, the governing equations between the "time-scale counter-flow heat recovery" and counter-flow heat exchangers are similar, which implies that a 100% heat recovery is theoretically achievable. The analysis in this chapter reveals the factors causing degradation from the 100% efficiency limit. This concept is further validated by a modified system dynamic model and experimental data.

4.1   *Time Scale Counter-Flow Heat Recovery*

This section is to introduce what the novel thermal-wave heat recovery (HR) process is and how it works in the following order:

- Provide an overview of the novel thermal-wave design concept for high conductivity solid application

- Propose the principle of "time scale counter-flow heat recovery process"

- Explain how to use a fluid with temperature gradient to achieve the "time scale counter-flow heat recovery process"

- Explain how to design the heat recovery process to generate and maintain the fluid with such a temperature gradient
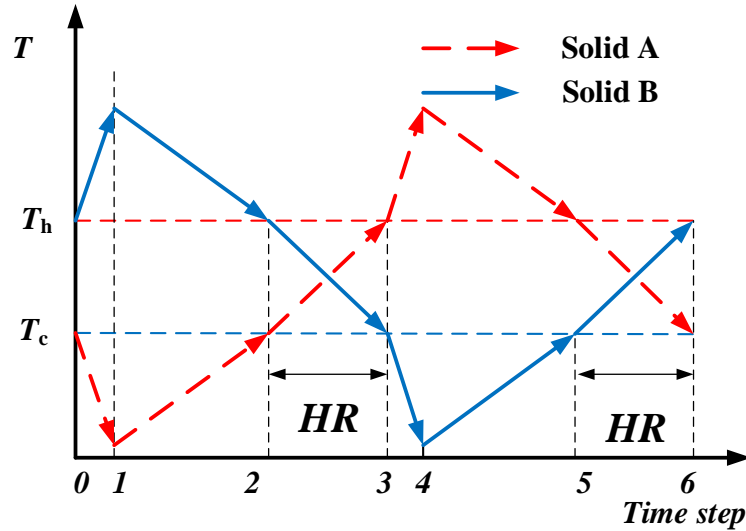
Figure 4-1: Illustration of the role of heat recovery in a cyclic solid-state cooling cycle.

Figure 4-1 explains the role of heat recovery following the Brayton cycle design introduced in Chapter 3. To accomplish the cycle, two solid heat exchangers (solid A and solid B) are needed. The beginnings of first half cycle and second half cycle ($0\rightarrow1$ and $3\rightarrow4$) are adiabatic, which occur when the governing mechanism release or absorb latent heat, such as compression/tension for thermoelastic cooling and magnetization/demagnetization for magnetic cooling. The second parts ($1\rightarrow2$ and $4\rightarrow5$) are the heat transfer processes between the solids with two streams of fluid from the heat sink (T_h) and heat source (T_c). The heat recovery processes are right after heat transfer processes ($2\rightarrow3$ and $5\rightarrow6$) between solid A and solid B internally. It should be noted that the temperatures of two solids switch between T_c and T_h as the cycle continues at the beginning of the heat recovery process.

The HR process is to recuperate the sensible heat between two solid-state materials that have the same amount of thermal mass. For example, solid A (a.k.a. solid heat

exchanger A) starts from the low temperature and solid B begins with the high temperature. The objective is to "swap" the temperature level between these two solids. Since the solid won't flow like a fluid, usually a fluid is needed to achieve the "temperature swap" process between solid A and B. During the HR process, the fluid needs to absorb sensible energy from solid B and provide cooling to solid B at the same time, and then deliver the absorbed heat to solid A. To conserve energy, the amount of energy taken from solid B has to be the same as that absorbed by solid A. One can expect a direct contact of the two solids would result in the reach of equilibrium after a certain period of time, however, with a good design, one can achieve even higher efficiency, that solid A ends up with temperature even higher than solid B. In the ideal case, solid B could be completely cooled down to the initial temperature of solid A, as shown in section 4.2, while in practical, it is always higher than that due to limited heat transfer capability.

The concept of novel thermal-wave heat recovery is introduced here by comparing between the traditional thermal-wave used for low-conductivity solids heat recovery application (adsorption cycle), and the novel thermal-wave developed for solid materials with high conductivity (solid-state cooling), as shown in Figure 4-2. Both Figure 4-2 (a) and (b) use color to indicate the temperature level of solid, and use the solid line position to indicate the temperature of fluid. The three figures of Figure 4-2 (a) depicts two thermal waves moving from left to right to heat solid A and to cool solid B, respectively. The left thermal-wave heats up solid bed A by a moving thermal-wave front bearing a tiny wave length, which represents a fluid having a steep temperature gradient. That wave front heats up solid bed A gradually as it

97

moves through solid A, and finally heats up almost all the bed. Since the solid bed conductivity is low enough, the thermal wave moves much faster than the heat conduction through the solid. The initially steep temperature gradient of the fluid can therefore be developed into a square shape as the wave sweeps through the solid A.

(i) Beginning of the heat recovery

(ii) Heat recovery in progress

(iii) End of heat recovery

(iv) Schematic

(a) Low conductivity solid thermal-wave for adsorption cycles (Shelton et al., 1990)
- Ideal wave length: zero (steep wave)
- Ideal wave pattern: square wave

(b) High conductivity solid thermal-wave for solid-state cooling cycles (this study)
- Ideal wave length: half loop length (smooth wave)
- Ideal wave pattern: ramp (triangle) wave

Figure 4-2: Illustration of traditional adsorption thermal-wave for low conductivity solid desiccant application, and novel thermal-wave for high conductivity solid material.

Nevertheless, the thermal-wave can only be formed by the fluid between Solid A and Solid B with a smooth temperature gradient, or a large wave length, as indicated by Figure 4-2 (b), since the materials themselves could not form large temperature gradient for the solid-state materials with high conductivities. The wave lengths for both cases, measured by the distance between the onset and end of one thermal wave, are labeled in the beginning stage of Figure 4-1. Taking solid A for example, the long wave length thermal-wave heats up solid A in a step at a time during the heat recovery process in a different manner from that in Figure 4-2 (a). At the beginning of the heat recovery process (say time t = 0), the inlet fluid temperature is the lowest, and the low temperature fluid heats up the solid by a tiny temperature difference at the beginning. As $t > 0$, the temperature of the fluid entering solid A varies from the lowest temperature to the highest temperature gradually, and as a result, the temperature of solid A increases gradually following the same pattern of fluid. At the end of the heat recovery process, the fluid temperature at the inlet of solid A is the highest, and solid A's temperature is close to the highest temperature of the fluid. The tracing particles in both Figure 4-2 (a) and (b) are added to assist the understanding of how the thermal-waves propagates and how the fluid with temperature gradient moves. As shown in Figure 4-2 (a), since it's better to regenerate the low conductivity adsorption bed by a uniform temperature, its thermal-wave prefers a shorter wave length or steeper temperature gradient (ideally square wave). On the other hand in Figure 4-2 (b), the high conductivity solid-state material needs to be regenerated uniformly, and therefore it prefers a longer wave length or smoother temperature gradient (ideally triangle wave).

4.1.1 Novel Thermal-Wave Heat Recovery Concept

The idea of the novel thermal-wave heat recovery cycle stems from the concept of a simple counter-flow heat exchanger, where the inlet temperature of fluid A is lower than that of fluid B. If the two streams share the same flow heat capacity rate and the heat transfer area is infinitely large, the outlet temperature of fluid A would be the same as the inlet temperature of fluid B. In reality, the outlet temperature of fluid A is always lower than that of fluid B. The idea of "counter-flow" design is to minimize the temperature difference between two flow streams everywhere throughout the heat exchanger. Such idea can be analogized on a "time scale", i.e. the temperature difference between solid and contacting fluid should be minimized "everywhere at any time".

Table 4-1: Analogy of spatial scale counter-flow heat transfer process to time scale counter-flow heat recovery process.

Spatial scale counter-flow heat transfer process		Time scale counter-flow HR process	
Inlet temperature	T_{in} (K)	Initial temperature	T_{init} (K)
Heat exchanger capacity	$\dot{Q}$ (W)	Heat transferred	Q (J)
Temperature slope	∇T (K·m^{-1})	Temperature slope	$\dot{T}$ (K·s^{-1})
Effectiveness	ε^* (-)	HR efficiency	η (-)
Max. effectiveness	100%	Max. efficiency	100%
Thermal resistance	R (K·W^{-1})	Transient resistance	R (K·J^{-1})
$\dot{Q} = \dot{m}_f c_{p,f} \left(T_{f,out} - T_{f,in}\right) = \dfrac{LMTD}{R}$		$Q = m_s c_{p,s} \left(T_{s,final} - T_{s,init}\right) = \dfrac{T_{s2,init} - T_{s1,init}}{R}$	

To follow this idea, the fluid entering both solid heat exchangers should have a minimum temperature difference from the solid heat exchangers at any moment

throughout the HR process. The analogy between the physical parameters describing the "spatial scale counter-flow" heat transfer process and "time scale counter-flow heat recovery process is quantitatively listed in Table 4-1. This analogy could also be expressed by Figure 4-3 (a) and (b).

(a) Spatial scale counter-flow heat
transfer process

(b) Time scale counter-flow HR process
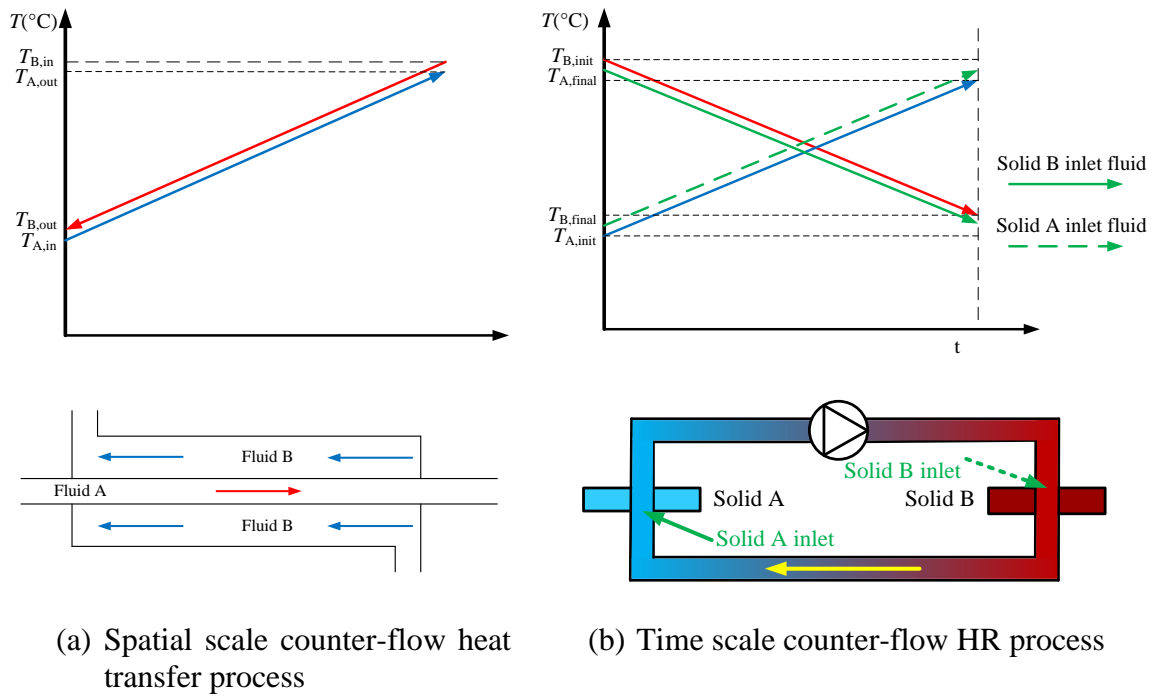
Figure 4-3: Temperature profiles of the "spatial scale counter-flow heat transfer process" and the time scale counter-flow heat recovery process" for the novel thermal-wave heat recovery process.

Figure 4-3 (a) demonstrates two fluids' temperatures on a spatial scale in a counter-flow heat transfer process with a large heat transfer area, where the outlet temperature of stream A is approaching the inlet temperature of stream B. Top plot of Figure 4-3 (b) demonstrates the two solids' temperature variations on a time scale during the HR process, together with the temperatures of their corresponding inlet fluid. Again, the

color here indicates the temperature level for both solids and fluid. The green solid and dashed lines are corresponding to the heat transfer fluid circulating between two solids. As indicated by the same figure, the inlet fluid temperature for A and B needs to vary with time accordingly to achieve the "counter-flow" design idea. Therefore, the next question is how to develop these two green lines in Figure 4-3 (b), i.e. fluid passing two solid heat exchangers while changing temperature with time.

4.1.2 How to Vary the Solid Inlet Fluid Temperature with Time

As it is demonstrated in the top plot of Figure 4-3 (b), during the "counter-flow" HR process, the fluid at the inlets of solids A and B should vary its temperature with time, so that solid A is heated gradually through one "counter-flow in time" process, and solid B is cooled down steadily through another one. Following two approaches were used to illustrate the physics behind this process.

Mathematical approach: the energy conservation equation for fluid inside the connecting pipe between A and B is shown in Eq. (4-1), where fluid conduction, viscous dissipation, and heat transfer with pipeline wall could be ignored:

$$\frac{\mathrm{D}T_f}{\mathrm{D}t} = \frac{\partial T_f}{\partial t} + \vec{u} \cdot \nabla T_f = \nabla \cdot \left(\alpha_f \nabla T_f \right) + \Phi + \frac{4h\left(T_{wall}\left(x,t \right) - T_f \right)}{\rho c_p D} = 0 \tag{4-1}$$

Here $\mathrm{D}T_f/\mathrm{D}t$ means the material time derivative of the spatial scalar field T_f. The solid A inlet fluid temperature can be obtained by solving Eq. (4-2):

$$\frac{\partial T_f\left(x,t \right)}{\partial t} \bigg|_{A,x=0} = -u\nabla T_f \left(ut,t=0 \right) \tag{4-2}$$

If the left side term is a constant, it indicates that T_f is changing linearly with time. As

a result, it means that an "initial condition" with uniform temperature gradient inside the pipe is required. It should be noted here that a linear temperature profile is not strictly needed for HR, but it's good for a better performance, as is discussed in section 3 regarding ideal HR cycle analysis.

Physical approach: As indicated by the snapshots in the bottom plot of Figure 4-3 (b), the fluid between solids A and B has a linear temperature gradient profile varying between $T_{A,init}$ and $T_{B,init}$. Now how the fluid temperatures of two solid inlets (green arrow positions in Figure 4-3 (b)) vary according to the incoming fluid temperature gradient is explained. Taking solid A inlet as an example, from the plot, it can be observed that hotter fluid arrives later than colder fluid. As a result, the solid A inlet fluid temperature varies from $T_{A,init}$ to $T_{B,init}$ when the fluid travels the exact distance of the connecting pipe between solids A and B, which is exactly our goal in the last section 4.1.1.

Both approach leads to one conclusion that a fluid between solids A and B with "preset" temperature distribution between $T_{A,init}$ and $T_{B,init}$ is required to achieve the "counter-flow" HR idea. It should be noted that based on our assumption in Eq. (4-1), the temperature gradient is required for the fluid inside the connecting pipe, rather than for the pipe wall. The contribution of connecting pipe wall to the HR efficiency is discussed later. The next question is: how to generate such a fluid with the required temperature gradient and how to maintain it?

4.1.3 How to Produce the Fluid with a Stored Temperature Gradient

The way to generate such a fluid with stored temperature gradient is in fact quite

simple: it's a naturally generated, and self-enhanced process, once the cycle duration is controlled precisely to be t_1 (defined in Table 4-3 of section 4.4). In other words, if the cycle duration is t_1, and the system reaches the so-called "cyclic steady state", there is a smooth fluid temperature profile close to linear distribution inside connecting pipe. Here cyclic steady state is referred to temperatures varying periodically over cycles at any locations in the system.
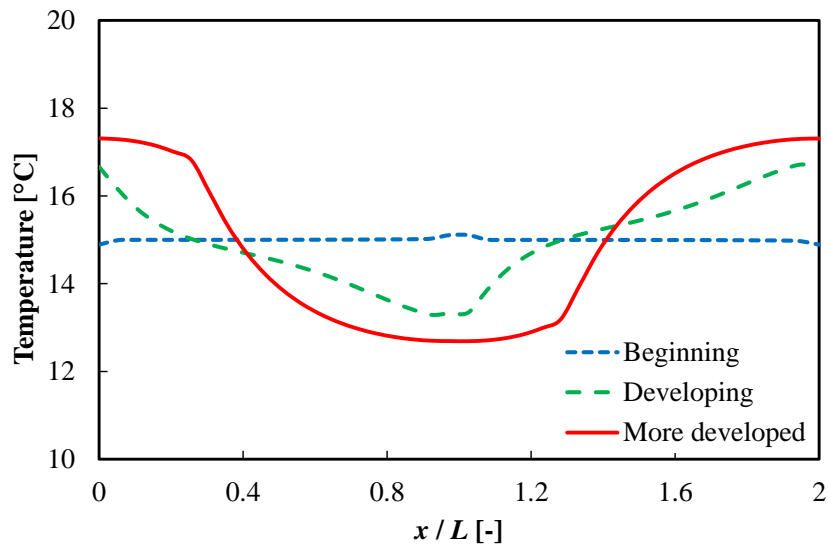
Figure 4-4: Snapshots of fluid temperature distribution along the connecting pipe at different time. (T_h = 20°C, T_c = 10°C)

First what it means by "naturally generated" is discussed. At the beginning, all solids and fluids are in equilibrium before one starts the cooling cycle and the heat recovery cycle. In other words, the temperature distribution at the beginning is uniform at an intermediate temperature. Figure 4-4 shows the snapshots of temperature distribution inside two connecting pipes at different time during the cyclic heat recovery process. Recall the role of heat recovery in the whole cycle in Figure 4-2, and keep in mind

that the solids A and B temperatures change either to T_h or T_c in every half cycle. At the very beginning, when solid A is at T_c and solid B is at T_h, the fluid temperature drops a little when passing through solid A, and generates a "low temperature peak". This part of fluid will pass solid B during the next half heat recovery cycle when solid B is switched to T_c, and the fluid will be further cooled down with the development of the "low temperature peak". As the cycle continues, when both the "hot peak" in the other part of fluid and the "cold peak" in this part of fluid are fully developed and do not change over cycles, a desired fluid with temperature distribution is developed between T_c and T_h in the connecting pipe. This "naturally-generated" temperature gradient is an evolving result from any initial temperature profile to the cyclic steady state temperature profile. The results are based on the ideal heat recovery cycle developed in section 4.2.

The feature of self-enhancing is more intuitive to understand. Take the connecting pipe from A to B in Figure 4-2 (b) as an example. If initially a fluid has a temperature gradient with higher temperature on the right side, as indicated by (i), the solid B is cooled down with minimum temperature difference between B and inlet fluid to solid B through the heat recovery process using the temperature gradient between solids A and B. Let us focus on the particle at lowest temperature inside this connecting pipe flowing towards solid B, as indicated by (ii). At the end of the heat recovery process, the particle moves to the outlet of the connecting pipe (iii). Meanwhile, a reversed temperature gradient has been established with higher temperature on the left as it compared with (i). Therefore, during the next heat recovery cycle when solid B is going to be heated up instead of cooled down, the reversed temperature gradient will

achieve the counter-flow heat recovery process once again. In this way, the fluid temperature gradient is developed as heat recovery cycle continues.

In a summary, the concept of "counter-flow in time scale" has been developed, focusing on minimizing the temperature difference between the fluid and solid during the heat transfer process, by passing fluid with varying temperature through the solids A and B. This fluid temperature variation inside solid is achieved by a self-generated and self-sustaining smooth temperature gradient in the connecting pipe between solids A and B.

4.2   *Ideal Heat Recovery Cycle Analysis*

4.2.1   What is Ideal Heat Recovery Cycle

Ideal heat recovery cycle analysis is to rank different parameters based on their impacts on the efficiency of heat recovery process. One can then neglect most of the minor irreversibility and simplify the heat recovery model. It should be noted that the ideal heat recovery cycle does not guarantee a 100% efficiency. Instead, it's a simple model that describe the most important features of the "time scale counter-flow heat recovery process" while ignoring those minor details.

The following assumptions are necessary to model the ideal heat recovery cycle:

- Solid conductivity is infinite.

- Solid acts as a point thermal mass with uniform temperature

- The wall of the connecting pipe has zero thermal mass

- The connecting pipe has uniform pipe diameter along the length

- Negligible fluid conductivity

- No viscous dissipation

- Uniform fluid temperature at any cross-section (one-dimensional simplification)

- No internal heat source/sink for fluid/solid
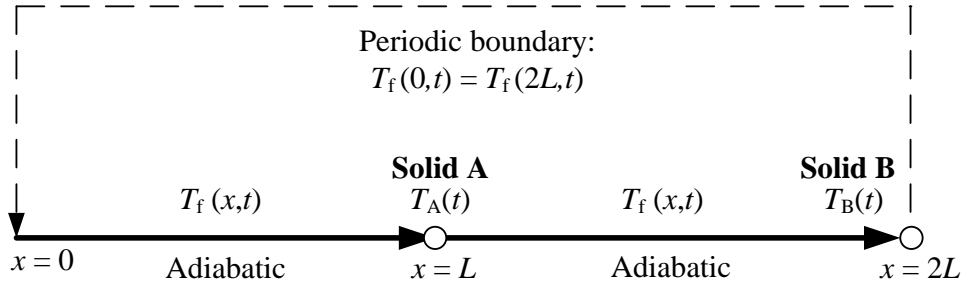
Figure 4-5: Illustration of the ideal heat recovery cycle model.

Figure 4-5 is an illustration of the ideal heat recovery cycle model with above assumptions. The two solids are located at $x = L$ and $x = 2L$, with a periodic boundary condition to characterize fluid circulation. A simple physical interpretation of the above assumptions is: the connecting pipes are adiabatic, and the only place where heat transfer can happen is at $x = L$ and $x = 2L$ i.e. the place where fluid is in contact with solid A or B. The governing energy equations for solids and fluid are shown in Eq. (4-3) and Eq. (4-4):

$$\frac{dT_s(t)}{dt} = -\frac{hA}{(mc_p)_s}\left[T_s(t) - T_f(L,t)\right] \tag{4-3}$$

$$\frac{\partial T_f(x,t)}{\partial t} + u\frac{\partial T_f(x,t)}{\partial x} = -\frac{hA}{(mc_p)_s}\left[T_f(x,t) - T_A(t)\right]\delta_{x,L} - \frac{hA}{(mc_p)_s}\left[T_f(x,t) - T_B(t)\right]\delta_{x,2L} \tag{4-4}$$

Here $\delta_{x,L}$ is the Kronecker's delta function, indicating that the heat transfer from solid to fluid only takes place at either $x = L$ (solid A) or $x = 2L$ (solid B). For any x other

107

than these two options, the right hand side of the equation is zero.

4.2.2 Sufficient Conditions for Ideal Heat Recovery Efficiency

Table 4-2: Non-dimensional ratios and time constants characterizing the ideal HR cycle.

Quantities	Definition	Physical interpretation	Contribution
$\bar{r}_1$ [-]	$\bar{r}_1 = \dfrac{\left(mc_p\right)_s}{\left(mc_p\right)_{f,HR}}$	- Thermal mass ratio between the solid and the fluid inside the connecting heat recovery pipe. - A non-dimensional measure of solid thermal mass.	Smaller $\bar{r}_1$, better efficiency
$\bar{r}_2$ [-]	$\bar{r}_2 = \dfrac{\left(mc_p\right)_{f,s}}{\left(mc_p\right)_s}$	- Thermal mass ratio between the fluid inside the solid heat exchanger and solid. - A non-dimensional measure of solid/fluid thermal mass ratio inside solid heat exchanger	Not significant
$\bar{r}_3$ [-]	$\bar{r}_3 = \dfrac{\left(\dot{m}c_p\right)_f}{hA}$	- Heat transfer rate ratio between convective flux rate through flow and conduction from the solid wall surface. - A non-dimensional measure of flow rate or h.	Smaller $\bar{r}_3$, better efficiency
t_1 [sec]	$t_1 = \dfrac{L}{u} = \dfrac{\left(mc_p\right)_{f,HR}}{\left(\dot{m}c_p\right)_f}$	- Ratio between fluid thermal mass inside connecting pipe and heat capacity rate. - It measures the time for fluid to travel between two solids.	Not independent variable
t_2 [sec]	$t_2 = \dfrac{\left(mc_p\right)_s}{hA}$	- Ratio between the thermal mass of solid and heat transfer coefficient. - It measures the transient response speed of solid.	Smaller t_2, better efficiency
t_3 [sec]	$t_3 = \dfrac{\left(mc_p\right)_{f,s}}{hA + \left(\dot{m}c_p\right)_f}$	- Ratio between the thermal mass of fluid inside solid heat exchanger and a sum of heat transfer coefficient and flow heat capacity rate. - It measures the transient response speed of fluid inside the solid when it interacts with flowing fluid and solid at the same time.	Not independent variable

An analytical analysis yields the following solution in Eq. (4-5), with an initial condition of linear temperature profile in Eq. (4-6). The three non-dimensional ratios and three non-dimensional time constants in Eq. (4-5) are defined in Table 4-2. To

investigate the sufficient conditions satisfying ideal heat recovery efficiency, the "cyclic steady state" condition is needed. In other words, one more condition needs to be considered to guarantee ideal heat recovery efficiency other than the efficiency itself is 100%, i.e. the temperature profile in the connecting pipe at the end of any heat recovery cycle should be the same as the initial temperature profile in the other heat recovery pipe, as shown in Eq. (4-7).

Solution for solid A during first heat recovery cycle with given initial condition is:

$$T_A(t) = T_h - \frac{(T_h - T_c)t}{t_1} + (T_h - T_c)\overline{r_1}\overline{r_3}\left(1 - \exp\left(-\frac{t}{t_2}\right)\right) \tag{4-5}$$

$$T_f(L,t) = T_h - \frac{(T_h - T_c)t}{t_1} + (T_h - T_c)\frac{\overline{r_1}\left((\overline{r_3}+1)1\left(1 - \exp\left(-\frac{t}{t_2}\right)\right) + \overline{r_2}(\overline{r_3} - \overline{r_2})\left(1 - \exp\left(-\frac{t}{t_3}\right)\right)\right)}{(\overline{r_3}+1-\overline{r_2})(\overline{r_3}+1)} \qquad 0 \le t \le t_1$$

Initial conditions are:
$$\begin{array}{l} T_A(0) = T_h \\ T_B(0) = T_c \end{array}, \quad \begin{array}{ll} T_f(x,0) = T_c + (T_h - T_c)\dfrac{x}{L} & 0 \le x \le L \\[2mm] T_f(x,0) = T_h - (T_h - T_c)\dfrac{x-L}{L} & L \le x \le 2L \end{array} \tag{4-6}$$

Equivalent conditions for an ideal heat recovery cycle efficiency under "cyclic steady state" are:

$$\eta_c = \frac{T_A(0) - T_A(t_1)}{T_A(0) - T_B(0)} = 1 - \overline{r_1}\overline{r_3}\left(1 - \exp\left(-\frac{t_1}{t_2}\right)\right) = 100\% \tag{4-7}$$

$$\Delta T_f(x,t_1) = T_f(x,t_1) - T_f(L+x,0) = (T_h - T_c)\frac{\overline{r_1}\left((\overline{r_3}+1)1\left(1 - \exp\left(-\frac{t_1 - \frac{x}{u}}{t_2}\right)\right) + \overline{r_2}(\overline{r_3} - \overline{r_2})\left(1 - \exp\left(-\frac{t_1 - \frac{x}{u}}{t_3}\right)\right)\right)}{(\overline{r_3}+1-\overline{r_2})(\overline{r_3}+1)} = 0$$

Both solid temperature and outlet fluid temperature in Eq. (4-5) consist of two parts: the first part is the first two terms, which are result of the upstream flow with an initial condition of linear temperature distribution. The second part is the third term

109

that represents the deviation from the upstream flow, caused by the unbalance between the solid thermal storage rate and fluid heat transfer rate. To satisfy the two equations in Eq. (4-7), the second part in both equation of Eq. (4-5) needs to be zero, which means that the both the solid and the fluid inside it need to precisely follow the incoming fluid temperature profile. That is to say the temperature patterns of both solid and fluid have to match with each other, or can be understood as a balance has to be made for the traditional heat exchangers in space scale:

- Solid absorbing/rejecting heat speed needs to be matched with incoming fluid temperature variation speed.

- Fluid inside solid heat exchanger absorbing/rejecting heat speed needs to be matched with incoming fluid temperature variation speed.

To quantitatively describe the flow balancing principle mentioned above, the two set of conditions below are sufficient to derive Eq. (4-7).

Sufficient condition #1: $\bar{r}_1 = 0$, finite other non-dimensional ratios and finite time constants. This means that either the solid thermal mass needs to be infinitesimal, or the fluid thermal mass inside the connecting pipe needs to be infinite. Under this case, there is no requirement for heat transfer coefficient.

Sufficient condition #2: $t_2 = 0$, $t_3 = 0$, $\bar{r}_3 = 0$, finite t_1, and finite other non-dimensional ratios. If both the solid and the fluid inside the connecting pipe have finite thermal mass, 100% efficiency is still achievable by letting hA to be infinite.

Both conditions are not achievable in reality, as a counter-flow heat exchanger with 100% effectiveness does not exist either. However, the design goal is always to minimize the heat transfer irreversibility, for both transient heat recovery here, and

steady state heat transfer as well. Nevertheless, the two conditions here provide some insight on how to improve the heat recovery efficiency, as their contributions are summarized in Table 4-2, and are still useful for "real" model analysis in the coming sessions.

4.3   *Validation Approach*

The theoretical aspects developed in 4.1 and 4.2 will be validated by experimental data and a modified dynamic model.

4.3.1   Experimental Setup

As shown in Figure 4-6, a small scale HR test facility was developed in the laboratory. Two stainless steel (SS316) tubes were adopted as the simulated solid-state material beds, since the thermo-physical properties of stainless steels are close to those of Ni-Ti alloy, which is one of the most promising thermoelastic materials. The two tested stainless steel were insulated externally. Water was used as the HTF for both heat recovery and temperature control. The HR was achieved by two HR pipes storing the required smooth temperature gradient and the flow was driven by a variable speed pump between two stainless steel test sections. Solenoid valves were installed on both sides to control the fluid flow. During the test, two objective temperatures were needed before each HR cycle, i.e. one high level temperature and one low level temperature. An inline heater and an ice-cooled coil were adopted as the heat source and heat sink, respectively, to control the targeted initial temperatures of the solid-state material. Pumps to circulate HTF and solenoid valves were installed on both cooling loop and heating loop for control purposes. The heater's capacity was

1.5 kW, and was controlled by "on-off" switch by the PID controller. The ice-cooled coils had a designed capacity around 0.5 kW, and the capacity was tuned with the mixing valve. Some detailed information in terms of the test facility are listed in Table 4-3.

Table 4-3: Some important parameters of the test facility.

	Test section	HR pipe		Cooling and heating loop
Material	Stainless steel SS316	PVC, clear PVC		Clear PVC
ID (mm)	11.8	25.4/12.7	for PVC/clear PVC	12.7
OD (mm)	12.7	28.6/15.9	for PVC/clear PVC	15.9
Length (m)	0.5	0.3/0.7	for PVC/clear PVC	/
Valves	/	2x electric actuated valves		8x solenoid valves
κ (-) *	/	1.09/1.24	for PVC/clear PVC	1.24

Note: κ is defined in Eq. (4-12) for connecting pipes between two test sections.
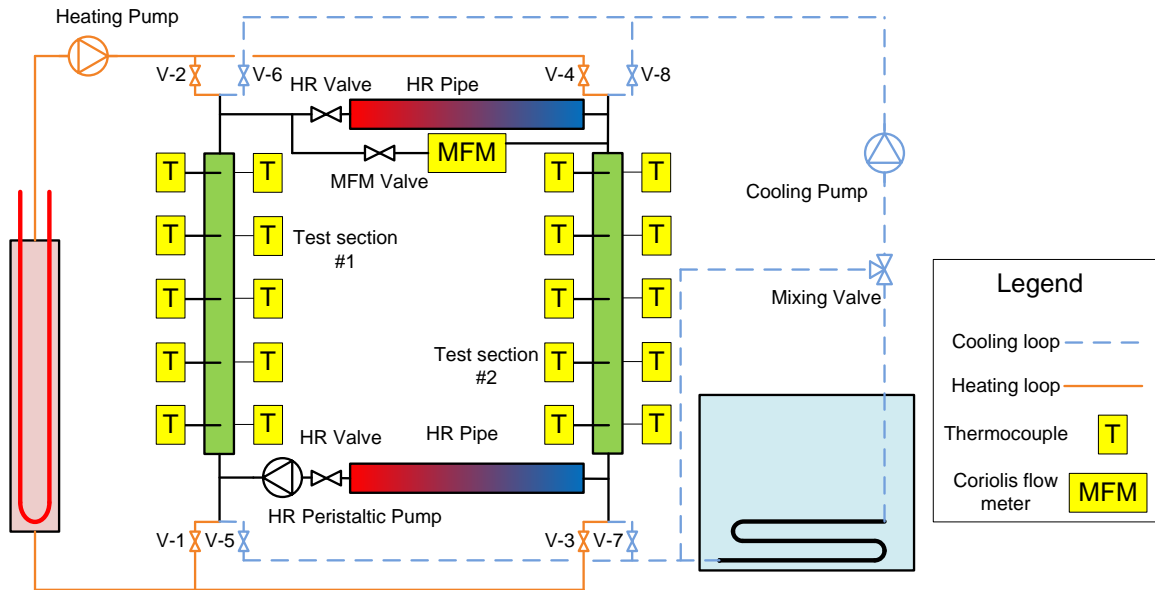
Figure 4-6: An illustration of the schematic of the HR test facility.

The test procedure is described below. During the first half cycle, #1 test section was heated and #2 test section was cooled to the desired temperature levels before the HR

112

cycle began. During the HR cycle, the fluid was circulated between two test sections following the proposed principle to cool test section #1 and heat up test section #2 in an opposite way. The second half cycle began after the first HR cycle and was operated in the opposite way compared with the first half cycle. The test section #1 and #2 were cooled and heated, respectively. The second HR cycle operated as the same manner to the first one, except the goal was to heat up the #1 test section and cool down the #2 test section. A detailed valve sequence is presented in Table 4-4.

Table 4-4: Valve and pump sequences for the HR test.

Valve and pump	1st half cycle		2nd half cycle	
	Temperature control	HR	Temperature control	HR
V1, V2	O	X	X	X
V3, V4	X	X	O	X
V5, V6	X	X	O	X
V7, V8	O	X	X	X
MFM Valve	X	X	X	X
HR valves	X	O	X	O
Cooling loop pump	O	X	O	X
Heating loop pump	O	X	O	X
HR pump	X	O	X	O

Note: O represents open; X represents closed.

During the test, the temperature profiles of both the test sections surface and the fluid inside them were measured by a grid of T-type thermocouples and were recorded in every second. There were ten thermocouples installed in each test section, including five inserted into the stainless steel tube to measure the fluid temperature and the other five attached onto the test section surface. A Coriolis mass flow meter was installed on the bypass line in order to measure the HR flow rate, with calibrated accuracy of 0.1 g/s. During the normal heat recovery testing, the flow meter was not used and therefore MFM valve was normally closed. Only under the flow rate testing

circumstances, the top HR valve was closed and MFM valve was switched to open. It should be noted that the flow meter was not intended to measure the instantaneous flow rate, but to generate a map to estimate the relative flow velocity under different HR pump operating speed conditions. The thermocouples were calibrated over the required temperature span within 0.3°C.

4.3.2 Dynamic Modeling

To help understanding the experimental results and investigate possible performance improvements, a one-dimensional transient model was developed and implemented into Simulink (Anon., 2012). This model was similar to the ideal case model to some extent, but some of the idealized assumptions were removed and was fitted to real case better. Table 4-5 lists the main differences for a better understanding. The following assumptions were used for this model:

Table 4-5: Comparison between ideal HR model and 1-D real case model.

Objects	Features	Ideal HR model	Real case model
Solid	Solid length	Infinitesimal	Finite
	Solid conduction	No	Yes, 1-D
Fluid inside solid heat exchanger	Fluid length	Infinitesimal	Finite
	Fluid conduction	No	Yes, 1-D
	Pipe wall effect	No	Yes, lumped
Fluid in HR connecting pipe	Heat loss to ambient through pipe wall	No	Yes
	Fluid conduction	No	Yes, 1-D

(1) Symmetric conduction in radial direction through solid test section could be simplified using lump method, since the Biot number using pipe thickness was less than 0.01, when assuming a free convection boundary condition with water. As a result, only the conduction through axial direction (or flow direction) inside

114

solid was considered.

(2) Adiabatic boundary condition between metal and surrounding ambient air.

(3) Uniform fluid temperature at any cross-section. Based on this assumption only the convection in flow direction was considered.

(4) No internal heat source/sink.

(5) No heat loss from the solid test section to surrounding ambient at fluid inlet and outlet boundaries.

(6) The transient response from the solid structures of the connecting HR pipe, valves and pumps to the fluid temperature variation was fast enough, so that the wall temperature of HR pipes were the same as local fluid temperature. The thermal mass of the pipe walls were added to the thermal mass of the corresponding fluid to consider their transient effect.

Based on the above assumptions, the transient one-dimensional model could be described by the temperature of fluid and the solid as follows:

$$\frac{\partial T_s}{\partial t} = \alpha_s \frac{\partial^2 T_s}{\partial x^2} - \frac{h}{\delta \cdot (\rho c_p)_s} (T_s - T_f) \tag{4-8}$$

$$\frac{\partial T_f}{\partial t} = \alpha_f \frac{\partial^2 T_f}{\partial x^2} - \frac{4h}{ID \cdot (\rho c_p)_f} (T_f - T_s) - u_f \frac{\partial T_f}{\partial x} \tag{4-9}$$

Here in both equations, the first right hand term was the conduction in the flow direction. The second term was the heat transfer between the fluid and solid. The third term was the most dominant one, the convection term, which was not appeared in Eq. (4-8) since there was no bulk movement in the solid. The internal flow heat transfer

coefficient could be evaluated based on Dittus-Boelter correlation or laminar flow analytical solution. The geometry parameter δ in Eq. (4-8) could be calculated based on Eq. (4-10):

$$\delta = \frac{\Delta V_s}{\Delta A} = \frac{\left(OD^2 - ID^2\right)}{4ID} \tag{4-10}$$

With boundary conditions for both solid and fluid:

$$\frac{\partial T_s}{\partial t}\bigg|_{x=0,x=L} = 0$$

$$T_f\big|_{x=0} = T_{f,in}$$

And initial condition

$$T_s(x) = T_0, T_f(x) = T_0, 0 \leq x \leq L$$

The connecting HR pipes, pump, and valves were also one-dimensional models, considering the thermal mass as the sum of the fluid and neighboring solid wall in Eq. (4-11):

$$\frac{\partial T_f}{\partial t} = \frac{k_f}{\kappa(\rho c_p)_f}\frac{\partial^2 T_f}{\partial x^2} - \frac{h}{\kappa(\rho c_p)_f \delta}\left(T_f - T_{amb}\right) - \frac{u_f}{\kappa}\frac{\partial T_f}{\partial x} \tag{4-11}$$

Eq. (4-11) is a combination of Eq. (4-8) and (4-9) to reduce the computation cost, where the fluid temperature and wall temperature were assumed to be the same, denoted by T_f. The thermal mass of pipe walls, pump body, and valves body were considered by the κ term in Eq. (4-11), defined as the ratio between the total thermal mass per unit length and the thermal mass of the fluid per unit length in Eq. (4-12). The values of this factor for the pipes applied in the test facility were listed in Table

4-3. For ideal cycle, $\kappa = 1$.

$$\kappa = \frac{\left(mc_p\right)_f + \left(mc_p\right)_s}{\left(mc_p\right)_f} = \frac{\left(\rho c_p\right)_f \Delta V_f + \left(\rho c_p\right)_s \Delta V_s}{\left(\rho c_p\right)_f \Delta V_f} = \frac{\left(\rho c_p\right)_f ID^2 + \left(\rho c_p\right)_s \left(OD^2 - ID^2\right)}{\left(\rho c_p\right)_f ID^2} \quad (4\text{-}12)$$

Finite difference routine was used and implemented to Simulink. Fixed-step ODE solver was chosen to solve the set of equations above.

4.4   *Results and Discussions*

The validation of the one-dimensional transient model by experimental data is given first, and some insight of the thermal-wave propagation using the modeling results are discussed afterwards. Parameters contributing to the HR performance are discussed based on the modeling results. A design guideline is provided for future work at last.

4.4.1   Experimental results and model validation

Figure 4-7 shows the average temperature profiles of two test sections over 5.5 cycles under one test condition. The heater's setpoint was 33°C and the ice-cooled HX was maintained at 18°C to provide a 15°C temperature span for the heat recovery process. Each half-cycle began with a 40 seconds temperature control process, when the temperature curves were approaching the two temperature limits. Then the HR process took place at the end of each half-cycle. The HR half-cycle ended before those small spikes in Figure 4-7, and the corresponding heat recovery efficiencies were calculated after the system reached a cyclic steady state condition. Those spikes were due to flow mixing at the beginning of temperature control process, between the T-junction of the heating/cooling loop and the T-junction of the heat recovery loop, as shown in Figure 4-7. The mixing effect should be minimized in real systems to

reduce the irreversibility generated by the flow mixing.
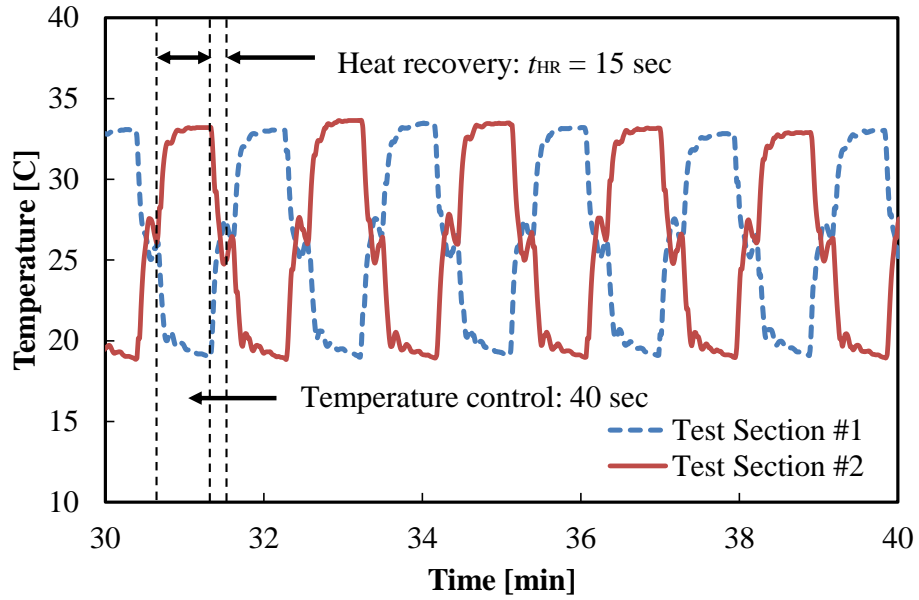
Figure 4-7: Temperature profile of two solid walls during the heat-recovery process (t_{HR} = 15 sec, η_h = 61%, η_c = 59%).
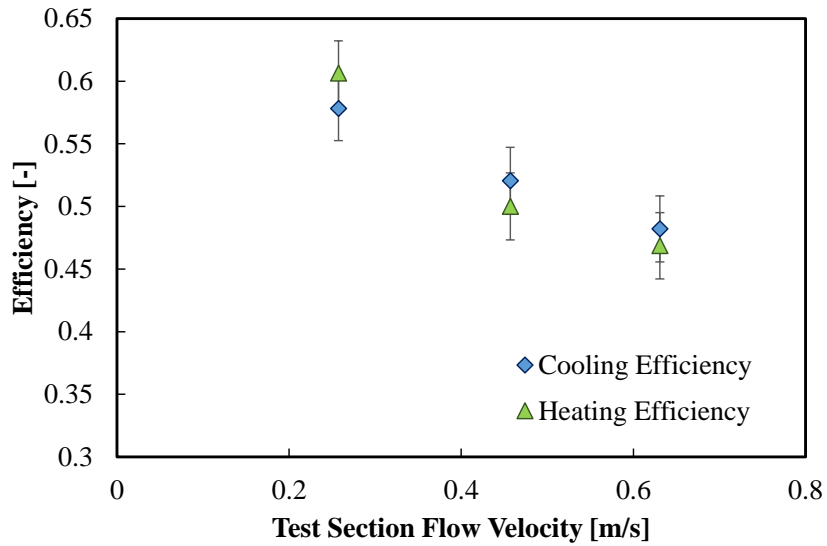
Figure 4-8: The influence of flow rate on the heat recovery efficiency.

Three sets of tests were conducted at different heat recovery flow rate conditions to

validate the model by varying the flow rate and the heat recovery duration. Only three optimum points were shown in Figure 4-8. Although there was slightly discrepancy between cooling and heating efficiencies, they were within the measurement uncertainty tolerance range. The maximum HR efficiency experimentally achieved was 61%, which could be regarded as a successful sign of the proposed method, since it already surpassed the 50% parallel-flow heat transfer limit. Nevertheless, there are still a lot to improve between 61% and 100%, and experimentally validated one dimensional numerical model is a good way to understand such gap and find the further improvement solutions.

Table 4-6: Experimental validation of one-dimensional model.

	t_{HR} (s)	u (m/s)	$\eta_{experimental}$ (-)	$\eta_{numerical}$ (-)	Deviation (%)	t^* (-)	l^* (-)
1	15	0.25	0.61	0.64	5%	1.34	0.18
2	13	0.46	0.5	0.52	4%	1.53	0.18
3	11	0.63	0.47	0.45	-4%	1.57	0.18

Note: t^* and l^* are defined in Eqs. (3-13) and (3-14), respectively.
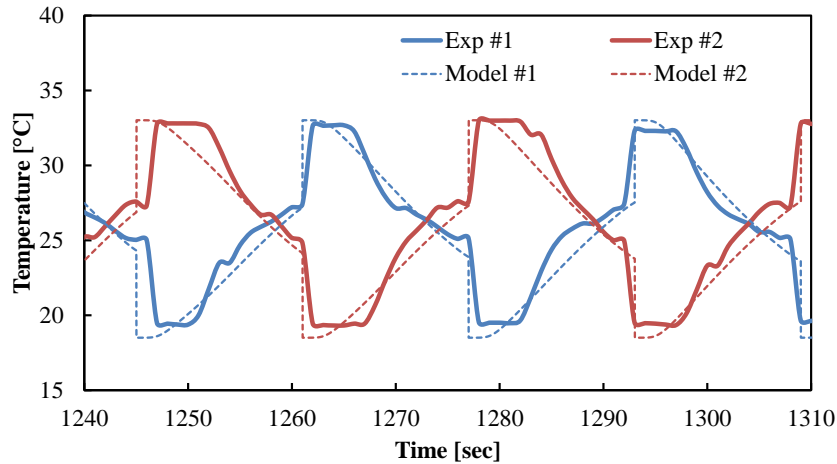
Figure 4-9: Experimental validation of one-dimensional model (t_{HR} = 15 sec).

The three data points in Figure 4-8 were compared with the model prediction under

the same operating conditions. Table 4-6 listed the comparison results, and less than

5% relative deviation was achieved in all cases. To visualize this small difference,

Figure 4-9 shows a comparison between the experimental data and simulation data in

the 15 seconds case (5% deviation case). Figure 4-9 already filtered the temperature

control process, and therefore, only HR processes were displayed during each cycle.

Two major differences could be observed: the "flat" period at the beginning of each

cycle was less-estimated by the model, and the model was not able to predict some

random non-smooth sections in the experimental curves. The first discrepancy could

be explained by the assumptions used in the model that the local HR pipe wall is in

equilibrium with the local fluid. In reality, however, the equilibrium is never

established during the transient heat recovery process in finite time, and the HR pipe

wall delays the thermal-wave propagation, therefore increases the duration of the

"flat" period. The second discrepancy could be caused by random disturbances during

the test, such as trapped bubbles in the HR pipe. Nevertheless, the model predicts a

similar pattern as the experiment, and therefore could be used in the next section to

investigate the validity and physics of the novel thermal-wave heat recovery design.

4.4.2   Insight of thermal-wave propagation

Earlier, the ideal cycle heat recovery was analyzed to have a linear temperature

distribution. Here, a "real" temperature profile snapshots analysis is presented based

on the experimentally validated "real" model in Figure 4-10, in order to compare

between ideal case and "real" case. Clearly, in Figure 4-10 the temperature profile

inside the connecting pipe is not a linear function, and this deviation from ideal case

120

is because of real case irreversibility.

(a) $t/t_{HR} = 0.05$

(b) $t/t_{HR} = 0.7$

(c) $t/t_{HR} = 0.99$

Legend

– – – – Fluid temperature	Particle 1
—— Solid temperature	
◄– – – – Pipe configuration	Particle 2
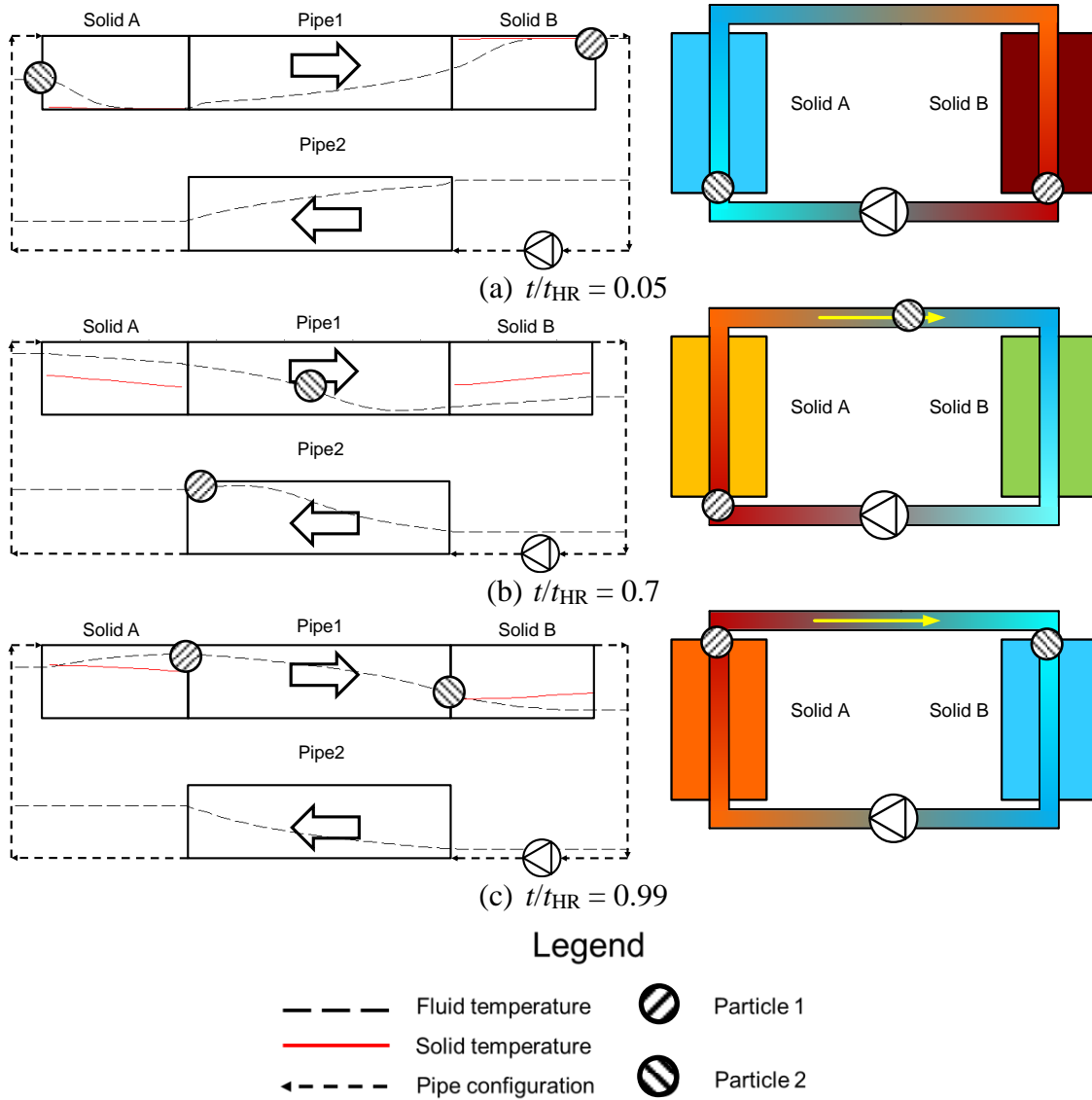
Figure 4-10: Illustration of thermal-wave propagation by snapshot of temperature profiles at different time step during one heat recovery process and corresponding particle trace on the schematic.

There are several observations from Figure 4-10:

(1) The two tracing particles travel the same distance during the HR process, which is

121

a little bit more than the length of one solid bed plus the length of one HR pipe. In ideal case, the cycle duration t_1 is the traveling time for a single heat recovery pipe, since the length of solid bed is negligible.

(2) The thermal-wave peak amplitude diminishes while along traveling through the HR pipe. In other words, the HR pipe wall acts as a damping force to the transient thermal-wave. In ideal case, the peak amplitude reduces much slower, since the damping effect caused by the heat recovery pipe wall is zero.

(3) There is slight temperature difference along the solid bed during the HR process. Based on the "counter-flow in time scale" principle, the temperature gradient inside solid bed itself neutralizes part of the additional heating/cooling, therefore limits a potentially higher efficiency. As a result, a shorter solid bed is possibly to achieve a higher heat recovery efficiency. In ideal case, the solid length is zero, and there is no such temperature glide.

There are a lot of variables contributing to the heat recovery efficiency, such as solid bed geometries, HR pipe geometries and thermal properties, flow rate, and cycle duration. However, these variables affect the HR efficiency through a few non-dimensional parameters rather than contributing independently. Here the most significant non-dimensional numbers are introduced. Eq. (4-13) is the non-dimensional heat recovery duration, which is defined by the ratio between the heat recovery duration and the time required by any particle in the flow to travel the distance that is equal to the length of one solid bed and one HR pipe. If $t^* = 2$, then during one HR cycle, a particle inside the flow travels one circuit to the same location where it starts. Eq. (4-14) is the non-dimensional length, characterizing the ratio of a

particle in the flow travels within one of the solid bed through the HR process. Case $l* = 1$ is corresponding to zero HR pipe length limit, and $l* = 0$ is corresponding to zero solid bed length limit. For ideal heat recovery cycle in section 4.2, $t* = 1$ and $l* = 0$.

$$t* = \frac{t_{\text{HR}}}{t_{\text{travel}}} = \frac{t_{\text{HR}}}{\dfrac{L}{u} + \dfrac{L_{\text{HR,A-B}}}{u_{\text{HR,A-B}}}} = \frac{t_{\text{HR}}\dot{V}}{V + V_{\text{HR,A-B}}} \tag{4-13}$$

$$l* = \frac{t_{\text{solid}}}{t_{\text{travel}}} = \frac{L/u}{L/u + L_{\text{HR,A-B}}/u_{\text{HR,A-B}}} = \frac{V}{V + V_{\text{HR,A-B}}} \tag{4-14}$$

Based on the definition of $t*$ and the observation (1) from Figure 4-10, $t*$ should be slightly higher than 1 to achieve the "counter-flow in time scale" HR design. Figure 4-11 plots simulation results with various solid bed geometry, HR pipe geometry as well as different cycle duration and flow velocity. It's obvious that the optimum efficiency occurs when $t*$ is around 1.25, which also validates the observation (1). Based on the operating principle, if the thermal mass of the HR pipe is zero, then the optimum $t*$ should be 1, which is the same as the ideal case. Such deviation comes from both the delay caused by the connecting pipe wall thermal mass, and the finite diffusion speed inside solid bed as well.

Figure 4-11 also indicates a minimum efficiency when $t*$ is around 0.9. The physical interpretation of $t* < 1$ case is that the thermal-wave peak from the opposite solid bed has not yet arrived at the reference solid bed. The limit case is when $t* \rightarrow$ zero, when the thermal-wave propagation speed is approaching zero, or solid bed/HR pipe length is approaching infinity, that the efficiency drop to zero. Beyond the peak efficiency

point $t^* = 1.25$, the efficiency decreases since the additional thermal-wave has the counter effect. The limit case is when $t^* \rightarrow$ infinity, or thermodynamic equilibrium state, that the efficiency becomes 0.5.
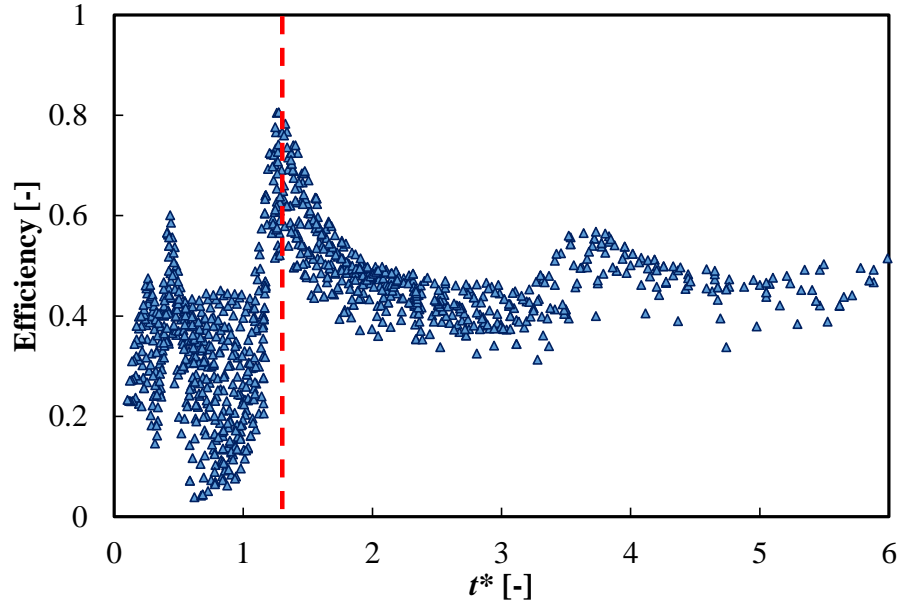
Figure 4-11: Parametric study of heat recovery efficiency with non-dimensional cycle time defined in Eq. (4-13).

(Conditions: 0.25 m < L < 0.75 m, 0.1 m < L_{HR} < 0.8 m, 19 mm < ID_{HR} < 38 mm, 12 sec < t_{HR} < 36 sec, 0.05 m/s < u < 0.15 m/s, corresponding 0.05< l^*< 0.9)

Figure 4-12 shows one of the $t^* = 0.9$ case when the efficiency is equal to 0.04. Figure 4-12 (a) shows the temperature profiles of two solid beds, and Figure 4-12 (b) plots the snapshots of the temperature distribution within the HR pipe. The steep slope inside the HR pipe is the reason leading to such a low HR efficiency, since the outlet temperature remains almost unchanged at least before $t/t_{HR} = 0.5$. The steep slope prevents the high temperature fluid from entering the solid bed, and depresses

the key principle to gradually change temperature based on the "time scale counter-flow heat transfer" principle. The remaining almost flat temperature distribution fluid at t/t_{HR} = 0.99 further aggravates the opposite steep "thermal-wave" propagation in the next cycle, and therefore, causes a continuous low efficient heat recovery performance. When the fluid temperature distributions in Figure 4-12 (b) and Figure 5 are compared, failure to generate the smooth temperature gradient inside HR pipe is the key reason leading to low HR efficiency. It should be noted that the steep thermal-wave in Figure 4-12 is in fact a desired pattern for the low conductivity application such as adsorption cooling.

(a) Solid A temperature curves   (b) HR pipe temperature distributions
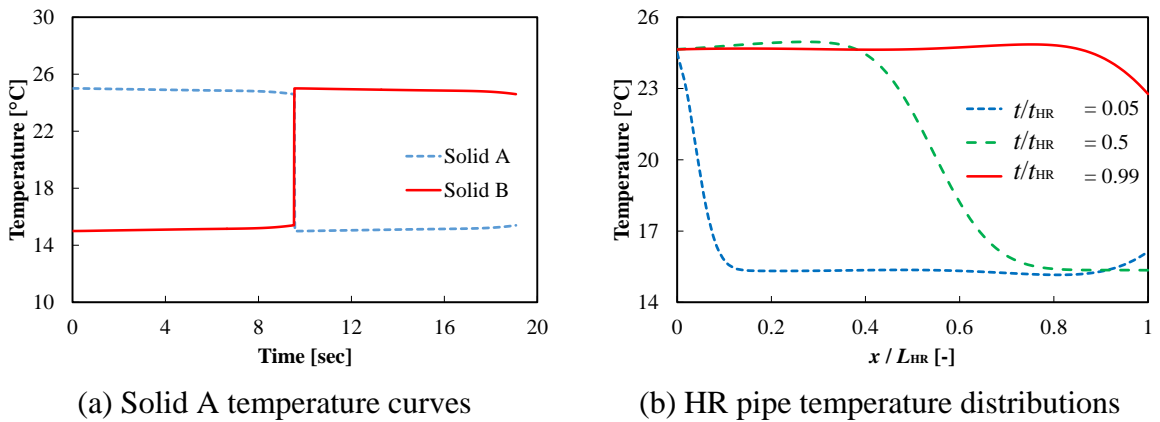
Figure 4-12: An illustration of the low heat recovery efficiency case near $t^* = 0.9$.

(Bad case example: L = 0.5 m, u = 0.1 m/s, L_{HR} = 0.15 m, ID_{HR} = 25.4 mm, t_{HR} = 9.5 s, or $t^* = 0.9$, $l^* = 0.4$)

One observation from Figure 4-11 is that the HR efficiency is not only dependent on t^* when t^* is less than 1, since it diverges at the same t^* value. The previous discussion explains the physics for case $t^* < 1$, that the thermal-wave peak has not yet arrived from the opposite solid-state beds. As a result, the efficiency is sensitive to

how far away is the peak, or in other words, the ratio of the solid bed traveling time l^*. Figure 4-13 plots the efficiency with various l^* when $0.8 < t^* < 1$. One can imagine Figure 4-13 is a plane perpendicular to Figure 4-11 with an additional 3rd coordinate of l^*.
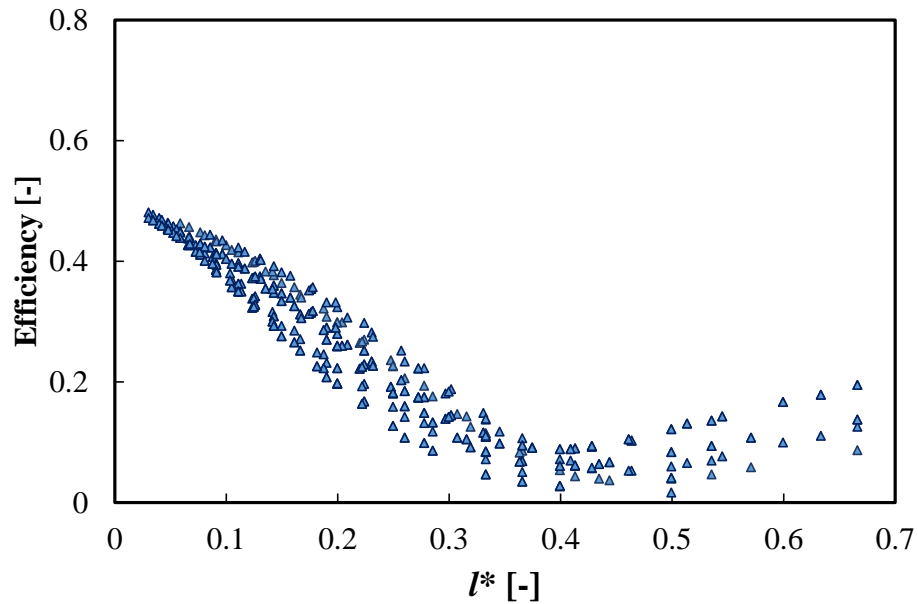
Figure 4-13: Parametric study of heat recovery efficiency with non-dimensional

length defined in Eq. (4-14).

(Conditions: 0.25 m $< L <$ 0.75 m, 0.1 m $< L_{HR} <$ 0.8 m, 19 mm $< ID_{HR} <$ 38 mm,

0.8 $< t^* <$ 1, 0.1 m/s $< u <$ 0.4 m/s)

When $t^* < 1$, the HR efficiency is no longer sensitive to t^*, but rather dependent on l^*, vice versa for $t^* > 1$ cases. Figure 4-13 also indicates that the minimum efficiency cases discussed in Figure 4-13 are determined by l^*, or the geometries of both solid bed and HR pipe. To enhance a high HR performance, a small l^* (less than 0.1) is recommended based on the trend. It should be noted that for ideal case, there is no

temperature gradient in solid and corresponding fluid inside it. However, when $l^* > 0$ in real case, the conduction loss caused by flow direction temperature gradient degrades the heat recovery performance.

Figure 4-14 shows the individual effects of some important design parameters: HR pipe length/diameter and flow velocity. Figure 4-14 indicates an optimum HR pipe length exists, since not sufficient temperature gradient is available in a short pipe, and too much pipe wall thermal mass damping effect neutralizes the temperature gradient on the other hand.
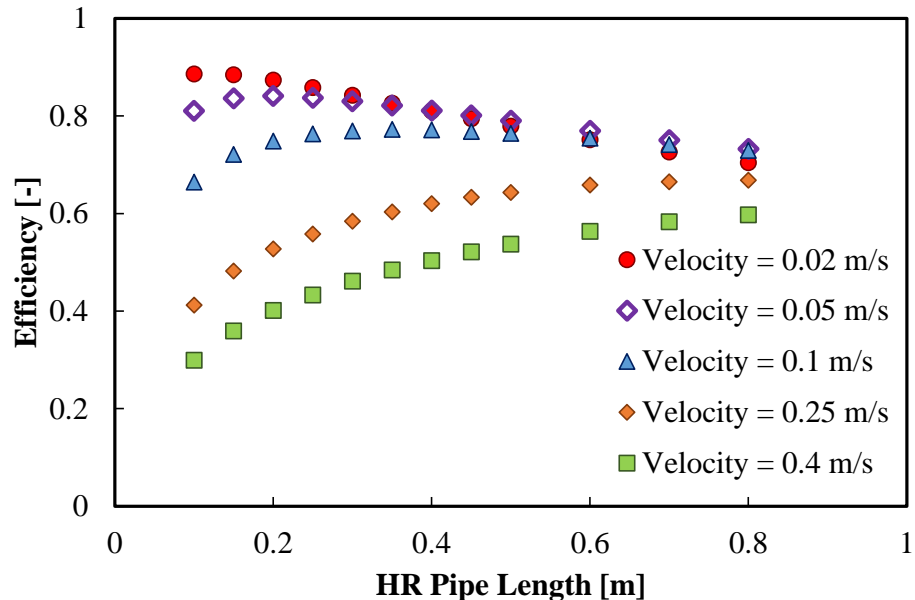
Figure 4-14: The influence of HR pipe length and velocity on heat recovery efficiency ($t^* = 1.2$, $ID_{HR} = 39$ mm).

Figure 4-14 also indicates that velocity is another key parameter to the HR performance. Lower flow rate results in better HR performance. In ideal cycle from 3.2, $\bar{r}_1$ is an indirect measure of the heat recovery pipe length, and it predicts better

performance with smaller $\bar{r}_1$. It is different from the "real" model result, since the counterpart effect from the connecting pipe wall thermal mass is not taken into account for ideal case. On the contrary, the trend that smaller velocity has better efficiency is the same as ideal case, where smaller $\bar{r}_3$ tends to have higher efficiency. Table 4-7 summarizes all the degradation factors (or irreversibility) and non-dimensional quantities characterizing them as discussed above. For both ideal case and "real" case, the finite solid thermal mass, finite heat transfer coefficient, and unmatched flow rate are key factors limiting the heat recovery efficiency. When considering real case limitations, if the cycle duration is not controlled appropriately, mixing could happen when a fluid with higher temperature enters the solid that is supposed to be cooled down. This mixing irreversibility is characterized by t^*. Another equally essential non-dimensional number is l^* to measure the irreversibility caused by conduction through solid and fluid.

Table 4-7: A summary of degradation factors (irreversibility) during the heat recovery process.

	Solid length (axial conduction)	Solid thermal mass	Connecting pipe thermal mass	Heat transfer coefficient	Fluid conduction	Mixing caused by inappropriate t_{HR}	Unmatched flow rate
Ideal	-	$\bar{r}_1$	-	t_2	-	-	$\bar{r}_3$
Real	l^*	$\bar{r}_1$	κ(Eq. 4-12)	t_2	Fo(t_1)	t^*	$\bar{r}_3$

4.4.3 Design guideline

Based on the previous discussion, several guidelines are proposed here for future studies:

- An appropriate HR cycle duration is the key point. The HR duration is slightly

higher than the time required for the flow to travel the distance of the solid bed and HR pipe, which is 25% longer than the traveling time in this chapter. Quantitatively speaking, $t* = 1.25$ is the optimum solution.

- A moderate HR pipe length and diameter is recommended. The HR performance is not sensitive to $l*$ if the cycle duration is chosen wisely, but a too short HR pipe or too long HR pipe could lead to performance degradation, based on Figure 4-13. Based on results in Figure 4-13, $l*$ ranging from 0.05-0.3 is recommended.

- A small flow velocity leads to a high HR performance. Velocity less than 0.1 m/s is recommended based on Figure 4-14.

- Any asymmetry in heat recovery pipe (length, diameter, material, etc.) should be avoided as much as possible.

- Appropriate sizing of the pump and valve is necessary. Unnecessary pump heat generation and valve heat generation could lead to imbalance between the cooling efficiency and heating efficiency.

4.5   *Chapter Summary and Conclusions*

This chapter first introduces a systematic approach to realize the high efficient heat recovery process for solid-state cooling applications by applying an analogy to the counter-flow heat transfer process. The "time scale counter-flow" heat recovery principle could be approached by fluid with a "smooth" temperature gradient between two solid-state materials. An ideal cycle model was developed to understand the physics and how to achieve an ideal heat recovery process. Two non-dimensional time constant ratios and one time constant were found to be critical parameters

129

affecting the ideal cycle performance, which are the thermal mass ratio between the solid and the fluid inside the heat recovery loop, the heat transfer rate ratio between convective flux rate and conduction heat transfer rate from the wall surface, and the solid transient response time constant.

In addition, both experiment and a more realistic model were used to validate the proposed heat recovery process. 60% efficiency was experimentally achieved and could be regarded as a successful sign for the method, since it overcame the 50% limit when comparing with a parallel-flow heat transfer. To understand why only 61% was achieved, experimentally validated numerical model was developed and used to investigate the heat recovery performance under a wide operating range. It was shown that failing to construct a smooth temperature gradient could cause low heat recovery performance by an opposite failure case analysis. Two more dimensionless numbers were found with significant contribution to the heat recovery performance besides the three already identified parameters, which are the dimensionless cycle duration and the dimensionless length. Based on the numerical results, a 1.25 dimensionless cycle duration t^*, a 0.05-0.3 dimensionless length l^* and flow velocity less than 0.1 m/s are recommended. Degradation factors including irreversibility from the thermal mass of connecting pipes, unmatched heat recovery flow rate, and inappropriate cycle duration should be minimized. The maximum achievable efficiency in this chapter was 0.6 and 0.88 by experimental and numerical approach, respectively. According to the results, several HR design guidelines were proposed for future studies.

Chapter 5: Proof-of-concept Prototype Design, Fabrication and Testing

The world first of-its-kind thermoelastic cooling prototype is designed, developed, and tested, based on the Brayton cycle in Chapter 3 and the heat recovery process proposed in Chapter 4.

5.1 Design and Development of a 100 W Compressive Thermoelastic Cooling Prototype

Based on the model proposed in the Chapter 3, for a two bed system, the nitinol tube quantity in each bed is sized to be 19, when operated under 0.05 Hz frequency. The nitinol tubes used for the prototype were purchased from NDC Inc.

The goal is to compress nitinol tubes. Based on the available proposed compression mechanism summarized in the literature review, a solid boundary is necessary around the nitinol tubes to prevent buckling. In order to conduct heat transfer, a liquid HTF needs to flow through those tubes during the compression process, and therefore any part in direct contact with the nitinol tubes are required to transport fluid as well. Based on the above mentioned two major concerns, Figure 5-1 presents the nitinol tube based assembly design for the 100 W prototype. Note that in Figure 5-1, the nitinol tubes are arranged in a hexagonal shape, and are surrounded by a steel holder with the same hexagonal internal shape to support the nitinol tubes. The loading head is located on each side of the nitinol tubes bundle. Flow channels are used to let the fluid flow and distribute the fluid into each nitinol tubes. The whole assembly was

designed to be mounted by two linear bearings, for both alignment and support purpose.
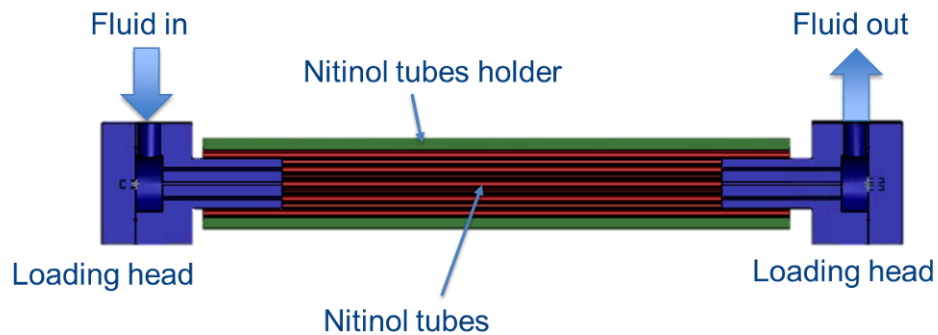
Figure 5-1: Illustration of a single nitinol tubes bed base assembly.

Based on the previous cycle design, when one bed is compressed, the other is released. Therefore, the layout of the two beds cannot be in series. In addition, when compressing one bed, ideally the unloading energy can be recovered as well. As a result, the two beds are designed to be implemented in parallel, and pre-loaded in a way that both of them are 50% compressed when the driving system is turned off, as shown in Figure 5-2. In Figure 5-2, the middle red box is a moving part to compress the two beds, with a rigid mount to the linear actuator. When the linear actuator is offline, the moving box is in the equilibrium position, allowing both nitinol beds to be 50% compressed. When the linear actuator is in operation and one bed is fully compressed, the other bed is stress-free.

With this mechanism design, a detailed system design was carried out in SolidWorks, as shown in Figure 5-3 (a). Note that the difference between Figure 5-2 and Figure 5-3 (a) is that the frames need to transfer the compression force to a common structure to balance the force between the linear actuator and nitinol tubes.
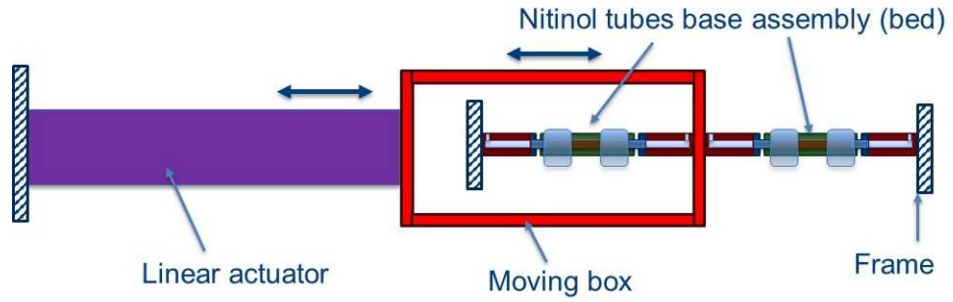
Figure 5-2: Illustration of the designed driving mechanism with supporting structures.
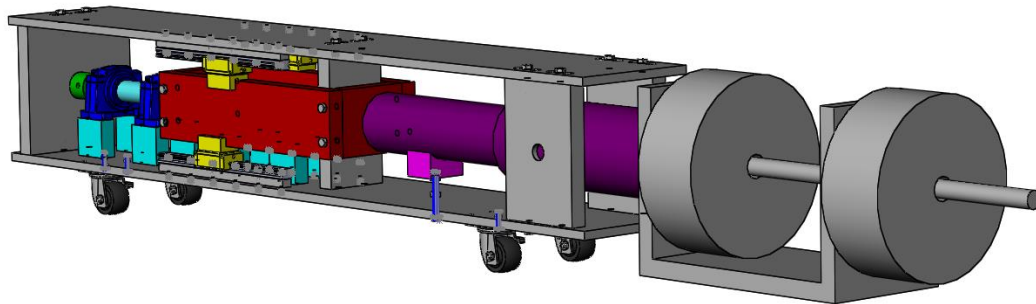
(a) SolidWorks drawing of the prototype without motors

(b) Photo of the assembled prototype with motors

Figure 5-3: Illustration of the 100 W prototype.

All the O1 tool steel based frame parts were machined and assembled based on the

design. The final assembled prototype was shown in Figure 5-3 (b). Some important geometries for reference are listed in Table 5-1, including both the nitinol tubes assembly and the whole prototype. More photos of the prototype can be found in Appendix B.

Table 5-1: List of some important geometries of the 100 W prototype.

	Geometry	Values	Units
Nitinol tubes assembly	Nitinol tube length	254.0	mm
	Nitinol tube ID	3.76	mm
	Nitinol tube OD	4.72	mm
	Holder diameter	50.8	mm
	Overall length (stress free state)	457.2	mm
Prototype	Overall length (without motors)	1981.2	mm
	Overall length (with motors)	2984.5	mm
	Overall height	444.5	mm
	Overall width	304.8	mm

5.2   *Experiment Setup*

To measure the performance of the prototype and ensure normal functioning, sophisticated water loops together with sensors are needed. As shown in Figure 5-4, the test facility consists of three water loops, to achieve heat rejection, cooling delivery and heat recovery, respectively. Heat source on the cold side is an electric heater, to compensate the cooling generated from the prototype. An air-cooled fan coil heat exchanger was used as the heat sink to reject heat from the prototype. The valve and pump sequence can be found in

Table 3-2. Eight thermocouples were installed to measure the water temperatures at various locations, including the inlet and outlet of two nitinol beds, heat source and

134

heat sink. The flow rates in both the cooling loop and heating loop were measured by two mass flow meters. The thermocouples were calibrated to 0.2°C. The flow meter has the rated and calibrated accuracy up to 0.2 g/s. Unless otherwised mentioned, all tested data were sampled under 2 Hz rate.
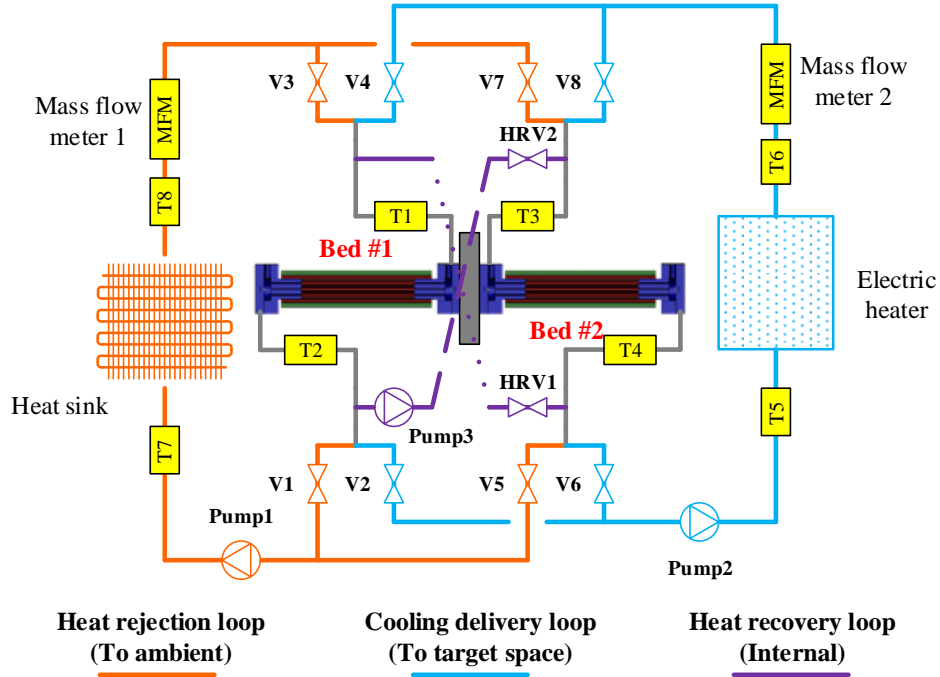
Figure 5-4: Schematic of the test facility for the 100 W prototype.

$$\dot{Q}_c = \dot{m}c_p \left(T_6 - T_5\right) \tag{5-1}$$

$$\Delta T_{lift} = \frac{T_7 + T_8}{2} - \frac{T_5 + T_6}{2} \tag{5-2}$$

$$\bar{Q}_c = \frac{\int_0^{Nt_{cyc}} \dot{Q}_c\left(t\right) dt}{Nt_{cyc}} \tag{5-3}$$

Based on the flow rate and temperature difference, the instantaneous cooling capacity inside the heat source can be evaluated, based on Eq. (5-1). Another important parameter is the system's temperature lift, which could be evaluated based on Eq. (5-

135

2). Eq. (5-3) transforms the instantaneous capacity to the time averaged cooling capacity. Note that the temperature sampling period used for Eq. (5-3) must be under the "cyclic steady state" condition.

5.3   *Results and Discussions*

5.3.1   Open-loop Testing
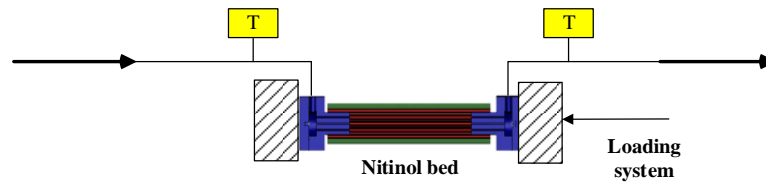
(a) Schematic of the open-loop test setup
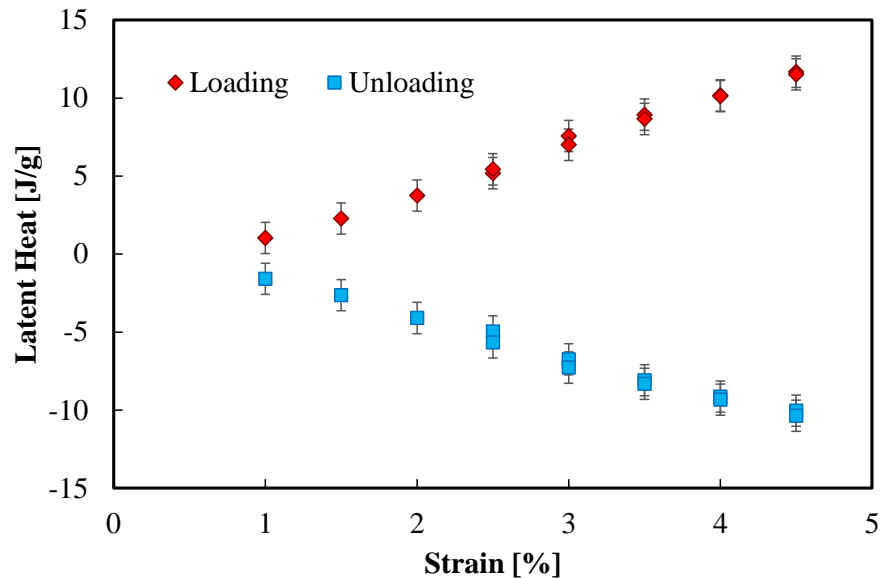
(b) Measured latent heat by water capacity when varying strain

Figure 5-5: Summary of the open-loop test results.

A so-called "open-loop" test was designed and conducted before any system level test, to first ensure the latent heat of the Ni-Ti tube as well as validate the existed numerical model developed in Chapter 3. The test rig is shown in Figure 5-5 (a). Only

136

a single bed is used, with one thermocouple attached to each side to record the instantaneous in-stream water temperature. The water flow rate was measured by the Coriolis mass flow meter. The method is based on Eq. (5-1), and an integration is needed to accumulate the instantaneous capacity to compute the overall latent heat transferred from the Ni-Ti tubes.

Figure 5-5 (b) illustrates the measured latent heat using the water capacity as the method described above. The latent heat reached 10 J/g under 4% strain, and is 11.7 J/g under 4.5% strain. This system level measurement confirmed the material level latent heat obtained by previous benchmark tests, i.e. DSC measurement, and guaranteed that the Ni-Ti tubes are functioning as designed.

5.3.2   Indication of Cooling

The first test conducted was to see whether or not the prototype was functioning well and providing cooling as designed. The "control group" was running everything, including all the valves and pumps following the designed sequence specified in previous chapters following the Brayton cycle, expect the linear actuator. Therefore, there is no phase change and thus no cooling generated in the control group. In the experimental group, everything including the linear actuator was turned on.

The comparison was plotted in Figure 5-6. Figure 5-6 (a) shows the recorded water temperatures for both heat source and heat sink, when the linear actuator driving system was turned off. The temperature increase was due to parasitic heat generation from the pumps and solenoid valves. In fact, with the slope of the temperature rising curve, the estimated parasitic heat generation rate was 12 W from pumps and solenoid

valves in total. When the linear actuator was turned on in Figure 5-6 (b), the water temperature at heat source side decreased as expected since cooling was delivered there. The water at heat sink was heated up and the temperatures increased. As a result, the temperature between the heat sink and the heat source separated. The existence of temperature lift indicated that the prototype was functioning and heat was pumped from the low temperature heat source to the high temperature heat sink.
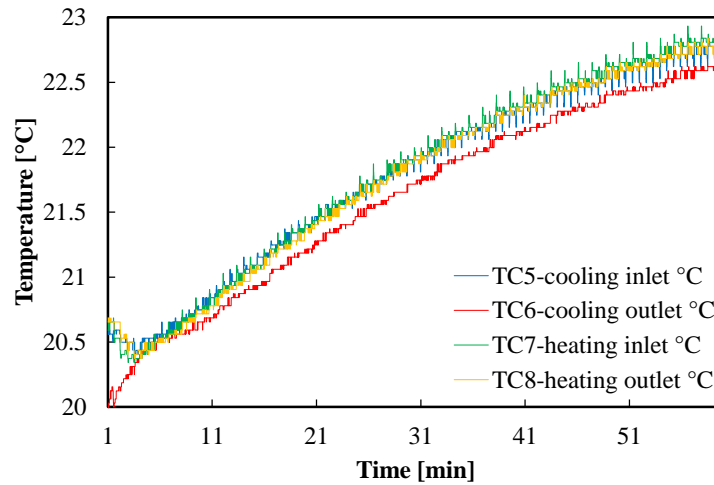
(a) Temperature profiles at heat source and sink of the control group
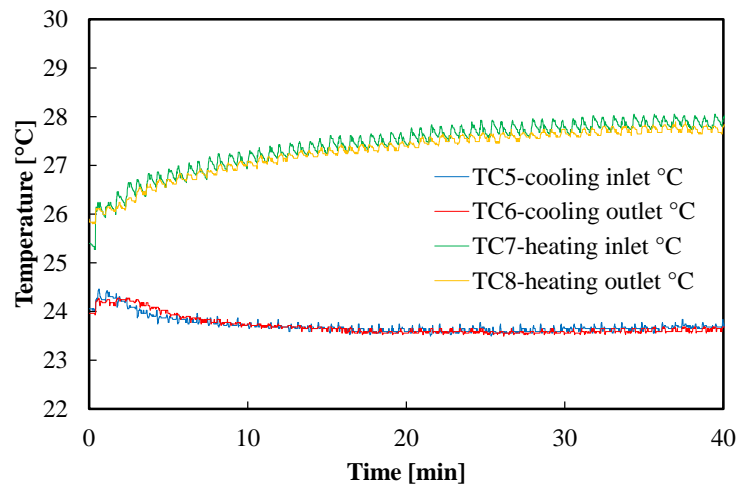
(b) Temperature profiles at heat source and sink of the experimental group

Figure 5-6: Indication of temperature lift.

5.3.3 Performance Improvement Methods

To improve the performance of the prototype, a few sources of limitations were identified and counter-measures were deployed accordingly. The first improvement was to reduce the friction problem caused by a few misalignment in the system, including the linear actuator's deviation from the axis, slight dislocation of the moving box, and slight vertical misalignment due to loose threaded mount between the linear actuator and the moving box. The second improvement, as is discussed into more details in Chapter 6, is to use some plastic tubes as insulation layer to minimize the heat loss from HTF to the metal loading heads. At last, the constraint from the double motors' torque problem was solved by replacing one of the motors to a gearbox. Details of the three major improvements are listed in Figure 5-7.
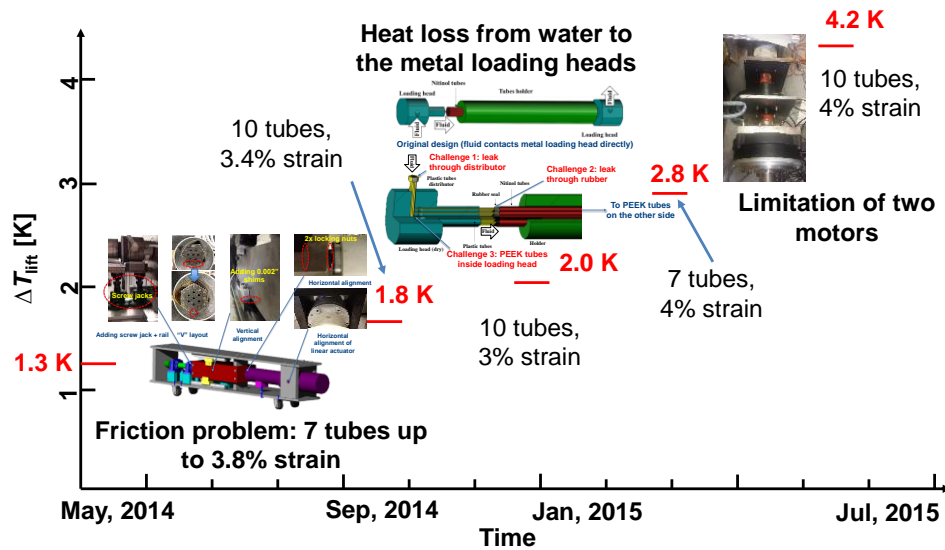
Figure 5-7: Highlighted challenges and improvement methods applied to the prototype.

The starting point was 1.3 K temperature lift. With the reduced friction, 3 more

nitinol tubes were able to be compressed in order to achieve a higher capacity, reaching the 1.8 K temperature lift. Plastic tube insulation boosted the temperature lift further to 2.8 K. Finally, the 4.2 K temperature lift was reached by compressing 10 tubes in each bed under 4% strain, as shown in Figure 5-6 (b).

5.3.4 Highlighted Results

Series of tests under various conditions have been conducted, including varying the cycling frequency, heat recovery duration, heat recovery pump speed, and heater/heat sink's capacity. The heater's capacity was controlled by the on/off ratio under 100 Hz rate. The heat sink's capacity was adjusted by on/off of the fan and air flow rate. Figure 5-8 is a summary of the most typical results. Without the polyether-ether-ketone (PEEK) tube as insulation, the maximum temperature lift measured was 1.3 ± 0.4 K with 28 ± 10 W cooling capacity. More details regarding this improvement with PEEK tube can be found in Chapter 6.
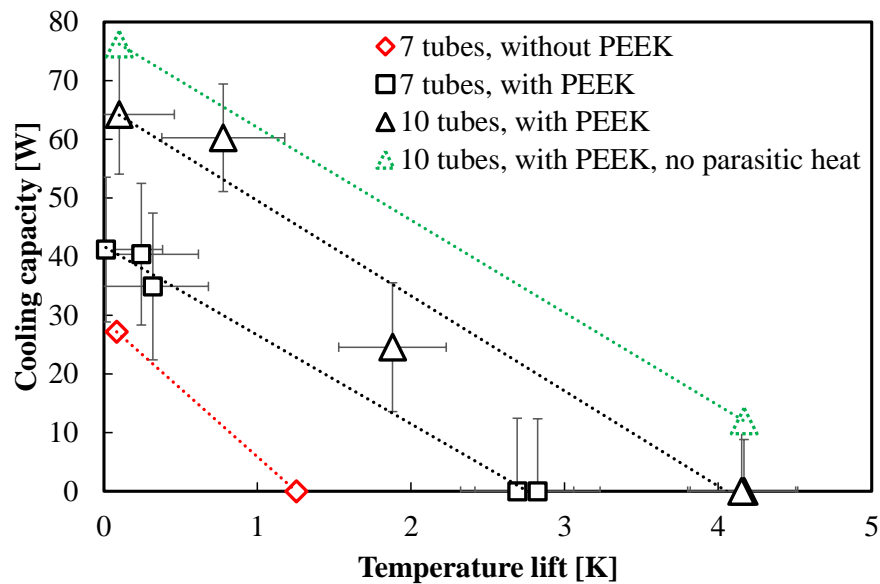
Figure 5-8: Highlighted test results.

The temperature lift was improved to 2.8 ± 0.4 K with 41 ± 11 W cooling capacity. It was further improved to 4.2 ± 0.4 K with 65 ± 10 W cooling capacity when 10 Ni-Ti tubes were implemented in each bed instead of seven tubes. A projection was made when assuming no parasitic heat generation from the pumps and valves, where the maximum cooling capacity could reach 77 W since the estimation of the parasitic heat was 12 W based on Figure 5-6 (a). By extrapolating the linear performance curve to the horizontal axis (zero capacity limit), 4.8 K temperature lift can be theoretically achieved.

5.3.5 Model Validation

The dynamic model developed in Chapter 3 was further validated by the open-loop testing results shown in section 5.3.1. The simulation was overlay to the measured water temperature difference across one of the Ni-Ti tube bed during the loading process. Comparison is visually shown in Figure 5-9. Two selected results, under 4.5% strain and 3% strain are presented in (a) and (b), respectively. The trend matched well with deviation less than 0.2°C at any time.
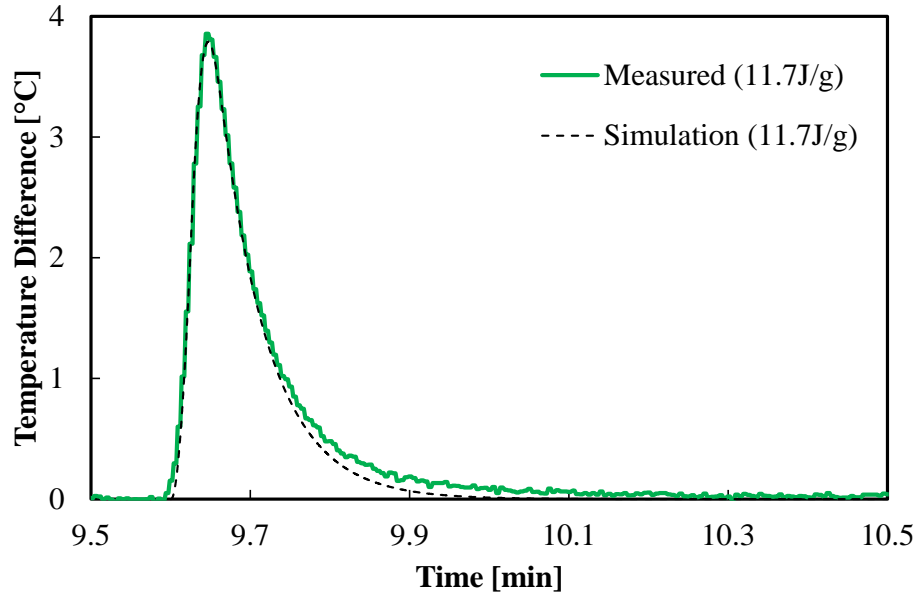
(a) Comparison under 4.5% strain.
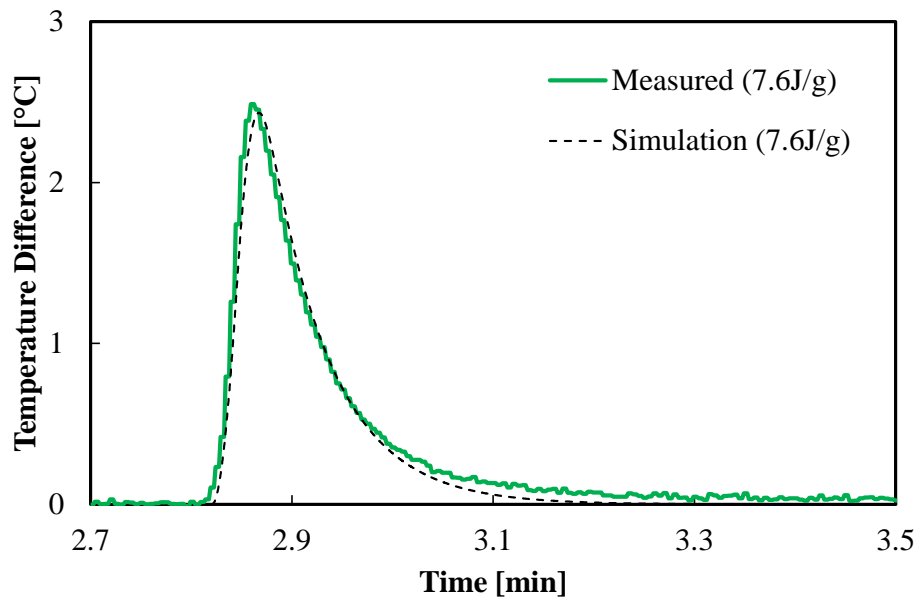
(b) Comparison under 3.0% strain.

Figure 5-9: Model validation by using open-loop transient water temperature

difference measurement results.
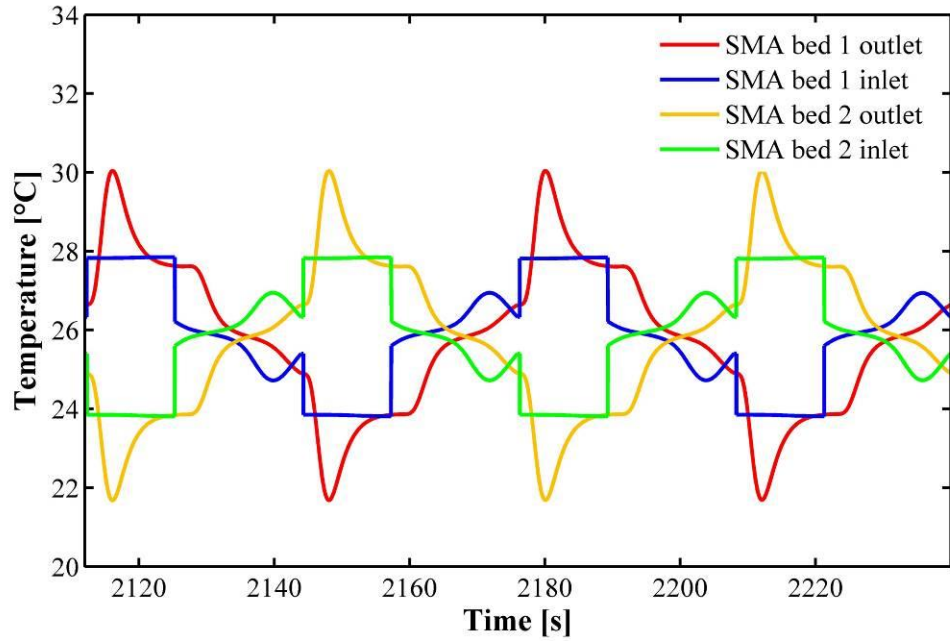
(a) Simulation
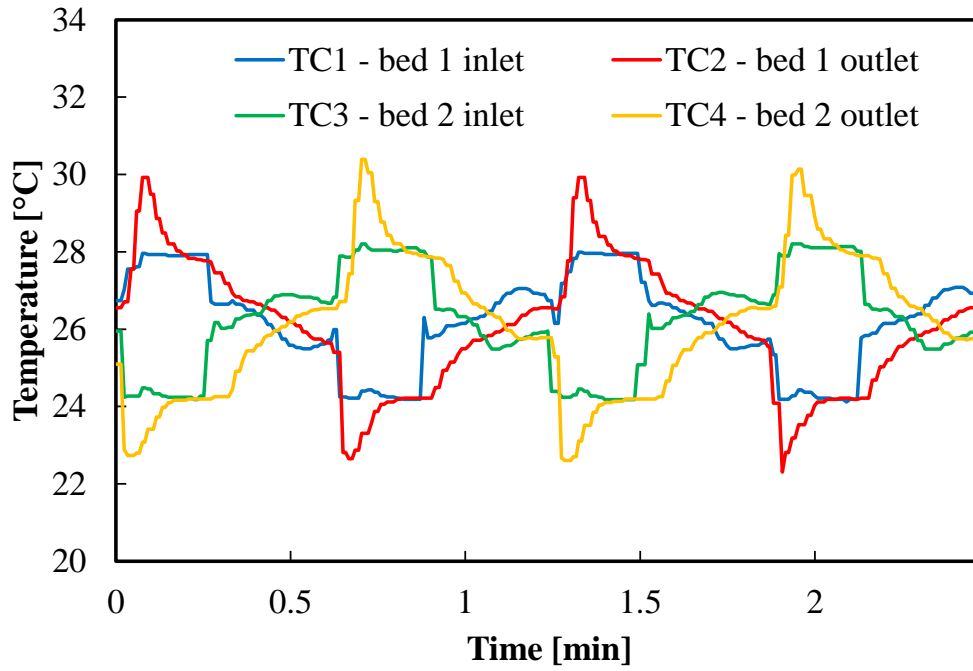
(b) Experiment

Figure 5-10: Model prediction versus measured data.

Then, the measured water temperature profiles with the simulation results were

compared under the same conditions. A graphical comparison is plotted in Figure 5-10. Though the model prediction had some minor discrepancy from the measured data, the overall trend, even some curvature change dynamics were well captured. The major difference between measured data and simulation data came from three reasons. First, there is always discrepancy in the estimated thermal mass based on some simple geometric measurement from the prototype, which contributes to the slope difference of water temperature curves at different stages of the cycle. Second, as demonstrated by Figure 5-5, the latent heat asymmetry between loading and unloading as a result of hysteresis contributed to the asymmetry in the water temperature curve between loading and unloading processes, which was under estimated by the model, especially Eq. (3-18). Third, in the prototype the flow was not entirely steady, especially some bubbles could flow with water as well. This led to the flow rate fluctuation and temperature fluctuation as well. Nevertheless, the model developed in Chapter 3 was able to predict the major dynamics inside the system, in addition to the bed level validation in Figure 5-9. This two level validation provides more confidence to use for performance predictions of more performance improvement designs in later chapters.

Figure 5-11 presents a further comparison between the measured data and simulation results, where the experimental data has been demonstrated in Figure 5-8. Based on the original designed dead thermal mass (DTM) in the system, the three solid lines are consistent with simulation results presented in Chapter 3. The real thermal mass in the prototype deviates from that of the designed value, which deteriorates the prototype's real performance. The dashed line is the updated simulation result by

using 80% more DTM. In addition, 4% strain and 90% active Ni-Ti material are used to follow the test condition. The updated simulation performance curve is close to the measured results within the measurement uncertainties. As discussed in more details in Chapter 8, the deviation caused by the additional DTM can be quantified by the ratio between active thermal mass of SMA and the DTM, which is a factor determining the slope of the solid lines in Figure 5-11. The vertical axis intercept is determined by the latent heat of the SMA (Δh) and the system operating frequency. For Ni-Ti alloy, the theoretical specific cooling power (SCP) is 1.2 $W \cdot g^{-1}$ based on 12 $J \cdot g^{-1}$ latent heat and 10 seconds half cycle duration. Therefore, increasing the cycling frequency could lead to a better performance as well.
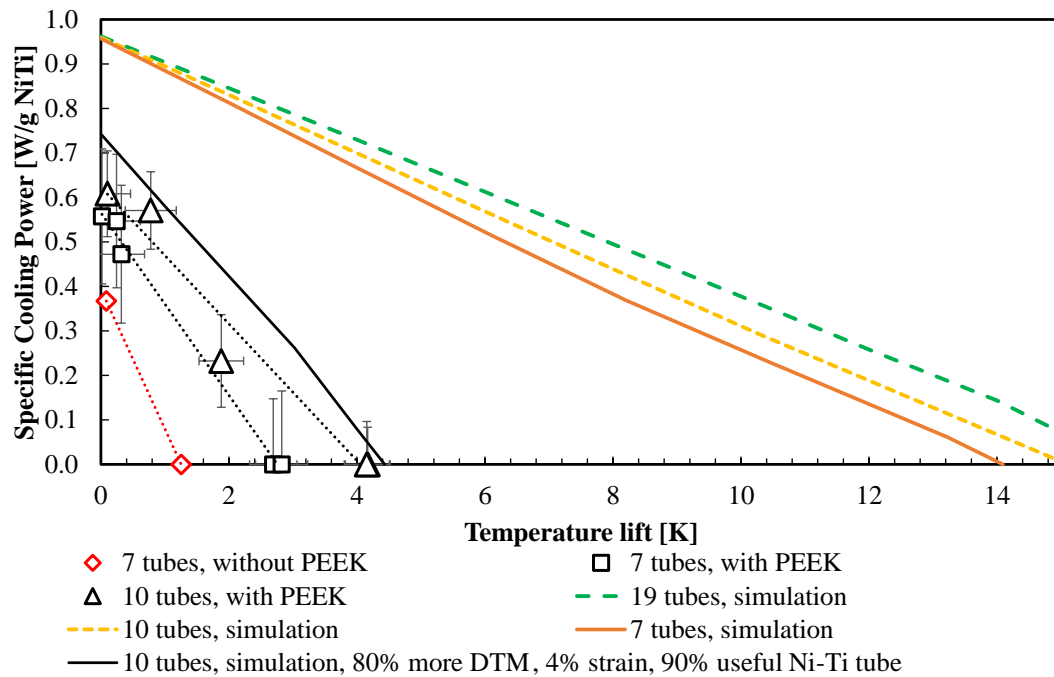
Figure 5-11: Comparison between measured data, original model prediction, and updated model prediction by tuning the dead thermal mass.

5.4   *Chapter Summary and Conclusions*

This chapter introduced the design, construction and testing results of the 100 W thermoelastic cooling prototype. A linear actuator (screw jack) driven by two motors was used to compress two nitinol beds, each consisting of 7 to 10 working tubes. The temperature lift was observed as the sign of cooling. The maximum achieved temperature lift was 4.2 ± 0.4 K, and the maximum measured cooling capacity was 65 ± 10 W excluded the parasitic power generation from pumps.

Chapter 6: Performance Improvements by Innovative Designs and Multi-Objective Optimization

The thermoelastic cooling system COP was predicted to be 1.7 under 10 K temperature lift from Figure 3-17. However, when considering the metal thermal mass impact using the real developed thermoleastic cooling prototype geometries from Chapter 5, the performance is degraded. The updated results showed that only 6.6 K temperature lift was achievable with the modification. Figure 6-1 plots the updated COP breakdown analysis chart. Clearly, the first stage's loss is due to the material property and is the most important and significant term to reduce. The lowest COP was zero because the maximum achievable temperature lift was 6.6 K. While the Stirling cycle with isothermal loading/unloading is difficult to approach, the second stage loss can be partially eliminated at least by applying hybrid cycle design. The third stage's loss is fixed due to the current state of the art mechanical driving system efficiency, unless breakthrough occurs in this component. All the above mentioned three losses are beyond the scope of this study, which lowers the COP from 28 to 5.6. Here, this chapter focuses on minimizing the heat transfer loss and the cyclic loss, which are closely related to the system level heat transfer and heat recovery processes.
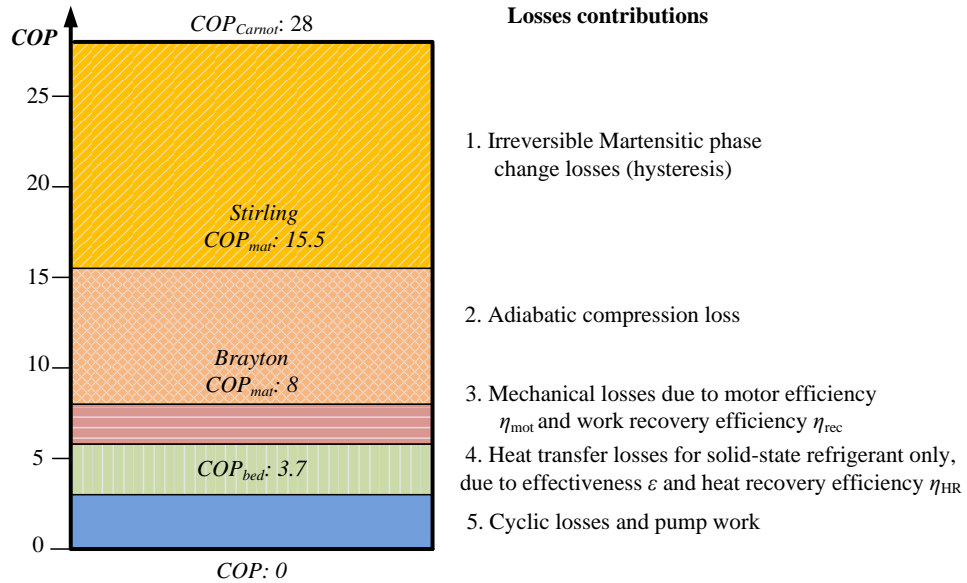
Figure 6-1: Illustration of loss breakdown chart for a compressive thermoelastic cooling system baseline scenario operated under 10 K temperature lift (COP was zero because the maximum achievable temperature lift was 6.6 K).

The novel designs introduced in this chapter focus on reducing the cyclic loss caused mostly by unnecessary dead thermal masses inside the system. Figure 6-2 is a schematic of the original design of a single SMA bed assembly using nitinol tubes to produce cooling and heating capacity.
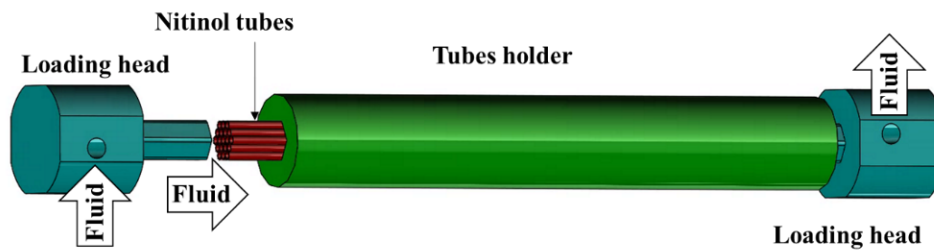
Figure 6-2: Drawing of the baseline/original design of the SMA bed assembly using nitinol tubes under compression mode.

Both beds share the same symmetric design. Under ideal circumstances, the only

necessary part in Figure 6-2 is the red tubes bundle in the middle, where anything else can be regarded as dead thermal mass since they do not generate useful cooling nor heating. The tube holders were designed to sustain radial direction stress from the nitinol tubes during the compression process, as well as avoid buckling. The two loading heads were originally designed to feed HTF into each of the nitinol tubes for heat transfer, and transfer the compression force directly into the nitinol tubes. In the original design, the top hexagon part of the loading head has multiple HTF flowing channel holes corresponding to each of the nitinol tubes inside. The HTF holes were gathered in another orthogonal channel, which was then connected to the external HTF pipes. The tube holders and loading heads were made of enhanced steel and, therefore, improvements are needed to minimize the heat transfer between the nitinol tubes and HTF to the tube holders and loading heads. Some important geometries and properties are listed in Table 6-1.

Table 6-1: Some important parameters of the baseline/original compressive thermoelastic cooling system.

Geometries			
Bed quantity [-]	2	Nitinol tubes per bed [-]	19
Nitinol tubes OD [m]	0.005	Nitinol tubes ID [m]	0.004
Nitinol tubes length [m]	0.254	Tubes holder diameter [m]	0.051
Loading head diameter [m]	0.064	Loading head depth: hexagon [m]	0.051
Loading head depth: top [m]	0.051		
Properties			
Nitinol ρ [kg·m^{-3}]	6500	Nitinol c_p [J·kg^{-1}·K^{-1}]	550
Nitinol k [W·m^{-1}·K^{-1}]	18	Nitinol entropy change [J·kg^{-1}·K^{-1}]	42
Stainless steel ρ [kg·m^{-3}]	8000	Stainless steel c_p [J·kg^{-1}·K^{-1}]	550
Stainless steel k [W·m^{-1}·K^{-1}]	30	HTF	water

6.1   *Novel Design Options*

6.1.1   Coating/Insulation Layer for Tubes Holders

As shown in Figure 6-2, the nitinol tubes were arranged in a hexagonal layout inside the tube holders, where the radial conduction took place between them. This conduction directly absorbs heat during the loading process and releases heat during the unloading process, which neutralizes part of the heating/cooling capacity while the heat exchanger process occurs between HTF and nitinol tubes.

To resolve this issue, a layer of low thermal conductivity material, such as insulation or a thin film of coating with low thermal conductivity can be applied on the tube holders as a heat resistance. To quantitatively investigate its applicability, the following equation is added to the original model for the film coating/insulation layer.

$$h_{coating} = \frac{\beta}{1/h_{contact} + \delta_{coating}/k_{coating}} \tag{6-1}$$

In Eq. (6-1), $h_{contact}$ is the contact resistance between the tube holders and the nitinol tubes, β is the contact area ratio between the tube holders and nitinol tubes, since nitinol tubes are only in line contact with the tube holders. In this chapter, β was assumed to be 0.1.

6.1.2   Coating/Insulation Layer Design

The same method can be introduced to the two loading heads. A thin film coating or an insulation layer reduces the heat transfer interaction between the loading head steel part and the HTF flowing inside the nitinol tubes. Similar to Eq. (6-1), the overall heat transfer coefficient between the HTF and the loading head metal can be

expressed in Eq. (6-2).

$$h_{coating,LH} = \frac{1}{1/h + \delta_{coating}/k_{coating}}$$
(6-2)

In addition, a 2-D model for the loading head was added to take the steel thermal mass into account, as shown in Eq. (6-3). Noting that the fluid was still modeled as 1-D in Eq. (6-4).

$$\frac{\partial T_{LH}(x,r,t)}{\partial t} = \alpha_{LH} \left[\frac{\partial^2 T_{LH}(x,r,t)}{\partial x^2} + \frac{\partial^2 T_{LH}(x,r,t)}{\partial r^2} + \frac{\partial T_{LH}(x,r,t)}{r\partial r} \right]$$
(6-3)

$$\frac{\partial T_f(x,t)}{\partial t} = \alpha_f \frac{\partial^2 T_f(x,t)}{\partial x^2} - u_f \frac{\partial T_f(x,t)}{\partial x} + \frac{h_{coating,LH}}{\rho c_p \delta_f} \left(T_f(x,t) - T_{LH}(x,t,r=R_{in}) \right)$$
(6-4)

$$\left. \frac{\partial T_{LH}(x,r,t)}{\partial x} \right|_{x=0,x=L} = 0$$

$$-k_{LH} \left. \frac{\partial T_{LH}(x,r,t)}{\partial r} \right|_{r=R_{out}} = 0$$
(6-5)

$$-k_{LH} \left. \frac{\partial T_{LH}(x,r,t)}{\partial r} \right|_{r=R_{in}} = h_{coating,LH} \left(T_{LH}(x,r,t) - T_f(x,t) \right)$$

$$T_f(x=0,t) = T_{f,in}(t)$$
(6-6)

Eq. (6-5) and Eq. (6-6) are boundary conditions. Eq. (6-5) assumes adiabatic boundary for the metal loading head, except for the contact side between HTF and metal. Eq. (6-6) is the inlet boundary condition for HTF.

Similar to the previous developed model in Chapter 3, a finite difference method was used in the updated model developed in Simulink^{TM} to solve the above set of equations.

A specific design of using a single thermal insulation layer, such as Teflon®, is presented in Figure 6-3 using the mentioned concept. In this design, there is only a single HTF pass inside the top hexagon part of the loading head, which can be insulated by the Teflon insulation layer. The HTF is then distributed by a meshed layer.
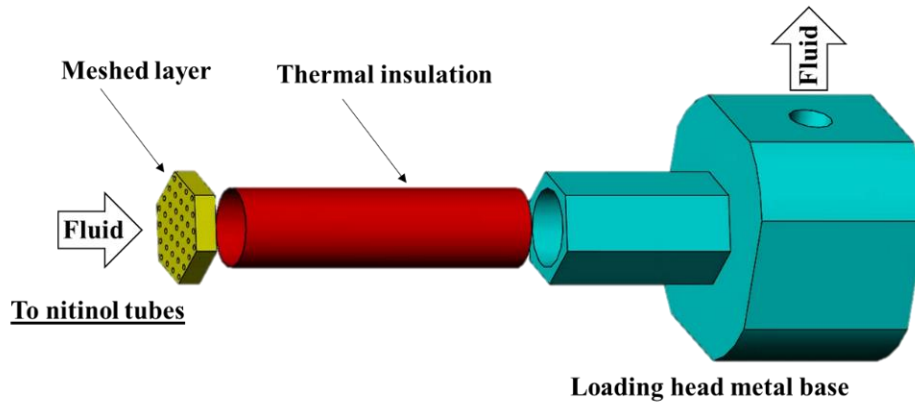
Figure 6-3: Illustration of the insulation layer design for loading head.

This design reduces the heat transfer between the HTF and the metal loading heads significantly. However, it cannot eliminate the heat transfer due to the finite thickness of the insulation layer. In fact, since the HTF diameter cannot be smaller than a certain threshold to guarantee sufficient flow for each nitinol tube, one needs to consider the tradeoff of losing the strength of the hexagonal steel loading head wall when increasing the insulation layer thickness. Therefore, adding a coating/insulation layer is not the ultimate solution for the loading heads. The next design can fully solve this issue, but has more implementation challenges.

6.1.3   Decoupling Design for Loading Head

To further reduce the impact from the loading head dead thermal mass, two more

innovative designs are proposed which aim to eliminate any HTF from contacting with the loading head metal surfaces. Both designs use smaller plastic tubes for the HTF flow, where the plastic tubes are inserted inside either the loading plate or the loading head metal part. The plastic tube OD is supposed to be smaller than the ID of the HTF holes within the loading head. Since the HTF only flows inside those plastic tubes and the loading heads are only for compression, the design concept developed here is also known as a decoupling design for loading heads. In addition, using smaller plastic tubes also reduce the dead thermal mass of the HTF itself.
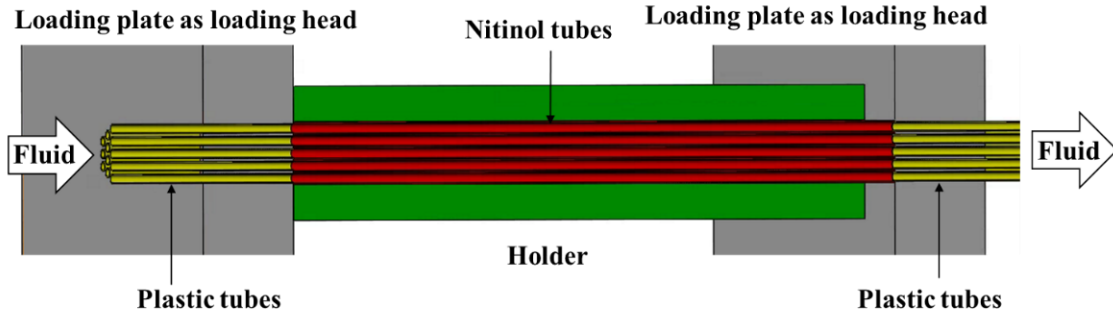
Figure 6-4: Illustration of the direct compression without loading head design.

The first approach following this decoupling concept is shown in Figure 6-4, which does not have loading heads. Instead, the two loading plates originally in contact with the loading heads compress the nitinol tubes directly. It should be noted that there are holes on both loading plates to allow those small plastic tubes to be inserted inside the nitinol tubes.

Figure 6-5 illustrates the second approach. By using less rigid thermoplastic tubes, such as PEEK tubes, this decoupling concept can be applied to the original loading head directly. The thermoplastic tubes have a 90° bend inside the loading head. The

outside of the loading head is sealed by a distributor against the external HTF loop fitting, and rubber plugs are used to seal the other side from the nitinol tubes.
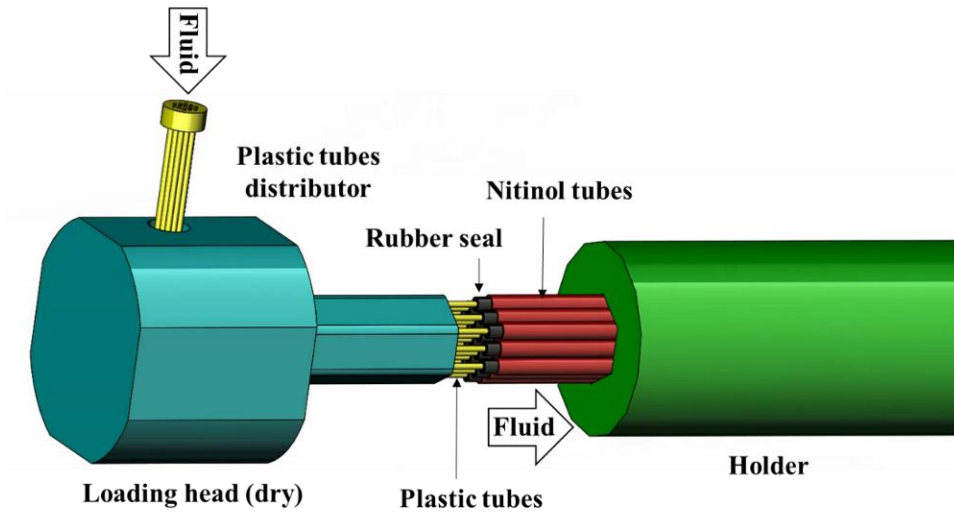
Figure 6-5: Illustration of the dry loading head design.

From a modeling perspective, there is no difference between the two approaches except the HTF thermal mass inside the plastic tubes. It is assumed that the plastic tubes are adiabatic from the loading head metal part, since there is a thin air gap in between. Therefore, the dead thermal mass of the metal loading head is totally reduced to zero in the model. Furthermore, the HTF thermal mass inside the loading head is also reduced accordingly.

6.1.4 Tube-in-tube and Rod-in-tube Designs

The previous concepts aim at reducing the dead thermal mass of metal parts and part of the HTF. However, the major HTF thermal mass is inside the nitinol tubes. One way to achieve this goal is to add internal insertion nitinol tubes/rods inside the original nitinol tubes, as shown in Figure 6-6.

154
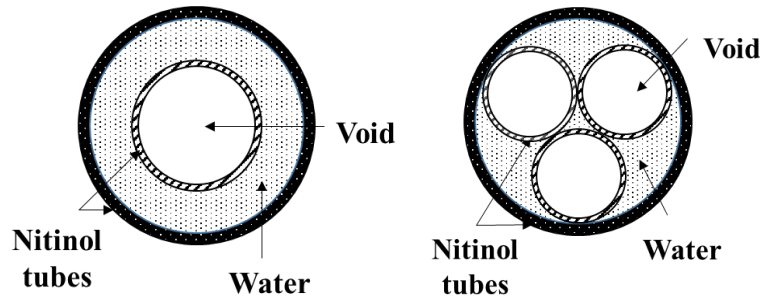
(a) Tube-in-tube design
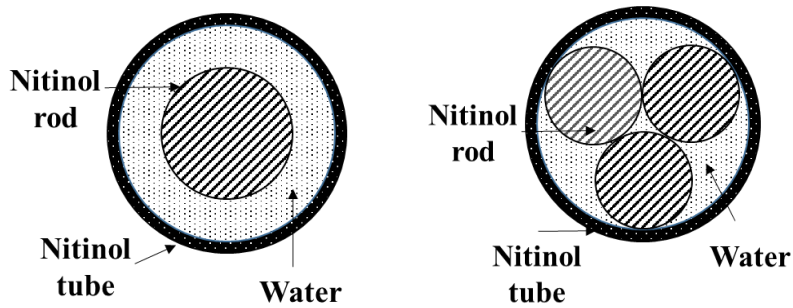
(b) Rod-in-tube design

Figure 6-6: Illustration of the tube-in-tube and rod-in-tube design using multiple

small tubes or rods inside each regular nitinol tube.

Figure 6-6 (a) shows the tube-in-tube design, where the HTF (water) only flows between the inner small insertion nitinol tubes and the external original nitinol tube. The inner tubes are sealed on both ends so that there is no HTF flowing within them. The only difference between Figure 6-6 (a) and Figure 6-6 (b) is the change from inner smaller tubes to rods. Compared with the baseline scenario where there are no insertion tubes/rods, the new designs shown in Figure 6-6 not only reduce the HTF thermal mass, but also increase the ratio between the nitinol heat transfer area and the nitinol volume. A higher ratio results in higher heat transfer area between HTF and nitinol so that more cooling can be transferred in a certain time frame, or heat transfer

155

can be accomplished within a shorter duration of time. As is shown from the results in the following section, this ratio significantly enhances the time constant related to the heat transfer dynamics.

To model the change of fluid thermal mass as well as the surface to volume ratio, the following parameters are updated accordingly.

$$A_{HTF} = \frac{\pi}{4}\left[ID^2 - N \cdot OD_{inner}^2\right]$$

(6-7)

$$dA_{HT} = \pi\left[ID + N \cdot OD_{inner}\right] \cdot dx$$

(6-8)

$$dV_{nitinol} = \frac{\pi}{4}\left[\left(OD^2 - ID^2\right) + N \cdot \left(OD_{inner}^2 - ID_{inner}^2\right)\right] \cdot dx$$

(6-9)

$$ra = \frac{dA_{HT}}{dV_{nitinol}} = \frac{4\left[ID + N \cdot OD_{inner}\right]}{\left[\left(OD^2 - ID^2\right) + N \cdot \left(OD_{inner}^2 - ID_{inner}^2\right)\right]}$$

(6-10)

$$N_{nitinol} \cdot dV_{nitinol} = N_{nitinol,bs} \cdot dV_{nitinol,bs}$$
$$N_{nitinol}\left[\left(OD^2 - ID^2\right) + N \cdot \left(OD_{inner}^2 - ID_{inner}^2\right)\right] = N_{nitinol,bs} \cdot \left(OD^2 - ID^2\right)$$

(6-11)

Eq. (6-7) evaluates the reduced HTF cross section area to the flow direction, where N denotes the insertion nitinol tubes/rods quantity. Eq. (6-8) represents the infinitesimal heat transfer area along the flow direction. The corresponding nitinol volume in contact with infinitesimal HTF is calculated by Eq. (6-9). Based on Eq. (6-8) and Eq. (6-9), the surface to volume ratio is computed from Eq. (6-10). When adding multiple small nitinol tubes/rods to the original external nitinol tube, the nitinol total volume or mass increases, and therefore cannot compare to the baseline scenario directly, unless the total volume or mass of the nitinol is kept constant by Eq. (6-11). Here, it is assumed that the nitinol tubes length is also fixed. $N_{nitinol}$ is the quantity of external

nitinol tubes, and *N* is the quantity of smaller insertion tubes/rods within each external nitinol tube.

All the aforementioned design updates were integrated into the original baseline transient model developed in Chapter 3. The model was solved using Simulink ode3 solver with fixed time step of 0.002 seconds (Simulink, 2014).

6.2 *Multi-objective Optimization Problem*

To further enhance the system performance beyond the proposed novel designs, system operating variables such as cycle frequency, heat recovery duration, and flow rates can be optimized. These variables considerably affect the heat transfer loss identified in Figure 6-1. The objective is to maximize the cooling capacity, as well as COP. Therefore, a multi-objective optimization problem needs to be formulated and solved. The baseline design for the optimization problem is the best design achieved using the proposed novel designs.

The formulation of the multi-objective optimization problem is shown in Table 6-2. The two objectives are maximizing both the cooling capacity and COP, which are conflicting with each other. The optimization design variables have the most significant impact on the system performance based on the parametric study conducted in Chapter 3. Heat transfer fluid and heat recovery fluid velocities influence the transient time constant directly, which are the first two design variables. The cycle frequency has a tradeoff between COP and cooling capacity since a slower cycle enhances the heat transfer and heat recovery, but simultaneously reduces the cooling capacity. The fourth design variable is the heat recovery duration coefficient

157

t^*, which is a non-dimensional number determining the heat recovery process duration defined in Eq. (4-13). The fifth design variable is the heat recovery pipe length, which is a key parameter contributing to the heat recovery efficiency as well as the system performance. The last design variable is the quantity of nitinol tubes in each bed.

Table 6-2: Formulation of the multi-objective optimization problem.

Objectives	Max. COP					
	Max. Q_c					

Design variables		u [m/s]	u_{HR} [m/s]	t_{cyc} [sec]	t^* [-]	L_{HR} [m]	$N_{nitinol}$ [-]
	Lower	0.4	0.1	8	1.0	0.1	15
	Upper	1.5	0.6	30	1.4	0.3	25

Constraints

$$N_{nitinol} \cdot L \cdot \left[OD^2 - ID^2 + N \cdot \left(OD_{inner}^{\;2} - ID_{inner}^{\;2} \right) \right] = const$$
$$= N_{nitinol,bs} \cdot L_{bs} \cdot \left[OD^2 - ID^2 \right] \tag{6-12}$$

$$t_{HR} = t^* \cdot \frac{\left[L \left(ID^2 - N \cdot OD_{inner}^{\;2} \right) + L_{HR} D_{HR}^{\;2} + 2 \cdot L_{header} D_{header}^{\;2} \right]}{N_{nitinol} \left(ID^2 - N \cdot OD_{inner}^{\;2} \right) u_{HR}} \tag{6-13}$$

$$\Delta T_{lift} = 10 \;°C \tag{6-14}$$

Constant parameters	N [-]	$N_{nitinol,bs}$ [-]	L_{bs} [m]	ID [m]	OD [m]
	7	19	0.254	0.004	0.005
	ID_{inner} [m]	OD_{inner} [m]	D_{HR} [m]	D_{header} [m]	L_{header} [m]
	0.0009	0.001	0.0191	0.0254	0.05

Since the total volume of the nitinol should be fixed to ensure a fair comparison, the first equality constraint shown in Eq. (6-12) (in Table 6-2) determines the length of each nitinol tube and insertion tubes/rods. The second constraint in Eq. (6-13) (Table

6-2) was proposed in the Chapter 3 based on the physics of the counter-flow heat recovery process. The third constraint in Eq. (6-14) (in Table 6-2) is to have all systems operating under the temperature lift of 10 K. Again, the baseline system for the optimization problem already included the proposed novel design concepts, which are tube holders' insulation, the decoupling loading head design, and seven insertion nitinol tubes in each original nitinol tube.

Multi-objective genetic algorithm (MOGA) from Matlab^{TM} was used to solve the problem. The population size was chosen to be 90. Tournament, crossover fraction, migration fraction, and Pareto front population fraction were set to be 2, 0.8, 0.2 and 0.35, respectively. The maximum generation was set to be 200 as a termination criterion. Figure 6-7 illustrates the problem solving procedure, which started from the problem initialization setup. The iteration optimization process, called the Simulink model for each design candidate, was developed in the Chapter 3 and modified with the improvement designs introduced in this chapter. The system COP and cooling capacity were computed by data reduction from the temperature profiles as results from the Simulink model. The optimization process is terminated, either by the changing of fitness functions in population or by maximum iteration. Finally, Pareto sorting generates the Pareto frontier among the last iteration population. The optimization was repeated to enhance the confidence from the Pareto frontier.

Problem Formulation:
Min. $-Q_c$, Min. $-COP$

Initial Population

Simulink Model
Evaluation

Matlab
gamultiobj.m
solver

Data Reduction:
Q_c, COP

Stop
Criterion

No

Yes

Feasible solution
(Blue diamonds)

No

Pareto
Sorting

Yes

Pareto front
(Green squares)
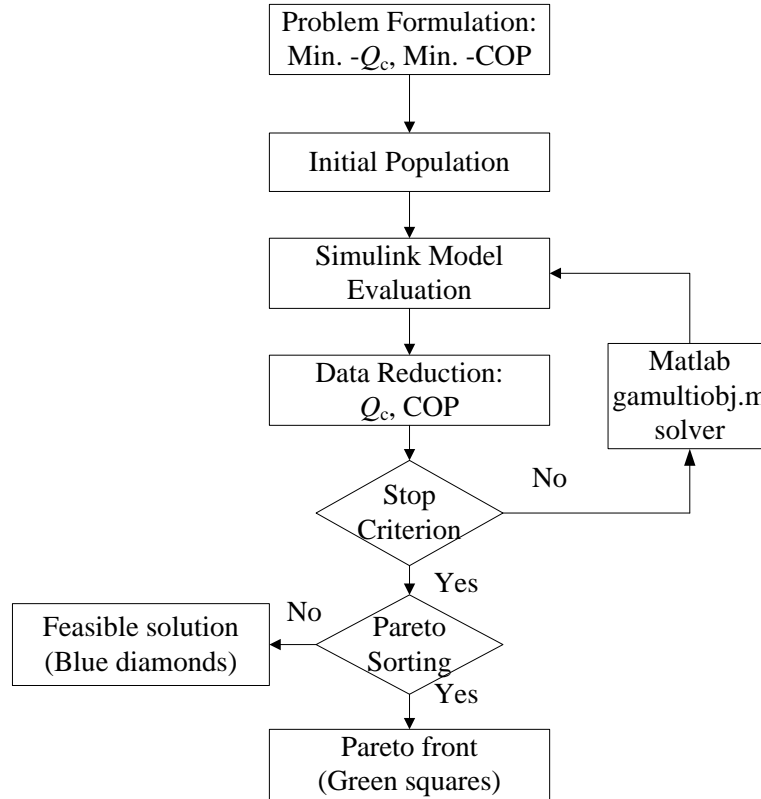
Figure 6-7: Flow chart of the multi-objective optimization problem solving

procedure.

6.3   *Results and Discussions*

In this section, the results using novel designs are discussed first, followed by the enhancement on the novel designs using optimization. Last, the potential of thermoelastic cooling using the improvement results from this chapter and the updated loss analysis chart are analyzed.

6.3.1   Performance Improvements with Novel Designs

Figure 6-8 is an overview of the performance enhancement results with the novel designs, which plots the maximum temperature lift achievable with the five different

designs proposed earlier. Here, dry loading head refers to the decoupling design for the loading head, since there is no more HTF in direct contact with the loading head. The reason why COP or cooling capacity was not used as an index here is due to the fact that the baseline could not reach the 10 K temperature lift. Nevertheless, the system maximum temperature lift is still a fair index to compare. The red bar on the left is the baseline temperature lift, which is 6.6 K. When adding the insulation layer to the tube holders as described in Section 6.1.1, there is an improvement of 0.5 K when compared with the baseline. Loading head insulation layer results in much higher enhancement, since the HTF is in direct contact with the loading head.
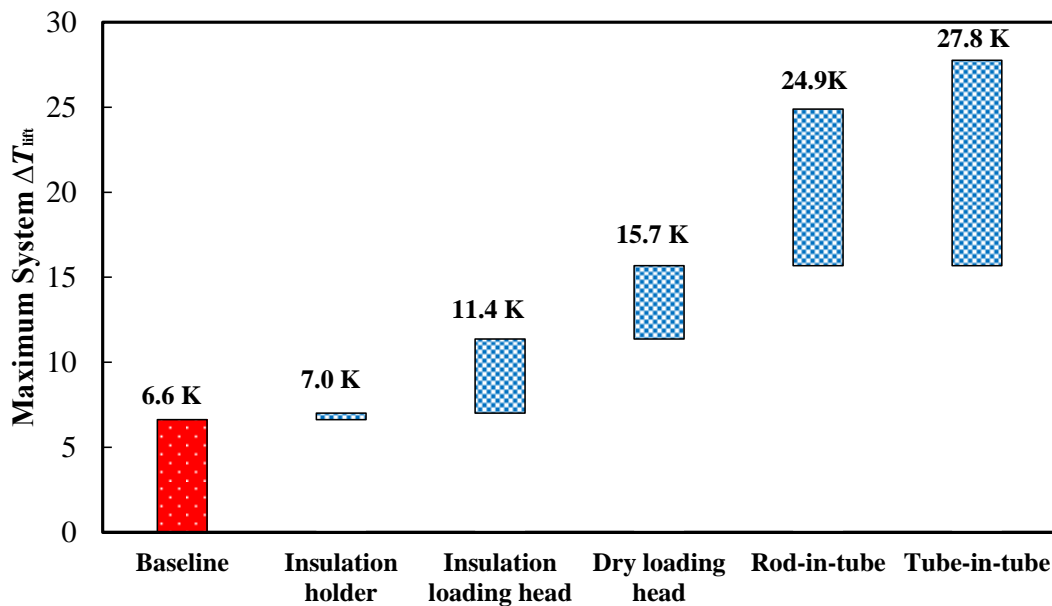
Figure 6-8: Summary of performance enhancement as results of novel designs. (all designs have the same nitinol volume and mass, $\Delta T_{\text{lift}} = 10$ [K], $u = 0.8$ [m/s], $u_{\text{HR}} = 0.4$ [m/s], $t_{\text{cyc}} = 10$ [sec])

Compared to the loading head, even with the much higher thermal mass, the tube holders did not contribute much to the loss initially, since it is only in line contact

161

with the nitinol tubes. The dry loading head design introduced in Section 6.1.3 adds an additional improvement of 4.3 K compared to the insulation layer in the loading head. This can be regarded as another important argument about the contribution of loading head to the loss. The next stage improvement is the most significant step towards achieving a better performance. A 9.2 K temperature lift enhancement was achieved by applying the rod-in-tube design, due to the simultaneous reduction in HTF thermal mass, as well as higher heat transfer surface to volume ratio for nitinol. Another 2.9 K improvement can be achieved by switching the rods to tubes without flowing any HTF inside. Note that for a fair comparison, the nitinol volume and mass was kept constant, as shown in Eq. (6-11).
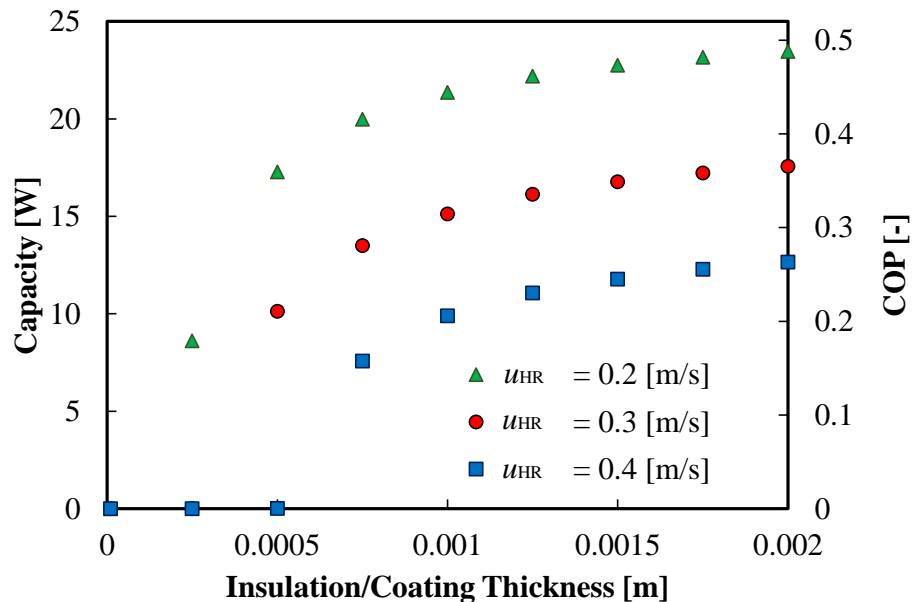
Figure 6-9: Capacity enhancement as a result of the coating/insulation layer design. ($\Delta T_{lift} = 10$ [K], $u = 0.8$ [m/s], $t_{cyc} = 10$ [sec])

The role of insulating the loading head is discussed in more detail in Figure 6-9. The

few points with the capacity of zero were due to insufficient maximum achievable temperature lift. As expected, increasing the insulation layer thickness reduced the heat transfer between the HTF and the metal loading head, and the associated losses as well. Eventually, the insulation approaches the critical thickness, which is around 2 mm from Figure 6-9. By applying the insulation layer, the maximum improvement for COP is from 0 to 0.5.
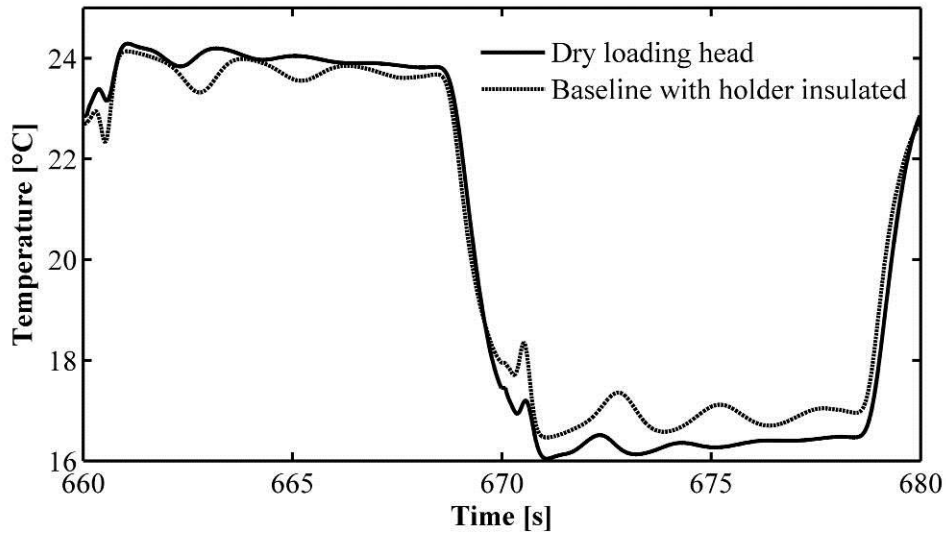
Figure 6-10: Illustration of capacity enhancement by applying plotting the exit fluid temperature of the outlet loading head using decoupling loading head design. (ΔT_{lift} = 5 [K], u = 0.8 [m/s], u_{HR} = 0.4 [m/s], t_{cyc} = 10 [sec])

Figure 6-10 shows the details when the dry loading head concept was applied as introduced in Section 6.1.3. The solid curve corresponds to the case where both the loading head and the tube holders were insulated, while the dry loading head design corresponds to the dashed curve. The first observation is that the solid curve has more temperature oscillation amplitude. Due to the thermal mass of the loading head, heat was absorbed from the HTF during the heat rejection process from 660 to 668

163

seconds and causing the additional temperature drop. The temperature oscillation was delayed in a solid line compared to the dashed line. This increase in the time constant was also due to the loading head thermal mass. In addition, when compared to the solid line, the dry loading head design had a higher fluid temperature during the heat rejection process from 660 to 668 seconds, and a lower fluid temperature during the cooling delivery process from 670 to 678 seconds. Therefore, more heating as well as more cooling is achieved using the two heat transfer processes.
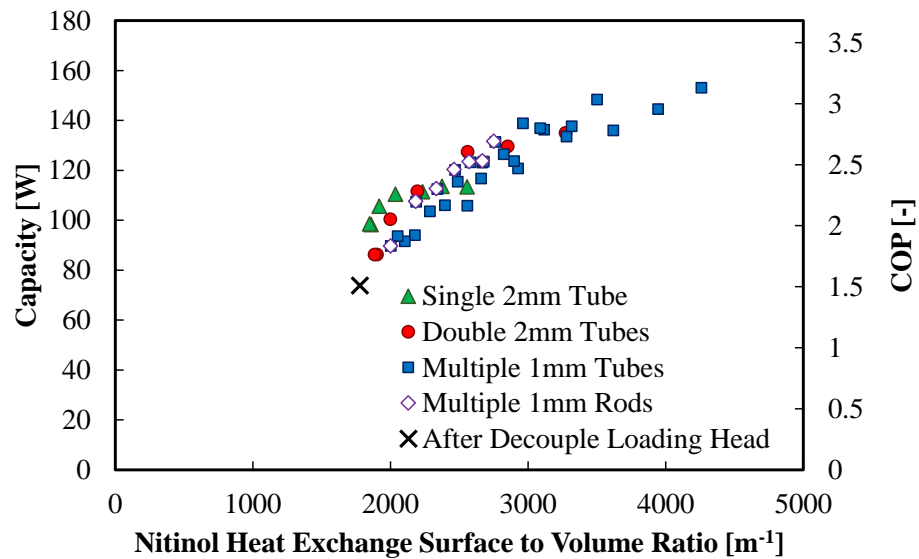
Figure 6-11: Capacity enhancement as a result of the tube-in-tube and rod-in-tube design. (ΔT_{lift} = 10 [K], u = 0.8 [m/s], u_{HR} = 0.4 [m/s], t_{cyc} = 10 [sec])

When both the tube holders' insulation and the decoupling loading head design were applied, the role of tube-in-tube and rod-in-tube designs can be studied. Inserting small nitinol rods or tubes helps reduce the HTF thermal mass inside the regular nitinol tube, as well as increasing the nitinol heat transfer surface to volume ratio. Figure 6-11 plots the performance enhancement of several different candidates using

the nitinol heat transfer area to volume ratio as the control variable. Figure 6-11 illustrates that the performance increased monotonically with the nitinol heat transfer area to volume ratio. A higher nitinol heat transfer area to volume ratio means smaller heat transfer time constant, or equivalently, more heating/cooling transferred per unit mass per unit time. Whenever any rod or small tubes were inserted in a regular tube, the nitinol heat transfer area to volume ratio is increased. Therefore, adding smaller tubes or rods enhances the capacity and COP. Also, inserting small tubes has the same surface heat transfer area as the small rods but with less volume per regular tube and, therefore, has a higher heat transfer surface to volume ratio. The best two points on Figure 6-11 for tube-in-tube and rod-in-tube designs are corresponding to the enhancement cases plotted in Figure 6-10.

6.3.2 Multi-objective Optimization Results

The optimization routine described in Figure 6-7 terminated after the 115th generation, when the relative change in fitness function evaluation was less than 0.01%. To visualize the convergence of the solution, Figure 6-12 shows how a few indices vary between generations. Both the COP and cooling capacity were normalized to the maximum COP or capacity evaluated. Figure 6-12 (a) shows the average indices among the entire population for each generation, and both of them oscillated due to the stochastic nature of genetic algorithm. The average indices will not converge to 1, so a well-developed spread can be guaranteed. On the contrary, both the maximum COP and capacity almost converged to 1. Again, the deviation of capacity from 1 is due to the random nature of genetic algorithm.
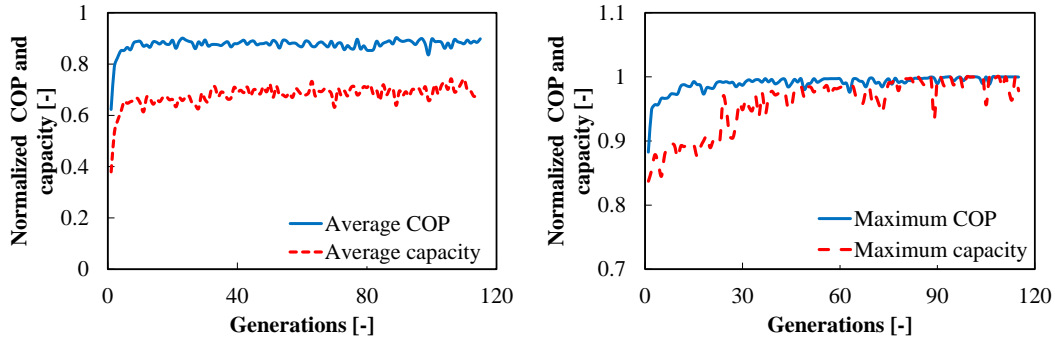
(a) Average COP and capacity among the entire population for each generation (normalized to the maximum values)

(b) Maximum COP and capacity among the entire population for each generation (normalized to the maximum values)

Figure 6-12: Solutions over iterations and illustration of convergence.

Figure 6-13 plots all the evaluated candidates and the final solution on the Pareto front. The Pareto front contained 218 final solutions out of the 10350 evaluated candidates. All the blue diamonds (evaluated candidates) consist of a triangle region, bounded by the (0, 0) origin, the maximum COP point, and the maximum capacity point. This triangle domain is determined by the design variables' upper and lower bounds, specified in Table 6-2. When the upper and lower bounds are further relaxed, the triangle domain spans more accordingly. The limiting case would be relaxing all the design variables to be no less than zero. In that case, it can be expected that the Pareto front to extend all the way to COP axis when the cycle duration approaches infinity, leading to almost zero capacity but finite COP. Comparing the Pareto front solutions to the baseline case with all the novel designs specified in Figure 6-8, optimization can further enhance the system performance by partially reducing the cyclic loss and reducing the heat transfer loss.

166
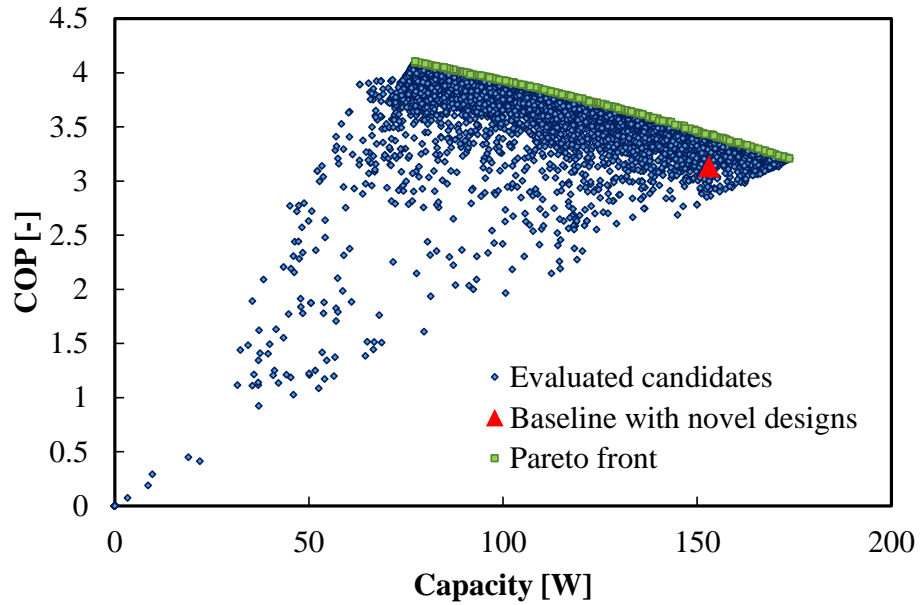
Figure 6-13: Multi-objective optimization results on the capacity-COP chart.

The maximum COP point reached a COP of 4.1, corresponding to almost 31% COP enhancement but had a capacity reduction tradeoff. If the cooling capacity remained constant, the COP enhancement was 9.3%. The capacity enhancement was 19.1% when the COP was fixed. The maximum capacity point reached 184 W, corresponding to a 20.5% capacity enhancement. One can expect to reach a higher capacity than this if the lower bound of cycle duration t_{cyc} can be relaxed, i.e. cycling faster. A detailed quantitative comparison from the baseline scenario with the tube-in-tube design shown as the highest COP/capacity point from Figure 6-11 can be found in Table 6-3. Compared to the variables' bounds specified in Table 6-2, it can be concluded that a slower cycle with less HR velocity and fewer, albeit longer, nitinol tubes are preferred for maximizing the COP perspective.

Table 6-3: Summary of the multi-objective optimization results.

	Baseline	Maximum COP	Maximum capacity	Same COP	Same capacity
Q_c	153.1	77.4 (-49.4%)	**184.5 (+20.5%)**	**182.4 (+19.1%)**	153.1 (0%)
COP	3.13	**4.10 (+30.8%)**	3.10 (-0.9%)	3.13 (0%)	**3.43 (+9.3%)**
u	0.89	1.04	1.48	1.47	1.00
$\underline{u}_{HR}$	0.40	0.10	0.36	0.34	0.23
t_{cyc}	10.0	25.2	8.0	8.2	10.6
t^*	1.20	1.27	1.22	1.22	1.24
L_{HR}	0.25	0.30	0.30	0.30	0.30
$N_{nitinol}$	17	17	22	22	21

6.3.3   Outlook

The ultimate design goal is to reduce the losses at all stages by 50%, as discussed in Chapter 4. Figure 6-1 establishes the baseline; the system COP was 0 due to the metal loading head and tube holders' thermal mass in the real prototype setup. With all the methods introduced in this chapter, the fourth and fifth losses have been successfully reduced, as shown in Figure 6-14. The fifth stage loss was reduced by 73%, with a COP of 3.4, considering the pump power consumption to be 20% of the driving system's work, as a result of including the novel designs and partially due to optimization. The fourth stage loss had a 37% reduction as a result of the optimization. The long term goal in Figure 6-14 also requires a substantial reduction in the second stage loss, which is from the inefficiency of the current Brayton cycle design using adiabatic loading. With a hybrid cycle combining Stirling (isothermal loading) and Brayton cycle (adiabatic loading), the goal of reaching COP of 7.7 could potentially be achievable.
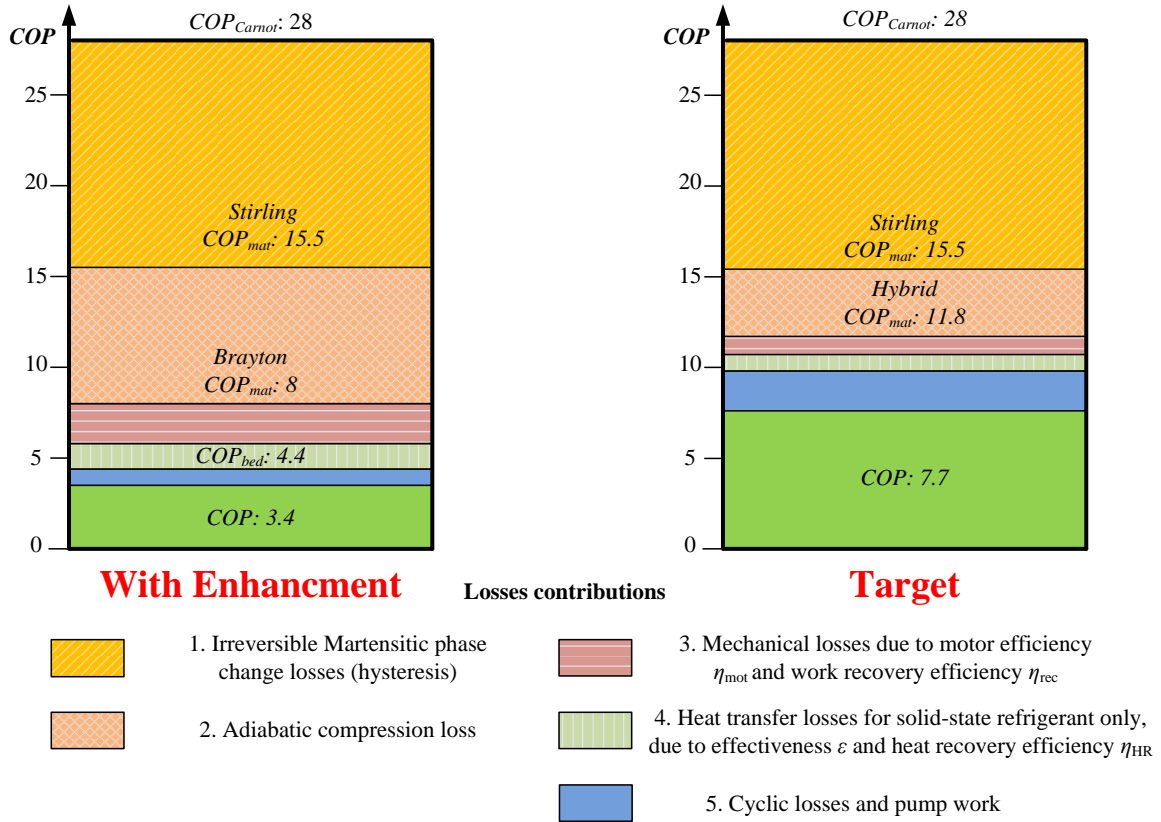
Figure 6-14: The updated losses analysis chart with performance enhancements as compared to the long term target. (ΔT_{lift} = 10 [K])

6.4   *Chapter Summary and Conclusions*

This chapter discussed multiple ways to improve the performance of a compressive thermoelastic cooling system, as guidelines to real prototypes under development. Several novel design options were investigated which reduced the cyclic loss from the thermal mass of the loading head and tube holders. These options include a thin film coating and insulating layer for both the tube holders and the loading head, two different decoupling designs for loading head, and finally the tube-in-tube or rod-in-tube design. The performance improvements were evaluated based on the previously

developed dynamic model with the modifications proposed in this chapter. It was found that the decoupling design for loading head paired with the tube-in-tube design resulted in the most significant improvement. In addition, multi-objective optimization was used to further enhance the system COP as well as capacity. It was found that the maximum temperature lift increased from 6.6 K to 27.8 K when applying the proposed novel designs. The cooling capacity can be enhanced from 0 W to 152 W with the novel designs before optimization, and up to 184 W with optimization, both at 10 K water-water system temperature lift. The COP enhancement is from 0 to 3.1 before optimization, and up to 4.1 with optimization. From the losses perspective, the heat transfer loss was reduced by 37%, and the cyclic loss was reduced by 73%. Future work on the performance enhancement should be focused on exploring the hybrid Brayton and Stirling cycle integration with thermoelastic cooling system.

Chapter 7: Not-in-kind Cooling Technologies Comparison

With the breakdown chart analysis method presented in Figure 3-17 and Figure 6-14, the materials level *COP* (only dependent on materials properties and the cycle path) represents the theoretical limit for a certain not-in-kind (NIK) cooling technology assuming that the system is fully reversible. Advances in materials properties in the future will extend this limit. System limitations add more irreversibilities, which are shown in Figure 6-14 as adiabatic compression losses due to the Brayton cycle operation, motor efficiency, heat transfer irreversibility and parasitic power, respectively. The bottom level *COP* represents the system level *COP* under the given operating conditions. With the additional freedom, assessment of the materials level *COP*s for different NIK technologies determines the theoretical limit of each technology, Similarly, assessment of the system level *COP*s reveals the system integration perfectiveness. These two level *COP*s and the normalized exergetic efficiencies are correlated and defined in Eq. (7-1) and Eq. (7-2). The Carnot *COP* is defined in Eq. (7-3) as well. In this study, the same terminology used by Brown and Domanski (2014) was used. Φ_{mat} is the normalized materials *COP*, or the materials level exergetic efficiency. Φ_{sys} is a measure of the perfectness of the system integration. Φ_{sys} equals one does not mean the system can reach the Carnot *COP*, but it rather indicates that all irreversibilities are results from the materials themselves.

$$COP_{mat} = COP_{carnot}\Phi_{mat} \tag{7-1}$$

$$COP_{system} = COP_{carnot} \Phi_{mat} \Phi_{sys} \qquad (7\text{-}2)$$

$$COP_{Carnot} = \frac{T_c}{\Delta T_{lift}} \equiv \frac{T_c}{T_h - T_c} \qquad (7\text{-}3)$$

The second added freedom is the temperature lift. Extending the temperature lift of 10 K used in Figure 6-14 reveals how these technologies would perform for different applications, i.e. small temperature lift coolers, medium temperature lift air-conditioners, and large temperature lift refrigerator/freezers.

Despite the diversity of refrigerants/materials, work input energy conversion principles and systems configuration of the various NIK cooling technologies, there are some universal common features that all cooling technologies share. Figure 7-1 demonstrates these features by using a vapor compression system as an example.
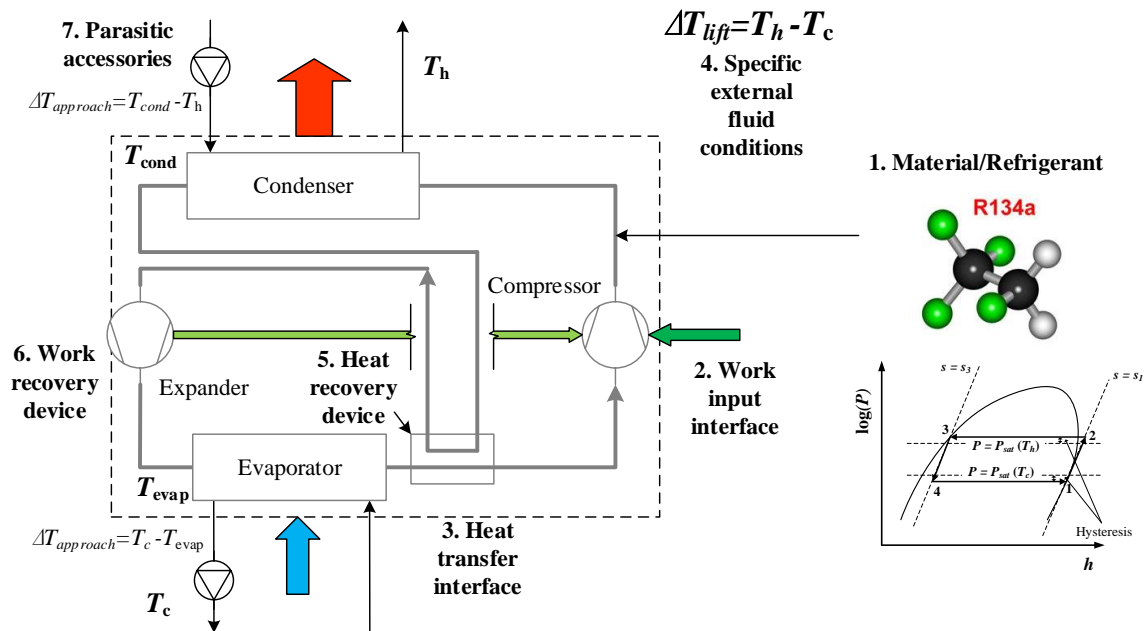
Figure 7-1: Illustration of common features for all cooling technologies using vapor compression cooling as an example.

172

The material/refrigerant is the core of all cooling systems, which convert the input work into cooling and heating. To enable the energy conversion process, a work input interface is needed, which can be a compressor for gas, a compression machine for shape memory alloys, a permanent magnet for magnetocaloric materials, or an electric field for electrocaloric materials. The heat transfer interface absorbs cooling load and rejects heat into ambient. For a vapor compression air-conditioner, the external fluid is air and the heat transfer interfaces are the refrigerant-air heat exchangers. In this study, the comparison application is water chiller, and therefore water heat exchangers are the heat transfer interface. It is important that the comparison basis is identical for all NIK cooling technologies, which means that the specific external fluid conditions are identical for all compared NIK cooling technologies in this study. The fluid temperatures T_c and T_h in Figure 7-1 are consistent with those in Eq. (7-3). The heat recovery device is to enhance the operating performance by precooling the refrigerant before the cooling process and preheating the refrigerant before the heat rejection process. The system performance can be further improved by applying the work recovery concept, since part of the work can be recovered to reduce the net work input. The last feature was often neglected, especially for NIK cooling technologies. The parasitic power consumption by water pumps, air fans and cooling tower fans are not trivial when compared with the main work input power consumption, especially for those high efficient cooling systems. The heat recovery methods and work recovery methods for various NIK cooling technologies are summarized in Table 7-1.

Table 7-1: Brief summary of the NIK cooling technologies in this study.

Technology	R and D status (*)	Cost/complexity (*)	Refrigerant	Work input form	Possible heat recovery method	Possible work recovery method	Reference
Vapor compression (baseline)	Mature	Low	R410A	$\int p\mathrm{d}v$	Suction-line heat exchanger	Expander	Radermacher and Hwang, 2005
Elastocaloric	R and D, recently started	Moderate	Ni-Ti	$\int \sigma \mathrm{d}\varepsilon$	Thermowave heat recovery	Multi-bed symmetric design	Chapter 3
Magnetocaloric	Advanced R and D	High	Gd	$\int \mu_0 H \mathrm{d}m$	Active magnetic regenerator	Multi-bed rotary bed design	Jacobs et al., 2014
Electrocaloric	R and D, recently started	Moderate	P(VDF-TrFE-CFE)	$\int E_e \mathrm{d}D$	Passive external regenerator	n/a	Gu et al., 2013
Thermoelectric	Well established, on-going materials research	Moderate	Bi-Sb-Te	n/a	n/a	n/a	Zhao and Tan, 2014
Stirling	Manufacturing issues	Moderate	Helium	$\int p\mathrm{d}v$	Regenerator	Piston	Razani et al., 2010
Brayton	Manufacturing issues	Moderate	Air	$\int p\mathrm{d}v$	Recuperative heat exchanger	Turbine	Ni et al., 1999

*: based on Bansal et al., 2012 and Goetzeler et al., 2014

Relevant information from literature has been summarized in Table 7-1 for those NIK technologies in this chapter. The listed refrigerant/materials are the most common ones for the NIK technologies, and are selected for calculation in this study. The work input form indicates the energy conversion form for each cooling technologies. For example, *p-v* diagram for vapor refrigerant is required to compute the work where gaseous refrigerant is compressed, and *σ-ε* diagram should be used for elastocaloric cooling where solid-state shape memory alloys are loaded. Only work input driven cooling technologies are compared in this study. Heat driven cycles is beyond current scope. Most systems require heat recovery or regeneration to operate efficiently. Examples of possible heat recovery methods used in literature are summarized in Table 7-1 as well. A counter-flow heat exchanger between the cold refrigerant and the hot refrigerant is commonly used for systems operated under steady state condition, i.e. vapor compression and Brayton cycle. Cyclically operated systems require a regenerator, such as Stirling cycle, magnetocaloric cooling and electrocaloric cooling, to cyclically store and release energy to the refrigerant. A separate heat recovery process can be also used for cyclically operated systems, such as elastocaloric cooling.

7.1 *Comparison of Refrigerants*

There are many quantities used as indices to compare the materials/refrigerants. Since the thermal performance and their potential energy conversion efficiency are the main focus of this study, the following two indices are selected.

- Non-dimensional latent heat (γ)

This is a normalized latent heat as described in Eq. (2-10). It represents the maximum useful latent heat to the parasitic heat loss ratio. The numerator is the specific latent heat of the material, i.e. evaporation heat for liquid refrigerant in vapor compression system, martensitic phase change latent heat in elastocaloric cooling, or the heat associated with the field induced entropy change for magnetocaloric cooling. The denominator is the parasitic sensible heat loss consumed by the material/refrigerant itself inside the heat pump to change temperature between the hot side (heat sink at T_h) and the cold side (heat source at T_c). For thermoelectric cooling, this term is the parasitic heat loss by conduction from the hot side to the cold side. Therefore, when the ratio is above 1, it means that the material is able to provide useful cooling in a system under the required temperature lift. Otherwise, the cycle would not produce useful cooling unless the heat recovery/regenerator cascaded cycle is applied. Details of the following equations are derived in the Appendix C. The specific heat (c_p) used in Eq. (7-4) to Eq. (7-11) is the specific heat measured in the low entropy phase, i.e. liquid, martensite, or magnetized state.

$$\gamma = \frac{\Delta h}{c_p \Delta T_{lift}} \tag{7-4}$$

$$\gamma_{VCC} = \frac{(h_1 - h_4)_T}{c_p \Delta T_{lift}} \tag{7-5}$$

$$\gamma_{thermoelastic} = \frac{T_c \Delta s}{c_p \Delta T_{lift}} \tag{7-6}$$

$$\gamma_{magnetocaloric} = \frac{T_c \Delta s (T_c)}{c_p \Delta T_{lift}} \tag{7-7}$$

$$\gamma_{electrocaloric} = \frac{T_c \Delta s(T_c)}{c_p \Delta T_{lift}}$$ (7-8)

$$\gamma_{thermoelectric} = \frac{\alpha_s I_{opt} T_c}{kx \Delta T_{lift}} = \frac{\alpha_s^2 T_c}{k\rho_e \left(\sqrt{1+ZT_m}-1\right)} = \frac{ZT_c}{\left(\sqrt{1+ZT_m}-1\right)}$$ (7-9)

$$\gamma_{Brayton} = \frac{h_6 - h_5}{c_p \Delta T_{lift}}$$ (7-10)

$$\gamma_{Stirling} = \frac{T_c \Delta s(T_c)}{c_p \Delta T_{lift}}$$ (7-11)

- *COP* based on material properties (Material *COP*, *COP*$_{mat}$)

The first index considers only the latent heat without any information about energy conversion efficiency, which depends on both the operating temperatures and the loading process for different technologies (adding magnetic or electric field, or applying mechanical stress) because work and heat are path dependent variables not state variables (Moran et al., 2011). Therefore, the energy conversion efficiency, *COP*$_{mat}$, as defined in Eq. (7-12), was a natural extension from the work by Cui et al., (2012), Moya et al. (2015) and Defay et al. (2013), by using only the materials properties under the pre-defined cycle paths. The *COP*$_{mat}$ does not include the system details such as limitations in driving system (compressor or motor) efficiency, system dynamics, regenerator effectiveness, heat or mass transfer and component geometries. This index can also be converted to the exergetic efficiency in a way similar to Brown and Domanski (2014). It can be regarded as the limit or the maximum potential the material has for each cooling technology. A lower value of *COP*$_{mat}$ means a certain cooling technology has more irreversibility fundamentally in its working principle.

As indicated by Eq. (7-12), calculation of COP_{mat} requires knowledge on the work/power input, which is path dependent in most cases. This path dependency suggests more information is needed beyond Eq. (7-12), such as the equations-of-states for vapor-liquid refrigerants, or the constitutive equation for SMAs in an elastocaloric cooling system. When using the equations-of-state, the COP_{mat} can be determined only based on state variables and materials properties. The detailed equations for the evaluated NIK cooling technologies are shown in Eq. (7-13) through Eq. (7-19). Vapor compression cycle's COP_{mat} neglecting all system losses can be found in text books for example Radermacher and Hwang (2005), and the cycle diagram is also shown in Figure 7-2(a). The hysteresis in Figure 7-2(a) corresponds to the additional pressure needed to induce condensation, as well as the additional vacuum to nucleate bubbles based on the Laplace equation (Carey, V.P., 2008). Elastocaloric cooling cycle's COP_{mat} has been developed in Chapter 1 and is shown in Figure 7-2(b) and Figure 7-2(c). Note here A^* is the material constant used in the martensitic phase change phenomenological model describing the martensitic phase change hysteresis. Magnetocaloric cooling cycle's COP_{mat} was also derived based on the thermodynamics of magnetocaloric effect using Ericsson cycle (Kitanovski and Egolf, 2006) in Figure 7-2(d) and Figure 7-2(e), and considering the magnetization hysteresis using a parameter $A_{magnetic}$. A similar method was applied for electrocaloric cooling operated under Ericsson cycle (Ozbolt et al., 2014), where the hysteresis stands for the polarization hysteresis when applying the electric field for electrocaloric materials. Thermoelectric cooling's COP_{mat} was well developed as a simplified system model and have been used in the past studies quite often (Riffat and

Ma, 2004). Standard Brayton and Stirling cycles using ideal gas were available in a book by Moran et al. (2011). Details can be found in the Appendix C.

$$COP_{mat} = \frac{q_c}{w_{net}} \tag{7-12}$$

$$COP_{mat,VCC} = \frac{q_c}{w_{compressor} - w_{expander}} = \frac{(h_1 - h_4)_T}{\left[(h_2 - h_1)_s - (h_3 - h_4)_s\right]} \tag{7-13}$$

$$COP_{mat,thermoelastic} = \frac{q_c(T_c)}{w_+(T_h) - w_-(T_c)} = \frac{T_c \Delta s - A^*}{(T_h - T_c)\Delta s + 2A^*} \tag{7-14}$$

$$COP_{mat,magnetocaloric} = \frac{q_c}{w_{net}} = \frac{T_c \Delta s - A^*_{magnet}}{(T_h - T_c)\Delta s + 2A^*_{magnet}} \tag{7-15}$$

$$COP_{mat,electrocaloric} = \frac{q_c}{w_{net}} = \frac{T_c \Delta s - A^*_{electrocaloric}}{(T_h - T_c)\Delta s + 2A^*_{electrocaloric}} \tag{7-16}$$

$$COP_{mat,thermoelectric} = \frac{q_c(I_{opt})}{w_{net}(I_{opt})} = \frac{T_c\left(\sqrt{1 + ZT_m} - T_h/T_c\right)}{(T_h - T_c)\left(\sqrt{1 + ZT_m} + 1\right)} \tag{7-17}$$

$$COP_{mat,Brayton} = \frac{q_c}{w_{compressor} - w_{expander}} = \frac{(h_6 - h_5)_P}{\left[(h_2 - h_1)_s - (h_4 - h_5)_s\right]} \tag{7-18}$$

$$COP_{mat,Stirling} = \frac{q_c(T_c)}{w_+(T_h) - w_-(T_c)} = \frac{T_c(s_1 - s_4)}{T_h(s_2 - s_3) - T_c(s_1 - s_4)} \tag{7-19}$$

Other thermal criteria have also been used widely in literature for different cooling technologies, each having its own unique advantages in describing the corresponding NIK technology, such as *ZT* value (dimensionless figure-of-merit) for thermoelectric cooling and thermoionic cooling (Zhao and Tan, 2014), and relative cooling power (*RCP*) for magnetocaloric cooling and elastocaloric cooling materials (Gschneidner and Pecharsky, 2000). However, these criteria cannot be applied universally for all NIK cooling technologies and therefore, are not used in this study.
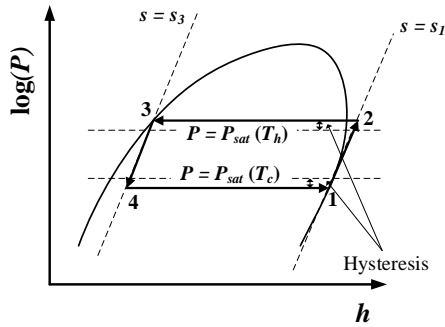
(a) Vapor compression cycle on a *P-h* diagram. State 1 is saturated vapor. State 3 is saturated liquid. Process from state 1 to 2 is isentropic compression. Process from state 3 to 4 is isentropic. No suction-line heat exchanger is applied here since there is no benefit for most refrigerants on the material level.
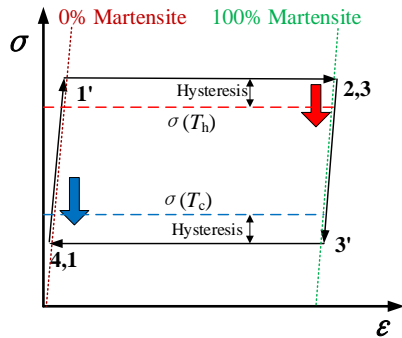
(b) Elastocaloric Stirling cooling cycle on a *σ-ε* diagram
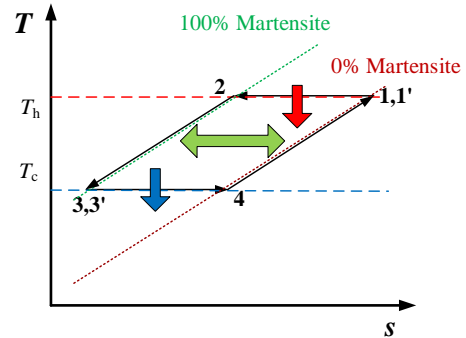
(c) Elastocaloric Stirling cooling cycle on a *T-s* diagram
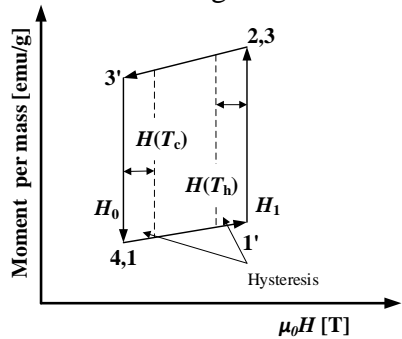
(d) Magnetocaloric Ericsson cooling cycle on a moment-field diagram
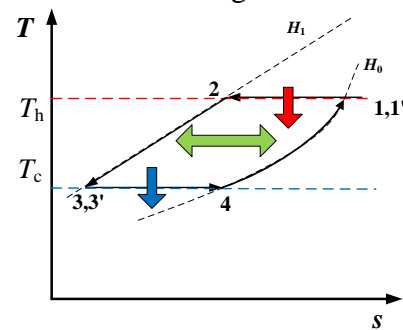
(e) Magnetocaloric Ericsson cooling cycle on a *T-s* diagram
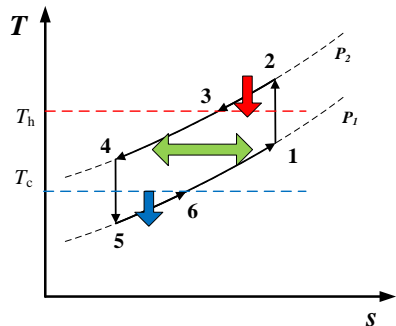
(f) Brayton cooling cycle on a *T-s* diagram
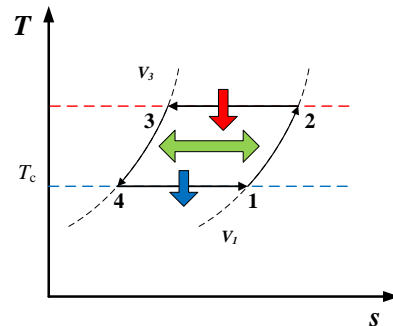
(g) Stirling cooling cycle on a *T-s* diagram

Figure 7-2: Ideal cycle description of different cooling technologies.

Table 7-2 summarizes results from the materials comparison using the aforementioned two indices and the phase change temperature range. The operating temperature lift was chosen to be 10 K from 288 K (15°C) to 298 K (25°C) as the same basis for comparison, and enabling using Carnot *COP* as a metric to normalize. One can also choose the basis according to AHRI 210/240 standard (2008), if the target application is residential air-conditioners, or AHRI 550/590 (2003) for commercial building water chillers.

Table 7-2: Materials/refrigerants comparison summary.

Category	Refrigerant	Phase change temperature [K]	γ [-]	Φ_{mat} (*)	Reference
Vapor compression	Water	273 ~ 647	57.9	0.86	Haar et al., 1984
	Ammonia	195 ~ 405	24.4	0.89	TillnerRoth et al., 1993
	R32	136 ~ 351	14.4	0.89	TillnerRoth and Yokozeki, 1997
	R134a	172 ~ 374	12.4	0.91	TillnerRoth and Baehr, 1994
	R410A	118 ~ 344	11.3	0.88	Lemmon, 2003
Elastocaloric	Ni-Ti	73 ~ 373	2.20	0.63	Cui et al., 2012, Tusek et al., 2015a
	Cu-Al-Ni	73 ~ 387	1.36	0.55	Chen et al., 2009
	Cu-Zn-Al	73 ~ 380	1.53	0.71	Manosa et al., 2009
	Ti-Ni-Cu	300 ~ 345	1.08	0.69	Bechtold et al., 2012
Magnetocaloric (**)	Gd	280 ~ 325	0.78	0.91	Tishin and Spichkin, 2003
	Gd-Si-Ge	272 ~ 298	1.03	0.79	Moore et al., 2009, Gschneidner et al., 2005
	La-Fe-Si	185 ~ 205	0.70	0.88	Liu et al., 2011
	La-Fe-Si-Co	276 ~ 310	0.35	0.88	Yan et al., 2008
Electrocaloric	Pb-Zr-Ti-O	323 ~ 553	0.80	0.31	Mischenoko et al., 2006
	P(VDF-TrFE)	303 ~ 383	1.22	0.33	Neese et al., 2008
	P(VDF-TrFE-CFE)	300 ~ 350	1.80	0.41	Liu et al., 2010
Thermoelectric	Bi-Te	200 ~ 600	2.32	0.12	Tritt, 2011
	Bi-Sb-Te	200 ~ 600	2.50	0.20	Yamashita et al., 2009
Brayton (***)	Air	77 ~ 400	10.6	0.08	
	He	4 ~ 400	13.7	0.06	Ideal gas
Stirling	He	4 ~ 400	18.5	1.00	

*: based on T_c = 288K and T_h = 298K, Carnot *COP* is 28.8.
**: based on 0~5T data.
***: based on pressure ratio of 3.

Since not all NIK cooling technologies are mature enough to be operated under these two standards, and also as pointed out in the literature (Brown and Domanski, 2014, Bansal et al., 2012), niche markets may be more applicable for these NIK cooling technologies. As is demonstrated by the results, some NIK cooling technologies favor small temperature lift while others favor large temperature lifts. Thus, a medium temperature lift at 10 K is selected as a comparison standard. Figure 7-3 plots the results in Table 7-2, using both the COP_{mat} absolute values and the normalized COP_{mat} (or exergetic efficiency, second law efficiency) versus the non-dimensional latent heat.
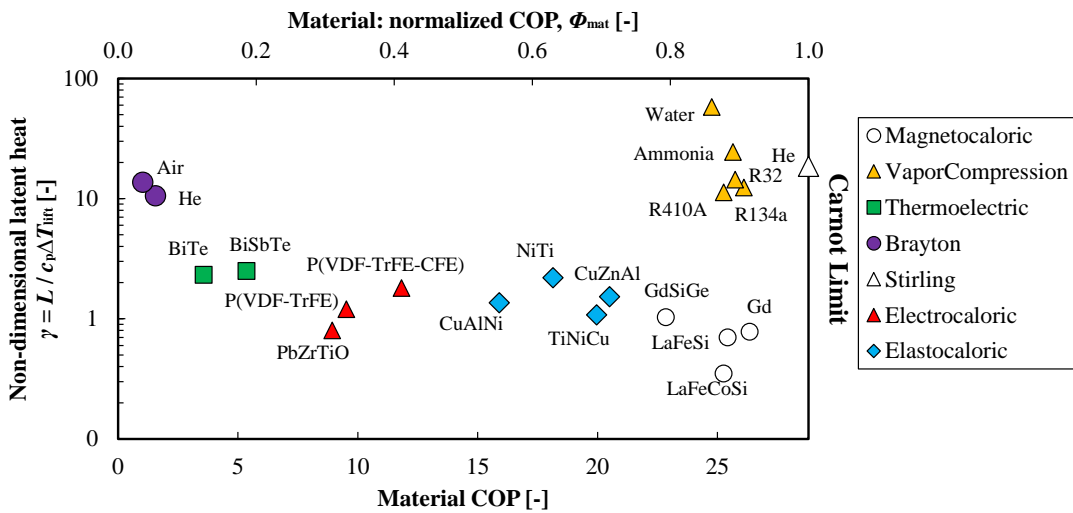
Figure 7-3: Comparison of the materials/refrigerants of various cooling technologies on the COP_{mat} and non-dimensional latent heat diagram (T_c = 288K, T_h = 298K, Carnot COP = 28.8).

The liquid-vapor refrigerants dominate solid-state materials significantly. The range of non-dimensional latent heat spans more than one order of magnitude, which is consistent with the fact that mass based energy density is vastly different between

solids and liquids. The solid-state materials can be divided into three groups: magnetocaloric materials with high *COP* but low latent heat (right-bottom corner), thermoelectric materials with low *COP* but relative high latent heat (left-top among solid-state materials), and medium *COP* and latent heat group (SMAs and electrocaloric cooling materials).

7.2   *Comparison of Cooling Technologies*

The following conditions are used for performance comparison of all cooling technology systems, unless otherwise noted:

$$T_h = 293 + 0.5\Delta T_{lift} \ [K] \tag{7-20}$$

$$T_c = 293 - 0.5\Delta T_{lift} \ [K] \tag{7-21}$$

$$\Delta T_{approach} = 5 \ [K] \tag{7-22}$$

$$W_{parasitic} = 0.2 W_{cycle,20K} \tag{7-23}$$

A water-cooled water chiller is used as the same comparison basis. The heat sink water temperature is maintained at T_h specified in Eq. (7-20), and the heat source (cooling load side) water temperature is at T_c specified in Eq. (7-21). The approach temperature in Eq. (7-22) is used for any cooling technology requiring an additional heat exchanger for the water side. Figure 7-1 displays schematic of a vapor compression system as an example showing Eq. (7-20) to Eq. (7-22). The two streams of water are maintained at the specified temperature lift. The refrigerant-water heat exchangers, i.e. evaporator and condenser in this case, have the same approach temperature. Eq. (7-23) represents the assumption of a constant parasitic power

consumption, which is equal to 20% of the driving system power (compressor power in Figure 7-1) when evaluated under 20 K temperature lift. This rough assumption should be updated when a better estimation or direct measurement of the parasitic power becomes available.

7.2.1 Vapor Compression Cooling (baseline)

Figure 7-4 shows the normalized *COP* breakdown chart for the baseline vapor compression system (Radermacher and Hwang, 2005).

Loss 1: material hysteresis

Loss 2: compressor efficiency and expansion loss

Loss 3: pressure drop in two heat exchangers

Loss 4: external heat transfer irreversibility

Loss 5: parasitic power (pump, fan, etc.)
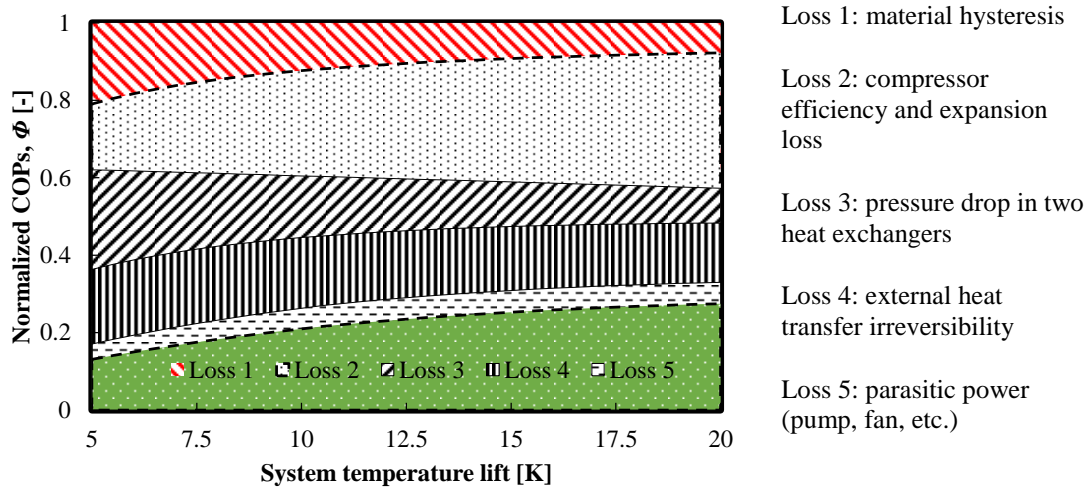
Figure 7-4: Loss analysis chart for the vapor compression cooling system.

The material hysteresis effect diminishes as the temperature lift increases, since the fraction of additional pressure, and therefore power requirement to induce evaporation and condensation is being reduced. The compressor isentropic efficiency loss and the expansion loss increase with pressure ratio of the compressor (or temperature lift). Here it is assumed that the compressor isentropic efficiency is 0.75. The expansion loss decreases the efficiency by losing the expansion work and vaporizes part of the refrigerant as a result of deviation from the isentropic expansion

184

process. The 60 kPa pressure drop effect in both the condenser and the evaporator contributes to the third loss. The cost of approach temperature is that a higher internal temperature lift is needed to drive the external heat transfer between the refrigerant and the water loops in Figure 7-1. The parasitic power consumption reduces the overall system normalized *COP* to be 0.21 under 10 K temperature lift condition.

7.2.2   Elastocaloric Cooling (Single Stage)

Elastocaloric cooling (a.k.a. thermoelastic cooling) system uses latent heat associated with martensitic transformation in shape memory alloys (SMAs). This concept is under development since 2012 (Cui et al., 2012) and is still at a very early RandD stage. There are a few groups conducting materials level studies developing higher latent heat SMAs, including Cu-Zn-Al (Manosa et al., 2009), Cu-Al-Ni (Chen et al., 2009), Cu-Al-Mn (Sutou et al., 2004), and the Ni-Ti (Tusek et al., 2015a). The reported system level study is very limited, and so far have all been based on Ni-Ti alloys. Schmidt et al. (2015) demonstrated a lab test facility without heat transfer fluid using Ni-Ti ribbon under tensile mode, and was able to achieve 4 K internal temperature lift (metal heat sink-metal heat source). A possible future design called active elastocaloric regenerator (AECR) was proposed following the AMR design, which was explored by a preliminary numerical study published recently (Tusek et al., 2015b).

Figure 7-5 shows the breakdown chart using the model developed in Chapter 3 and Chapter 6. The materials level hysteresis irreversibility limits the potential *COP* significantly in the low temperature lift range. Advances in new materials with high

185

latent heat as well as smaller hysteresis, such as Ti-Ni-Cu, can help improve the efficiency of this cooling technology. The cycle is a single stage Brayton cycle, which could potentially be reduced by a more advanced cycle. The adiabatic compression irreversibility due to Brayton cycle was also reported by Tusek et al. (2015a) as the "temperature hysteresis" using a tension test rig. The mechanical driving system is assumed to have a 70% efficiency, contributing to the third loss. The heat recovery loss increases with increasing temperature lift, since more energy is wasted due to inefficient heat recovery at higher temperature lift, so does the cyclic loss caused by the cyclic temperature variation of any parasitic thermal mass in the system, i.e. metal supporting parts and part of the heat transfer fluid. Overall, the system normalized *COP* is 0.14 at 10 K temperature lift, and reaches its maximum at 17 K.
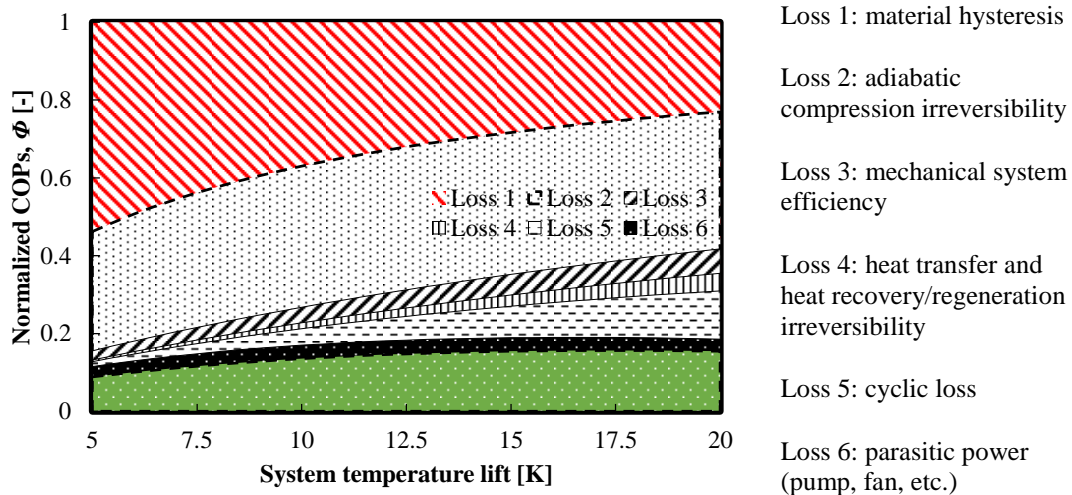
Figure 7-5: Loss analysis chart for the elastocaloric cooling system.

7.2.3 Magnetocaloric Cooling (AMR)

Modern magnetocaloric cooling using an active magnetic regenerator (AMR) design has been developed rapidly in the past two decades. In the AMR, a magnetocaloric

material is used as both the refrigerant and the regenerator. It can be reciprocating (Gomez et al., 2013) or rotary (Engelbrecht, 2008) in design and can consist of a plurality of regenerator beds. When a magnetocaloric material moves in the permanent magnet field, heat is generated during the magnetization process and is rejected by the heat transfer fluid. The material then absorbs heat when it is demagnetized. Recently, quite a few large scale AMR prototypes have been reported, including ones by Astronautics (Jacobs et al., 2014), Bahl et al. (2014), and Aprea et al. (2014).

Loss 1: material hysteresis

Loss 2: AMR internal loss

Loss 3: parasitic power (pump, motors)

Loss 4: external heat transfer irreversibility
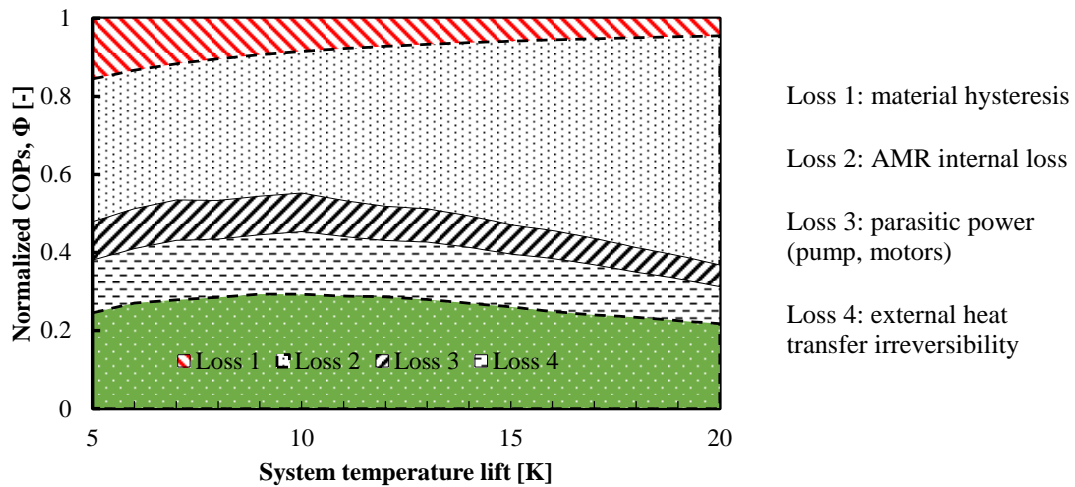
Figure 7-6: Loss analysis chart for the AMR system.

The materials level loss 1 for magnetocaloric materials are less than that of SMAs, as shown in Figure 7-6. The next stage loss is predicted by the experimental validated AMR model, which was developed by Engelbrecht (2008). This loss 2 includes all of the internal irreversibilities inside the regenerator beds. It also takes into account the magnetic field reduction from 0-5 Tesla to the 0-1.5 Tesla to estimate the COP_{mat} in a real system. Loss 3 considers a 90% efficiency for the driving motor, and 70%

efficiency for the high pressure pump to drive the AMR. The last loss factor is due to the external heat transfer loss. Ideally, the AMR itself uses water or other liquid as heat transfer fluid and no external heat transfer lost needs to be taken into account. Since AMR can only be operated under a relative small flow rate, a 2 K temperature difference is assumed as an expense of small flow rate in both the cold- and hot-side. The normalized system *COP* of AMR system is 0.29 at 10 K temperature lift condition, which is higher than the baseline vapor compression systems. In addition, the AMR normalized *COP* reaches its maximum of 0.30 at 9 K temperature lift. Overall, advances in both magnetocaloric materials and permanent magnets to induce higher magnetic field, as well as highly efficient system integration are still needed. Major drawbacks in size, mass, pumping power, and especially the cost of the magnetocaloric materials are still challenges prohibiting its market penetration.

7.2.4 Electrocaloric Cooling

Electrocaloric cooling was also recently developed as one of NIK cooling technologies. When exposed to an electric field, electric (dipole) moments in the material become oriented and the entropy is reduced. This is similar to the magnetic field induced magnetic moments change in magnetocaloric materials (Ozbolt et al., 2014). Quite a few materials candidates have been developed so far, most of which are polymers or ceramics. P(VDF-TrFE) and P(VDF-TrFE-CFE) have shown superior latent heat to other materials (Moya et al., 2015).

One challenge for this technology is the limitation in the shape of the materials. Only thin films can be applied since a high electric field is needed (hundreds of MV/m). Jia

and Ju (2012) demonstrated a laboratory scale prototype using a multi-layer ceramic electrocaloric materials, and reported maximum of 1 K system temperature lift. Gu et al. (2013) reported a chip scale electrocaloric cooling prototype using solid-state external regenerator, and the maximum system temperature lift was almost 5 K. Guo et al. (2014) developed a system model for an electrocaloric cooling system using heat transfer fluid. However, no power efficiency, parasitic pump power and other losses were reported. More studies on both materials level and system level are still needed to fully understand the potential for this NIK technology.

7.2.5 Thermoelectric Cooling

Thermoelectric cooling is a relatively mature NIK technology as compared with the aforementioned three solid-state cooling technologies. It is based on the Peltier effect, in which a temperature difference is generated by flowing current between two junctions of different materials. The dimensionless figure-of-merit, *ZT*, has been used to guide the materials development, which is around 1.0 for commercially available bulk materials (Zhao and Tan, 2014). The system integration for this NIK technology is much simpler than other NIK technologies, with no cyclic operation and no moving parts. Advances in materials development is the key to expand the applications from its niche market.

The COP_{mat} described by Eq. (7-17) already accounts for a few materials level irreversibility, i.e. additional voltage to compensate the resistance, parasitic heat generation by resistance, and parasitic heat conduction from the hot junction to the cold junction. This is the reason why the materials level *COP* is the lowest among all

189

NIK technologies, as shown in Figure 7-7 ($ZT = 1.4$). The possible system integration loss is less than other NIK technologies. The external heat transfer loss caused by the water chiller approach temperature and the parasitic power consumption attributes to only 0.47 exergetic inefficiency, which places the Φ_{sys} of thermoelectric cooling at the top of the list.

Loss 1: material hysteresis

Loss 2: external heat transfer irreversibility

Loss 3: parasitic power (pump, fan, etc.)
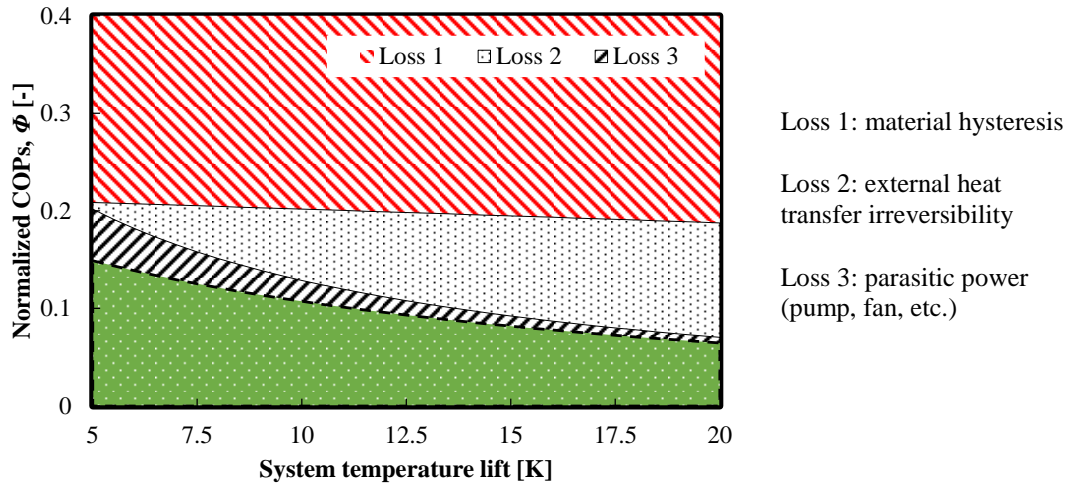
Figure 7-7: Loss analysis chart for the thermoelectric cooling system ($ZT = 1.40$ for Bi-Sb-Te).

7.2.6 Stirling/Brayton Cooling Cycles

Stirling refrigerators are mainly used for cryogenic applications in industry. The concept of Stirling cycle is old, and practically there were many modified cycles and machines built similar to the original concept. A good example is the Gifford-McMahon (G-M) cryocooler (McMahon and Gifford, 1960). Another heat activated version of a Stirling cooler is the Vuilleumier heat pump listed in Figure 1-1, which is driven by fuel heat to create cooling/heating based on a coupled Stirling engine and heat pump (Carlsen, 1989). Working fluid for Stirling refrigerators can be assumed to

be an ideal gas under its working temperatures and pressures, including the most widely used helium, air, hydrogen, water, and sodium-potassium eutectic (Thombare and Verma, 2008). The major drawback of Stirling refrigerators is the complicated mechanical-thermal coupling design they required.

Loss 1: regenerator exergy loss due to pressure drop

Loss 2: compressor/expander efficiency

Loss 3: regenerator, phase and external heat transfer irreversibility

Loss 4: parasitic power (pump, fan, etc.)
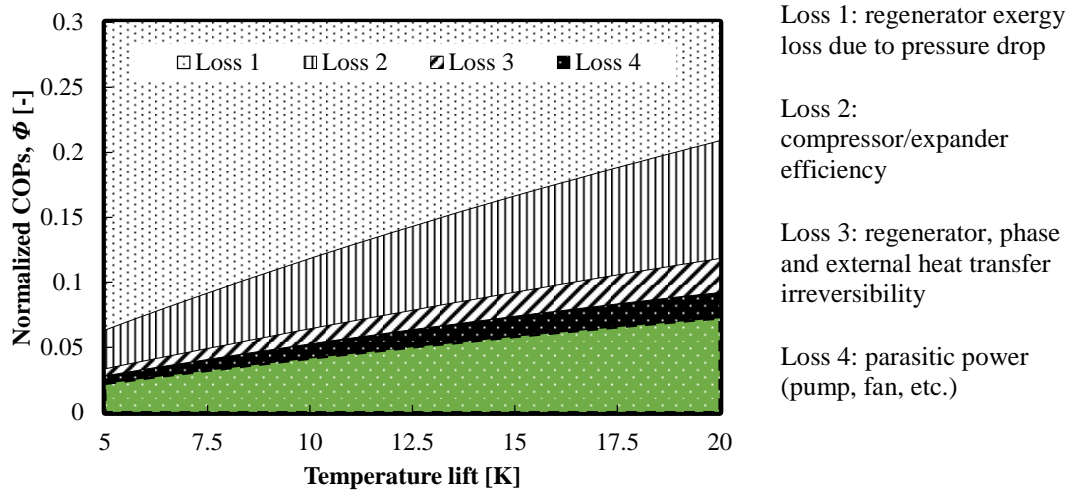
Figure 7-8: Loss analysis chart for the Stirling cycle.

The model and the exergetic efficiency analysis developed by Razani et al. (2010) were used in this study. Figure 7-8 shows the breakdown chart for the Stirling cycle. As indicated in Table 7-2, there is no materials level loss by using the ideal gas laws. However, the first stage loss caused by the pressure drop across the regenerator severely reduces the exergetic efficiency, especially under the small temperature lift conditions, which is consistent with findings of the original study (Razani et al., 2010). The pressure ratio across the regenerator was assumed to be 0.8 based on that study. The second loss is due to the compressor and expansion efficiency, which were assumed to be 0.8 and 0.9, respectively. The regenerator effectiveness, non-ideal phasing and external heat transfer contributes to the next stage loss. The regenerator

effectiveness contribution is relatively small under low temperature lift conditions as compared to solid-state NIK technologies, since the non-dimensional latent heat for helium is much higher than those of solid-state refrigerants, according to Table 7-2. Another significant difference is the temperature lift associated with the maximum system normalized *COP*. Helium under the Stirling cycle reaches the maximum system normalized *COP* of 0.15 at 64 K.
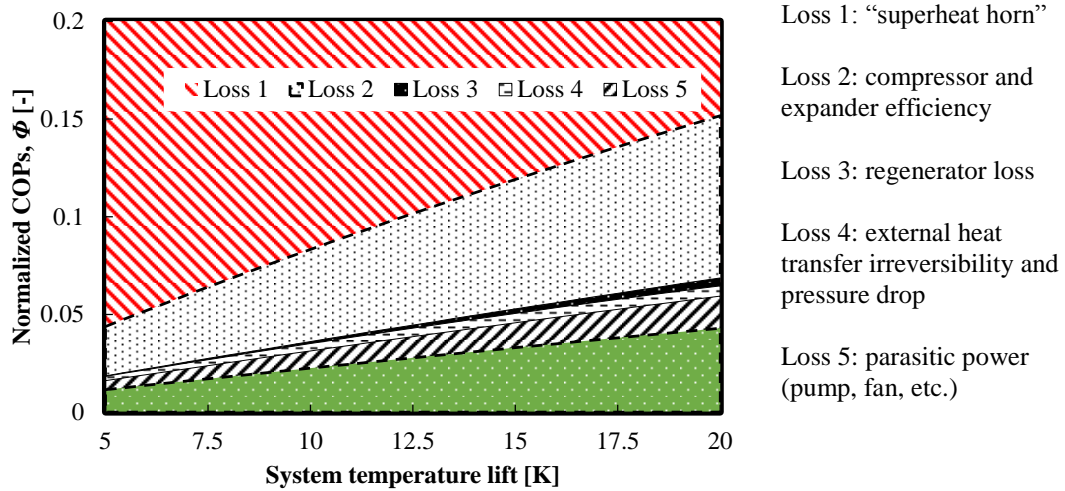
Figure 7-9: Loss analysis chart for the Brayton cycle.

With air as the refrigerant, Figure 7-9 presents the *COP* breakdown chart for Brayton cycle, following the model proposed by Ni et al., (1999) and assumes the compression ratio to be 3. The first loss on the materials level, using the ideal gas equation-of-state, is caused by the additional temperature difference between the compressor discharge and the heat sink. If the application has a variable temperature heat sink and heat source such as a domestic hot water tank with a finite flow rate, the performance of a Brayton cycle would be significantly better. In addition, for higher temperature lift applications, the materials level normalized *COP* also increases,

which reaches 0.6 around the temperature lift of 200 K. Assuming the compressor efficiency of 0.8, and expansion efficiency of 0.9, the mechanical losses contribute to another significant portion of *COP* reduction. The overall trend is similar to that of a Stirling cycle. The maximum system normalized *COP* reaches its maximum of 0.15 at temperature lift of 130 K.

7.3 *Discussions*

Table 7-3 summarizes the results from the previous two sections. The three left columns were evaluated under the temperature lift of 10 K as specified by Eqs. (20-21). The three right columns show the maximum Φ under their corresponding temperature lift conditions. Based on the summary, the following observations can be deduced.

Table 7-3: Quantitative comparison of NIK cooling technologies.

Technology	Φ_{mat}	Φ_{sys} @ $\Delta T_{lift} = 10$ K	$\Phi_{mat}\cdot\Phi_{sys}$	$\Phi_{mat,max}$ @ ΔT_{lift}	$\Phi_{sys,max}$ @ ΔT_{lift}	$(\Phi_{mat}\cdot\Phi_{sys})_{max}$ @ ΔT_{lift}
Vapor compression (baseline)	0.88	0.24	0.21	0.94 @ 37 K	0.30 @ 25 K	0.28 @ 26 K
Elastocaloric (single stage)	0.63	0.21	0.14	1.00 @ ∞ K	0.22 @ 13 K	0.16 @ 17 K
Magnetocaloric (AMR)	0.91	0.32	0.29	1.00 @ ∞ K	0.33 @ 9 K	0.30 @ 9 K
Electrocaloric	0.41	n/a	n/a	1.00 @ ∞ K	n/a	n/a
Thermoelectric	0.20	0.53	0.13	0.21 @ 5 K	0.70 @ 5 K	0.15 @ 5 K
Stirling	1.00	0.04	0.04	1.00	0.12 @ 64 K	0.12 @ 64 K
Brayton	0.08	0.27	0.02	1.00 @ ∞ K	0.32 @ 82 K	0.15 @ 130 K

The materials *COPs* for magnetocaloric, electrocaloric, and elastocaloric increases monotonically with temperature lift, since the hysteresis irreversibility is a material constant. For vapor compression, however, the materials irreversibility is also effected by the "superheat horn" (Radermacher and Hwang, 2005), which also

increases with the increasing temperature lift. Therefore, the vapor compression material exergetic efficiency has a peak at 37 K temperature lift. In terms of thermoelectric cooling, the parasitic heat loss from conduction scales linearly with the temperature lift, and therefore, it favors small temperature lift applications.

Since the evaporation-condensation process is highly reversible, only the magnetocaloric materials and ideal gas under a Stirling cycle are competitive to the baseline. Materials advances for elastocaloric cooling, electrocaloric cooling and thermoelectric cooling are desirable.

Thermoelectric cooling is simple to integrate on the system level, and the Φ_{sys} of thermoelectric cooling is the best among all evaluated NIK technologies.

The magnetocaloric cooling system is the only NIK technology superior to the baseline.

The four evaluated solid-state cooling technologies are only efficient under low temperature lift conditions, based on the last column in Table 7-3 (the temperature lift when the maximum normalized system COP is reached). Therefore, they would be better to be applied for small temperature lift applications, unless a high efficient cascaded system integration is realized.

Gaseous cycles are more efficient under high temperature lift conditions, as seen in the last column in Table 7-3. They have been used for cryogenic applications in the past. Significant modifications have to be made, in order to fit the small and moderate temperature lift applications with a better system efficiency.

Elastocaloric cooling has potential due to higher latent heat when compared with other solid-state NIK technologies. More research efforts are still needed to improve

its system efficiency, such as a hybrid Stirling cycle or a regeneration design similar to AMR. Both its COP_{mat} and the temperature lift for the maximum system normalized COP indicate the potential of elastocaloric cooling to become competitive for small and medium temperature lift applications.

More system integration research are urgently needed to assess the system level performance of electrocaloric cooling. Materials advances are also needed to reduce the hysteresis and enhance the latent heat.

7.4 *Chapter Summary and Conclusions*

The COP breakdown analysis method was proposed in this study as a quantitative comparison for NIK cooling technologies. First, comparing the materials level performance for each NIK refrigerants using only the materials properties under the specified cycle path provides insight on the limit for each NIK technologies assuming the system can be ideal. Then the system integration losses were taken into account for the same operating conditions for a fair comparison. It was found that from both the materials and the system perspective, magnetocaloric cooling is so far the only NIK technology better than the vapor compression cooling. The four evaluated solid-state NIK technologies are more beneficial for small temperature lift applications, among which the elastocaloric cooling could be potentially applicable for a wider temperature lift range with advances in both materials and system integration. The evaluated two gaseous NIK technologies are superior in high temperature lift applications, and efforts in major components modifications are needed to increase their performance if medium temperature lift applications are required.

Chapter 8: Thermoelastic Cooling: Revisiting and Prospects

The previous chapters have already addressed different aspects of developing a thermoelastic cooling system. A few performance indices are proposed in this chapter to guide the future work.

8.1 *Ideal Thermoelastic Cooling System*

The first metric introduced in this chapter is the time constant to evaluate the heat transfer rate from the solid material to the HTF, as shown in Eq. (8-1). More details regarding this time constant can be found in Appendix D.

$$\tau_{SMA} = \frac{2}{\frac{1}{t_2} + \frac{1}{t_1} \cdot (1+TMR) - \sqrt{\left(\frac{1}{t_2} - \frac{1}{t_1} \cdot (1-TMR)\right)^2 + \frac{4TMR}{t_1^2}}} \tag{8-1}$$

where t_1 and t_2 are two time constants defined in Eq. (8-2) and Eq. (8-3), and *TMR* is defined in Eq. (8-4).

$$t_1 = \left(\rho c_p\right)_{SMA} \cdot h^{-1} \cdot \left(\frac{A}{V}\right)^{-1} \tag{8-2}$$

$$t_2 = \frac{V_f}{\dot{V}_f} \tag{8-3}$$

In Eq. (8-2), the time constant is similar to that of a lumped system problem in any heat transfer textbooks (Bergman, 2011), when assuming the fluid temperature remains constant over time. Eq. (8-3) is the time constant measuring the time for any fluid particle to travel throughout the SMA bed. If t_2 approaches zero, it means that

196

the particle can flow through the bed infinitely fast.

In fact, Eq. (8-1) degrades back to Eq. (8-2) under the infinity flow rate limit, when t_2 approaches zero. This limit is shown in Eq. (8-4). This is also in consistent with the fact that the fluid temperature converges to the constant when flow rate reaches infinity.

$$\lim_{t_2 \to 0} \tau_{SMA} = t_1 \tag{8-4}$$

The second metric is shown in Eq. (8-5). It measures the thermal mass ratio between the SMA bed and the dead thermal mass caused by the fluid stored inside the SMA bed.

$$TMR = \frac{\left(mc_p \right)_{SMA}}{\left(mc_p \right)_{HTF,DTM}} \tag{8-5}$$

Eq. (8-6) shows the third metric, defined as the thermal mass ratio between the SMA bed and the HTF inside each HR pipe, for the two-beds with HR system configuration. In fact, Eq. (8-6) can be also expressed as a function of TMR and $l*$ (defined in Eq. (4-14)), as shown in Eq. (8-7).

$$TMR_{HR} = \frac{\left(mc_p \right)_{SMA}}{\left(mc_p \right)_{HTF,\text{regenerator}}} \tag{8-6}$$

$$TMR_{HR} = TMR \cdot \frac{l*}{1-l*} \tag{8-7}$$

The last metric is shown in Eq. (8-8). It is a phase change uniformity index. According to Eq. (8-9), the solid material particles have a high level (equals to 1) $\sigma*$ if phase change has occurred locally, i.e. $\sigma \geq \sigma_{\text{sat}}(T)$. The uniformity index reaches one

only under the condition that the entire SMA bed undergoes full phase change.

$$\Psi = \frac{\iiint_V \sigma^* dV}{V} \qquad (8\text{-}8)$$

$$\sigma^* = \begin{cases} 0 & \text{if} \quad \sigma < \sigma_{sat}(T) \\ 1 & \text{if} \quad \sigma \geq \sigma_{sat}(T) \end{cases} \qquad (8\text{-}9)$$

Based on our knowledge from the previous chapters, a smaller heat transfer time constant in Eq. (8-1) is preferred, since it enables more efficient heat transfer and heat recovery, as well as allowing more frequent cycles and enhances the cooling capacity per unit SMA mass.

Figure 8-1 plots the relation between the heat transfer time constant versus both the COP and the SCP. As expected, a smaller heat transfer time constant is preferred for both COP and SCP. A smaller heat transfer time constant can be achieved by the suggested three designs: tube-in-tube (Chapter 6), thinner tubes and smaller tubes. For the tube-in-tube design, the surface to volume ratio is increased as well as the *TMR*. Only the surface to volume ratio is increased for the thinner tubes design, while the OD of nitinol tubes is constant and the fluid dead thermal mass is adjusted by insertion blocked area ratio. The smaller tube design increases both the surface to volume ratio and the *TMR* as well. There are also tradeoffs by applying these three design candidates. The tube-in-tube design introduces more complexity in flow configuration and the loading head design to guarantee that there is no flow for the inside SMA tube. When the mass of the SMA is fixed, it implies that the total tube number is increased by using both smaller tubes and thinner tubes, which could enlarge the profile of the entire system. A comprehensive analysis needs to consider

both the benefit of reducing the heat transfer time constant and the tradeoff hidden behind those novel designs.
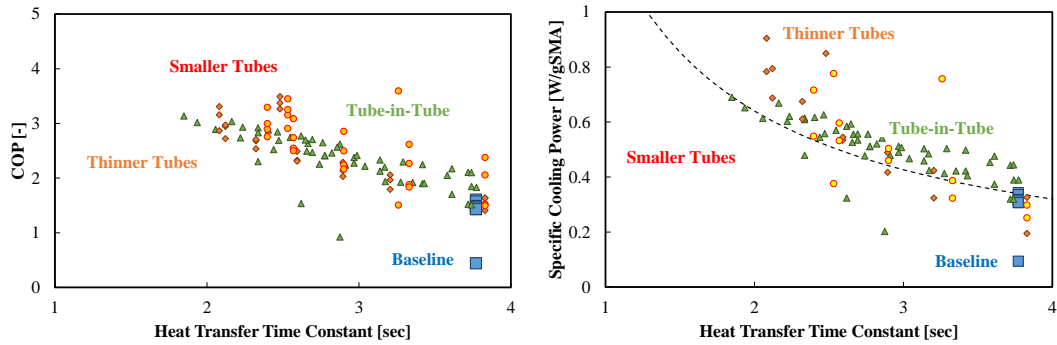
Figure 8-1: Illustration of varying the heat transfer time constant by different approaches to improve COP (nitinol tubes).
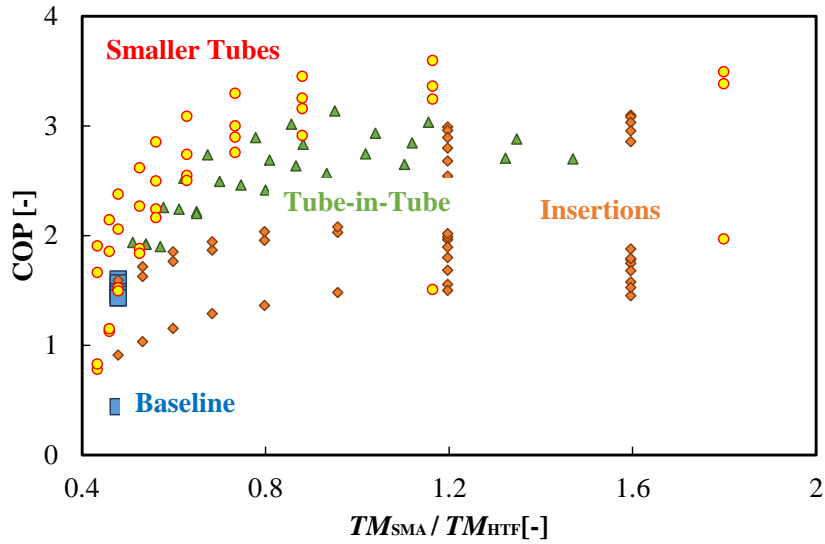
Figure 8-2: Illustration of varying the thermal mass ratio between SMA and the HTF by different approaches to improve COP.

The second metric needs to be optimized, since a small *TMR* results in high cyclic loss (Chapter 3), and a high *TMR* dominates and increases the heat transfer time constant in Eq. (8-1). The baseline *TMR* is smaller than the optimum *TMR*, as

indicated by Figure 8-2, and therefore needs to be increased. As shown in Figure 8-2, the COP can be improved significantly when the *TMR* is increased from 0.47 (baseline) to around 1, and then the benefit starts to saturate and eventually vanish when *TMR* reaches 2. The most straightforward way to increase *TMR* is to simply fix the nitinol tubes and block the fluid dead thermal mass by insertions. It is also a secondary effect when smaller tubes or tube-in-tube design are introduced as aforementioned.

The second metric can be extended to a more general metric using the entire DTM involved in the system, as shown in Eq. (8-10), where term *i* indicates each component contributing to DTM, such as HTF in Eq. (8-5), the steel holder and the loading head, which are insulated as much as possible in Chapter 6, and any HTF pipe walls.

$$TMR_{DTM} = \frac{\left(mc_p\right)_{SMA}}{\sum_i \left(mc_p\right)_{i,DTM}} \tag{8-10}$$

Unlike *TMR*, this extended metric *TMR*DTM needs to be maximized by all means necessary, as has been demonstrated by the improvement designs in Chapter 6. In fact, the cyclic loss mentioned through this thesis should be a function of *TMR*DTM and the cycling frequency, which determines the performance curve slope in Figure 5-11. The three simulation cases share the identical DTM and operating frequency, while the active TM of SMA increases with tube quantity in each bed. Consequently, the slope of the 7 tubes case is deepest since it has the worst *TMR*DTM among three cases. Figure 8-3 discusses more options by varying both the *TMR*DTM, operating

frequency and system configuration. Reducing the TMR_{DTM} results in a deeper slope, and consequently has a lower maximum ΔT_{lift}. When the operating frequency increases, the SCP increases as well. The tradeoff is the ΔT_{lift} reduces due to a less efficient HR and HT processes. There is one possible system configuration using an advanced cascaded cycle called active elastocaloric regenerator (AECR), as proposed by Tusek et al. (2015b). By cascading the SMA with AECR cycle, the HT and HR are conducted simultaneously, allowing a significantly higher cycling frequency and SCP. Cascaded system also provides a higher ΔT_{lift}. However, the system COP may become lower, since only partial SMA in the cascaded configuration exports useful cooling and heating to the heat source and heat sink, respectively, while the driver consumes the same power as a single-stage system.

(a) SCP - ΔT_{lift} chart   (b) SCP – COP chart
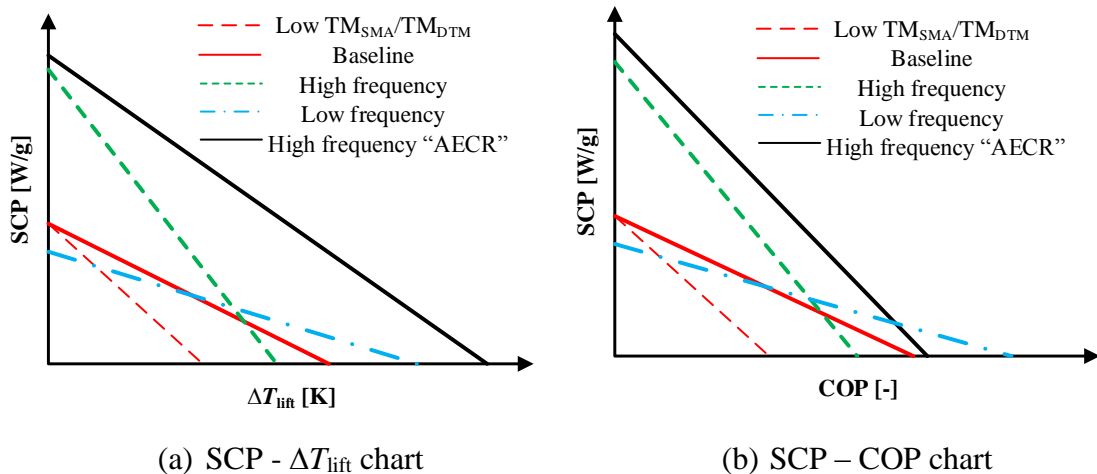
Figure 8-3: Performance curve variation as a result of changing the TMR, the operating frequency and system configuration.

The third metric, the TMR_{HR} needs to be optimized as well. A higher TMR_{HR} means that the regenerator thermal mass becomes relatively smaller compared with that of the SMA. This implies that a shorter HR is achievable since less time is needed to

circulate inside the HR pipes between the two SMA beds. However, the tradeoff is that the HR efficiency drops as a result of reducing the thermal mass of the HTF stored within the HR pipes, as indicated by Figure 4-13 and Eq. (8-7). Although Figure 4-13 only focuses on the HR process efficiency, the entire system COP also increases with a smaller l^* and smaller TMR_{HR}, as shown in Figure 8-4. It should be noted that the baseline TMR_{HR} is around 0.5.
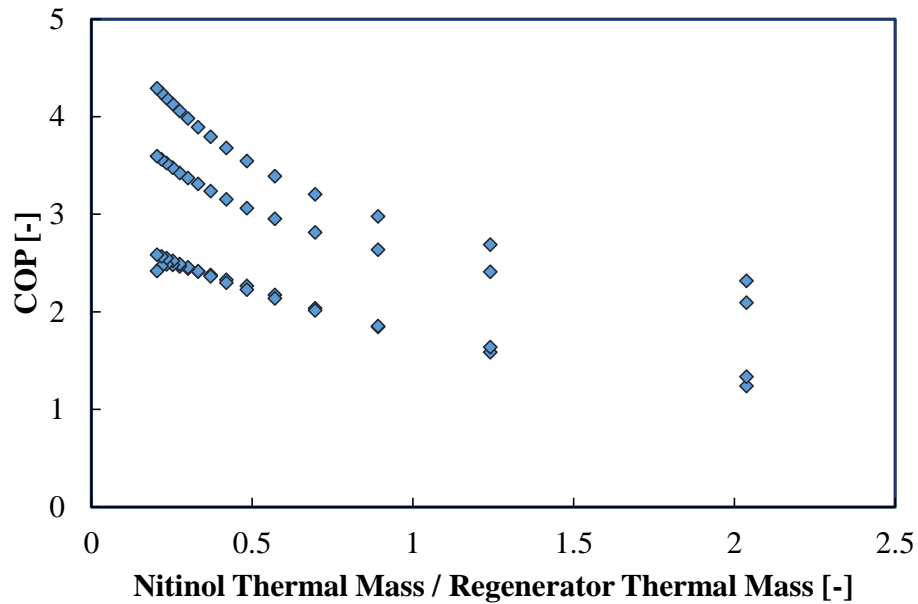
Figure 8-4: Illustration of varying the thermal mass ratio between the SMA and the regenerator HTF (heat recovery pipes) to improve COP.

The last metric defined in Eq. (8-8) needs to be maximized, i.e. approaching the upper boundary 1. For a single tube/wire under uniaxial compression or tension mode, the axial stress is uniform enough to assume a complete phase change within the SMA, i.e. uniformity index equals to one. It does not deviate much from one if a 2D configuration of the tube/wire is used under uniaxial loading. However, this index

may deviate from one significantly if 3D structures are involved without opportunity to apply uniaxial loading. For example, Figure 8-5 shows the stress distribution for a 3D SMA porous structure, where color uniformity represents the stress uniformity. Note that the compression force is applied from top and bottom sides. The stress difference from the plot can be as large as four times, which means that the maximum stress domains undergo phase change when they exceed the stress threshold, while the majority of the SMA structure is still below the threshold. Therefore, 3D structure may require more sophisticated and advanced loading settings, such as asymmetric loading (tension + compression from different sides for example) in order to maximize the uniformity index.
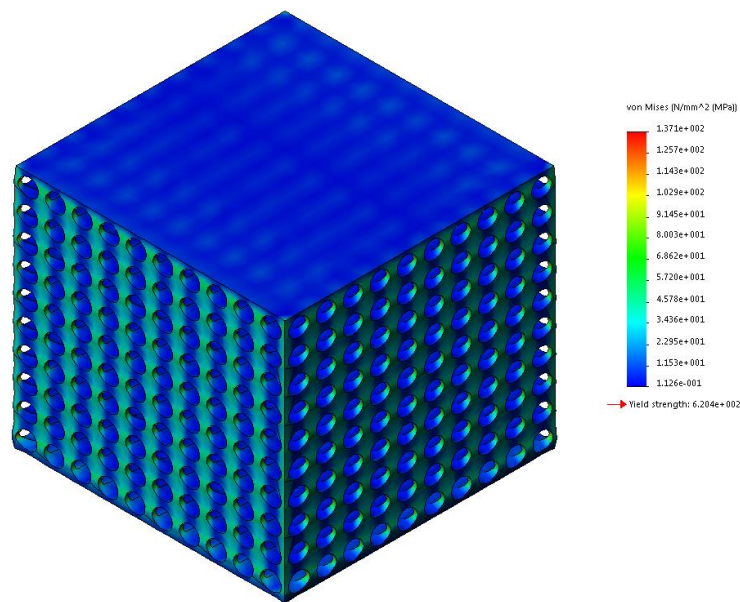
Figure 8-5: Illustration of the von Mises stress distribution in a 3D SMA porous structure.

Table 8-1 is an evaluation summary using the above mentioned four indices for a few novel design candidates. Some of the design candidates were proposed in Chapter 6,

and the remaining are introduced in Figure 8-6. In terms of the first three designs, i.e. tube-in-tube design, smaller tubes and thinner tubes with insertions, they all achieve higher surface to volume ratio as well as reduce the HTF dead thermal mass. Therefore, the first index is reduced and the second index is increased as compared to the baseline. The uniaxial loading for these three designs guarantees that the uniformity index remains approximately one.

Table 8-1: Beneficial assessment of a few novel SMA layouts using the proposed four metrics.

Goal	Index 1: Eq. (8-1) Minimizing	Index 2: Eq. (8-5) Optimizing*	Index 3: Eq. (8-7) Optimizing**	Index 4: Eq. (8-8) Maximizing
Tube-in-tube (rod-in-tube)	√	√	√	√
Thinner tubes + insertions	√	√	√	√
Smaller thinner tubes	√	√	√	√
2D honeycomb structure	√		√	√
2D porous structure	√	√	√	√
2D plate structure	√	√	√	√
3D porous structure	√	√	√	
3D lattice structure + air		√	√	

*: needs to increase from the baseline design level.
**: needs to decrease from the baseline design level.

The 2D honeycomb structure is shown in Figure 8-6 (a). It can be either a bulk material with hexagon holes, or simply a 2D layout of hexagon shaped tubes. The motivation to change from round tube to hexagon shaped tubes is to improve the structure stability when loaded by avoiding the void spaces and increasing the inter tubes contact area. Depending on the geometries, the dead thermal mass of the HTF increases under most cases, and therefore the second index decreases compared to the baseline, which is not desirable. The surface to volume ratio increases and therefore

the 1st index reduces.
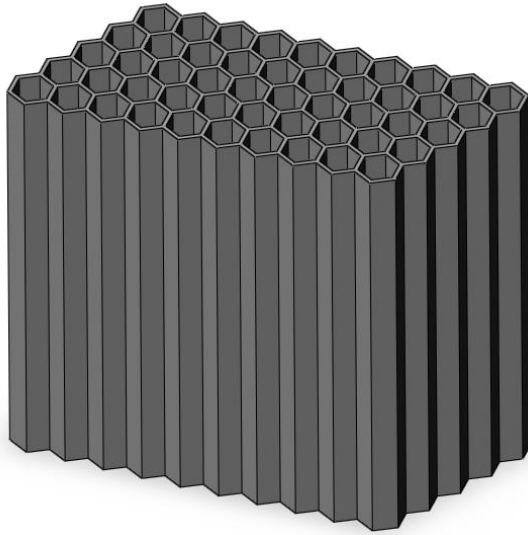
(a) 2D honeycomb structure
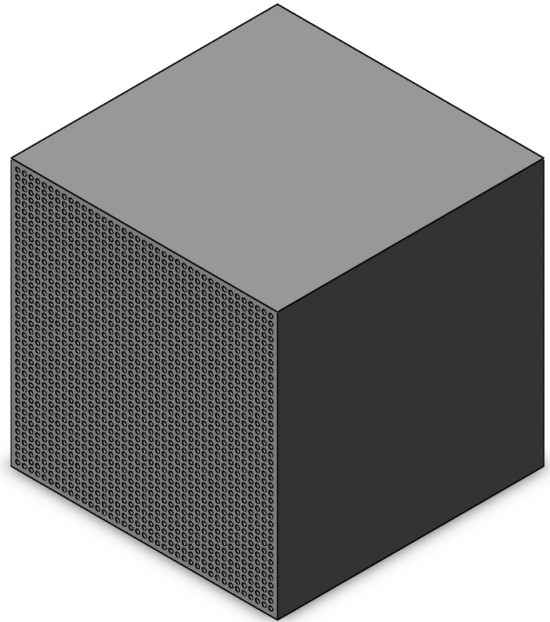
(b) 2D porous structure
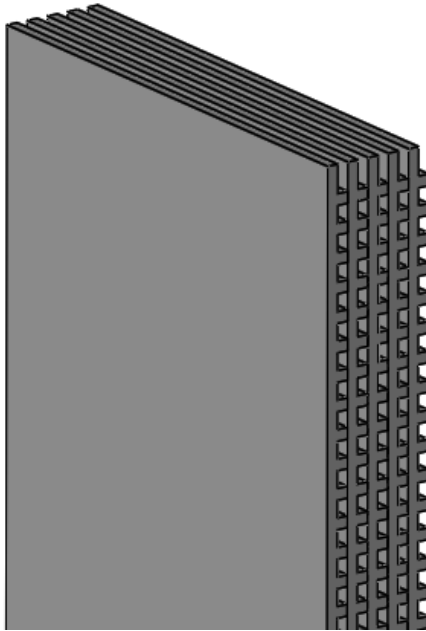
(c) 2D plate structure
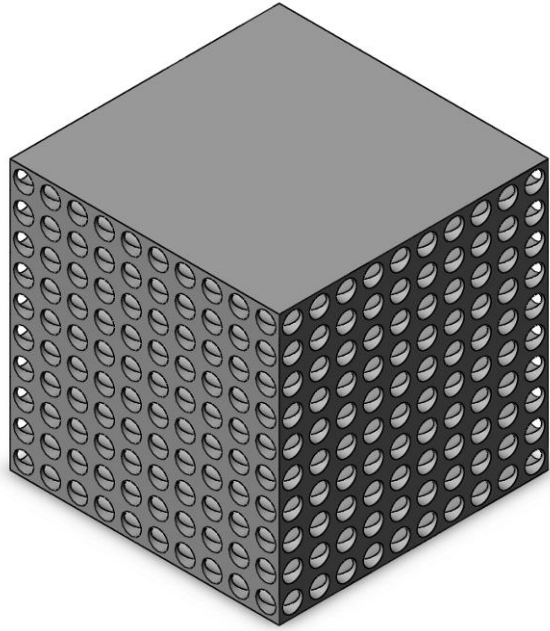
(d) 3D porous structure
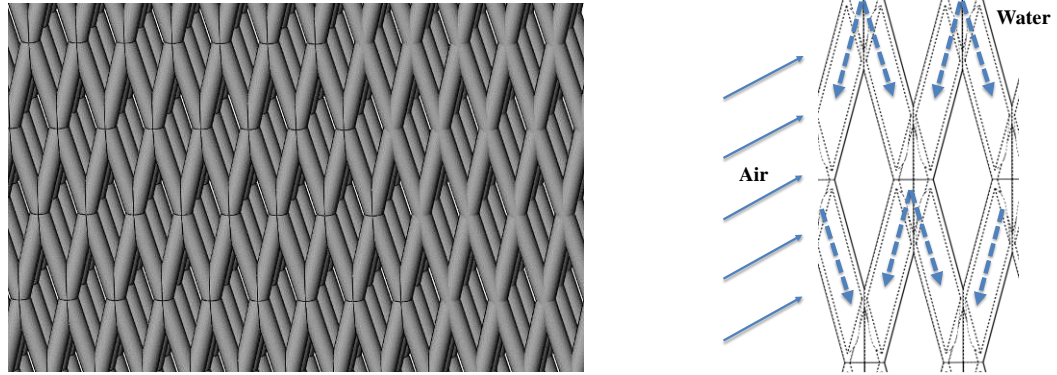
(e) 3D lattice structure + air as HTF

Figure 8-6: Drawing of a few novel SMA structure design candidates.

Figure 8-6 (b) shows the drawing of the 2D porous structure. It can be a bulk SMA material with parallel tiny through holes in one direction, regardless of the shape of the holes (circle, diamond, triangle, hexagon, etc.). This layout is an integration of the small tubes design, and therefore shares the same conclusion with it.

When compressing a SMA material, the loading force is only dependent on the cross-section area on the loading direction, and is independent of the material length, with the tradeoff of increasing the stroke or displacement of the loading system. Therefore, if minimizing the loading system maximum force (profile) is a concern, reducing the cross-section area can be introduced by Figure 8-6 (c). Plates are directly compressed from the vertical direction. The "fins" in between the two plates are used to enhancing the heat transfer as well as increasing stability of the structure by eliminating the buckling. HTF flows within the channels formed by neighboring plates and the "fins". The 1st index can be reduced by thinner plates, with a tradeoff by losing structure stability. The 2nd index increases by tuning the "fin" height.

The 3D porous design is shown in Figure 8-6 (d). The major difference between the 3D and the 2D cases is that the holes exist on two directions. The loading direction

can be either vertical or horizontal. As discussed in Figure 8-5, the single direction

loading results in non-uniform stress distribution. Therefore, the uniformity index is

lower than other previous candidates, unless design improvements are made. Figure

8-6 (e) shows the 3D lattice structure design using air as the heat transfer fluid. It

should be noted that the structure is hollow inside to allow water or other liquid HTF

flowing inside as heat recovery medium. The major motivation to use air directly as

HTF is to save a water-air heat exchanger to minimize excessive temperature lift

required for this heat exchanger. Similar to the 3D porous structure, the lattice layout

also faces the same low uniformity index challenge. Another difficulty is that

choosing air as HTF significantly reduces the heat transfer time constant. Since air

has a low heat transfer coefficient h, and also less density, the *TMR* term becomes a

few magnitudes higher than using liquid phase HTF. As shown by Appendix D Eq.

(D-10), the time constant increases significantly as well with *TMR*.

A more intuitive illustration is shown in Figure 8-7. Here, a few different HTF

options are plotted onto the *TMR*-heat transfer time constant chart. There are three

clusters: water and brines (water salt solutions), other non-water liquids, and air. The

brines and water have similar ρc_p, and therefore are close to each other. Other liquids

have less specific heat compared with water. For air, the ρc_p term is three magnitude

less than that of water. The *TMR* of air is large, which is preferred from the system

COP perspective, since it reduces the cyclic loss. However, the heat transfer time

constant is even beyond 100 seconds. Nevertheless, a compromise has to be made

between losing the system frequency and cyclic loss.
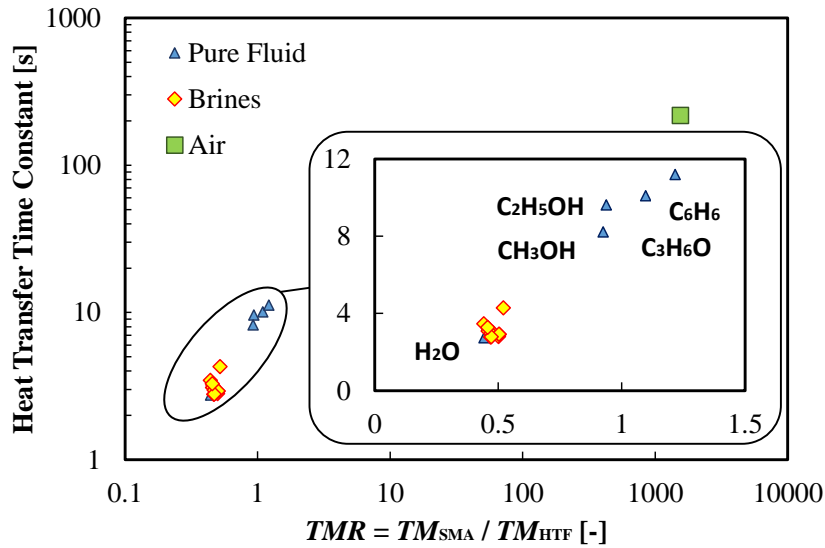
Figure 8-7: Choosing the HTF based on the first two metrics defined in Eq. (9-1) and Eq. (8-5).

8.2 *Performance Assessment Methodology*

Another remaining problem is how to assess the thermoelastic cooling system. The vapor compression cooling systems have a relation between the capacity/COP with the ambient temperature (or system temperature lift). Nevertheless, according to Figure 6-13, thermoelastic cooling has one more degree of freedom, where the COP and capacity are not fixed under the same operating temperature levels (system temperature lift).

Figure 8-8 is a comprehensive summary of the related three variables: *COP*, cooling capacity and the system temperature lift (ΔT_{lift}). There are four extreme points on the 3-D performance domain, i.e. the maximum *COP* and maximum cooling capacity points on the *COP*–Q_c plane, the maximum achievable temperature lift $\Delta T_{\text{lift,max}}$ and the origin point. The two projections in Figure 8-8 have been used in the previous

chapters to evaluate the system performance. The projection on COP–ΔT_{lift} plane has been used in Figure 3-9. The COP under 0 K ΔT_{lift} and the maximum ΔT_{lift} equations can be found in Eq. (3-27) and Eq. (3-28), respectively. The projection on COP–Q_c plane under 10 K temperature lift was shown in Figure 6-13, where the Pareto line represents the optimum performance states under a specific ΔT_{lift}. The third projection on Q_c–ΔT_{lift} plane was used in Chapter 5 to evaluate the performance of the world's first compressive thermoelastic cooling prototype, which is not shown in Figure 8-8.
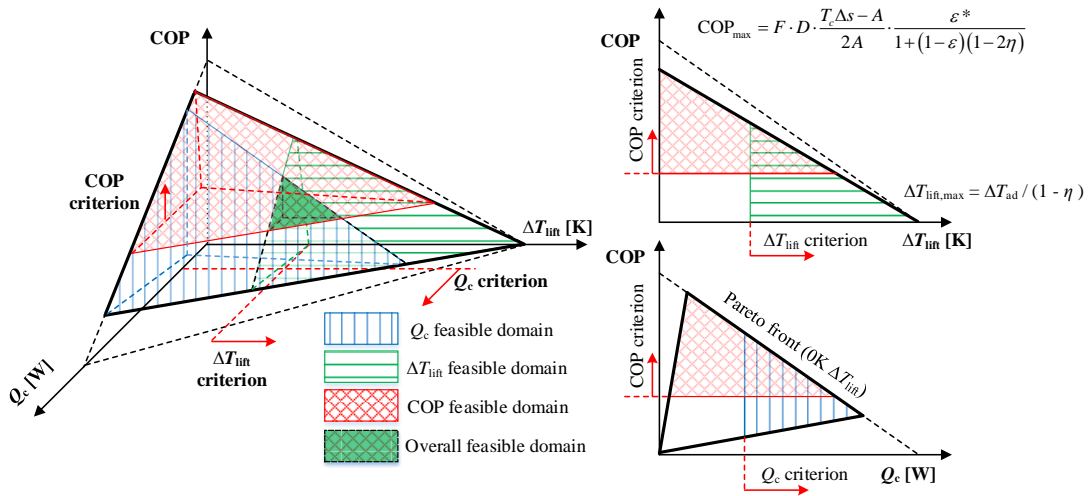
Figure 8-8: Illustration of the performance assessment diagram and its projections on the COP-cooling capacity plane and the COP-temperature lift plane.

The Pareto surface on top represents those states with best performance when the operating conditions vary, which is also an assembly of the Pareto front lines on the COP–Q_c chart with varying ΔT_{lift}. The three extreme points are located on the Pareto front, and therefore, can be used to simply describe the performance of a thermoelastic cooling system. The system's performance states could be anywhere on

or underneath the Pareto surface. When a system is rated, a minimum system Q_c, temperature lift, and *COP* are usually specified. The three different fills in Figure 8-8 represents the three feasible domains when the above mentioned three minimum constraints are applied, respectively. The green domain is the overall feasible domain when all three constraints are considered. When compared with the three extreme states, i.e. COP_{max}, $Q_{c,max}$ and $\Delta T_{lift,max}$, the values in the green feasible domain is much less. This indicates that the system needs to be sized under the constrained ΔT_{lift} and targeting *COP* and Q_c during the design process, not just the extreme Q_c and ΔT_{lift}.

$$COP_{max} = F \cdot D \cdot \frac{T_c \Delta s - A}{2A} \cdot \frac{\varepsilon *}{1 + (1-\varepsilon)(1-2\eta)}$$

$$\Delta T_{lift,max} = \Delta T_{ad} / (1 - \eta)$$
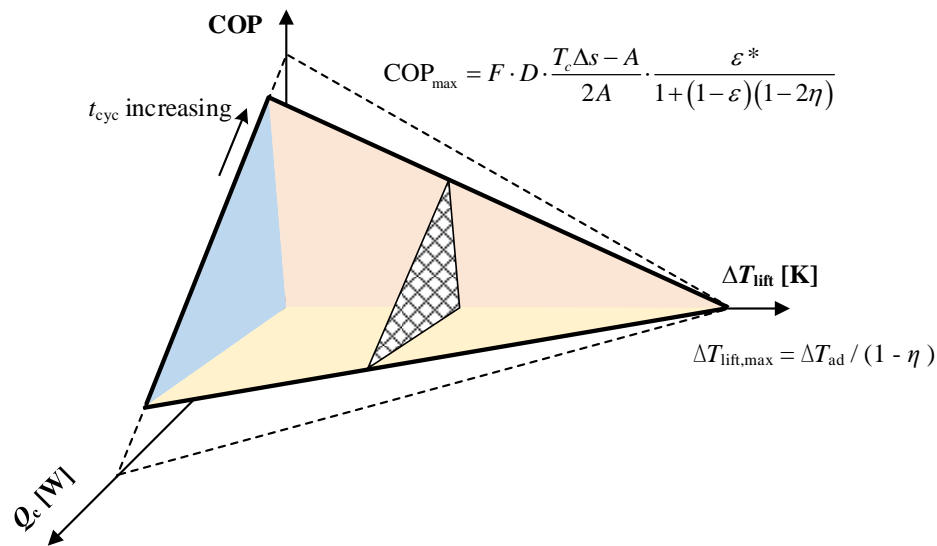
Figure 8-9: Illustration of the performance assessment diagram and the performance map between COP and cooling capacity under the constant system temperature lift.

As to a potential commercial product, for example a window AC unit, usually the industrial standards (AHRI 210/240) only rate the system's performance under a single or a few well defined ΔT_{lift}. The 3-D performance domain is now simplified to

a 2-D problem under such circumstances, as illustrated in Figure 8-9. Only the highlighted cross-section under the determined ΔT_{lift} is of interest now.

Overall, the 3-D performance assessment diagram is important during the design, testing and performance evaluation process. The three extreme points are useful and simple information to evaluate the system's performance. When the standard ΔT_{lift} is specified, a projection on the 2-D COP–Q_c plane may be used.

Chapter 9:   Conclusions and Future Work

This dissertation reveals that thermoelastic cooling systems, under current research status, is not as efficient as the conventional vapor compression cooling systems. But this research shows that it is technically viable, and therefore offers an environmental friendly technical alternative to those vapor compression systems, despite the lack of this energy efficiency benefit, which could be potentially improved and finally solved in the future.

(1) The material level irreversibility accounts for a major performance degradation, which is corresponding to 40% ~ 50% efficiency loss for the state-of-the-art elastocaloric material, Ni-Ti alloy. The simple analytical material COP equation derived in this dissertation identifies hysteresis as the source of material level irreversibility. Materials may be operated under different proposed cycles, including the Stirling cycle, Brayton cycle, a hybrid cycle, or cascaded Brayton cycle with an active regenerator design. The simplest cycle from design is the single stage Brayton cycle, which contributes to an intrinsic cycle loss depending on the material properties, corresponding to an additional 20% ~ 25% efficiency loss.

(2) The simple analytical system COP equation and method is useful to study the effect of varying material properties and a few system level parameters. More importantly, a dynamic model considering some of the system level losses is needed to assist prototype design and explore the potential performance of a real thermoelastic cooling system. The elastocaloric effect can be modeled as a heat

source term in the conduction energy equation. When accounting for the mechanical system inefficiency (9% efficiency loss), heat transfer and heat recovery inefficiency (6% efficiency loss), cyclic loss resulted from parasitic parts and dead thermal mass of HTF (6% efficiency loss), and pumps power consumption, the system overall COP is 1.7 under 10 K temperature lift, corresponding to 0.06 overall efficiency.

(3) The heat recovery process is one key solution to enhance the system performance. A counter-flow in time scale thermos-wave HR method is proposed based on the analogy to the counter-flow heat exchanger. The HR method is then validated by experimental and numerical results. Although 100% efficiency is achievable in theory, under the realistic physical constraints of cycling frequency, Ni-Ti tube geometries and physical properties of HTF, 60% ~ 80% HR efficiencies are practically achievable.

(4) Based on the knowledge developed in this thesis, the world first compressive thermoelastic cooling prototype was designed, fabricated and tested. The Ni-Ti tubes were arranged in a hexagonal layout in two conjugated beds to achieve work recovery. The system was driven by a screw-jack powered by two motors. The prototype has been modified, upgraded and tested for more than a year, to reduce the friction and cyclic heat loss by all means necessary. The maximum water-water system temperature lift achieved so far is 4.2 ± 0.4 K, and a separate test showed that the maximum measured cooling capacity is 65 ± 10 W. Unfortunately, the performance is still limited by the huge parasitic loss caused by the HTF friction heat dissipation, conduction loss to the metal parts in the system

and dead thermal mass. Nevertheless, the proposed cycle and system configuration functions normally as expected, and the dynamic model was also validated by the data.

(5) To explore the performance improvement potentials, a few novel design candidates were proposed and a few simplest operating conditions were tuned by the genetic-algorithm. With the PEEK-tube design, tube-in-tube design, and by optimizing the operating parameters, the system COP could be enhanced to 4.1, corresponding to 0.14 exergetic efficiency. Given the context of the vapor compression cooling system under the identical operating conditions, the exergetic efficiency is 0.21.

(6) One observation is that thermoelastic cooling prefers small to medium temperature lift applications (sensible cooling for A/C, bottle cooler but not refrigerators) when the operating system temperature lift varies, while the vapor compression cooling favors medium to large temperature lift conditions (A/C and refrigerators).

Future Work

As indicated by Figure 9-1, this dissertation kicked off the first-step development of this novel NIK cooling technology. More rapid development and much better results are expected in the coming few years based on the current development speed observed during the simulation and experiment in this thesis. It should also be mentioned that a second compressive thermoelastic cooling prototype was already developed and is now under testing.
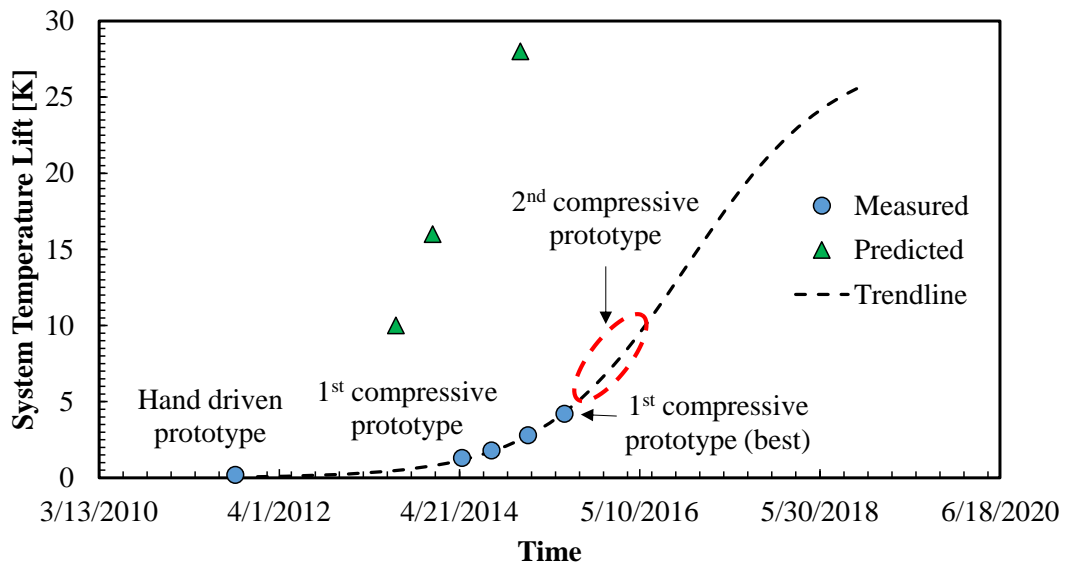
Figure 9-1: Prospects for future based on current development speed of thermoelastic cooling systems.

This thesis also established the framework of thermoelastic cooling for future work. Future directions can be summarized in Table 9-1. Development of thermoelastic cooling system requires resources from various disciplines, and coordinated efforts are essential to its success in the future.

Table 9-1: Summary of key issues to be addressed in future studies.

Research area	Key issues
Materials	• Low hysteresis • High latent heat • Long fatigue life • Small transformation stress • Low cost
Material structure design	• Minimum friction • Uniform phase change (Ψ) • Large heat transfer surface to volume ratio
Driver	• Low cost • Compact • Moderate precision • Large force and small displacement
System structure design	• Compact design capable to handle to large force • Light weight
Heat transfer design	• Compact • High heat transfer surface to volume ratio • Small heat transfer time constant τ • High efficient heat recovery/regeneration (TMR_{HR}) • Minimum pressure drop • Minimum parasitic parts and loss • Optimum fluid thermal mass (TMR) • Active regeneration design (AECR)

Materials and Material Structure Design

Engineering better elastocaloric materials is necessary to compete with high efficient vapor compression cooling systems. Based on the analysis from this dissertation, low hysteresis and high latent heat are two priorities to enhance the system performance. A good fatigue life, small transformation stress and low cost are conditions to be guaranteed before mass production of commercial products. In addition, less specific heat is also welcome.

Ni-Ti is the benchmark material. Cu-based alloys, modifications to Ni-Ti, and

216

exploring the magnetic shape memory alloys are urgently needed.

Driver

The state-of-the-art linear actuators, including screw-jacks, hydraulic cylinders, pneumatic cylinders, linear motors and piezoelectric actuators, are not designed for this application, where a large force and small displacement are needed. Current linear motors and pneumatic cylinders are still far away from the application required force level. Hydraulic cylinders and screw-jacks are mature technologies for decades, however, bringing down the cost of a residential and commercial cooling application is challenging. The most promising driver is the piezoelectric actuator for future products. The displacement needs to be enhanced.

System Design

System structural design can be divided into two groups: static SMA beds with cyclical fluid flow and motive SMA beds with static fluid flow. Most past elastocaloric heat engines were based on the motive SMA design. The prototype developed in this dissertation is based on the static SMA beds design, and should be the trend for the future. The layout of the beds and their coordination with the driver, however, still needs to be optimized to achieve a compact system with light weight.

Heat Transfer Design

This is the most important aspect. Even though the majority work of this thesis relates to the design and improvement of heat transfer design, much more optimization and developments should be done in the future. As mentioned in Chapter 8, a higher surface to volume ratio design of the SMA beds to minimize the heat transfer time constant is the direction. Heat recovery with higher cycling frequency and better

performance is also the goal. Another promising way to pursue is the AECR, by an analogy to the active regenerator design used in magnetocaloric cooling systems. By combining the heat transfer and regeneration processes together, this design could potentially boost the operating frequency for a few times, and therefore, saves the material and increases the cooling capacity. The concept of AECR, and its requirement for elastocaloric materials' properties, such as thermal conductivities, specific heat and others, are worthy of future investigations.

Chapter 10:   Contributions

10.1 *List of Major Contributions*

- Thermodynamic Fundamental of Elastocaloric Materials

    o Developed the COP_{mat} equation to study the performance of a SMA

    o Ranked 12 elastocaloric materials with 3 indices

    o Developed the 3-D phase diagram for any SMA and interpreted the martensitic phase transformation from thermodynamics perspective

- Cycle Design, Analysis and Dynamic Modeling

    o Proposed three feasible thermodynamic cooling cycles for thermoelastic cooling applications

    o Derived a simple physics based analytical COP and cooling capacity equations for the thermoelastic cooling system under Brayton cycle

    o Developed a physics based dynamic system model

- Novel Thermal-wave Heat Recovery

    o Proposed the "counter-flow in time scale" heat recovery method

    o Developed the ideal heat recovery cycle to demonstrate the method

    o Proposed heat recovery design guidelines for future studies

- Proof-of-concept Prototype Design, Fabrication and Testing

    o Development of the world first of-its-kind prototype and test facility

    o Confirmed the Ni-Ti tubes' latent heat by water capacity measurement

    o Measured maximum 65 W cooling capacity

- o   Measured maximum 4.2 K system water-water temperature lift

- o   Extensively validated the developed dynamic model

- Performance Enhancement by Multi-Objective Optimization and New Designs

   - o   Optimized 6 operation and design variables in a compressive thermoelastic cooling system using MOGA

   - o   Proposed 6 novel designs to enhance the system performance

   - o   Evaluated the feasibility of the proposed performance enhancement measures via a modified dynamic model

- Not-in-kind Cooling Technologies Comparison

   - o   Proposed an universal breakdown analysis method for all not-in-kind cooling technologies

   - o   Ranked 21 materials from 6 different cooling technologies

   - o   Ranked 6 not-in-kind cooling technologies using the proposed method

10.2 *Publications*

Peer-reviewed Journal Papers:

S. Qian, L. Huang, V. Aute, Y. Hwang, R. Radermacher. "Applicability of Entransy Dissipation Based Thermal Resistance for Design Optimization of Two-Phase Heat Exchangers", Appl. Therm. Eng., 2013, 55: 140-8.

S. Qian, K. Gluesenkamp, Y. Hwang, R. Radermacher, H. Chun. "Cyclic steady state performance of adsorption chiller with low regeneration temperature zeolite", Energy, 2013, 60:517-26.

G. Li, **S. Qian**, H. Lee, Y. Hwang, R. Radermacher. "Experimental investigation of

energy and exergy performance of short term adsorption heat storage for residential application", Energy, 2014, 65:675-91.

S. Qian, J. Ling, J. Muehlbauer, Y. Hwang, R. Radermacher. "Study on high efficient heat recovery cycle for solid-state cooling", Int. J. Refrig., 55, 102-119.

S. Qian, J. Ling, Y. Hwang, R. Radermacher, I. Takeuchi. "Thermodynamic cycle analysis and numerical modeling of thermoelastic cooling systems", Int. J. Refrig., 56, 65-80.

S. Qian, A. Alabdulkarem, J. Ling, Muehlbauer, J., Y. Hwang, R. Radermacher, I. Takeuchi. "Performance enhancement of a compressive thermoelastic cooling system using multi-objective optimization and novel designs", Int. J. Refrig., 57, 62-76.

S. Qian, D. Nasuta, A. Rhoads, Y. Wang, Y. Geng, Y. Hwang, R. Radermacher, I. Takeuchi. "Not-in-kind cooling technologies: a quantitative comparison of refrigerants and system performance", Int. J. Refrig. 2015 (in-press).

S. Qian, Y. Geng, Y. Wang, J. Ling, Y. Hwang, R. Radermacher, I. Takeuchi. "A review of elastocaloric cooling: materials, cycles and system integrations", Int. J. Refrig. 2015 (under review).

S. Qian, Y. Geng, Y. Wang, T.E. Pillsbury, R. Radermacher, I. Takeuchi. "Elastocaloric effect in CuAlZn and CuAlMn shape memory alloys under compression", Philos. Mag., 2015 (invited, under review).

Conference Papers:

S. Qian, L. Huang, V. Aute, Y. Hwang, R. Radermacher. "Effectiveness of Entransy Dissipation Metric and Entropy Generation Units in The Design of Fin-Tube Heat

Exchangers", International Refrigeration and Air Conditioning Conference at Purdue. Purdue University, West Lafayette, 2012.

S. Qian, K. Gluesenkamp, Y. Hwang, R. Radermacher. "Experimental study on transient performance of a residential combined cooling, heating and power system", ASME ES FuelCell, Minneapolis, July 2013.

J. Ling, **S. Qian**, S. Li, L. Huang, Y. Hwang, R. Radermacher. "The Winner Design of the Max Tech and Beyond Competition: A High-efficient Residential Air-conditioning System", ASHRAE Winter Conf. 2013.

S. Qian, J. Hartsog, K. Gluesenkamp, Y. Hwang, R. Radermacher. "Performance of Trigeneration Systems with Adsorption Heat Pump Under Various Climates", International Sorption Heat Pump Conference 2014, College Park, MD, April 2014.

S. Qian, J. Ling, Y. Hwang, R. Radermacher. "Dynamic Performance of a Compression Thermoelastic Cooling Air-Conditioner under Cyclic Operation Mode", International Refrigeration and Air Conditioning Conference at Purdue. Purdue University, West Lafayette, 2014.

S. Qian, A. Alabdulkarem, J. Ling, Y. Hwang, R. Radermacher. "Study on performance improvement of a compressive thermoelastic cooling system using single objective optimization". Power and Energy Conversion Conference 2015, San Diego, USA.

S. Qian, Y. Wu, J. Ling, J. Muehlbauer, Y. Hwang, I. Takeuchi, R. Radermacher. "Design, development and testing of a compressive thermoelastic cooling prototype". International Congress of Refrigeration 2015, Japan.

S. Qian, J. Ling, Y. Hwang, I. Takeuchi, R. Radermacher. "Modeling and

optimization of a novel heat recovery design for thermoelastic cooling systems", IMECE 2015, Houston, Texas.

Invention Disclosures:

R. Radermacher, I. Takeuchi, Y. Hwang, Y. Wu, **S. Qian**, J. Ling, Designs for Thermoelastic Cooling Systems and System Applications, PS2013087.

S. Qian, R. Radermacher, J. Ling, Y. Hwang, Novel designs improving the performance of a compressive thermoelastic cooling system, PS2014182.

Appendices

Appendix A: SMA Material COP Calculation

Based on Eq. (2-17) and Eq. (2-18), two more material properties need to be determined to calculate the two material level COPs, which are the phase change entropy change Δs and the material constant A^* measuring the hysteresis.

The phase change entropy change Δs can be either calculated from the latent heat following Eq. (A-1), or be retrieved from the literature directly.

$$\Delta s = \frac{\Delta h}{T} \tag{A-1}$$

The second parameter, A^*, requires more information from the loading-unloading performance curves on the stress-strain diagram. When the stress-strain curves are available, the following two integrals can be calculated.

$$w_+ = \frac{1}{\rho} \cdot \int_0^{\varepsilon_{max}} \sigma_{ld}(\varepsilon) d\varepsilon \tag{A-2}$$

$$w_- = \frac{1}{\rho} \cdot \int_0^{\varepsilon_{max}} \sigma_{uld}(\varepsilon) d\varepsilon \tag{A-3}$$

Recall Eq. (2-15) and Eq. (2-16), if the loading and unloading curve from any literature is isothermal, the subtraction between these two equations can be related to the stress-strain curve following Eq. (A-4).

$$w_+ - w_- = 2A = \frac{1}{\rho} \cdot \left(\int_0^{\varepsilon_{max}} \sigma_{ld} d\varepsilon - \int_0^{\varepsilon_{max}} \sigma_{uld} d\varepsilon \right) \tag{A-4}$$

Therefore, for the isothermal loading and unloading curves obtained from literature,

the material hysteresis constant is as following.

$$A* = \frac{\left(\int_0^{\varepsilon_{max}} \sigma_{ld} d\varepsilon - \int_0^{\varepsilon_{max}} \sigma_{uld} d\varepsilon \right)}{2\rho}$$ (A-5)

If the loading and unloading curves from literature are not isothermal, i.e. adiabatic, that means the loading and unloading energy are different from above based on the analysis in Chapter 2. The loading-unloading energy is shown in Eq. (A-6) and Eq. (A-7). The material constant is introduced in Eq. (A-8) for adiabatic loading and unloading.

$$w_+(T) = \left[\sigma_{AM}\left(T + \frac{\Delta T_{ad}}{2}\right)\cdot\Delta + \frac{\sigma_{AM}^2\left(T + \frac{\Delta T_{ad}}{2}\right)}{2K} \right] / \rho$$ (A-6)

$$w_-(T) = \left[\sigma_{MA}\left(T - \frac{\Delta T_{ad}}{2}\right)\cdot\Delta + \frac{\sigma_{AM}^2\left(T + \frac{\Delta T_{ad}}{2}\right)}{2K} \right] / \rho$$ (A-7)

$$A* = \frac{\left(\int_0^{\varepsilon_{max}} \sigma_{ld} d\varepsilon - \int_0^{\varepsilon_{max}} \sigma_{uld} d\varepsilon \right)}{2\rho} - \frac{\Delta T_{ad}\cdot\Delta s}{2}$$ (A-8)

For example, the loading-unloading curve for Ni-Ti alloy was reported under adiabatic conditions (Cui et al., 2012a), and therefore Eq. (A-8) should be used. The loading energy was 25.6 MJ·m^{-3} for compression, and unloading energy was 19 MJ·m^{-3}. Using ΔT_{ad} = 22 K in this case, Δs = 42 J·g^{-1}·K^{-1} and density of 6.5e6 g·m^{-3} in this case, the material constant for Ni-Ti under compression mode is 45 J·kg^{-1}.
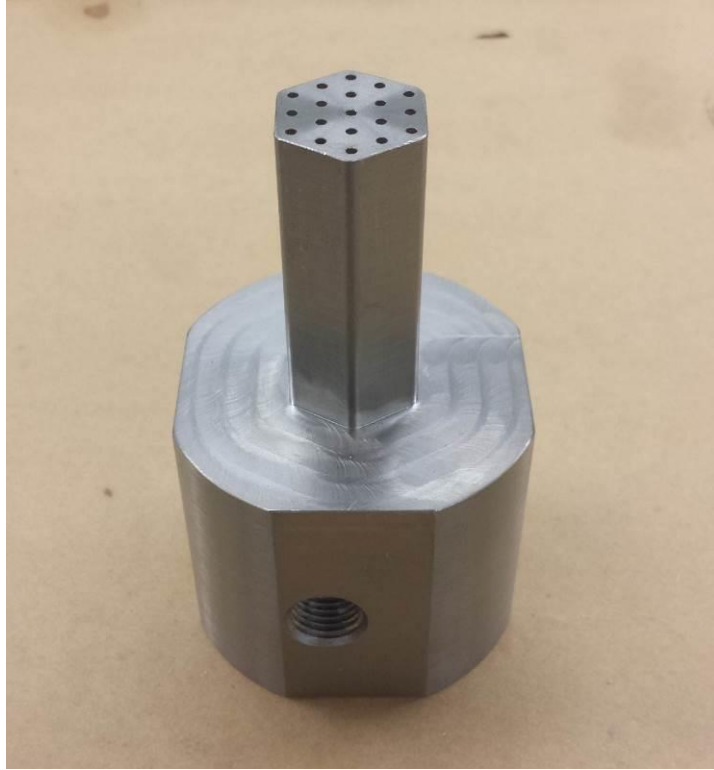
Figure B-1: The loading head used in the 100 W prototype.
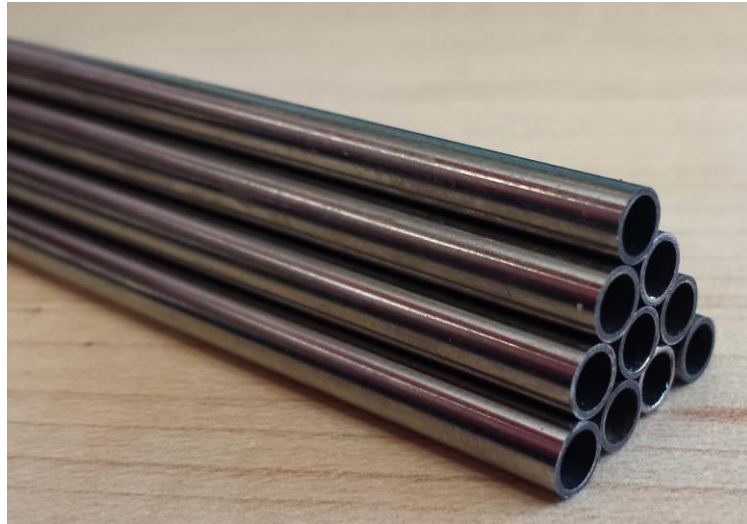
Figure B-2: Ni-Ti tubes (ID = 3.76mm and OD = 4.72 mm) used in the prototype.
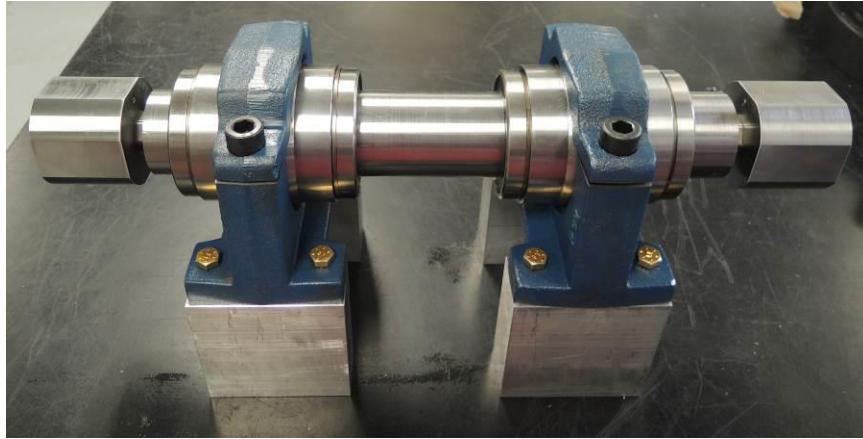
Figure B-3: A single bed assembly.
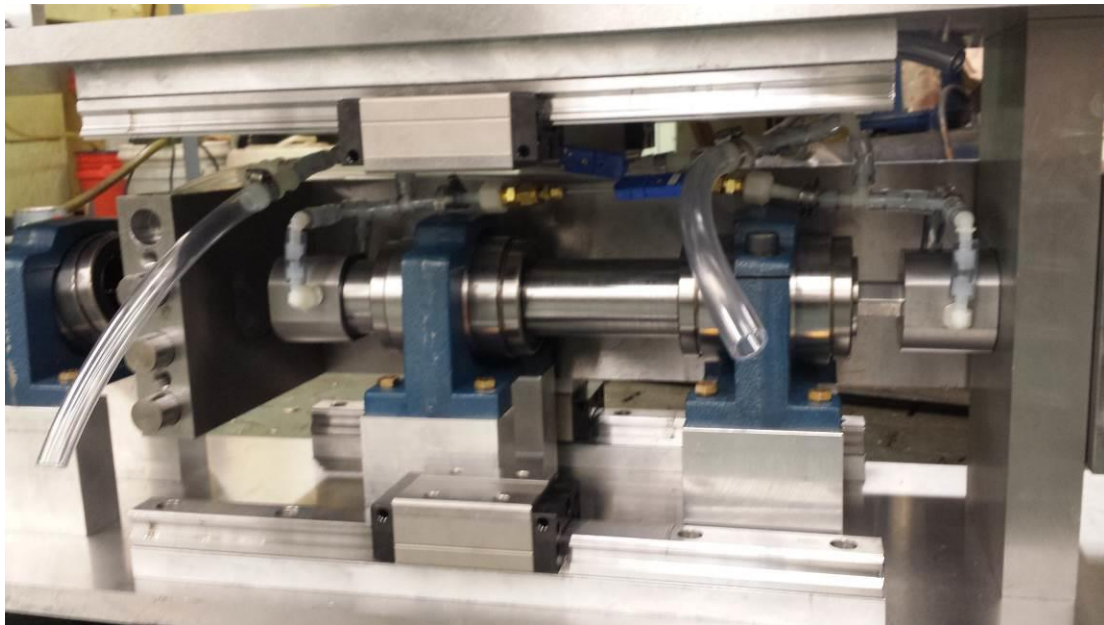
Figure B-4: One bed inside the moving box.
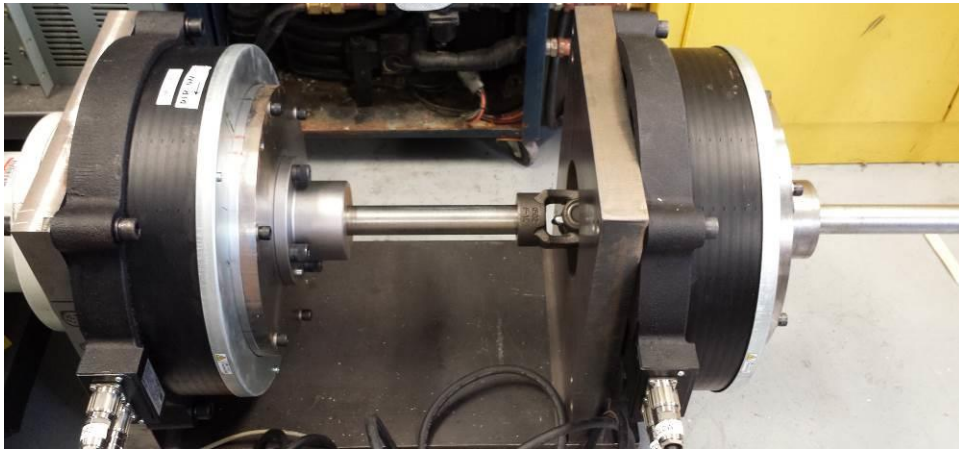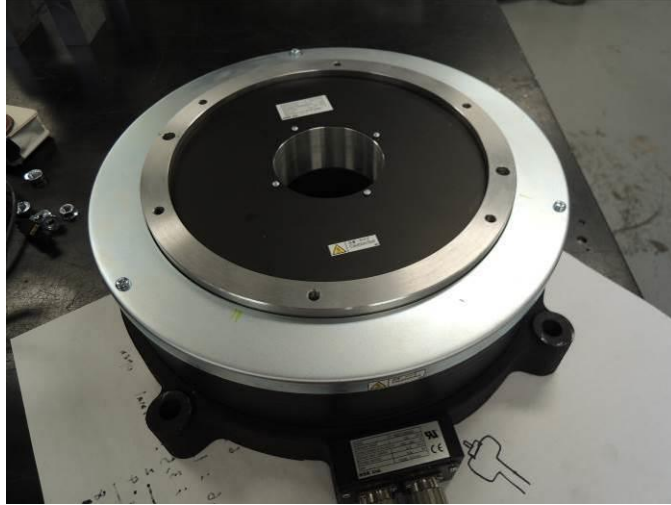
Figure B-5: Motors used in the prototype.
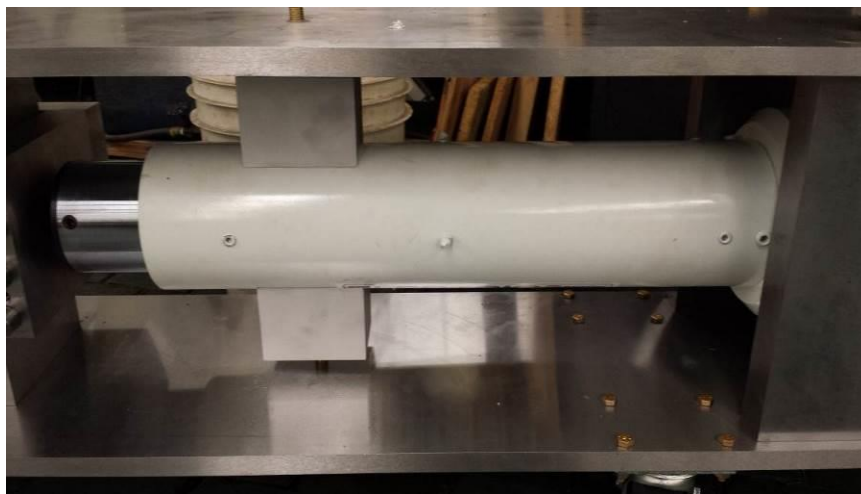
Figure B-6: The linear actuator (screw-jack) used in the prototype.

Appendix C: NIK Cooling Technologies

For the vapor compression cycle plotted in Figure 7-2 (a), the latent heat term in Eq. (7-4) is:

$$\Delta h = h_1 - h_4 \tag{C-1}$$

Therefore, Eq. (7-4) for vapor compression cooling becomes Eq. (7-5).

For both the elastocaloric cooling, the magnetocaloric cooling and electricaloric cooling, the latent heat term in Eq. (7-4) is:

$$\Delta h = T_c \Delta s \tag{C-2}$$

As a result, Eq. (7-6) to Eq. (7-8) can be obtained by substituting Eq. (C-2) into Eq. (7-4). The highlight of entropy change at T_c for magnetocaloric cooling is due to a strong temperature dependence of entropy change for those materials around Cuire temperature.

Thermoelectric cooling is the only NIK technology without a cycle. The denominator in Eq. (7-4) for thermoelectric cooling is changed to the parasitic heat conduction loss through the material. The physical meaning of Eq. (7-4) for thermoelectric cooling then becomes the ratio between the useful cooling and the parasitic heat loss due to conduction, which is similar to other NIK technologies. If this ratio is beyond 1, it means the generated cooling by Seebeck effect can afford the parasitic conduction heat loss. Otherwise, the thermoelectric material will not be functional.

$$\gamma_{thermoelectric} = \frac{q_c}{q_{cond}} = \frac{\alpha_S I_{opt} T_c}{kx\Delta T_{lift}} \tag{C-3}$$

The optimum current, according to Riffat and Ma (2004), is as following:

$$I_{opt} = \frac{\alpha_S \Delta T_{lift}}{R\left(\sqrt{1+ZT_m}-1\right)}$$

(C-4)

Substituting Eq. (C-4) to Eq. (C-3) yields

$$\gamma_{thermoelectric} = \frac{\alpha_S{}^2 \Delta T_{lift} T_c}{kx\Delta T_{lift}\cdot R\left(\sqrt{1+ZT_m}-1\right)} = \frac{\alpha_S{}^2 T_c}{k\rho_e\left(\sqrt{1+ZT_m}-1\right)}$$

(C-5)

where x is the characteristic length, defined as ratio between the cross section area and the height, i.e. $x = \text{area} / l$.

Recall the definition of the figure-of-merit, Z, defined in Eq. (C-6), we can get the final equation for thermoelectric cooling in Eq. (7-9).

$$Z \equiv \frac{\alpha_S{}^2}{k\rho_e}$$

(C-6)

For Brayton cycle, the cooling capacity is induced by the temperature difference between state 6 and state 5, and therefore the "latent heat" term in Eq. (7-4) should be replaced by the sensible heat during the cooling process:

$$\Delta h = h_5 - h_6$$

(C-7)

Combining Eq. (C-7) and Eq. (7-4) will result in Eq. (7-10) for Brayton cycle.

For Stirling cycle, the cooling capacity is the isothermal entropy change between state 1 and state 4, which is shown in the following equation.

$$\Delta h = T_c \Delta s\left(T_c\right) = T_c\left(s_1 - s_4\right)$$

(C-8)

Combining Eq. (C-8) and Eq. (7-4) will be Eq. (7-11) for gaseous Stirling cycle.

The *COP* is a path dependent variable based on its physical definition, since both heat and work are determined by the path. It can be simplified to a state variable by using

only the material properties, when assuming the material equation-of-state (so that the path are "pre-defined"). An example is the COP_{mat} for Stirling cycle when using the ideal gas equation-of-state, which yields the Carnot COP (Thombare and Verma, 2008).

For vapor compression cooling, Eq. (7-13) is well-defined using the evaporator capacity for the numerator, and the net work input for the denominator (Radermacher and Hwang, 2005). The hysteresis was considered by the fact that additional vacuum is needed to grow bubble in evaporator, and additional pressure is required to induce droplet growth during condensation. This pressure difference can be converted to the temperature difference between the heat source and the saturation temperature of refrigerant, as shown in Eq. (C-9), which was assumed to be 1 K. The same temperature difference was assumed in the condenser.

$$\Delta T = T_c - T_{sat}\left(T_c\right) = 1 \ [K] \tag{C-9}$$

Eq. (7-14) was defined in Chapter 1 based on a phenomenological model for SMAs. The material constant $A*$ can be retrieved based on material stress-strain measurement data. Most literature reported the isothermal loading-unloading curves on the stress-strain diagram, and some reported the adiabatic loading-unloading curves (Cui et al., 2012). The following two equations can be used to determine the material constant $A*$.

$$A* = \frac{\left(\displaystyle\int_0^{\varepsilon_{max}} \sigma_{ld}\,d\varepsilon - \int_0^{\varepsilon_{max}} \sigma_{uld}\,d\varepsilon\right)}{2\rho} \quad \text{where } \rho \text{ is density } [kg\cdot m^{-3}] \text{ for isothermal} \tag{C-10}$$

$$A^* = \frac{\left(\int_0^{\varepsilon_{max}} \sigma_{ld} d\varepsilon - \int_0^{\varepsilon_{max}} \sigma_{uld} d\varepsilon \right)}{2\rho} - \frac{\Delta T_{ad} \cdot \Delta s}{2} \quad \text{for adiabatic} \tag{C-11}$$

Eq. (7-15) was defined following the same method with the SMAs, with the analogy from the stress-strain hysteresis to the field-magnetization hysteresis. It was assumed that the field-magnetization magnetization and demagnetization curves follow the ideal linear assumptions as graphically shown in Figure 7-2 (d). The magnetization hysteresis A^*_{magnet} can be associated with the surrounded area of the isothermal curve under the same temperature.

$$A^*_{magnet} = \left(\int_{m_{min}}^{m_{max}} \mu_0 H_{magnet} dm - \int_{m_{min}}^{m_{max}} \mu_0 H_{demagnet} dm \right) / 2 \tag{C-12}$$

The denominator in Eq. (7-15) can be derived in Eq. (C-13) using the graphical interpretation of Figure 7-2 (d). The surrounded area of the magnetization and demagnetization processes under the two temperatures is the net work for the magnetocaloric Ericsson cycle, including the hysteresis already. The third step simplification used the variant of the Clausius-Clapeyron equation under the equilibrium condition in Eq. (C-15), which is derived from its original format in Eq. (C-14) (Gshneidner and Pecharsky, 2005). The cooling is calculated in Eq. (C-16).

$$\begin{aligned} w_{magnet} - w_{demagnet} &= \left[H(T_h) - H(T_c) + \Delta H_{hysteresis} \right] \cdot \Delta m \\ &= \left[H(T_h) - H(T_c) \right] \cdot \Delta m + 2A^*_{magnet} \\ &= (T_h - T_c) \Delta s + 2A^*_{magnet} \end{aligned} \tag{C-13}$$

$$\left(\frac{dH}{dT} \right)_{eq} = \frac{\Delta s}{\Delta m} \tag{C-14}$$

$$\frac{H(T_h) - H(T_c)}{T_h - T_c} = \frac{\Delta s}{\Delta m} \tag{C-15}$$

$$q_c = T_c \Delta s - A*_{magnet} \tag{C-16}$$

All the equations here are based on the results obtained for SMA using the linear phenomenological model proposed by Ziolkowski (1993). The method proposed here is an engineering simplification to compute the work needed to drive a magnetocaloric cooling cycle on the material level under various operating conditions. Direct experimental measures are more accurate, but have difficulty in estimating work under conditions other than the tested ones.

The same method can be applied to electrocaloric cooling as well. The electrocaloric hysteresis can be calculated using the measured *D-E* diagram, as shown in Eq. (C-17). Polarization *P-E* diagram can be converted using Eq. (C-17).

$$A*_{electrocaloric} = \frac{\int_0^{D_{max}} E_{e,ld}\,dD - \int_0^{D_{max}} E_{e,uld}\,dD}{2\rho} \tag{C-17}$$

$$D = P + \varepsilon_0 E_e \tag{C-18}$$

where ε_0 is the vacuum permittivity constant (8.854 x 10^{-12} F·m^{-1}).

Eq. (7-17) is directly used from Riffat and Ma (2004).

Eq. (7-18) and Eq. (7-19) are also straightforward using the cycle diagram in Figure 7-2.

Appendix D: Heat Transfer Time Constant Derivation

A simplified solid-fluid heat transfer problem can be illustrated by Figure D-1.
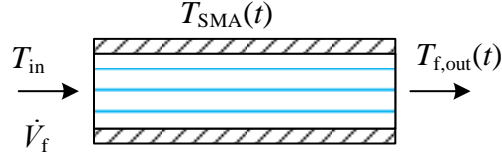
Figure D-1: Illustration of the simplified lumped SMA-HTF problem.

First, the SMA's temperature is assumed to be uniform. The fluid temperature is also assumed to be uniform. Therefore, the uniform temperature difference between the SMA and fluid is the driving potential to determine the instantaneous heat transfer rate, and the dynamic equations can be determined in Eqs. (D1-D2).

$$\frac{dT_{SMA}(t)}{dt} = -\frac{hA}{(\rho c_p)_{SMA} V_{SMA}} \left[T_{SMA} - T_{f,out}(t) \right] \tag{D-1}$$

$$\frac{dT_{f,out}(t)}{dt} = \frac{\dot{V}_f}{V_f} \left[T_{f,in} - T_{f,out}(t) \right] + \frac{hA}{(\rho c_p)_f V_f} \left[T_{SMA} - T_{f,out}(t) \right] \tag{D-2}$$

The above linear ordinary differential equations set can be simplified to the following second order linear ordinary differential equation in Eq. (D-3).

$$\frac{d^2 T_{SMA}(t)}{dt^2} + \left[\frac{1}{t_1}(1+TMR) + \frac{1}{t_2} \right] \frac{dT_{SMA}(t)}{dt} + \frac{1}{t_1 t_2} = const \tag{D-3}$$

It is not necessary to solve the entire Eq. (D-3) to obtain the two time constants associated with it. In fact, we know that the two time constants (eigenvalues) must be positive to be physically correct without disobeying the 2nd Law of Thermodynamics. Therefore, the general solution has the following formation in Eq. (D-4).

$$T_{SMA}(t) = c_1 \exp(\lambda_1 t) + c_2 \exp(\lambda_2 t) \tag{D-4}$$

The two eigenvalues (time constants) can be determined by solving the characteristics equation formed by the coefficients in Eq. (D-3), which are shown in Eq. (D-5).

$$\tau_1 = -\lambda_1 = \frac{2}{\dfrac{1}{t_2} + \dfrac{1}{t_1} \cdot (1 + TMR) - \sqrt{\left(\dfrac{1}{t_2} - \dfrac{1}{t_1} \cdot (1 - TMR)\right)^2 + \dfrac{4TMR}{t_1^2}}}$$

$$\tau_2 = -\lambda_2 = \frac{2}{\dfrac{1}{t_2} + \dfrac{1}{t_1} \cdot (1 + TMR) + \sqrt{\left(\dfrac{1}{t_2} - \dfrac{1}{t_1} \cdot (1 - TMR)\right)^2 + \dfrac{4TMR}{t_1^2}}} \tag{D-5}$$

Obviously, the second time constant is greater than the first one. Giving the heat transfer process after loading for example, the SMA temperature T_{SMA} is decreasing over time as a result of rejecting heat to the HTF. The fluid temperature $T_{f,out}$ is increasing by absorbing heat from the SMA. We know the fact that the fluid outlet temperature $T_{f,out}$ will approach the solid temperature first, and then converge to the inlet fluid temperature limit, as shown in Figure D-2. As a result, the smaller time constant τ_2 is corresponding to the fluid, and the other time constant is τ_1 for the SMA, as shown in Eq. (D-6) and Eq. (D-7), respectively.

$$\tau_{SMA} = \frac{2}{\dfrac{1}{t_2} + \dfrac{1}{t_1} \cdot (1 + TMR) - \sqrt{\left(\dfrac{1}{t_2} - \dfrac{1}{t_1} \cdot (1 - TMR)\right)^2 + \dfrac{4TMR}{t_1^2}}} \tag{D-6}$$

$$\tau_{fluid} = \frac{2}{\dfrac{1}{t_2} + \dfrac{1}{t_1} \cdot (1 + TMR) + \sqrt{\left(\dfrac{1}{t_2} - \dfrac{1}{t_1} \cdot (1 - TMR)\right)^2 + \dfrac{4TMR}{t_1^2}}} \tag{D-7}$$
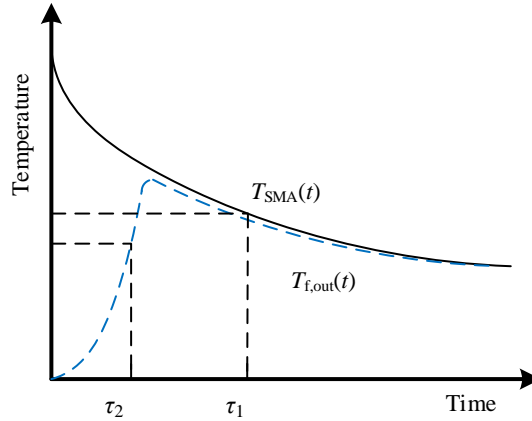
Figure D-2: Illustration of the temperature profiles during a heat rejection from SMA

to fluid process after loading the SMA.

There are a few interesting observations when considering the limits of the above mentioned two time constants.

When Eq. (8-3), i.e. t_2 becomes zero, it means that the flow rate is infinity compared with the dead HTF volume within the SMA heat transfer domain. The limit can be solved as shown in Eq. (D-8) and the result is also in Eq. (8-4). On the other hand, the fluid time constant limit is 0, as shown in Eq. (D-9). The physical interpretation of these two limits are as following. The fluid outlet temperature converges back to the inlet temperature infinitely fast. As a result, the solid-fluid problem degrades to the lumped system problem, and the time constant limit is also equal to that of the lumped system problem.

$$\lim_{t_2 \to 0} \tau_{SMA} = \lim_{t_2 \to 0} \frac{2t_2}{1 + \frac{t_2}{t_1}(1+TMR) - \left[\left(1 - \frac{t_2}{t_1}(1-TMR)\right)^2 + \frac{4TMR}{t_1^2} \cdot t_2^2\right]^{1/2}}$$

$$= \lim_{t_2 \to 0} \frac{2t_2}{1 + \frac{t_2}{t_1}(1+TMR) - \left[1 - \frac{t_2}{t_1}(1-TMR)\right]}$$

(D-8)

$$= t_1$$

$$\lim_{t_2 \to 0} \tau_{fluid} = \lim_{t_2 \to 0} \frac{2t_2}{1 + \frac{t_2}{t_1}(1+TMR) + \left[\left(1 - \frac{t_2}{t_1}(1-TMR)\right)^2 + \frac{4TMR}{t_1^2} \cdot t_2^2\right]^{1/2}}$$

$$= \lim_{t_2 \to 0} \frac{2t_2}{1 + \frac{t_2}{t_1}(1+TMR) + \left[1 - \frac{t_2}{t_1}(1-TMR)\right]}$$

(D-9)

$$= 0$$

When the *TMR* approaches infinity, it means that the dead thermal mass of the HTF becomes negligible compared to the thermal mass of the SMA. Under this scenario, the time constant limits of the SMA and the HTF are calculated in Eq. (D-10) and Eq. (D-11), respectively.

$$\lim_{TMR \to \infty} \tau_{SMA} = \lim_{TMR \to \infty} \frac{2}{\frac{TMR}{t_1} + \frac{1}{t_2} + \frac{1}{t_1} - \sqrt{\left(\frac{TMR}{t_1} + \frac{1}{t_2} + \frac{1}{t_1}\right)^2 - \frac{4}{t_1 t_2}}}$$

$$= \lim_{x = \frac{TMR}{t_1} + \frac{1}{t_2} + \frac{1}{t_1} \to \infty} \frac{2}{x - \left(x^2 - c\right)^{1/2}}$$

$$= \lim_{x = \frac{TMR}{t_1} + \frac{1}{t_2} + \frac{1}{t_1} \to \infty} \frac{2}{x\left(1 - \left(1 - \frac{c}{x^2}\right)^{1/2}\right)}$$

(D-10)

$$= \lim_{x = \frac{TMR}{t_1} + \frac{1}{t_2} + \frac{1}{t_1} \to \infty} \frac{4}{x\left(1 - 1 + \frac{c}{2x^2}\right)} = \lim_{x = \frac{TMR}{t_1} + \frac{1}{t_2} + \frac{1}{t_1} \to \infty} \frac{8x}{c} = \infty$$

237

$$\lim_{TMR \to \infty} \tau_{fluid} = \lim_{TMR \to \infty} \cfrac{2}{\cfrac{TMR}{t_1} + \cfrac{1}{t_2} + \cfrac{1}{t_1} + \sqrt{\left(\cfrac{TMR}{t_1} + \cfrac{1}{t_2} + \cfrac{1}{t_1}\right)^2 - \cfrac{4}{t_1 t_2}}}$$

$$= \lim_{x = \frac{TMR}{t_1} + \frac{1}{t_2} + \frac{1}{t_1} \to \infty} \cfrac{2}{x + \left(x^2 - c\right)^{1/2}}$$

$$= 0$$

(D-11)

Eq. (D-11) means that when the fluid dead thermal mass is negligible (note that this condition is ideal for cycle to minimize cyclic loss), the fluid outlet temperature approaches the solid temperature infinitely fast, diminishing the entire heat transfer driving potential. As a result, Eq. (D-10) shows that the time to fully transfer heat from the SMA to the fluid is infinity, regardless of the heat transfer area to volume ratio and the heat transfer coefficient.

One comment here is that for Stirling cryocoolers, the second time constant for fluid should be used instead of for solid, since the fluid is the refrigerator and the solid is only the regenerator. Taking $t_1 = 2$ [sec], $t_2 = 0.01$ [sec] and $TMR = 10$ for example, the fluid time constant is 0.0095 [sec], and therefore the fluid can be operated under high frequency (over 100 Hz). The natural difference between Eq. (D-6) and Eq. (D-7) causes the huge difference and asymmetry between the gas cooling and the solid-state cooling applications.

References

Agrawal, N., & Bhattacharyya, S. (2008). Performance evaluation of a non-adiabatic capillary tube in a transcritical CO2 heat pump cycle. *International Journal of Thermal Sciences, 47*, 423-430.

Ahler, M. (1975). On the usefulness of Martensitic transformations for energy conversion. *Scripta Metallurgica, 9*, 71-74.

Amar, N., Sun, L., & Meunier, F. (1996). Numerical analysis of adsorptive temperature wave regenerative heat pump. *Applied Thermal Engineering, 16*, 405-418.

Anon. (2003). *AHRI 550/590. Standard for performance rating of water-chilling packages using the vapor compression cycle.*

Anon. (2008). *AHRI 210/240. Performance rating of unitary air-conditioning and air-source heat pump equipment.*

Anon. (2010a). *ASHRAE refrigeration handbook.* Atlanta, GA: American Society of Heating, Refrigeration, and Air-Conditioning Engineers.

Anon. (2010b). *ASHRAE refrigeration handbook.* Atlanta, GA: American Society of Heating, Refrigeration and Air-Conditioning Engineers.

Anon. (2010c). *ASHRAE refrigeration handbook.* Atlanta, GA: American Society of Heating, Refrigeration and Air-Conditioning Engineers.

Anon. (2014, Nov). *Simulink.* Retrieved from http://www.mathworks.com/products/simulink/

Aprea, C., Greco, A., & Maiorino, A. (2011). A numerical analysis of an active

magnetic regenerative refrigerant system with a multi-layer regenerator. *Energy Conversion and Management, 52*, 97-107.

Bahl, C., Engelbrecht, K., Eriksen, D., Lozano, J., Bjork, R., Geyti, J., . . . Pryds, N. (2014). Development and experimental results from a 1 kW prototype AMR. *International Journal of Refrigeration, 37*, 78-83.

Banks, R. (1975). *USA Patent No. US3913326 A.*

Bansal, P., & Yang, C. (2005). Reverse heat transfer and re-condensation phenomena in non-adiabatic capillary tubes. *Applied Thermal Engineering*, 3187-3202.

Bansal, P., Vineyard, E., & Abdelaziz, O. (2011). Advances in household appliances - A review. *Applied Thermal Engineering, 31*, 3748-3760.

Bansal, P., Vineyard, E., & Abdelaziz, O. (2012). Status of not-in-kind refrigeration technologies for household space conditioning, water heating and food refrigeration. *International Journal of Sustainable Built Environment, 1*, 85-101.

Barclay, J. (1983). *USA Patent No. US4408463 A.*

Barclay, J. (1994). Active and parssive magnetic regenerators in gas magnetic refrigerators. *Journal of Alloys and Compounds, 207*, 355-361.

Barclay, J., & Steyert, W. (1982). *USA Patent No. US4332135 A.*

Barclay, J., Moze, O., & Paterson, L. (1979). A reciprocating magnetic refrigerator for 2-4K operation: Initial results. *Journal of Applied Physics, 50*, 5870-5877.

Basinski, Z., & Christian, J. (1954). Crystallography of deformation by twin boundary movements in indium-thallium alloys. *Acta Metallurgica, 2*, 101-116.

Bechtold, C., Chluba, C., Lima de Miranda, R., & Quandt, E. (2012). High cyclic stability of the elastocaloric effect in sputtered TiNiCu shape memory films. *Applied Physics Letters, 101*, 091903.

Beghi, M., Berra, M., Caglioti, G., & Fazzi, A. (1986). A thermoelastic method to measure the thermal expansion coefficient. *Materials and Structures, 19*, 65-69.

Bekker, A. B. (1997). Temperature-induced phase transformation in a shape memory alloy: phase diagram based kinetics approach. *Journal of Mechanics and Physics of Solids*, 949-988.

Bergman, T. L. (2011). *Fundamentals of Heat and Mass Transfer (7th edition).* John Wiley & Sons, Inc.

Bonnot, E., Romero, R., Manosa, L., Vives, E., & Planes, A. (2008). Elastocaloric effect associated with the martensitic transition in shape memory alloy. *Physics Review Letters, 100*, 4.

Bosel, J., & Trepp, C. (1999). An alternative stack arrangement for thermoacoustic heat pumps and refrigerators. *Journal of the Acoustical Society of America, 106*, 707-715.

Brown, G. (1976). Magnetic heat pumping near room temperature. *Journal of Applied Physics, 47*, 3673-3680.

Brown, J., & Domanski, P. (2014). Review of alternative cooling technologies. *Applied Thermal Engineering, 64*, 252-262.

Browne, A., Johnson, N., & Wittorf, M. (2012). *USA Patent No. US8104278 B2.*

Buehler, W., Gilfrich, J., & Wiley, R. (1963). Effect of low temperature phase

changes on the mechanical properties of alloys near composition TiNi. *Journal of Applied Physics, 34*, 1475-1477.

Calm, J. (2008). The next generation of refrigerants - historical review, considerations, and outlook. *International Journal of Refrigeration, 31*, 1123-1133.

Carey, V. (2008). *Liquid-vapor phase-change phenomena (2nd edition).* New York: CRC Press.

Carlsen, H. (1989). Development of a gas fired Vuilleumire heat pump for residential heating. *Energy Conversion Engineering Conferences (IECEC).*

Castillo-Viall, P., Soto-Parra, D., Matutes-Aquino, J., Ochoa-Gamoa, R., Planes, A., Manosa, L., . . . Flores-Zuniga, H. (2011). Caloric effects induced by magnetic and mechanical fields in a Ni50Mn25-xGa25Cox magnetic shape memory alloy. *Physical Review B, 83*, 174109.

Ceperley, P. (1979). A pistonless Stirling engine-the traveling wave heat engine. *Journal of the acoustical society of America, 66*, 1508-1513.

Chang, L., & Read, T. (1951). Plastic deformation and diffusionless phase changes in metals - The gold-cadmium beta-phase. *Transactions of the American Institute of Mining and Metallurgical Engineers, 191*, 47-52.

Chen, C., Wang, R., Xia, Z., Kiplagat, J., & Lu, Z. (2010). Study on a compact silica gel-water adsorption chilelr without vacuum valves: Design and experimental study. *Applied Energy, 87*, 2673-2681.

Chen, Y., Zhang, X., Dunand, D., & Schuh, C. (2009). Shape memory and superelasticity in polycrystalline Cu-Al-Ni microwires. *Applied Physics*

Letter, 95, 171906.

Chua, H., Ng, K., Chakraborty, A., Oo, N., & Othman, M. (2002). Adsorption characteristics of silica gel + water systems. *Journal of Chemical & Engineering Data, 47*, 1177-1181.

Chua, H., Wang, X., & Teo, H. (2006). A numerical study of the Hampson-type miniature Joule-Thomson cryocooler. *International Journal of Heat and Mass Transfer, 49*, 582-593.

Cochran, R. (1962). *USA Patent No. US3036444 A.*

Cornelis, I., & Wayman, C. (1974). The shape memory effect in AgZn alloys. *Scripta Metallurgica, 8*, 1321-1326.

Critoph, R. (1994). Forced convective enhancement of adsorption cycles. *Heat Recovery Systems & CHP, 14*, 343-350.

Critoph, R. (1998). Forced convection adsorption cycles. *Applied Thermal Engineering, 18*, 799-807.

Cross, C., Barclay, J., DeGregoria, A., Gaeger, S., & Johnson, J. (1988). Optimal temperature-entropy curves for magnetic refrigeration. *Advances in Cryogenic Engineering, 33*, 767-775.

Cui, J., Takeuchi, I., Wuttig, M., Wu, Y., Radermacher, R., Hwang, Y., & Muehlbauer, J. (2012b). *USA Patent No. US20120273158 A1.*

Cui, J., Wu, Y., Muehlbauer, J., Hwang, Y., Radermacher, R., Fackler, S., . . . Takeuchi, I. (2012a). Demonstration of high efficiency elastocaloric cooling with large Delta T using NiTi wires. *Applied Physics Letters, 101*, 073904.

Cummingham, B., & Ashbee, K. (1977). Marmem engines. *Acta Metallurgica, 25*,

1315-1321.

da Silva, D., Ronzoni, A., Melo, C., & Hermes, C. (2011). A study of transcritical carbon dioxide through diabatic capillary tubes. *International Journal of Refrigeration, 34*, 834-843.

de Monte, F. (1997). Thermal analysis of the heat exchangers and regenerators in Stirling cycle machines. *Journal of Propulsion and Power, 13*, 404-411.

de Waele, A. (2011). Basic operation of cryocoolers and related thermal machines. *Journal of Low Temperature Physics, 164*, 179-236.

Defay, E. C. (2013). The electrocaloric efficiency of ceramic and thin films. *Advanced Materials*, 3337-3342.

DeGregoria, A. (1994). *USA Patent No. WO1994010517 A1.*

DeGregoria, A. (1995). *USA Patent No. US5465781 A.*

DeGregoria, A. e. (1993). *USA Patent No. US005249424A.*

DeGregoria, A., Feuling, L., Laatsch, J., Rowe, J., Trueblood, J., & Wang, A. (1991). Test resutls of an active magnetic regenerative refrigerator. *Advanceds in Cryogenic Engineering, 37B*, 875-882.

Delaey, L., & Lepeleire, G. (1976). The temperature-entropy diagram of "solid state engines" and "solid state heat pumping systems" with shape memory alloys. *Scripta Metallurgica, 10*, 959-964.

Derking, J., Holland, H., Lerou, P., Tirolien, T., & ter Brake, H. (2012). Micromachined Joule-Thomson cold stages operating in the temperature range 80-250 K. *International Journal of Refrigeration, 35*, 1200-1207.

Domanski, P., & Didion, D. (1994). Evaluation of suction-line/liquid-line heat

exchanger in the refrigeration cycle. *International Journal of Refrigeration, 17*, 487-493.

Douss, N., Meunier, F., & Sun, L. (1988). Predictive model and experimental results for a 2-adsorber solid adsorption heat-pump. *Industrial & Engineering Chemistry Research, 27*, 310-316.

Engelbrecht, K. (2008). *A numerical model of an active magnetic regenerator refrigerator with experimental validation.* PhD Dissertation, University of Wisconsin-Madison.

Engelbrecht, K., Bahl, C., & Nielsen, K. (2011). Experimental results for a magnetic refrigerator using three different types of magnetocaloric material regenerators. *International Journal of Refrigeration, 34*, 1132-1140.

EPA Global Warming Potentials of ODS Substitutes. (n.d.). Retrieved from http://www.epa.gov/ozone/geninfo/gwps.html

Fedelich, B., & Zanzotto, G. (1991). One-dimensional quasistatic nonisothermal evolution of shape-memory material inside the hysteresis loop. *Continuum Mechanics and Thermodynamics, 3*, 251-276.

Fernandez, N., Hwang, Y., & Radermacher, R. (2010). Comparison of CO2 heat pump water heater performance with baseline cycle and two high COP cycles. *International Journal of Refrigeration, 33*, 635-644.

Fischer, S., Tomlinson, J., & Hughes, P. (1994). *Energy and Global Warming Impacts of Not-in-Kind and Next Generation CFC and HCFC Alternatives.* Oak Ridge, USA.

Flamensbeck, M., Summerer, F., Riesch, P., Ziegler, F., & Alefeld, G. (1998). A cost

effective absorption chiller with plate heat exchangers using water and hydroxides. *Applied Thermal Engineering, 18*, 413-425.

Foos, M., Frantz, C., & Gantois, M. (1975). Shape memory effect and anelasticity associated with the martensitic transformation in the Stoechiometric Fe3Pt alloy. In J. Perkins, *Shape Memory Effects in Alloys* (pp. 407-417). New York, USA: Springer.

Foster, A., Brown, T., Gigiel, A., Alford, A., & Evans, J. (2011). Air cycle combined heating and cooling for the food industry. *International Journal of Refrigeration, 34*, 1296-1304.

Friend, C., & Hamilton, S. (1995). The thermomechanical behavior of a metastable Cu-Al-Ni single crystal alloy. *Journal de Physique IV France, 5*, C2 453-458.

Fung, Y. (1965). *Foundation of Solid Mechanics.* Englewood Cliffs, NJ: Prentice-Hall Inc.

Furst, S., Crews, J., & Seelecke, S. (2012). Numerical and experimental analysis of inhomogeneities in SMA wires induced by thermal boundary conditions. *Continuum Mechanics and Thermodynamics, 24*, 485-504.

Gall, K., Sehitoglu, H., Maier, H., & Jacobus, K. (1998). Stress-induced martensitic phase transormations in polycrystalline CuZnAl shape memory alloys under different stress states. *Metallurgical and Materials Transactions A, 29*, 765-773.

Gao, Q., Yu, B., Wang, C., Zhang, B., Yang, D., & Zhang, Y. (2006). Experimental investigation on refrigeration performance of a reciprocating active magnetic regenerator of room temperature magnetic refrigeration. *International Journal*

of Refrigeration, 29, 1274-1285.

Gardner, D., & Swift, G. (1997). Use of inertance in orifice pulse tube refrigerators. *Cryogenics, 37*, 117-121.

Garrett, S. (2004). Resource letter: TA-1: Thermoacoustic engines and refrigerators. *American Journal of Physics, 72*, 11-17.

Garrett, S., Adeff, J., & Hofler, T. (1993). Thermoacoustic refrigerator for space applications. *Journal of thermophysics and heat transfer, 7*, 595-599.

Ge, Y., & Tassou, S. (2011). Thermodynamic analysis of transcritical CO2 booster refrigeration systems in supermarket. *Energy Conversion and Management, 52*, 1868-1875.

Gerlach, D. (2009). Design concepts and development of elastomer heat engines/pumps. *Proceedings of the ASME 2009 International Mechanical Engineering Congress & Exposition.* Lake Buena Vista, FL.

Gerlach, D., Alvarado, J., Mina, E., & Newell, T. (2002). Anaylsis of Elastomer Refrigeration Cycles. *International Refrigeration and Air Conditioning Conference.* West Lafayette, IN.

Gil, F., & Planell, J. (1999). Thermal efficiencies of NiTiCu shape memory alloys. *Thermochimica Acta, 327*, 151-154.

Goetzler, W., Zogg, R., Young, J., & Johnson, C. (2014). *Energy Savings Potential and RD&D Opportunities for Non-Vapor-Compression HVAC Technologies.* Burlington, MA: Navigant Consulting Inc.

Goetzler, W., Zogg, R., Young, J., & Schmidt, J. (2012). *Energy Savings Potential and RD&D Opportunities for Residential Building HVAC Systems.*

Burlington, MA: Navigant Consulting Inc.

Golberg, D., Xu, Y., Murakami, Y., Morito, S., & Otsuka, K. (1995). Characteristics of Ti50Pd30Ni20 high-temperature shape memory alloy. *Intermetallics, 3*, 35-46.

Gomez, J. G. (2013). Magnetocaloric effect: a review of the thermodynamic cycles in magnetic refrigeration. *Renewable and Sustainable Energy Review*, 74-82.

Gschneidner, K., & Pecharsky, V. (2000). Magnetocaloric materials. *Annual Review of Material Science, 30*, 387-429.

Gschneidner, K., Pecharsky, V., & Tsokol, A. (2005). Recent developments in magnetocaloric materials. *Reports on Progressin Physics, 68*, 1479-1539.

Gu, H., Qian, X., Li, X., Craven, B., Zhu, W., Cheng, A., . . . Zhang, Q. (2013). A chip scale electrocaloric effect based cooling device. *Applied Physics Letters, 102*, 4.

Guo, D., Gao, J., Yu, Y., Santhanam, S., Slippey, A., Fedder, G., . . . Yao, S. (2014). Design and modeling of a fluid-based micro-scale electrocaloric refrigeration system. *International Journal of Heat and Mass Transfer, 72*, 559-564.

Guo, D., McGaughey, A., Gao, J., Fedder, G., Lee, M., & Yao, S. (2013). Multiphysics modeling of a micro-scale Stilring refrigeration system. *International Journal of Thermal Sciences, 74*, 44-52.

Gutierrez-Urueta, G., Rodriguez, P., Venegas, M., Zieler, F., & Rodriguez-Hidalgo, M. (2011). Experimental performances of a LiBr-water absorption facility equipped with adiabatic absorber. *International Journal of Refrigeration, 34*, 1749-1759.

Haar, L. G. (1984). *NBS/NRC Steam Tables.* New York: Hemisphere Publishing Corp.

Harkonen, M., & Aittomaki, A. (1991). The principle of internal regeneration as applied to the adsorption heat pump process. *Heat Recovery Systems & CHP, 11*, 239-248.

Hermes, C., Melo, C., & Goncalves, J. (2008). Modeling of non-adiabatic capillary tube flows: A simplified approach and comprehensive experimental validation. *International Journal of Refrigeration, 31*, 1358-1367.

Herold, K., Radermacher, R., & Klein, S. (1996). *Absorption Chillers and Heat Pumps.* Boca Raton, FL: CRC Press.

Hu, J., & Xiao, J. (1995). New method for analysis of active magnetic regenerator in magnetic refrigeration at room-temperature. *Cryogenics, 35*, 101-104.

Huang, W. (2003). On the selection of shape memory alloys for actuators. *Materials & Design, 23*, 11-19.

Hugenroth, J. (2002). *USA Patent No. US6367281 B1.*

Hutchinson, W. (1971). *USA Patent No. US3599443 A.*

Jacobs, S., Auringer, J., Boeder, A., Chell, J., Komorowski, L., Leonard, J., . . . Zimm, C. (2014). The performance of a large-scale rotary magnetic refrigerator. *International Journal of Refrigeration, 37*, 84-91.

Jani, J., Leary, M., Subic, A., & Gibson, M. (2014). A review of shape memory alloy research, applications and opportunities. *Materials & Design, 56*, 1078-1113.

Jia, Y., & Ju, Y. (2012). A solid-state refrigerator based on the electrocaloric effect. *Applied Physics Letter, 100*, 242901.

Johnson, A. (1977). *USA Patent No. US4055955 A.*

Johnson, A. (1985). *USA Patent No. US4490976 A.*

Kanada, T. (2008). A new drive system using a shape memory alloy (SMA) heat engine and its applications. *Journal of Optoelectronics and Advanced Materials, 10*, 1061-1063.

Kaneko, K., & Enomoto, K. (2011). Development of reciprocating heat engine using shape memory alloy. *Journal of Environment and Engineering, 6*, 131-139.

Kang, H., Choi, K., Park, C., & Kim, Y. (2007). Effects of accumulator heat exchangers on the performance of a refrigeration system. *International Journal of Refrigeration, 30*, 282-289.

Kirkpatrick, S., Siahmakoun, A., Adams, T., & Wang, Z. (2008). *USA Patent No. US20060162331 A1.*

Kitanovski, A. E. (2006). Thermodynamics of magnetic refrigeration . *International Journal of Refrigeration*, 3-21.

Klein, S., Reindl, D., & Brownell, K. (2000). Refrigeration system performance using liquid-suction heat exchangers. *International Journal of Refrigeration, 23*, 588-596.

Krishnan, R., & Brown, L. (1973). Pseudoelasticity and the strain-memory effect in an Ag-45 at. pct Cd alloy. *Metallurgical Transactions, 4*, 423-429.

Kuriyama, T., Ohtani, Y., Takahashi, M., Nakagome, H., Nitta, H., Tsukagoshi, T., . . . Hashimoto, T. (1996). Optimization of operational parameters for a 4K-GM refrigerator. *Advances in Cryogenic Engineering, 41*, 1615-1622.

Lashley, J., Drymiotis, F., Safarik, D., & Smith, J. (2007). Contribution of low-

frequency modes to the specific heat of Cu-Zn-Al shape-memory alloys. *Physics Review B, 75*, 064304.

Legait, U., Guillou, F., Kedous-Lebouc, A., Hardy, V., & Almanza, M. (2014). An experimental comparison of four magnetocaloric regenerators using three different materials. *International Journal of Refrigeration, 37*, 147-155.

Lemmon, E. (2003). Pseudo-pure fluid equations of state for the refrigerant blends R-410A, R-404A, R-507A, and R-407C. *International Journal of Thermophysics*, 991-1006.

Lerou, P., Veenstra, T., Burger, J., ter Brake, H., & Rogalla, H. (2005). Optimization of counterflow heat exchanger geometry through minimization of entropy generation. *Cryogenics, 45*, 659-669.

Liang, C. R. (1992). One-dimensional thermomechanical constitutive relations for shape memory alloys. *Journal of Engineering Mathematics*, 429-443.

Lieberman, D., Wechsler, M., & Read, T. (1955). Cubic to orthorhombic diffusionless phase change - experimental and theoretical studies of AuCd. *Journal of Applied Physics, 26*, 473-484.

Liu, J. K. (2011). Systematic study of the microstructure, entropy change and adiabatic temperature change in optimized La-Fe-Si alloys. *Acta Materialia*, 3602-3611.

Liu, P. W. (2010). Huge electrocaloric effect in Langmuir-Blodgett ferroelectric polymer thin films. *New Journal of Physics*, 023035.

Liu, Y. (2004). The work production of shape memory alloy. *Smart Materials and Structures, 13*, 552-561.

Liu, Y., Wang, R., & Xia, Z. (2005). Experimental study on a continuous adsorption water chiller with novel design. *International Journal of Refrigeration, 28*, 218-230.

Lu, Z. W. (1997). Martensitic transformation and stress-strain relations of shape memory alloys. *Journal of Mechanics and Physics of Solids*, 1905-1928.

Lyon, R., Wang, D., Farris, R., & MacKnight, W. (1984). Polyurethane-urea elastomers as working substances in rubber heat engines. *Journal of Applied Polymer Science, 29*, 2857-2872.

Maki, T. (1998). Ferrous shape memory alloys. In K. Otsuka, & C. Wayman, *Shape Memory Materials* (pp. 129-131). Cambridge: Cambridge University Press.

Maki, T., Kobayashi, K., Minato, M., & Tamura, I. (1984). Thermoelastic martensite in an ansaged Fe-Ni-Ti-Co alloy. *Scripta Metallurgica, 18*, 1105-1109.

Manosa, L., Farnos, S., Vives, E., & Planes, A. (2013). Large temperature span and giant refrigerant capacity in elastocaloric Cu-Zn-Al shape memory alloys. *Applied Physics Letter, 103*, 4832339.

Manosa, L., Planes, A., & Ortin, J. (1993). Entropy change of martensitic transformations in Cu-based shape memory alloys. *Physical Review B, 48*, 3611-3619.

Manosa, L., Planes, A., & Vives, E. (2009). The use of shape-memory alloys for mechanical refrigeration. *Functional Materials Letter, 2*, 73-78.

Mastrullo, R., Mauro, A., Tino, S., & Vanolo, G. (2007). A chart for predicting the possible advantage of adopting a suction/liquid heat exchanger in refrigerating system. *Applied Thermal Engineering, 27*, 2443-2448.

Matsumoto, K., & Hashimoto, T. (1990). Thermodyanmic anaylsis of magnetically active regenerator from 30 to 70-K with a Brayton-like cycle. *Cryogenics, 30*, 840-845.

Maytal, B., Nellis, G., Klein, S., & Pfotenhauer, J. (2006). Elevated-pressure mixed-coolants Joule-Thomson cryocooling. *Cryogenics, 46*, 55-67.

McMahon, H., & Gifford, W. (1960). A new low-temperature gas expansion cycle. *Advances in Cryogenic Engineering, 5*, 354-367.

McNicholds, J. C. (1987). Thermodynamics of nitinol. *Journal of Applied Physics*, 972.

Mikulink, E., Tarasov, A., & Shkrebyonock, M. (1984). Low-temperature expansion pulse tubes. *Advances in Cryogenic Engineering, 29*, 629-637.

Miles, D., & Shelton, S. (1996). Design and testing of a solid-soprtion heat-pump system. *Applied Thermal Engineering, 16*, 389-394.

Mischenoko, A. Z. (2006). Giant electrocaloric effect in thin-film PbZr0.95Ti0.05O3. *Science*, 1270-1271.

Mitchell, J., & Meier, D. (1968). Rapid stress-induced crystallization in natural rubber. *Journal of Polymer Science Part A-2: Polymer Physics, 6*, 1689-1703.

Miura, S., Maeda, S., & Nakanishi, N. (1974). Pseudoelasticity in Au-Cu-Zn thermoelastic matensite. *Philosophical Magazine, 30*, 565-581.

Miura, S., Moruta, Y., & Nakanishi, N. (1975). Superelasticity and shape memory effect in Cu-Sn alloys. In J. Perkins, *Shape Memory Effects in Alloys* (pp. 389-405). New York, USA: Springer.

Miya, N., Sakamotor, S., & Watanabe, Y. (2008). Effect of copper mesh at interface

between stack and heat source in thermoacoustic cooling system. *Japanese Journal of Applied Physics, 47*, 4235-4238.

Mohanraj, M., Jayaraj, S., & Muraleedharan, C. (2009). Environment friendly alternatives to halogenated refrigerants - a review. *International Journal of Greenhouse Gas Control, 3*, 108-119.

Moore, J. M. (2009). Metamagnetism seeded by nanostructural features of single-crystalline Gd5Si2Ge2 . *Advanced Materials*, 3780-3783.

Moran, M. S. (2011). *Fundamentals of Engineering Thermodynamics (7th edition).* Hoboken, NJ: John Wiley & Sons.

Moya, X. D. (2015). Too cool to work. *Nature Physics*, 202-205.

Muller, I., & Xu, H. (1991). On the pseudo-elastic hysteresis. *Acta Metallurgica et Materialia, 39*, 263-271.

Nam, T., Saburi, T., & Shimizu, K. (1990). Cu-content dependence of shape memory characteristics in Ti-Ni-Cu alloys. *Materials Transactions JIM, 31*, 959-967.

Nast, T., Olson, J., Roth, E., Evtimov, B., Frank, D., & Champagne, P. (2007). Development of remote cooling systems for low-temperature, space-borne systems. *Cryocoolers, 14*, 33-40.

Navarro-Esbri, J., Cabello, R., & Torrella, E. (2005). Experimental evaluation of the internal heat exchanger influence on a vapour compression plant energy efficiency working with R22, R134a and R407C. *Energy, 30*, 621-636.

Neese, B. C. (2008). Large electrocaloric effect in ferroelectric polymers near room temperature. *Science*, 821-823.

Ng, K., Xue, H., & Wang, J. (2002). Experimental and numerical study on a

miniature Joule-Thomson cooler for steady-state characteristics. *International Journal of Heat and Mass Transfer, 45*, 609-618.

Nielsen, K., Bahl, C., Smith, A., Pryds, N., & Hattel, J. (2010). A comprehensive parameter study of an active magnetic regenerator using a 2D numerical model. *International Journal of Refrigeration, 33*, 753-764.

Nietsch, T. (1996). Isothermal curves and kinetics in a metal hydride. *International Journal of Hydrogen Energy, 21*, 985-991.

Nikitin, S., Myalikgulyev, G., Annaorazov, M., Tyurin, A., Myndyev, R., & Akopyan, S. (1992). Giant elastocaloric effect in FeRh alloy. *Physics Letters A, 171*, 234-236.

Nsofor, E., & Ali, A. (2009). Experimental study on the performance of the thermoacoustic refrigerating system. *Applied Thermal Engineering, 29*, 2672-2679.

Organ, A. (1999). The miniature, reversed Stirling cycle cryo-cooler: integrated simulation of performance. *Cryogenics, 39*, 253-266.

Ossmer, H. M. (2015). Elastocaloric heat pumping using a shape memory alloy foil device. *2015 TRANSDUCERS.* Anchorage, AL, USA.

Otsuka, K. R. (2005). Physical metallurgy of Ti-Ni-based shape memory alloys. *Progress in Material Science*, 511-678.

Otsuka, K., & Wayman, C. (1998). *Shape Memory Materials.* Cambridge, UK: Cambridge University Press.

Ozbolt, Z., Kitanovski, A., Tusek, J., & Poredos, A. (2014). Electrocaloric refrigeration: Thermodynamics, state of the art and future perspective.

International Journal of Refrigeration, 40, 174-188.

Pachter, J. (1979). *USA Patent No. US4150544 A.*

Paek, I., Braun, J., & Mongeau, L. (2007). Evaluation of standing-wave thermoacoustic cycles for cooling applications. *International Journal of Refrigeration, 30*, 1059-1071.

Pataky, G. E. (2015). Elastocaloric cooling potential of NiTi, Ni2FeGa, and CoNiAl. *Acta Materialia, 96*, 420-427.

Peyroux, R. C. (1998). Thermomechanical couplings and pseudoelasticity of shape memory alloys. *International Journal of Engineering Science*, 489-509.

Piao, M., Miyazaki, S., & Otsuka, K. (1992). Characteristics of deformation and transformation in Ti44Ni47Nb9 shape memory alloy. *Materials Transactions, JIM, 33*, 346-353.

Picornell, C., Pons, J., & Cesari, E. (2001). Stabilisation of Martensite by applying compressive stress in Cu-Al-Ni single crystals. *Acta Materialia, 49*, 4221-4230.

Picornell, C., Pons, J., & Cesari, E. (2004). Stress-temperature relationship in compression mode in Cu-Al-Ni shape memory alloys. *Materials Transactions, 45*, 1679-1683.

Picornell, C., Pons, J., & Cesari, E. (2004). Stress-temperature relationship in compression mode in Cu-Al-Ni shape memory alloys. *Materials Transactions, 45*, 1679-1683.

Planes, A., Manosa, L., Rios-Jara, D., & Ortin, J. (1992). Martensitic transformation of Cu-based shape-memory alloys: Elastic anisotropy and entropy change.

Physical Review B, 45, 7633-7639.

Pons, M., & Feng, Y. (1996). Characteristic parameters of adsorptive refrigeration cycles with thermal regeneration. *Applied Thermal Engineering, 17*, 289-298.

Pons, M., & Guilleminot, J. (1986). Design of an experimental solar-powered, solid-adsorption ice maker. *Journal of Solar Energy Engineering-Transactions of the ASME, 108*, 332-337.

Pons, M., & Poyelle, F. (1999). Adsorptive machines with advanced cycles for heat pumping or cooling applications. *International Journal of Refrigeration, 22*, 27-37.

Pons, M., Laurent, D., & Meunier, F. (1996). Experimental temperature fronts for adsorptive heat pump applications. *Applied Thermal Engineering, 16*, 395-404.

Pratt, W., Rosenblum, S., Steyert, W., & Barclay, J. (1977). A continuous demagnetization refrigerator operating near 2 K and a study of magnetic refrigerants. *Cryogenics, 17*, 689-693.

Qian, S., Gluesenkamp, K., Hwang, Y., Radermacher, R., & Chun, H. (2013). Cyclic steady state performance of adsorption chiller with low regeneration temperature zeolite. *Energy, 60*, 517-526.

Qiu, T., Wang, R., & Wang, W. (2001). Study on heat and mass recovery in adsorption refrigeration cycles. *Applied Thermal Engineering, 21*, 439-452.

Radebaugh, R. (2009). Cryocoolers: the state of the art and recent developments. *Journal of Physics: Condensed Matter, 21*, 9-18.

Radebaugh, R., Zimmerman, J., Smith, D., & Louie, B. (1986). A comparison of

three types of pulse tube refrigerators: new methods for reaching 60K. *Advances in Cryogenic Engineering, 31*, 779-789.

Radermacher, R. H. (2005). *Vapor Compression Heat Pumps with Refrigerant Mixtures.* New York: Taylor and Francis.

Razani, A. D. (2010). A model for exergy analysis and thermodynamic bounds of Stirling refrigerators. *Cryogenics*, 231-238.

Recarte, V. S. (1999). Dependence of the martensitic transformation characteristics on concentration in Cu-Al-Ni shape memory alloys. *Material Science Engineering A*, 380-384.

Reid, R., & Swift, G. (2000). Experiments with a flow-through thermoacoustic refrigerator. *Journal of the Acoustical Society of America, 108*, 2835-2842.

Riffat, S. M. (2004). Improving the coefficient of performance of thermoelectric systems: a review. *International Journal of Energy Resources*, 753-768.

Rodriguez, C., & Brown, L. (1980). The thermal effect due to stress-induced Martensite formation in beta-CuAlNi single crystals. *Metallurgical and Materials Transactions A, 11*, 147-150.

Rodriquez, E., & Filisko, F. (1982). Thermoelastic temperature changes in poly(methyl methacrylate) at high hydrostatic pressure: Experiment. *Journal of Applied Physics, 53*, 6536-6540.

Romero, R., & Pelegrina, J. (2003). Change of entropy in the martensitic transformation and its dependence in Cu-based shape memory alloys. *Materials Science and Engineering A, 354*, 243-250.

Rowe, A., & Barclay, J. (2003). Ideal magnetocaloric effect for active magnetic

regenerators. *Journal of Applied Physics, 93*, 1672-1676.

Saburi, T. (1998). Ti-Ni shape memory alloys. In K. Otsuka, & C. Wayman, *Shape Memory Materials* (pp. 75-79). Cambridge, UK: Cambridge University Press.

Sakamoto, S., & Watanabe, Y. (2004). The experimental studies of thermoacoustic cooler. *Ultrasonics, 42*, 53-56.

Sarlah, A., Kitanovski, A., Poredos, A., Egolf, P., Sari, O., Gendre, F., & Besson, C. (2006). Static and rotating active magnetic regenerators with porous heat exchangers for magnetic cooling. *International Journal of Refrigeration, 29*, 1332-1339.

Sato, H., Takezawa, K., & Sato, S. (1984). Analysis of stress-strain curves in the tensile test of Cu-Zn-Al alloy single crystals. *Transactions of the Japan Institute of Metals, 25*, 332-338.

Sato, Y., Kobayashi, M., Kobayashi, Y., Morimoto, H., & Miyawaki, H. (2011). Output power characteristics of a shape memory alloy engine. *Electrical Engineering in Japan, 174*, 19-27.

Sato, Y., Yoshida, N., Tanabe, Y., Fujita, H., & Ooiwa, N. (2008). Characteristics of a new power generation system with application of a shape memory alloy engine. *Electrical Engineering in Japan, 165*, 8-15.

Schiller, E. (2002). *Heat Engine Driven by Shape Memory Alloys: Prototyping and Design.* Blacksburg, VA: Virginia Polytechnic Institute and State University (Master Thesis).

Schimidt, M. S. (2015). Scientific test setup for investigation of shape memory alloy based elastocaloric cooling processes. *International Journal of Refrigeration,*

54, 88-97.

Schroeder, T., & Wayman, C. (1977). The formation of martensite and the mechanish of the shape memory effect in single crystals of Cu-Zn alloys. *Acta Metallurgica, 25*, 1375-1391.

Sharp, J., Bierchenk, J., & Lyon, H. (2006). Overview of solid-state thermoelectric refrigerators and possible applications to on-chip thermal management. *Proceedings of IEEE, 94*, 1602-1612.

Shelton, S., Miles, D., & Wepfer, W. (1990). Ramp wave analysis of the solid-vapor heat pump. *Journal of Energy Resources Technology, 112*, 69-78.

Shelton, S., Wepfer, W., & Miles, D. (1989). Square wave analysis of the solid-vapor adsorption heat pump. *Heat Recovery Systems & CHP, 9*, 233-237.

Shimizu, S., Xu, Y., Okunishi, E., Tanaka, S., Otsuka, K., & Mitose, K. (1998). Improvement of shape memory characteristics by precipitation-hardening of Ti-Pd-Ni alloys. *Materials Letters, 34*, 23-29.

Shin, M., Kim, C., Chuang, Y., & Jee, K. (1987). *USA Patent No. US4683721 A.*

Sittner, P., & Novak, V. (2000). Anisotropy of martensitic transformations in modeling of shape memory alloy polycrystals. *International Journal of Plasticity, 16*, 1243-2168.

Smaili, A., & Chahine, R. (1998). Thermodynamic investigations of optimum active magnetic regenerators. *Cryogenics, 38*, 247-252.

Smith, J., Luck, R., Jiang, Q., & Predel, B. (1993). The heat capacity of solid Ni-Ti alloys in the temperature range 120 to 800 K. *Journal of Phase Equilibria, 14*, 494-500.

Steyert, W. (1978). Stirling-cycle rotating magnetic refrigerators and heat engines for use near room-temperature. *Journal of Applied Physics, 49*, 1216-1226.

Sun, L., Feng, Y., & Pons, M. (1997). Numerical investigation of adsorption heat pump system with thermal wave heat regeneration under uniform-pressure conditions. *International Journal of Heat and Mass Transfer, 40*, 281-293.

Sun, L., Feng, Y., & Pons, M. (1997). Numerical investigation of adsorptive heat pump systems with thermal wave heat regeneration under uniform-pressure conditions. *International Journal of Heat and Mass Transfer, 40*, 281-293.

Sutou, Y. O. (2004). Characteristics of Cu-Al-Mn-based shape memory alloys and their applications. *Materrials Science and Engineering A, 378*, 278-282.

Swalin, R. (1962). *Thermodynamics of Solids.* New York: John Wiley & Sons, Inc.

Swift, G., D.L., G., & Backhaus, S. (1999). Acoustic recovery of lost power in pulse tube refrigerators. *The Journal of the Acoustical Society of America, 105*, 711-724.

Thombare, D. V. (2008). Technological development in the Stirling cycle engines. *Renewable and Sustainable Energy Review*, 1-38.

Tijani, M., Zeegers, J., & de Waele, A. (2002). The optimal stack spacing for thermoacoustic refrigeration. *Journal of the Acoustical Society of America, 112*, 128-133.

TillnerRoth, R. B. (1994). An international standard formulation for the thermodynamic properties of 1,1,1,2-tetrafluoroethane (HFC-134a) for temperatures from 170 K to 455 K and pressures up to 70 MPa. *Journal of Physical and Chemical Reference Data*, 657-729.

TillnerRoth, R. H.-W. (1993). Eine neue fuandamentalgleichung fur ammoniak. *DKV-Tagungsbericht*, 167-181.

TillnerRoth, R. Y. (1997). An international standard formulation for difluomethane (R32) fro temperatures from the triple point at 136.34 K to 435 K and pressures up to 70 MPa. *Journal of Physical and Chemical Reference Data*, 1273-1328.

Tishin, A. S. (2003). *The magnetocaloric effect and its applications.* Bodmin: IOP Publishing Ltd.

Tong, H., & Wayman, C. (1974). Characteristic temperatures and other properties of thermoelastic martensites. *Acta Metallurgica, 22*, 887-896.

Tritt, T. (2011). Thermoelectric phenomena, materials, and applications. *Annual Review of materials research*, 433-448.

Tusek, J. E. (2015a). Elastocaloric effect of Ni-Ti wire for application in a cooling device. *Journal of Applied Physics*, 124901.

Tusek, J. E. (2015b). The elastocaloric effect: a way to cool efficiently. *Advanced Energy Materials*, DOI: 10.1002/aenm.201500361.

Tusek, J., Kitanovski, A., Prebil, I., & Poredos, A. (2011). Dynamic operation of an active magnetic regenerator (AMR): Numerical optimization of a packed-bed AMR. *International Journal of Refrigeration, 34*, 1507-1517.

Tusek, J., Kitanovski, A., Tomc, U., Favero, C., & Predos, A. (2014). Experimental comparison of multi-layered La-Fe-Co-Si and single-layered Gd active magnetic regenerators for use in a room-temperature magnetic refrigerator. *International Journal of Refrigeration, 37*, 117-126.

Tward, E., Chan, C., Raab, J., Nguyen, T., Colbert, R., & Davis, T. (2002). High efficiency pulse tube cooler. *Cryocoolers, 11*, 163-167.

Vasile, C., & Muller, C. (2006). Innovative design of a magnetocaloric system. *International Journal of Refrigeration, 29*, 1318-1326.

Ventas, R., Vereda, C., Lecuona, A., & Venegas, M. (2012). Experimental study of a thermochemical compressor for an absorption/compression hybrid cycle. *Applied Energy, 97*, 297-304.

Veprik, A., Riabzev, S., Vilenchik, G., & Pundak, N. (2005). Ultra-low vibration split Stirling linear cryogenic cooler with a dynamically counterbalanced pneumatically driven expander. *Cryogenics, 45*, 117-122.

Wakjira, J. (2001). *The VT1 Shape Memory Alloy Heat Engine Design.* Blacksburg, VA: Virginia Polytechnic Institute and State University (Master Thesis).

Walker, G., & Vasishta, V. (1971). Heat-transfer and flow-friction characteristics of dense-mesh wire-screen Stirling-cycle regenerators. *Advances in Cryogenic Engineering, 16*, 324-332.

Watanabe, A., Swift, G., & Brisson, J. (1996). Measurements with a recuperative superfluid Stirling refrigerator. *Advances in Cryogenic Engineering, 41*, 1527-1533.

Wayman, C., & Tong, H. (1975). On the efficiency of the shape memory effect for energy conversion. *Scripta Metallurgica, 9*, 757-760.

Wittorf, M., Browne, A., Johnson, N., & Brown, J. (2012). *USA Patent No. US8299637 B2.*

Xiao, F. J. (2015). Elastocaloric effect in Ni50Fe19Ga27Co4 single crystals. *Acta*

263

Materialia, 96, 292-300.

Xiao, F., Fukuda, T., & Kakeshita, T. (2013). Significant elastocaloric effect in a Fe-31.2Pd (at. %) single crystal. *Applied Physics Letters, 102*, 161914.

Xue, H., Ng, K., & Wang, J. (2001). Performance evaluation of the recuperative heat exchanger in a miniature Joule-Thomson cooler. *Applied Thermal Engineering, 21*, 1829-1844.

Yamashita, O. O. (2009). Effect of the cooling rate on the thermoelectric properties of p-type Bi0.25Sb0.75Te3 and n-type Bi2Te0.94Se0.06 after melting in the bismuth-telluride system. *Material Research Bulletin*, 1352-1359.

Yan, A. M. (2008). Magnetocaloric effect in LaFe11.8-xCoxSi1.2 meltspun ribbons. *Journal of Alloys Compound*, 18-21.

Yang, C., & Bansal, P. (2005). Numerical investigation of capillary tube-suction line heat exchanger performance. *Applied Thermal Engineering, 25*, 2014-2028.

Yazaki, T., Biwa, T., & Tominaga, A. (2002). A pistonless Stirling cooler. *Applied Physics Letter, 80*, 157-159.

Yin, H., Yan, Y., Huo, Y., & Sun, Q. (2013). Rate dependent damping of single crystal CuAlNi shape memory alloy. *Materials Letters, 109*, 287-290.

Yu, B., Liu, M., Eggolf, P., & Kitanovski, A. (2010). A review of magnetic refrigerator and heat pump prototypes built before the year. *International Journal Refrigeration, 33*, 1029-1060.

Zagarola, M., & McCormick, J. (2006). High-capacity turbo-Brayton cryocoolers for space applications. *Cryogenics, 46*, 169-175.

Zhang, L., Sherif, S., DeGregoria, A., Zimm, C., & Veziroglu, T. (2000). Design

optimization of a 0.1-ton/day active magnetic regenerative hydrogen liquefier. *Cryogenics, 40*, 269-278.

Zhao, D. T. (2014). A review of thermoelectric cooling: materials, modeling and applications. *Applied Thermal Engineering*, 15-24.

Zhu, J., Liang, N., Huang, W., & Liew, K. (2001b). Energy conversion in shape memory alloy heat engine Part II: simulation. *Journal of Intelligent Material Systems and Structures, 12*, 133-140.

Zhu, J., Liang, N., Liew, K., & Huang, W. (2001a). Energy conversion in shape memory alloy heat engine Part I: theory. *Journal of Intelligent Material Systems and Structures, 12*, 127-132.

Zhu, S., Zhou, S., Yoshimura, N., & Matsubara, Y. (1997). Phase shift effect of the long neck tube for the pulse tube refrigerator. *Cryocoolers, 9*, 269-278.

Zimm, C., Boeder, A., Chell, J., Sternbery, A., Fujita, A., Fujieda, S., & Fukamichi, K. (2006). Design and performance of a permanent-magnet rotary refrigerator. *International Journal of Refrigeration, 29*, 1302-1306.

Ziolkowski, A. (1993). Theoretical analysis of efficiency of shape memory alloy heat engines (based on constitutive models of pseudoelasticity). *Mechanics of Materials, 16*, 365-377.